UNIVERSIDAD NACIONAL AUTÓNOMA DE MÉXICO
PROGRAMA DE MAESTRÍA Y DOCTORADO EN INGENIERÍA
ENERGÍA – SISTEMAS ENERGÉTICOS

ANALYSIS OF THE THERMAL-HYDRAULIC AND STRUCTURAL PERFORMANCE OF A PRINTED CIRCUIT HEAT EXCHANGER OF A HYDROGEN PRODUCTION SYSTEM COUPLED TO A HIGH-TEMPERATURE GAS NUCLEAR REACTOR

TESIS
QUE PARA OPTAR POR EL GRADO DE:
DOCTOR EN INGENIERÍA

PRESENTA:
RACIEL DE LA TORRE VALDÉS

TUTOR PRINCIPAL
DR. JUAN LUIS FRANÇOIS LACOUTURE, FI-UNAM
COMITÉ TUTOR
DRA. CECILIA MARTIN DEL CAMPO MÁRQUEZ, FI-UNAM
DR. JAIME BALTAZAR MORALES SANDOVAL, FI-UNAM
DR. GILBERTO ESPINOSA PAREDES, UAM-IZTAPALAPA
DR. WILLIAM VICENTE Y RODRÍGUEZ, IE-UNAM

CIUDAD UNIVERSITARIA, CD. MX., NOVIEMBRE 2020

JURADO ASIGNADO:

Presidente:	DR. WILLIAM VICENTE Y RODRIGUEZ
Secretario:	DRA. CECILIA MARTIN DEL CAMPO MÁRQUEZ
1 er. Vocal:	DR. JUAN LUIS FRANÇOIS LACOUTURE
2 do. Vocal:	DR. GILBERTO ESPINOSA PAREDES
3 er. Vocal:	DR. JAIME BALTAZAR MORALES SANDOVAL

Lugar o lugares donde se realizó la tesis:

TUTOR DE TESIS:

DR. JUAN LUIS FRANÇOIS LACOUTURE

FIRMA

ACKNOWLEDGMENTS

To my little son Ryan de la Torre

ABSTRACT

The Printed Circuit Heat Exchanger (PCHE) is an important candidate to be used as Intermediate Heat Exchanger (IHX) in High Temperature Gas-cooled Reactor (HTGR) plants due to its advantages in terms of heat transfer and compactness. As well as the heat transfer is relatively high in the PCHE, the pressure drop is also greater than the values in the conventional designs of similar dimensions. The IHX presents challenging operating conditions that include fluid temperatures up to 1223 K and pressures higher than 7 MPa. Therefore, the thermal-hydraulic performance and the structural integrity of the device must be investigated in depth to achieve a highly efficient and safety operation. In this research, computational models of the PCHE were developed using computational fluid dynamics (CFD) and finite element analysis (FEA) to analyze its thermal-hydraulic and structural performances under operating conditions as those in the IHX of an HTGR plant.

The thermal-hydraulic performance study was conducted in straight and zigzag channels PCHE within wide design parameter ranges using three-dimensional models. The Nusselt number and the Fanning friction factor obtained from simulations were validated by experimental data available. The Taguchi method was used to consider the interaction among the parameters with a reduced computing time. Optimized designs were proposed to reach the highest Nusselt number and lowest friction losses using the signal to noise ratio as an objective function. It was found that the zigzag angle has contribution ratios around 50% and 70% on the values of pressure drop and heat transfer, respectively. To consider the heat transfer and the friction loss, blending parameters were used to propose general optimized designs. Finally, Nusselt number and Fanning friction factor correlations were proposed as functions of the Reynolds number and the zigzag channel dimensions. The new correlations were found to be more accurate as compared to existing ones in the literature.

The structural assessment of the PCHE was done considering the temperature gradient and the internal pressures as loads. The mechanical stress caused by pressure in the channel wall was evaluated for different geometric designs. The influence of the thermal field and the geometric parameters on the thermal stress was investigated. The temperature gradient between channels was changed in a range from 10 K to 250 K. However, these values were found as the mean values of the temperature difference between the cold and hot fluids. The real temperature gradient between the channel walls was lower than those. The design of the straight channel PCHE was studied changing the cross-sectional dimensions in a pseudo-two-dimensional model, while the design of the zigzag channel PCHE was analyzed for different zigzag dimensions in a three-dimensional model. The isochronous strain–stress curves presented in the American Society of Mechanical Engineers (ASME) Boiler and Pressure Vessel Code (BPVC) for use of the Alloy 617 (UNS N06617) at high temperature, were used to develop a multilinear plasticity material model. A proportional relationship between the thermal stress and the thermal gradient between channels was found. The rounded tip radius of the semicircular cross-section was found as the main dimension to reduce both thermal and mechanical stresses reducing the stress concentration in this zone. The reduction of the zigzag angle was decisive to decrease the thermal stress concentration at zones where the fluids change their direction. The roundness of the zigzag bend was essential to reduce the effect of the change of direction at high zigzag angles. Based on the allowable stress of the structural material, the safety ranges of the geometric parameters in the PCHE design were proposed. The structural integrity of the zigzag channel PCHE with different designs were assessed under IHX and laboratory conditions.

RESUMEN

El intercambiador de calor de unión por difusión (PCHE) es un importante candidato para ser usado como intercambiador de calor intermedio (IHX) en las instalaciones con reactores nucleares de alta temperatura enfriados por gas (HTGR) debido a las ventajas que éste ofrece en términos de transferencia de calor y compactación. En los PCHE puede obtenerse una mayor transferencia de calor que en los diseños convencionales de intercambiadores con dimensiones similares, pero las pérdidas por caída de presión también son considerables. Las complejas condiciones de operación presentes en esta aplicación incluyen temperaturas del fluido caliente tan altas como 1173 K y presiones de los fluidos superiores a 7 MPa. Por lo tanto, el funcionamiento termo-hidráulico y estructural de los PCHE debe ser investigado de forma exhaustiva. En esta investigación fueron desarrollados modelos computacionales de los PCHE empleando dinámica de fluidos computacional (CFD) y análisis de elementos finitos (FEA) para analizar el rendimiento termo-hidráulico y estructural de estos equipos bajo condiciones de operación similares a las presentes en los IHX en instalaciones con HTGR.

El estudio del funcionamiento termo-hidráulico de los PCHE de canales rectos y en zigzag fue realizado considerando amplios rangos de los parámetros de diseño y utilizando modelos computacionales en tres dimensiones. Estos fueron validados mediante la comparación de los resultados obtenidos con datos experimentales del número de Nusselt y del factor de fricción de Fanning disponibles en la literatura. Con el objetivo de considerar la interacción entre los parámetros de estudio en un tiempo de cálculo reducido, el método de Taguchi fue utilizado para reducir la cantidad de diseños geométricos a considerar en el estudio. Fueron propuestos diseños optimizados para obtener el mayor número de Nusselt y el menor factor de fricción. También fueron empleados dos factores para encontrar diseños óptimos considerando la transferencia de calor y la caída de presión en un único parámetro. El ángulo del zigzag fue obtenido como el de mayor influencia en el rendimiento del intercambiador, con una contribución media de alrededor del 50% en la caída de presión y del 70% en la transferencia de calor. El mayor aporte de este análisis fue la obtención de correlaciones para calcular el número de Nusselt y el factor de fricción de Fanning en los PCHE de canales en zigzag como funciones del número de Reynolds y de las dimensiones características de los estos canales. Estas nuevas correlaciones mostraron mayor exactitud que las encontradas en la literatura.

La evaluación estructural de los PCHE fue realizada considerando el gradiente de temperatura y la presión de los fluidos como condiciones de carga. El esfuerzo mecánico causado por las presiones en la pared de los canales se evaluó para diferentes diseños geométricos. Fue obtenida la influencia de la distribución de temperatura y de los parámetros geométricos en la distribución de esfuerzo térmico. El gradiente de temperatura entre la pared de los canales fue estudiado en un rango desde 10 K hasta 250 K. No obstante, estos valores fueron encontrados como valores medios de la diferencia de temperatura entre los fluidos frío y caliente. El valor real del gradiente de temperatura entre las paredes de los canales fue menor. El diseño del PCHE de canales rectos fue estudiado para diferentes dimensiones de la sección transversal usando un modelo pseudo bidimensional, mientras que el diseño del PCHE de canales en zigzag fue analizado para diferentes dimensiones del camino zigzagueante empleando un modelo tridimensional. Las gráficas isócronas de esfuerzo vs. elongación de la aleación 617 (UNS N06617) a alta temperatura presentada en el ASME BPVC fueron utilizadas para desarrollar un modelo de plasticidad del material multilineal. Fue observada una relación proporcional entre el esfuerzo térmico y el gradiente de temperatura entre los

6

canales. El radio de las esquinas redondeadas del perfil semicircular del PCHE fue encontrado como el principal parámetro para reducir la concentración de los esfuerzos térmicos y mecánicos en estas zonas. La reducción del ángulo del camino zigzagueante fue decisiva para disminuir la concentración de esfuerzo térmico en las zonas donde el fluido cambia su dirección. Lo más efectivo para reducir este efecto fue redondear la esquina de cada zigzag cuando el ángulo para el cambio de dirección se incrementa. Teniendo en cuenta el esfuerzo admisible del material estructural, fueron propuestos rangos confiables de los parámetros de diseño. Por último, la integridad estructural del PCHE de canales en zigzag con diferentes diseños fueron evaluados bajo condiciones de operación de laboratorio y como IHX.

TABLE OF CONTENTS

LIST OF FIGURES

12

15

LIST OF TABLES

SYMBOLS AND ACRONYMS

Symbols

A	Heat transfer area [m^2]		P_m	Primary membrane stress [Pa]
A_{cs}	Cross-sectional area of the channel [m^2]		P_L	Local primary membrane stress [Pa]
b_i	Body force [N/m^3]		Pr	Prandtl number
Br	Zigzag bend radius [m]		q	Heat transfer rate [W]
C_C	Capital cost ($)		Q_b	Secondary bending stress [Pa]
C_E	Electricity cost ($/kWh)		Q_m	Secondary membrane stress [Pa]
C_M	Material cost ($/kg)		r	Rounded tip radius [m]
C_O	Operating cost ($/y)		Re	Reynolds number
c_p	Specific heat at constant pressure [W/(kgK)]		R_f''	Fouling resistance [m^{2}K/W]
D	Channel diameter [m]		s_i	Displacement [m]
D_h	Hydraulic diameter [m]		S	Stress intensity [Pa]
E	Young's modulus [Pa]		S_a	Allowable stress for a given number of cycles [Pa]
f	Fanning friction factor			
F	Peak stress [Pa]		S_m	Time-independent allowable stress [Pa]
G	Shear modulus [Pa]		S_{mt}	Allowable stress intensity [Pa]
h	Local heat transfer coefficient [W/(m^{2}K)]		S_o	Maximum allowable stress intensity under Design Loadings [Pa]
H	Enthalpy [J]			
i	Specific enthalpy [J/kg]		S_t	Time-dependent allowable stress [Pa]
I	Unit tensor		S_u	Ultimate tensile stress [Pa]
j	Colburn factor		S_y	Yield Stress [Pa]
JF	JF factor (relates j and f)		SNR	Signal-Noise Ratio
k	Thermal conductivity [W/(m^{2}K)]		T	Temperature [K]
K	Geometry factor to assess stress intensity		T_b	Bulk temperature of the fluid [K]
l_Z	Zigzag length [m]		t_f	Ridge thickness [m]
L_R	Real channel length [m]		t_p	Plate thickness [m]
$\dot{m}$	Mass flow rate [kg/s]		T_s	Surface temperature [K]
M	Mass [kg]		u	Flow velocity [m/s]
NPS	Noise performance statistics		U	Overall heat transfer coefficient [W/(m^{2}K)]
NTU	Number of heat transfer units		V	Volume [m^3]
Nu	Nusselt number		W_E	Compressor work [W]
P	Internal pressure [Pa]		x_{hl}	Hydrodynamic entry length [m]
P_b	Primary bending stress [Pa]		x_{tl}	Thermal entry length [m]
P_{cs}	Cross-sectional perimeter of the channel [m]		y	Value of the objective function

Greek symbols

α	Zigzag angle [degrees]		ε_{ij}	Shear strain
α_L	Coefficient of linear expansion [1/K]		η	Predicted values of the NPS

δ_{TM}	Relative error of the Taguchi method prediction [%]		λ	Zigzag phase-shift
ΔP	Pressure drop [Pa]		μ	Fluid viscosity [Pa $\cdot$ s]
ΔT	Temperature gradient [K]		v	Poisson's ratio
ΔT_{ml}	Log. mean temperature difference [K]		ρ	Density [kg/m^3]
ε_i	Normal strain		σ	Tensile stress [Pa]
			τ	Shear stress [Pa]

Subscripts

ac	Acceleration loss		m	Mechanical
ave	Average value		max	Maximum value
c	Cold fluid		o	Channel outlet
f	Fluid domain		s	Solid domain
$fric$	Friction loss		t	Total
h	Hot fluid		th	Thermal
i	Channel inlet			

Acronyms

ASME	American Society of Mechanical Engineers
BPVC	Boiler and Pressure Vessel Code
CFD	Computational Fluid Dynamics
CHE	Compact Heat Exchanger
FEA	Finite Element Analysis
FSI	Fluid-Structure Interaction
HTE	High Temperature Electrolysis
HTGR	High Temperature Gas-cooled Reactor
IHX	Intermediate Heat eXchanger
NGNP	Next Generation of Nuclear Plants
OSFHE	Offset Strip-Fin Heat Exchanger
PCHE	Printed Circuit Heat Exchanger
PCU	Power Conversion Unit
PFHE	Plate Fin Heat Exchanger
PHE	Plate Heat Exchanger
SFR	Sodium-cooled Fast Reactor
SHX	Secondary Heat eXchanger
SMR	Small Modular Reactor
TRISO	TRistructural ISOtropic fuel
VHTR	Very High Temperature Reactor

INTRODUCTION

The High Temperature Gas-cooled Reactor (HTGR) is one of the most important technologies currently being investigated in the energetic industry. The advantages of the HTGR include the possibilities of a highly efficient power cycle and hydrogen production using clean processes. Helium is the coolant of this reactor, which is planned to reach a temperature of up to 1223 K with pressures of 7~8 MPa. Many plant configurations have an Intermediate Heat Exchanger (IHX), which isolates the primary loop from the rest of the system. The high temperature condition is a challenging problem both in the reactor and in the IHX because of the structural property degradation of the materials. The low heat transfer coefficient of the gas working fluid causes a large size of the IHX if a conventional heat exchanger design is selected; compact designs have been studied in recent years for this application. The Printed Circuit Heat Exchanger (PCHE) has captured the attention of several research because it allows high compactness and improved material strength. That is a result of the high integrity reached in the diffusion bonding prosses employed during the construction stage.

The PCHE channels are chemically etching with hydraulic diameters that can be lower than 1 mm. Different configurations of the channel paths have been considered, but the most tested have been those with semicircular cross-section and straight or zigzag flow paths. The helium flow in a PCHE under IHX conditions in an HTGR plant must be in the laminar regime or low transition-to-turbulent regime because the heat transfer is enhanced with the large heat transfer area density, but the hydraulic loss is also increased. Numerous efforts have been dedicated to describing the thermal-hydraulic performance of the PCHE under the mentioned conditions.

Due to the large thermal gradient, it has been proved that the hydraulic and thermal boundary layers of the fluids in the PCHE channels do not achieve full developments. Several heat transfer correlations have been obtained through experimental tests and simulation tools. Most of them have described the Nusselt number and the Fanning friction factor in the zigzag channel designs. However, these correlations have been determined within limited ranges of the Reynolds number and the geometric design parameters. These parameters affect the creation of vortices and stagnation zones due to the constant change of the flow direction. The correlations' accuracy has not been demonstrated under different conditions to which these were obtained. The influence of the simultaneous variation of the design parameters on the thermal-hydraulic performance has not been studied enough, and the quantification of the effect of each parameter modification on the heat transfer and the hydraulic process has also not been accomplished.

The temperature gradients are inherent to the heat exchangers functioning, which must be carefully managed in the IHX function because of the thermal stress can be most dangerous than in the conventional applications. Some troubles that have been found are the notable reduction of the allowable stress of materials, the creep deformation in a prolonged time of service, and the thermal fatigue during the operation. Nevertheless, the experimental tests to study the stress and strain fields in the PCHE are unfeasible, and the analytical calculations are very imprecise due to the presence of complex temperature fields and complex geometries. The simulation has been the main option to investigate the structural performance of the PCHE, however, there are very few works on this topic in the open literature. Many issues are pending to be studied, such as the effect of the design parameters on the stress fields and the effect of the time of service on the

plastic strain. Overall, there is not a structural assessment of the PCHE safe operation under the current conditions of temperature and pressure.

This thesis was motivated by the research gaps briefly commented before, which will be presented in detail in Chapters 1 and 2. Therefore, the general objective of this research was to accomplish the analysis and the optimization of the thermal-hydraulic and structural performances of the PCHE under IHX conditions in an HTGR plant. The goals of the thermal-hydraulic study were: first, to develop more accurate heat transfer correlations within wider parameter ranges, in which the effects of the zigzag dimensions are considered; and second, to optimize the PCHE designs by considering the highest Nusselt number, the lowest Fanning friction factor, and different blending parameters as the targets. But different from previous optimizations, the interaction among the geometric parameters and the contribution ratio of each one for many Reynolds numbers were considered. The goals in the structural study were: first, to find the influence of the temperature gradient, and the cross-sectional and zigzag dimensions on the thermal and mechanical stresses and the plastic strains; second, to propose allowable design parameter ranges of the PCHE considering allowable stress of the structural material after various times of service; and third, to assess the compliance of the American Society of Mechanical Engineers (ASME) Boiler and Pressure Vessel Code (BPVC) for the PCHE under IHX conditions. For these purposes, the temperature fields obtained from the thermal-hydraulic analysis were used for the structural calculations.

Organization of this thesis

This document consists of six chapters. The high temperature gas-cooled reactor technology and the possible plant distributions are briefly presented in Chapter 1. The importance of the intermediate heat exchangers in those plants is evidenced and the available heat exchanger types for this application is compared. The advantages of the PCHE design are demonstrated and the methods to analyze the heat transfer in this design are discussed. A review of the available heat transfer correlations and the optimization studies using Computational Fluid Dynamics (CFD) techniques in the open literature is presented.

In Chapter 2, the particularities to carry out the structural analysis of the PCHE under IHX conditions in an HTGR are described. The procedures to assess the safe operation of the heat exchanger in the nuclear facilities at high temperature, according to the ASME BPVC, are presented. The special metals with better structural properties in the current conditions are compared. The analytical methods for the stress calculation are discussed and the need to use Finite Element Analysis (FEA) simulation to study stress fields in detail is demonstrated.

The computational models of the PCHE developed by means of CFD and FEA techniques are described in Chapter 3, which allows conducting the thermal-hydraulic and structural studies, respectively. The geometric domains of the PCHE and the boundary conditions applied in each study are presented. The independence of the model results with the geometry discretization is analyzed. The simplification of the geometric domains to reduce the computational cost is assessed.

Chapter 4 presents the validations of the thermal-hydraulic computational model considering the results of the available experimental data in the open literature. This model is used to analyze the influence of the

cross-sectional and zigzag dimensions on the heat transfer process. Correlations to calculate the Nusselt number and the friction factor as functions of the Reynolds number and the geometric parameters are proposed to the zigzag channel PCHE.

In Chapter 5, the results of the structural analysis of the PCHE using FEA models are discussed. The influence of the cross-sectional dimensions on the thermal and mechanical stresses is studied through a pseudo-2D model presented in Chapter 3, while the influence of the zigzag dimensions is investigated using a reduced 3D model of a single zigzag bend. The fluid-structure interaction is considered to obtain more realistic thermal stress fields as functions of the temperature fields. Safe geometric designs are proposed according to the allowable stresses of the structural material at different times of service.

Finally, Chapter 6 presents the most important conclusions of this research. The main contributions of the thermal-hydraulic and structural performance analysis of the PCHE are highlighted. Possible future work about the PCHE use in the Very High Temperature Reactors is recommended by the author based on the results of this research.

1. INTERMEDIATE HEAT EXCHANGER OPERATION IN AN HTGR PLANT

One of the most important objectives of science today is to achieve a sustainable energy scenario worldwide. The increase in the electricity demand coupled with increasingly higher levels of pollution because of the use of fossil fuels has boosted the interest in the Next Generation of Nuclear Plants (NGNP). The Very High Temperature Reactor (VHTR) is one of the most important technologies within this next generation. The efficient hydrogen production coupled with the nuclear reactor is an important possibility that allows the VHTR. In this chapter, the main characteristics of those plants are presented and the functions of the heat exchangers there are described.

1.1. Hydrogen production system coupled in a high temperature gas-cooled reactor plant

The VHTR can be cooled by molten salts, liquid metals, or gases [1]. All these designs present the common behavior of complex fluid conditions that include high temperatures and pressures, and corrosive environments. The High Temperature Gas-cooled Reactors (HTGR) are those cooled by helium. They allow the electricity generation using a Brayton cycle, which has been demonstrated to be more efficient and simpler than the Rankine cycles [1]. The Brayton cycle potentially allows thermal efficiencies of up to 65% (although 45-55% is more typical) compared with a maximum of 47% for the Rankine cycle (with a typical range of 33-40%) [2].

The use of hydrogen as an energy carrier is a prominent topic in the current development of the energy sector since it avoids greenhouse gas emissions, and many applications such as fuel cells and large power stations are possible [3]. Nowadays, the main hydrogen production methods are the conventional inefficient electrolysis and the natural gas reforming, which are fossil fuel dependent and low efficient. But the hydrogen production coupled to an HTGR plant can reach high efficiency by means of high temperature processes, as the sulfur-iodine thermochemical water splitting system [4][5] or the high temperature electrolysis (HTE) [4]. That is a fundamental attraction of HTGR technology. Other high temperature applications such as water desalination, petroleum refining, bio-fuels production are also available [1].

Among the HTGR characteristics highlight the presence of a thermal neutron spectrum, the use of tristructural isotropic (TRISO) fuel, graphite as moderator, and helium as coolant. The reactor outlet temperature is in a range from 1173 K to 1223 K with fluid pressure around 7 MPa [6]. Two HTGR design concepts are being studied: the prismatic reactor and the pebble bed reactor. The first one has cylindrical fuel compacts stacked inside channels, which are penetrated hexagonal graphite blocks. The fuel blocks form an annulus between an inner reflector and an outer reflector. The annular core array guarantees the inherent safety under all accident and transient conditions. The pebble bed reactor design is an annular bed filled with fuel spheres that are introduced at the top of the bed and removed at the bottom. That offers the possibility of a continuous refueling, which reduces the required shut-down frequency and allows operation with very small excess reactivity. Helium coolant fills the interstitial void that makes up about 39% of the pebble bed volume [6].

The HTGR technology has been tested since the 1960's decade through some designs with different sizes, outlet temperatures, primary fluids, and purposes [1][6]. The prismatic reactors examined are Dragon in the

United Kingdom, High Temperature Test Reactor (HTTR) in Japan, and Peach Bottom 1 and Fort St. Vrain (FSV) in the United States. The pebble-bed reactors investigated are Arbeitsgemeinschaft Versuchsreaktor (AVR) in Germany, Thorium Hochtemperatur Reaktor (THTR) in Germany, and High Temperature Reactor-10 (HTR-10) in China. Other test reactors have been studied in India, Russia, France, and South Africa [7].

Several configurations of the HTGR systems have been analyzed, which determinate the operating conditions of all components. The plant configuration with two or more loops helps the primary fluid (reactor coolant) isolation. Davis et al. [8] and Sherman et al. [9] studied up to nine configurations with different loop arrangements divided by heat exchangers. The analysis developed by Ohashi and Sherman [10] showed that the presence of an intermediate heat exchanger (IHX) is critical to reducing the tritium concentration in the hydrogen production processes. The most advantageous configuration to decrease the contamination of the secondary fluid and other fluids of processes is the indirect parallel cycle with three fluid loops [11]. Figure 1.1 illustrates this configuration, where the IHX isolates the primary fluid to the rest of the plant. The secondary fluid is divided towards the power generation unit and the remainder going through a secondary heat exchanger (SHX) that produces heat for the HTE plant. Fluids from the hot side of the SHX and the power conversion unit (PCU) are mixed to feed the cold side IHX.
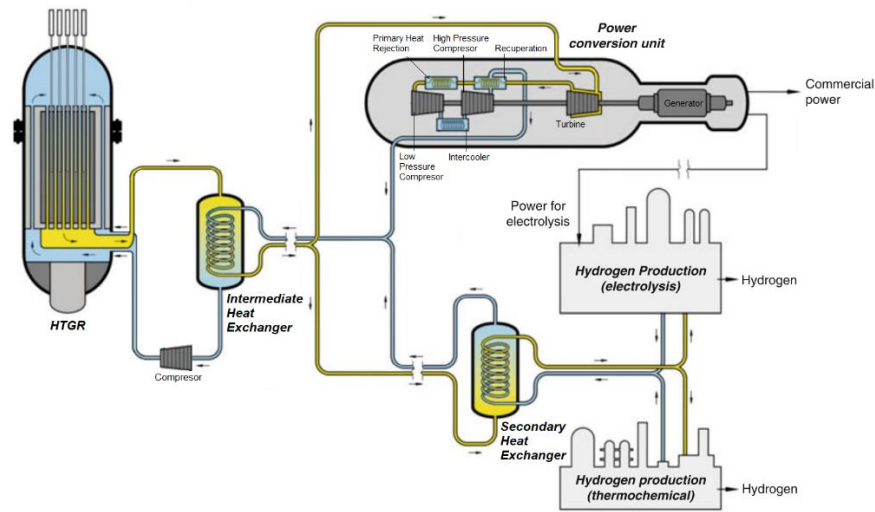
Figure 1.1: Plant configuration with an indirect electrical cycle and a parallel SHX or indirect parallel cycle (adapted from [1], [8] and [9]).

The IHX is the device with the highest values of temperature and pressure in a plant with an indirect parallel cycle. It exchanges the highest thermal power transferring the heat from the helium coolant to the secondary fluid. In 2009, the Technology Readiness Level status published that the level for all components associated with the IHX for reactor outlet temperatures from 1023 K to 1073 K was 3 on a 1–10 scale, with 10 indicating complete technological maturity [12]. Another essential function of the IHX is the heat extraction from the reactor under accident scenarios, although a decay heat exchanger can be included in the system. Mente et al. [13] found that the plant configuration and the operating conditions have a great influence on

heat removal in a Prototype Fast Breeder Reactor. Helium, supercritical carbon dioxide (S-CO$_2$), and water steam were used as secondary fluids in the IHX. Bae et al. [14] studied the performance of the components in a small modular HTGR of 20 MWt and considered Brayton cycles of helium and S-CO$_2$ in the PCU. They found that the S-CO$_2$ is a better option for those small systems. However, a higher thermal duty was considered in this research, as it will present later, and helium was selected as primary and secondary fluid. Also, an indirect parallel cycle was defined to analyze the IHX performance in an HTGR plant.

After setting the plant configuration, the selection of the type of the heat exchanger design and the operation mode is important. Oh and Kim [11] demonstrated that the operation in a two-stages arrangement can offer advantages over a single-stage. However, most of the research, including the present one, have focused on studying the IHX performance in a single-stage arrangement because of a higher analysis simplicity.

1.2. Heat exchanger functioning

The heat transfer is the thermal energy in transit due to a spatial temperature difference. There are three modes for the process: conduction, convection, and radiation. The convection occurs when a surface and a moving fluid are at different temperatures. The heat exchanger is a device in which two fluids moving at different temperatures and separated by a solid wall exchange thermal energy. The heat loaded from the hot fluid and received in the cold fluid can be calculated knowing the mass flow rate of the fluids and the enthalpy difference between the inlet and the outlet of the channels. If the heat loss by radiation and other possible lacks are neglected, the loaded and received heats are the same and can be calculated through Eq. 1.1.

$$q = \dot{m}_h\left(i_{h,i} - i_{h,o}\right) = \dot{m}_c\left(i_{c,o} - i_{c,i}\right) \tag{1.1}$$

where q is the heat transfer rate in Watts, $\dot{m}$ is the mass flow rate in kg/s and i is the specific enthalpy of the fluids in J/kg. The subscripts h and c represent the hot and cold fluids, respectively, while i and o denote the channel inlet and outlet, respectively. In some fluids like helium, the change of the specific heat at constant pressure with the temperature is negligible, hence, Eq. 1.1 can be written as:

$$q = \dot{m}_h c_{p_h}\left(T_{h,i} - T_{h,o}\right) = \dot{m}_c c_{p_c}\left(T_{c,o} - T_{c,i}\right) \tag{1.2}$$

where c_p is the specific heat at constant pressure in W/(kg K) and T is the temperature of the fluid in Kelvins. Equations 1.1 and 1.2 are essential in the design procedures of the heat exchangers, but the mass flow rate per channel sometimes needs to be calculated, and Newton's law of cooling is used to obtain the heat transferred, according to Eq. 1.3.

$$q = hA(T_s - T_b) \tag{1.3}$$

where h is the local heat transfer coefficient in W/(m^2 K), A is the heat transfer area of the surface in m^2, T_s is the surface temperature and T_b is the fluid bulk temperature. These temperature values most of the time are not available and instead Eq. 1.4 is employed.

$$q = UA\Delta T_{ml} \tag{1.4}$$

where U is the overall heat transfer coefficient in W/(m²K), and ΔT_{ml} (or LMTD) is the logarithmic mean temperature difference. The LMTD depends on the temperature values at the inlets and the outlets of the heat exchanger and can be only calculated for simple designs. The procedure to calculate the LMTD for different device configurations can be found in several heat transfer handbooks [15]. Eq. 1.5 is used to calculate the LMTD in the counter-flow configuration.

$$\Delta T_{ml} = \frac{(T_{h,o} - T_{c,i}) - (T_{h,i} - T_{c,o})}{\ln\left(\frac{T_{h,o} - T_{c,i}}{T_{h,i} - T_{c,o}}\right)} \tag{1.5}$$

The overall heat transfer coefficient is obtained considering the local heat transfer coefficient of the cold and hot fluids (h_c and h_h, respectively), the conduction in the solid structure, and the resistance to the transference caused by fouling. In many heat exchangers, the heat transfer areas of the cold and hot sides are similar, and U can be calculated by Eq. 1.6.

$$\frac{1}{U} = \frac{1}{h_h} + R''_{f,h} + \frac{t}{k_s} + R''_{f,c} + \frac{1}{h_c} \tag{1.6}$$

where R''_f is the fouling resistance in m²K/W, t is the wall thickness in meters and k_s is the wall thermal conductivity in W/(m²K). The approximate values of the fouling resistance are known for many cases [15], although in numerous coarse calculations are neglected. Because U is a value that depends on the fluid, the heat transfer surface, the heat exchanger configuration, the mass flow rate, etc., its calculation is the key point in most heat transfer problems.

Non-dimensional numbers are usually used in the calculation of the heat transfer coefficients. The Reynolds number (Re) and the Nusselt number (Nu) are two of them. The first one defines the characteristics of the hydraulic boundary layer and it is the ratio of the inertial forces and the viscous forces, as shown in Eq. 1.7.

$$Re = \frac{\rho u D_h}{\mu} \tag{1.7}$$

where D_h is the hydraulic diameter of the channel in meters, and ρ is the fluid density in kg/m³, u is the flow velocity in m/s and μ is the fluid viscosity in Pa · s. The hydraulic diameter can be calculated in the cross-sections of channels as Eq. 1.8.

$$D_h = \frac{4A_{cs}}{P_{cs}} \tag{1.8}$$

where A_{cs} is the cross-sectional area of the channel in m² and P_{cs} is the cross-sectional perimeter of the channel in meters.

The Nusselt number is the ratio of the convective and conductive heat transfer, as shown in Eq. 1.9. The calculation of Nu through empirical correlations is the objective of several works because it directly allows

obtaining the local heat transfer coefficient. There are many correlations to obtain *Nu* in different conditions, and some of those for the current problem will be discussed later.

$$Nu = \frac{hD_h}{k} \qquad (1.9)$$

where k is the thermal conductivity of the fluid in W/m^{2}K.

Many heat transfer problems are dedicated to increasing the heat transfer, but the energy losses should be also considered. The total energy loss of a thermodynamic system can be calculated through the exergy loss from an initial state until a final state. In an open system as a heat exchanger, there are different types of exergy change: the heat exergy variation associated to the external heat exchanging, the static exergy variation related to the volume change, and the flow exergy that depends on the inlet and outlet values of enthalpy, fluid velocity, potential energy and cost [16]. The heat and static exergies can be considered constant in a heat exchanger if radiation is neglected. There is a loss of flow exergy mainly due to the enthalpy and entropy changes, which depend on the friction losses. Therefore, the energy losses in a heat exchanger can be estimated through the pressure drop, which is calculated from Eq. 1.10.

$$\Delta P = P_i - P_o \qquad (1.10)$$

where ΔP is the pressure drop and P is the fluid pressure in Pascals. The Fanning friction factor is a non-dimensional number used to compare the friction losses and it is related to the pressure drop according to Eq 1.11.

$$f = \frac{\Delta P D_h}{2 L_R \rho u^2} \qquad (1.11)$$

where L_R is the real length traveled by the fluid in meters.

1.3. Heat exchanger types

The design of the heat exchangers determines their thermal-hydraulic performance. There are many types of heat exchangers that have been considered in the current application. They can be classified according to several criteria as the process function, the heat transfer process, the number of fluids, the construction type, the compactness, the flow configuration, etc. [2]. Here, the heat exchanger should work as a heater with indirect contact between two fluids. In this section, some types of heat exchangers are described.

The double pipe heat exchanger is the simplest type created by two concentric tubes, where one fluid flows through the inside tube and another one flows in the outside. Although its low efficiency and the high space occupied in large scales have motivated modern industries to use more efficient technologies, it is presented for comparative purposes later. The shell and tube heat exchanger is the most common type used in the industry. This is shaped by a shell capable of containing high pressures with a bundle of tubes inside it with their axes parallel to that of the shell. One fluid flows through the tubes and another one flows over the tubes (through the shell) [17]. The ease of manufacturing and their relatively low cost have been the

principal reasons for their widespread use in engineering applications. The shell and tube configuration can present straight-tube with one tube pass or U-tube with two tube passes. The baffles are plates that support the tubes bundle reducing vibrations and change the flow direction through the shell. Figure 1.2 presents a schematic representation of this type of heat exchanger.
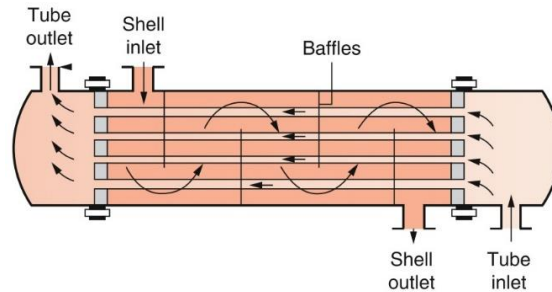
Figure 1.2: Shell and tube heat exchanger with one shell pass and one tube pass [15].

The helical coil heat exchanger is also a tubular based design, but in this case, the tubes bundle forms a spiral path inside the shell. Its main advantage is the efficient use of space, especially when the fluids require a large heat transfer area difficult to reach with a straight path. The helical coil heat exchanger has been used with good experience as IHX in the HTTR plant in Japan. The partial geometry of that was thermal-hydraulically analyzed by Inagaki et al. [18] considering 54 tubes with an outer diameter of 31.8 mm and a thickness of 3.5 mm. In general, the tubular technologies have shown several difficulties as IHX such as a great size of the device, a low heat transfer area density, and a reduced time of service [11][18].

The compact heat exchangers (CHE) with higher area density can be preferable alternatives [19]. The typical shell and tube heat exchangers have an area density of around 100 m^2/m^3 [19], while the CHE present values above 700 m^2/m^3 [2]. This parameter obtained as the quotient between the heat transfer area and the volume of the device is namely compactness. Other criteria to consider a heat exchanger as compact is a hydraulic diameter lower than 6 mm with gas fluids or an area density of 400 m^2/m^3 with liquid or multiphasic fluids [19]. A high area density increases the heat transfer by volume unit, as can be deducted in Eq. 1.3, but also increase the pressure drop. The small hydraulic diameters of the CHE causing flow regimes in the laminar region are common. Some of the CHE designs include the plate heat exchanger (PHE), the plate fin heat exchanger (PFHE), and the printed circuit heat exchanger (PCHE), which are plate types with different manufacture technologies and flow passages designs.

The PHE uses plates to transfer heat between fluids, which shape the flow channels. These plates are mounted on a frame and two clamped plates that compact them. Each plate has nozzles through the fluids flow; one fluid is driven by the even plates and the other one by the odd ones. Figure 1.3 shows the configuration and parts of a PHE. Its area density ranges from 120 to 660 m^2/m^3, with hydraulic diameters between 2 mm and 10 mm [19]. One advantage of the PHE is the reduced size requirements. For the same effective heat transfer area, the weight and volume of the PHE are approximately 30% and 20%, respectively, of those of shell and tube heat exchangers [20],
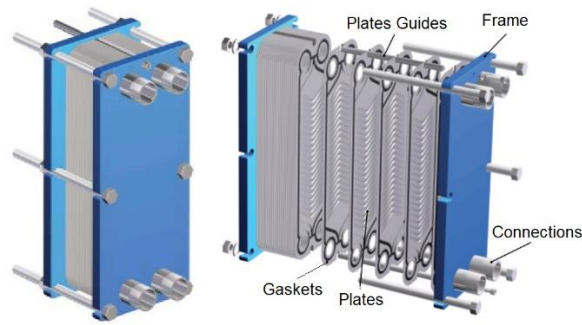
Figure 1.3: Plate heat exchanger (courtesy of Comeval).

The PFHE is a compact design with alternating layers of corrugated sheets or fins, divided by parting sheets and enclosed at the edges by side bars to create a series of finned chambers. The fins and the parting sheets are assembled by brazing to become a single rigid core. The plates and the fins separate the fluids and form the individual flow channels, as shown in Figure 1.4. The fins have several functions as increase the effective heat transfer surface area and withstand the design pressure at the design temperature as a structural component. The compactness of a typical PFHE is in the range of 700-800 m^2/m^3, although more recent designs have reached values up to 5900 m^2/m^3 [19]. Its volume can be around 10% of a shell and tube heat exchanger with a hydraulic diameter of 19 mm [21]. Among the different designs of the PFHE, the offset strip-fin heat exchanger (OSFHE) is one of the those with better thermal-hydraulic performance [22]. The PFHE design presents some limitations, but the most significant can be the presence of brazed joints where the failure is more feasible [23][24]. To be used at very high temperature applications, the fin thickness should be relatively high to contain the structural loading condition.
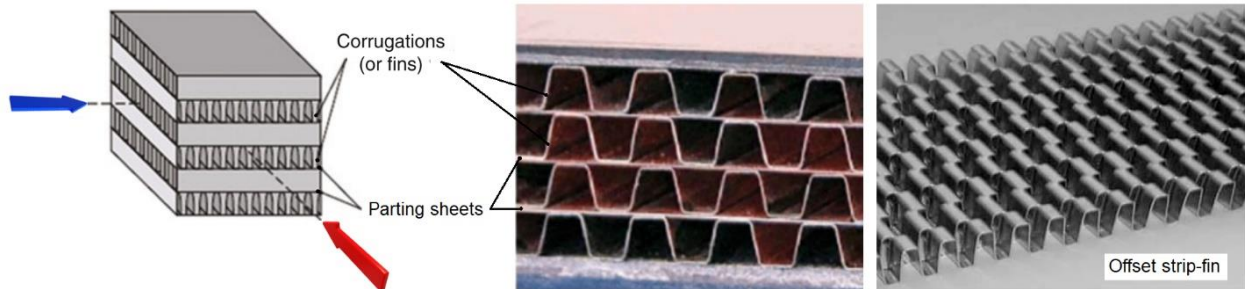
Figure 1.4: Plate fin heat exchanger functioning and offset strip-fin structure (adapted from [2]).

PCHE offers many advantages in terms of compactness and thermal-hydraulic performance. Their manufacturing process is based on the diffusion bonding of plates with channels photo-chemical etched in one or both plate sides [25]. That allows to obtain a solid structure without interfaces, which makes it possible to contain high pressures. The area density of the PCHE is higher than 2500 m^2/m^3, therefore, it has a relatively high global heat transfer coefficient. Their thermal efficiency or effectiveness, defined as

$(T_{h,i} - T_{h,o})/(T_{h,i} - T_{c,i})$, can exceed 98% [25]. Although cross-sections of channels with circular [26], rectangular [27], trapezoidal [28], and semielliptical [29] shapes have been studied, the fluid channels usually have a semicircular shape with typical hydraulic diameters from 0.5 mm to 2 mm. The distance between channels in each plate is around 0.5 mm [19]. Better thermal-hydraulic performance of the PCHE designs in comparison with the OSFHE was found by Bartel et al. [22]. The volume of the PCHE is typically 4 or 6 times smaller and lighter than conventional shell and tube heat exchangers designed for the same thermal duty and pressure drop [19]. The average mass-to-duty ratio in tones/MW of the PCHE and PFHE is 0.2, while that of the shell and tube heat exchanger is 13.5, which implies a significant material cost reduction for compact designs [30]. Although even tubular heat exchangers with microtubes (diameters 1~3 mm) have been studied as compact designs for the NGNP [31], the PCHE advantages makes it a great candidate. Figure 1.5 illustrates the parts of the core of a PCHE and a set device developed by Heatric Company [25].
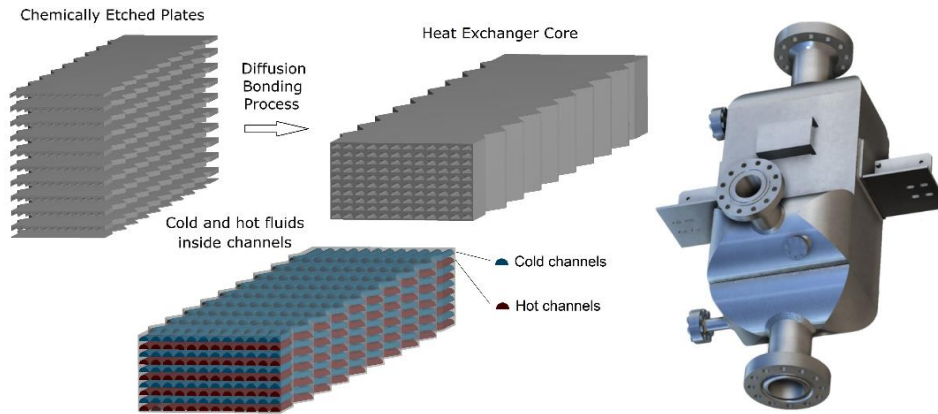
Figure 1.5: Schematic representation of the diffusion bonding process of a PCHE core, fluids inside channels, and a set device from Heatric [25].

The heat exchanger designs presented above can be feasible or not for different applications. Although some comparative data among them have been presented, a comparison of the thermal design calculation of them will be accomplished in the next section considering the operating conditions of an IHX in an HTGR plant.

1.4. Comparison of heat exchanger types as IHX

The characteristics of the four conceptual designs of the HTGR studied in the United States shows several similitudes [32]. One of those is the power output from the reactors, which is from 500 MWt to 600 MWt, except in the Fort St. Vrain HTGR that produces 842 MWt. For this reason, many works have been considered a power duty around 600 MWt in the thermal-hydraulic analyses [8][10]. Oh and Kim [11] took this value and other similar parameters to calculate and compare heat exchanger designs such as the PCHE, the helical coil, and the conventional shell and tube, used as IHX in a parallel indirect configuration. Table

1.1 presents the operating conditions considered in the corresponding calculations by Oh and Kim, where the primary and secondary fluids were helium.

Table 1.1: Heat exchanger design conditions used by Oh and Kim [11].

Parameter	Value
Power duty (MWt)	611
Primary fluid	Helium
Secondary fluid	Helium
Mass flow of primary fluid (kg/s)	385.3
Primary fluid inlet temp. (K)	1173
Primary fluid outlet temp. (K)	867.5
Primary fluid pressure (MPa)	7.0
Mass flow of secondary fluid (kg/s)	300
Secondary fluid inlet temp. (K)	765.5
Secondary fluid outlet temp. (K)	1157
Secondary fluid pressure (MPa)	7.58
Log Mean Difference Temp. (K)	45.37

Oh and Kim [11] studied the thermal-hydraulic performance of the heat exchanger designs through the overall heat transfer coefficient, the heat transfer surface area, the total volume of the core, and the pressure drop. The logarithmic mean temperature difference in Table 1.1 was obtained according to Eq. 1.5. The comparative results obtained are summarized in Figure 1.6 considering a parallel indirect configuration with a single stage.

Two flow configurations of the straight channels PCHE were considered, the counter-flow and the cross-flow. Also, both straight pipe and U tube designs of the shell and tube types were calculated. The overall heat transfer coefficient reached by the PCHE designs is two or more times higher than those for the tubular ones. Therefore, the heat transfer surface area is up to five times lower than that of the straight pipe shell and tube device. Considering the area density of each design, the volume of the heat exchange core of the PCHE is at least one order lower than those of the tubular ones. The lower pressure drop was obtained in the straight pipe design, but great differences for all designs were not evidenced. These calculations were carried out with constant values of the Reynolds number, but it was different for each design. In the current research, wider ranges of the Reynolds number were analyzed considering the IHX conditions of Table 1.1. Also, additional designs such as a zigzag channels PCHE with a zigzag angle of 15°, an OSFHE, and a double pipe heat exchanger, were considered. The counter-flow configuration was defined because Figure 1.6 also showed that the heat transfer of this configuration is lower than that of the cross-flow configuration, but the pressure drop increase is significant with cross-flow. Furthermore, the work of Kim et al. [33] demonstrates a higher thermal-hydraulic performance of the counter-flow configuration under the defined conditions. Some equations used in the thermal design calculation of the heat exchanger were presented in Section 1.2, but all the calculation procedure and the used heat transfer correlations are presented in Appendix A. Figure 1.7 shows the results of the thermal-hydraulic parameters.
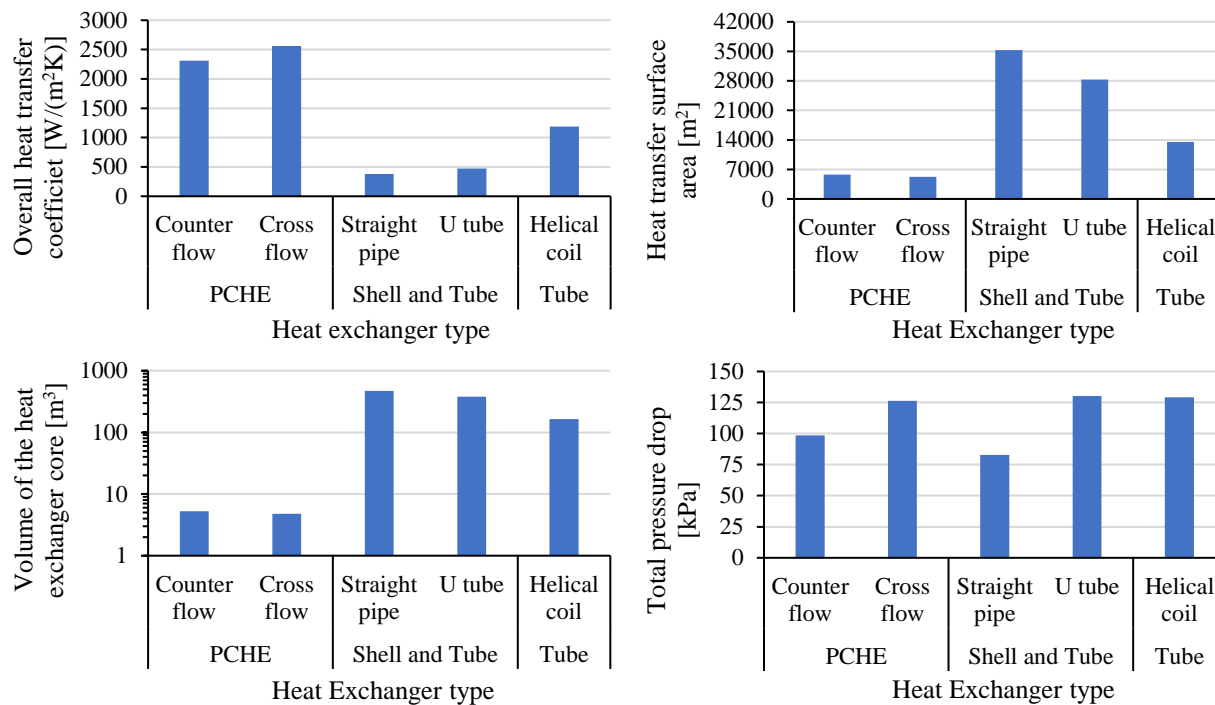
Figure 1.6: Comparative results of the heat exchanger designs reported by Oh and Kim [11].

The compact designs demonstrate a high overall heat transfer coefficient even with very low Reynolds numbers in the laminar region. However, the tubular designs need very high Reynold numbers to achieve acceptable thermal-hydraulic performances and total volume. The pressure drop of the compact designs is considerably higher than that of the double pipe heat exchanger for the same Reynold number. But, considering that the tubular designs require to operate at high Reynolds numbers, the pressure drops can reach similar values. The straight and zigzag channels PCHE and the OSFHE present similar heat transfer parameters, although the zigzag channels PCHE evidence the highest overall heat transfer coefficient. Furthermore, the PCHE has shown benefits over the plate fin designs in safety terms, such as the reduction in the tritium permeation [11], a higher rupture time under, and equivalent stress conditions [34][35], and the capacity to contain higher pressures [25]. Hence, this research is focused on the performance analysis of the PCHE design as IHX with helium fluids. In these conditions, the operation at low Reynolds numbers is recommended to reduce the pressure drop.
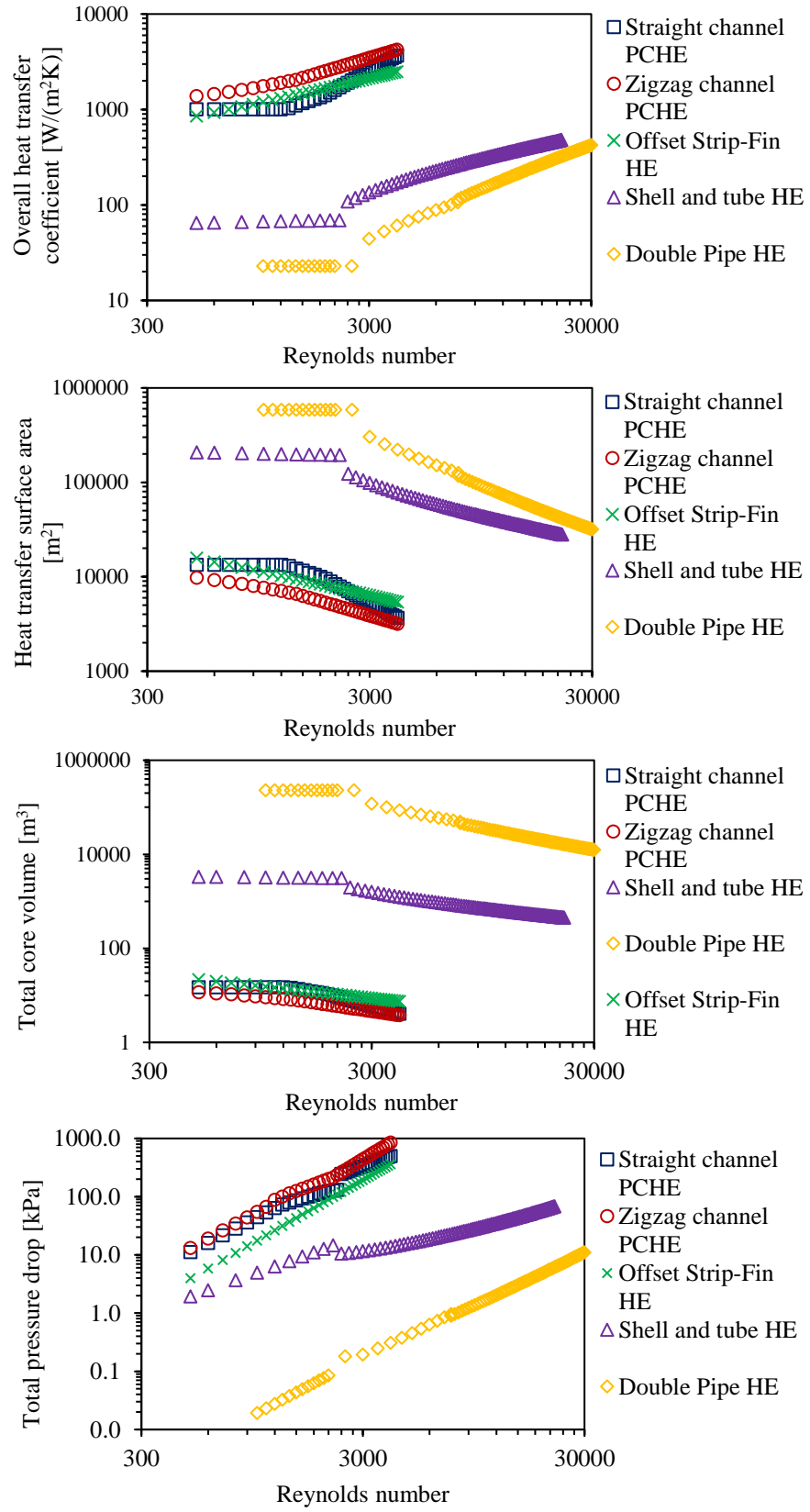
Figure 1.7: Comparative results of the heat exchanger designs for several Reynolds numbers.

1.5. Configuration of the diffusion bonded channels

There are many designs of the PCHE, but a common feature among them is the manufacturing process using diffusion to bond the plates with the flow channels etched, as was commented before. Diffusion bonding is a solid-state welding process that bonds two contacting surfaces (the bonded interface) in a vacuum environment with defined values of temperature and pressure. The structural material defines the process temperature, which is close to its melting point, and the applied pressure to avoid the notable deformation of the channel geometry. The diffusion rates are high at very high temperatures, and the normal mechanisms of grain growth cause grain boundaries to cross the interface, leaving a joint with a very similar structural strength that the base metal. A detailed description of the diffusion bonding process can be found in the work of Sabharwall et al. [36].

The fluid flows configuration in the PCHE depends on the flow directions in the channels that can be in parallel-flow, counter-flow, or cross-flow. These heat exchangers are often in the laminar region for helium fluids because of the small hydraulic diameter of the channels. Heat transfer can generally be improved by increasing the distance of the flow path, although this increase affects the energy loss by friction. Then, the channel path design is a process that requires detailed thermal-hydraulic studies. Four path designs have been mainly manufactured and tested for the diffusion bonded channels of the PCHE: the straight [12][37], the zigzag [38][39], the S-shaped [40], and the airfoil channels [41][42][43], which are shown in Figure 1.8. They were analyzed by Yoon et at [44] under conditions of the IHX in HTGR and Sodium-cooled Fast Reactor (SFR) plants. It was found that the airfoil path design has a higher overall heat transfer coefficient than those of the straight path and the zigzag path with a zigzag angle of 15° in the laminar region. However, the zigzag channel PCHE proved to be competitive with optimized zigzag angles. The thermal-hydraulic performance of the zigzag path design with an angle of 30° was similar to the airfoil design. Yoon et al. recommend the zigzag channel PCHE for IHX application with helium fluids in the laminar region, because of its lowest pressure drop and relatively high heat transfer area. The work of Ngo et al. [45] offered values of the heat transfer and the pressure drop of the zigzag and S-shape designs as functions of the Reynolds number using S-CO_2 as fluids. The Nusselt number of the zigzag ones was 24~34% higher than that of S-shaped ones, but the pressure-drop was 4~5 times larger, depending on the Reynolds number.
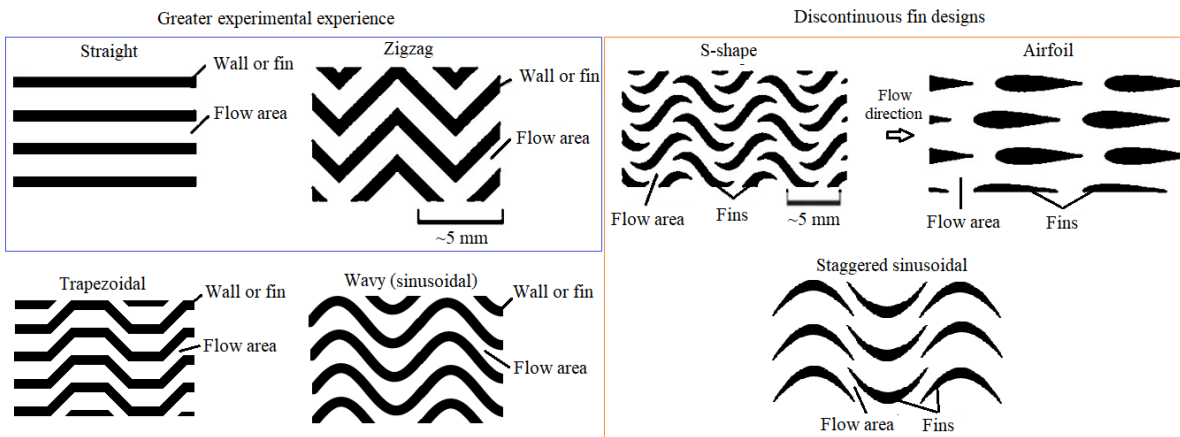
Figure 1.8: Configurations of the most common diffusion bonded channel paths of the PCHE.

Other channel path designs of the PCHE have been considered in several works, such as trapezoidal, wavy or sinusoidal, and staggered sinusoidal, as shown in Figure 1.8. The wavy channel designs of the PCHE were studied by Biak et al. [46] and by Wen et al. [47], and the increment of heat transfer with waviness was evidenced concerning the straight channel design. Trapezoidal and wavy paths were studied by Lee et al. [48] and Zhao et al. [49]. Enhancements of the thermal-hydraulic performance of the trapezoidal channel PCHE were evidenced in both works with specific conditions. Aneesh et al. [50] obtained similar results analyzing the heat transfer and the pressure drop of trapezoidal, wavy, and zigzag channels PCHE, although only sharp-shape of the zigzag bends was considered. The larger heat transfer rate and pressure drop in the trapezoidal design were attributed to a higher degree of fluid mixing and boundary layer breaking than those in the wavy and zigzag designs. The same phenomenon took place in the PCHE with rectangular paths studied by Jing et al. [51], in which the heat transfer was increased in comparison to the straight channel design, but an increment of the pressure drop of more than 10 times was observed. Saeed and Kim [52] proposed staggered sinusoidal paths for PCHE. They found a hydraulic performance of the optimized proposed path up to 2.5 times better than a zigzag path with identical thermal characteristics.

The number of etching faces per plate and the channel locations to bond those faces have been also studied. Zigzag fins with double-faced etching on the plates were analyzed and optimized by Lee et al. [53], which showed higher heat transfer and pressure drop than the single-faced design with S-CO$_2$ as fluids. These authors, as well as Aneesh et al. [54] with helium fluids, analyzed single-banking (one hot channel plate per one cold channel plate) and double-banking (two hot channel plates per one cold channel plate) arrays, and they found the highest heat transfer and exergy saving, respectively, in the single-banking device. The increase of the heat transfer in the PCHE has also been studied employing modifications to reach a greater mixing fluid. Tangled trapezoidal channels were designed and tested by Sung et al. [55] with a maximum temperature of 448 K, and heat transfer improvements were obtained. Although surface interruptions, such as extended surfaces, hurdles, and baffles, are complex to reach using a chemical etching process, Aneesh et al. [54] numerically studied the influence of some dimples in straight channel ways and better heat transfer was noticed. Jing et al. [51] added some ribs to the channel paths and a 7.3% improvement of the Nusselt number was obtained concerning the design without ribs. However, a significant increase in the friction factor was evidenced.

Overall, the channel paths with discontinuous fins have shown good thermal-hydraulic performance with S-CO$_2$ fluids in high turbulent regimes, but their manufacturing processes are more complex than those of the continuous fin designs, which are competitive working with helium fluids in laminar regimes. Alternative path designs are not as easily available as straight and zigzag designs, whereby is even more difficult to study. The most important limitation of the discontinuous fins designs is the structural strength reduction, which is particularly valuable at very high temperatures. The structural performance of designs with trapezoidal and rectangular channel paths can be a problem in high temperature applications because of their great number of sharp corners, where the stress concentration can take place. The ribs addition to improving the heat transfer can also increase the stress concentration. Furthermore, the double-faced plates and the obstacles in the channel paths can become challenging in the manufacturing process. Then, the PCHE designs with straight and zigzag channel paths, single-banking array, and without obstacles are great options to be used as IHX with helium fluids; hence, in this research, the thermal-hydraulic and structural performances analysis is focused on those.

1.6. Approaches to analyzing the thermal-hydraulic performance of the PCHE

The difficulty of the geometric configurations of the PCHE and the relatively low experimental data about its performance cause that the numerical studies are fundamental. In the last decades, the increase of computational capabilities has offered the possibility of resolving complex problems through computational fluid dynamics (CFD). The CFD techniques solve the Navier-Stokes equations, which guarantee the compliance of the conservation of mass, energy, and momentum, as will be seen in Chapter 3. Then, simulations and experimental tests have been employed to calculate the heat transfer and the energy loss in the PCHE operation under several conditions. Several approaches have been applied to assess the best combination of benefits by the heat transfer and losses by the hydraulic process. The attainment of an optimum balance can change as a function of the weights that are assigned to each thermal-hydraulic parameter in the different applications.

Optimization methods of the heat exchangers based on their costs have been developed for several types, such as that by Caputo et al. [56] for the shell and tube heat exchangers. For the PCHE type, a methodology based on the total cost analysis was proposed by Kim et al. [57], in which the heat transfer is associated with the capital cost and the friction losses are related to the operating cost. That is, the size of the heat exchanger core is calculated from the heat transfer value, and the capital cost per year is analyzed as a function of the structural material cost and the time of service. Then, the energy consumed in the compression or pumping work of the fluid is obtained from the pressure drop value, and the operating cost per year is calculated knowing the energy cost. Kim and No [58] used simulation results and the cost methodology to optimize a zigzag channel PCHE in IHX conditions with helium fluids. Yoon et al. [44] used this methodology to optimize the PCHE performance with helium fluids and with a combination of sodium and S-CO$_2$ as fluids. The total cost criterion was considered by Kim et al. [40] to optimize a PCHE used as SHX in an SFR plant with a combination of primary and secondary fluids of FLiNaK and S-CO$_2$, respectively. Gyu et al. [41] also took the total cost as an objective function to evaluate the performance of an airfoil PCHE with S-CO$_2$ fluids. In the work of Figley et al. [26], an IHX in a power plant based on a small modular reactor (SMR) was optimized with the minimization of the total cost. In general, the cost methodology to optimize the thermal-hydraulic performance of the PCHE has been useful to define weights to parameters of different nature as the heat transfer and the friction losses. Nevertheless, some values can be taken differently by each author like the energy cost, the structural material cost, and the time of service of the device. Therefore, the weight and the optimization criterion differ by authors.

Other criteria have been considered to assess the thermal-hydraulic performance of the PCHE. Lee et al. [53] proposed a multi-objective evolutionary algorithm to reach designs with an exergy saving advantage over the reference design. The enhanced designs showed different characteristics: the first one has a great decrease of the pressure drop, but the effectiveness also decreases; and the second one presents an increment of the thermal efficiency with a higher pressure drop. The flow mass rate distribution and the pressure drop were also used as multi-objective functions by Koo et al. [59] to optimize the inlet part of a PCHE. In summary, obtaining two optimization functions considering the heat transfer and the energy loss has been a good procedure. The maximization of the Nusselt number and the minimization of the friction factor can be used as non-dimensional numbers to reach optimized designs. Therefore, the development of correlations to calculate these numbers for the PCHE is one of the most important goals of much recent research.

1.7. Design studies of the straight and zigzag channels

Some optimized HTGR plants have demonstrated the need for the high effectiveness of this device [60]. Then, the design of the PCHE considering the thermal-hydraulic performance is a critical issue for its application as IHX. In this research, the PCHE with straight and zigzag channels were studied, which have geometric parameters of the cross-section and the zigzag path as Figure 1.9 presents, where the hot and the cold fluids are symbolized in red and blue colors, respectively.
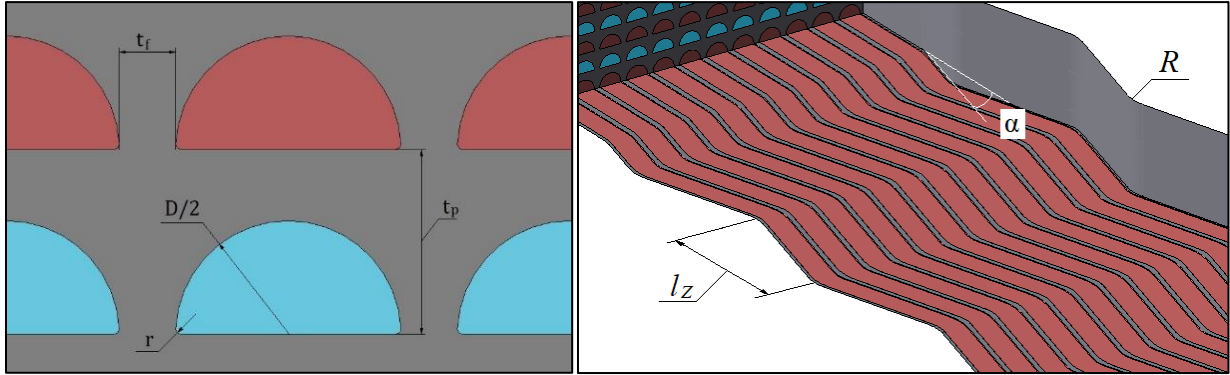
Figure 1.9: Geometric parameters of the cross-section and the zigzag path of a PCHE.

The channel diameter (D), the plate thickness (t_p), the ridge thickness (t_f), and the rounded tip radius (r) are the geometric parameters that characterize the cross-section, while the zigzag angle (α), the zigzag pitch length (l_Z) and the bend radius (Br) define the zigzag path. The cross-sectional dimensions need to be analyzed to reach the highest thermal-hydraulic performance in a straight channel PCHE, but both cross-sectional and zigzag dimensions require study in a zigzag channel PCHE. Much research on this topic has been supported in computational fluid dynamics (CFD) models, as will be seen later. Some alternative designs of that presented in Figure 1.9 have also been studied using simulation tools. For example, narrowed semicircular cross-sections of channels showed a reduction of the device volume for an equivalent heat transfer with CO_2 fluid in the work of Yang et al. [29], and the rectangular cross-section presented the lowest heat transfer area with friction factor penalties among circular, semicircular and trapezoidal cross-sections in the work of Lee and Kim [28]. However, the semicircular cross-section has been preferable because of its well-known characteristics of high heat transfer area density, moderated hydraulic losses, and easy manufacture, in addition to better structural performance than rectangular and trapezoidal sections, which have many corner tips.

Several works have been focused on the optimization of the zigzag path design. A validated CFD model was used by Kim et al. [58] to analyze the effects of the zigzag angle, the zigzag pitch, and the channel diameter with helium fluids in the laminar regime. An optimized design was proposed according to the total cost analysis commented before. The most decisive parameter was found to be the zigzag angle. The total cost decreased as either the angle increased, or the Reynolds number decreased. A double-faced type PCHE with supercritical CO_2 in a turbulent regime was studied in [53] by using a three-dimensional model. The

bend radius, the zigzag length and the zigzag height ($= l_z \tan \alpha$) were selected as the design variables and two optimized designs had an energy savings advantage over a reference design. A CFD model was used by Hassan et al. [61] to analyze the zigzag angle influence on the PCHE performance with helium fluids in a laminar regime. The heat transfer enhancement as compared to the pressure penalty was higher for the zigzag channel with values of 0°, 5°, 10°, and 15°. In [22] a zigzag channel PCHE with a 15° zigzag angle was found to offer the optimum combination of the heat transfer coefficient, compactness, and pressure drop as compared to other ones with zigzag angles between 0° and 20°, when helium in laminar regime was considered. Kim et al. [40] studied the PCHE with fluids FLiNaK and S-CO2 and designs as the straight channel, the zigzag channel with angles of 52° and 15°, S-shaped, and an OSFHE. The straight and zigzag channels were recommended. Kim and No [58] optimized a zigzag channel PCHE in IHX conditions with helium fluids and obtained that the optimum zigzag angle decreases with the Reynolds number. A similar result was found by Ma et al. [62] considering zigzag angles of 0°, 15°, 30°, and 45°, and hybrid channels with a straight channel plate and a zigzag channel plate. Hybrid straight-zigzag channels were recommended at high mass flow rates and straight channels at the highest ones. However, the contribution ratio of all the zigzag dimensions on the thermal-hydraulic performance of the PCHE and the analysis of the interaction of them have not been achieved. The zigzag phase-shift has also not been considered in previous studies.

1.8. Available heat transfer correlations for PCHE

The Nusselt number and the Fanning friction factor of fully developed laminar flows in straight ducts can be considered constant, being 4.089 and 15.78, respectively, in semicircular profiles [63]. However, these values are particularly accurate in channels with relatively high axial length [15]. The exactness of considering a constant Nusselt number requires fully developed flows to be present in a great part of the channel length. This condition is not reached in the PCHE under present conditions due to the great variation of the thermophysical properties for the common temperature gradients [64]. Chen et al. [65] used experimental results from straight channel PCHE in a helium test facility to develop a Nusselt number correlation within a Reynolds number range from 1200 to 2900. The experimental tests of Kwon et al. [66] and Mylavarapu et al. [67] employed available correlations for straight ducts to predict the heat transfer coefficient in a PCHE with acceptable accuracies.

Nevertheless, the development of heat transfer correlations for zigzag channel PCHE has been the goal of much research, which has used experimental data and numerical simulation within a specific scope. Kim et al. [38] developed Nusselt number correlations with Reynolds numbers between 350 and 1200 for a zigzag channel PCHE using a helium test facility and CFD. The local pitch-averaged Nusselt number correlation from CFD simulations was found more appropriate than the global Nusselt number correlation obtained from experimental data according to a system analysis code. Helium, water, and helium-CO_2 mixture fluids were investigated by Kim et al. in [68] and [69] with a Reynolds number up to 2500 and 3000, respectively, through experimental tests and CFD simulations. Nusselt number and Fanning friction factor correlations that consider the three fluids were presented. The Prandtl number dependency of the Nusselt number correlation is not necessary with helium fluid because the Prandtl number of helium remains almost constant around 0.66, but in both [68] and [69] the authors introduced this number in the proposed correlations to consider helium, water, and helium-CO_2 mixture fluids in only one correlation.

Table 1.2: Available Nusselt number and Fanning friction factor correlations of the PCHE with helium fluids.

Configuration	Geometric parameters (mm)	Re	Nusselt number correlation	Fanning friction factor correlation	Ref.
Straight	-	Critical: 2300	$Nu_T = 3.323$ $Nu_{H1} = 4.089$ $Nu_{H2} = 2.96$	$f \times Re = 15.78$	[63]
Straight	$D = 2.0$ $t_f = 0.54$ $t_p = 1.63$	1200-2900 Critical: 1850	$Nu = (0.01352 \pm 0.0094)Re^{(0.80058\pm0.0921)}$ $1200 \leq Re \leq 1850$ $Nu = (3.6361 \times 10^{-4} \pm 7.855 \times 10^{-5})Re^{(1.2804\pm0.0273)}$ $1850 < Re \leq 2900$	-	[65]
Straight	$D = 2.0$ $t_f = 0.54$ $t_p = 1.63$	Critical: 3200	$Nu_{H1} = \dfrac{\frac{f}{2}(Re - 1000)Pr}{1 + 12.7\left(Pr^{\frac{2}{3}} - 1\right)\sqrt{\frac{f}{2}}}$ $2300 \leq Re \leq 5 \times 10^6, \quad 0.5 \leq Pr \leq 2000$	$f = \dfrac{1}{4}\left(\dfrac{1}{1.8\log Re - 1.5}\right)^2$ $2300 \leq Re \leq 5 \times 10^6, \quad 0.5 \leq Pr \leq 2000$	[15] [63] [66] [67]
Straight	$D = 2.0$ $t_f = 0.54$ $t_p = 1.63$	Critical: 2300	$Nu_{H1} = 3.5239\left(\dfrac{Re}{1000}\right)^4 - 45.148\left(\dfrac{Re}{1000}\right)^3$ $+ 212.13\left(\dfrac{Re}{1000}\right)^2$ $- 427.45\left(\dfrac{Re}{1000}\right) + 316.08$ $2300 \leq Re \leq 3100$	-	[67]
Straight	$D_h = 1.83$ $t_p = 2.0$	8500-17000	$Nu = 0.0274Re^{0.78}Pr^{0.33}$	-	[66]
Zigzag	$D = 1.51$ $t_p = 1.63$ $\alpha = 15^o$ $L_Z = 12.3$	350-1200	$Nu = 4.065 + 0.00305 \times Re$ $350 < Re < 800, \ Pr = 0.66$ $Nu = 3.255 + 0.00729 \times (Re - 350)$ $350 < Re < 800, \ Pr = 0.66$	$f \times Re = 16.51 + 0.01627 \times Re$ $350 < Re < 1200$	[38]
Zigzag	$1.51 \leq D \leq 2.0$ $5^o \leq \alpha \leq 45^o$ $12.3 \leq L_Z \leq 24.6$	350-1200	[A] $Nu = 4.089 + c \times Re^d$	[A] $f \times Re = 15.78 + a \times Re^b$	[58]
Zigzag	$D = 1.51$ $t_p = 1.46$ $0 \leq \alpha \leq 20^o$ $L_Z = 12.3$	≤ 2200	[A] $Nu = 4.089 + c \times Re^d$	[A] $f * Re = 15.78 + a \times Re^b$	[22]
Zigzag	$D = 1.51$ $t_p = 1.63$ $\alpha = 15^o$ $L_Z = 12.3$	≤ 2500	$Nu = 4.089 + 0.00365 \times Re\,Pr^{0.58}$ $0 < Re < 2500, \ 0.66 < Pr < 13.41$	$f \times Re = 15.78 + 0.004868 \times Re^{0.8416}$ $0 < Re < 2600$	[68]
Zigzag	$D = 1.51$ $t_p = 1.63$ $\alpha = 15^o$ $L_Z = 12.3$	≤ 3000	$Nu = 4.089 + 0.00497 \times Re^{0.95}Pr^{0.55}$ $0 < Re < 3000$ $0.66 < Pr < 13.41$	$f \times Re = 15.78 + 0.0557 \times Re^{0.82}$ $0 < Re < 3000$	[69]
Zigzag	$D_h = 1.28$ $t_p = 1.5$ $\alpha = 40^o$	≥ 2300	$Nu = 0.1696 \times Re^{0.629}Pr^{0.317}$	$f \times Re = 0.1942 \times Re^{-0.091}$	[44]
Zigzag	$D = 2.0$ $t_p = 1.63$ $\alpha = 15^o$ $L_Z = 12.3$ $B_r = 4.0$	1400-3558 Critical: 2200	$Nu = (0.05516 \pm 0.00160)Re^{(0.69195\pm0.00559)}$ $1400 \leq Re \leq 2200$ $Nu = (0.09221 \pm 0.01397)Re^{(0.62507\pm0.01949)}$ $2200 < Re \leq 3558$	$f = \dfrac{17.639}{Re^{0.8861\pm0.0017}}$ $1400 \leq Re \leq 2200$ $f = 0.019044 \pm 0.001692$ $2200 < Re \leq 3558$	[39]
Zigzag	$D = 2.0$ $5^o \leq \alpha \leq 45^o$ $5.0 \leq L_Z \leq 40.0$ $0.5 \leq B_r \leq 1.0$	100-2000	$Nu_h = (0.71\alpha + 0.289)\left(\dfrac{l_z}{D_h}\right)^{-0.087} \times$ $Re^{\left(-0.11(\alpha-0.55)^2-0.004\left(\frac{l_z}{D_h}\right)\alpha+0.54\right)}Pr^{0.56}$ $Nu_c = (0.18\alpha + 0.457)\left(\dfrac{l_z}{D_h}\right)^{-0.038} \times$ $Re^{\left(-0.23(\alpha-0.74)^2-0.004\left(\frac{l_z}{D_h}\right)\alpha+0.56\right)}Pr^{0.58}$	Sharp-edged zigzag: $f = \dfrac{15.78}{Re} + \dfrac{6.7268}{1000}\exp(6.6705 \times$ $\alpha)\left(\dfrac{l_z}{D_h}\right)^{-2.3833\times\alpha+0.26648} + \dfrac{4.3551\times\alpha-1.0814}{100}$ Round-edged zigzag: $f = \dfrac{15.78}{Re} + \dfrac{2.9311}{100}\exp(1.9216 \times$ $\alpha)\left(\dfrac{l_z}{D_h}\right)^{-0.8261\times\alpha+0.031254} + \dfrac{4.7659\times\alpha-2.8674}{100}$	[70]

[A] The values of *a*, *b*, *c,* and *d* were calculated in [58] considering different zigzag angles, channel diameters, and zigzag length and in [22] considering different zigzag angles.

However, in [71] an exchanger with helium and FLiNaK fluids was numerically investigated and large differences were found between the correlation of Kim et al. [69] and CFD results on the FLiNaK side. Correlations for both non-dimensional numbers were reached by Chen et al. [39] through experimental data. The Fanning friction factor was up 29% lower than the results of Kim et al. [38] and the deviation could be caused by different PCHE geometric configurations according to the authors. The sharp-edged corner ($Br = 0$) was considered in [38] and a bend radius of 4 mm was considered in [39], although the zigzag angle was 15° in both works. These correlations were usually obtained considering only fixed geometric design.

Kim and No [58] included two tabulated coefficients in the Nusselt number and the Fanning friction factor correlations, which were based on CFD simulation. These coefficients depend on geometric parameters: channel diameter in a range from 1.51 mm to 2.0 mm, zigzag angle in a range from 5° to 45° and zigzag pitch length in a range from 6.15 mm to 12.3 mm. Zigzag angles from 0° to 20° of the zigzag channel PCHE were considered by Bartel et al. [22] to propose Nusselt number and Fanning friction factor correlations using numerical simulations. Similar to [58], two tabulated coefficients were introduced in the correlations, but these only depend on the zigzag angle. Yoon et al. [70] developed correlations using CFD simulation results in the laminar region that consider the influence of the geometric parameters of the zigzag channel. These correlations were created as functions of the geometric parameters, within zigzag angles from 5° to 45°, zigzag pitch length from 5.0 mm to 40.0. mm and bend radius from 0.5 mm to 1.0 mm. The Nusselt number correlation was not expressed as function of the bend radius, and just the Fanning friction factor correlation was obtained for sharp-shape and round-shape of the bend corners. The CFD-based Fanning friction factor correlation had a little deviation with experimental data, but the Nusselt number correlation showed an overestimation of up to 43% in the cold channel and 49% in the hot channel.

Table 1.2 sums up all the available correlations for the straight and zigzag channel PCHE in open literature. The subscripts *T*, *H1,* and *H2* represent the boundary conditions for fully-developed laminar flow of constant temperature axially and circumferentially; axially constant wall heat flux with circumferentially constant wall temperature, which is usually the conditions present in the current application; and axially and circumferentially constant heat flux, respectively [63]. Although the Nusselt number is a function of the Prandtl number, most of those correlations do not consider this value because they are only valid for helium fluid flows. It becomes evident that more precise information on the Fanning friction factor and the Nusselt number as a function of geometric parameters in wide ranges is valuable to analyze and optimize the thermal-hydraulic performance of the PCHE.

1.9. General issues in the PCHE operations

1.9.1. Tritium permeation

The tritium is a radioactive isotope of hydrogen and its concentrations in the different loops of an HTGR plant is an essential safety issue that has been studied by several works. The tritium permeation causes that it crosses from the primary loop to the hydrogen generation station. The mechanisms of the tritium generation in the reactor are ternary fission of fuels as ^{233}U, ^{235}U, ^{239}Pu, and ^{241}Pu due to thermal neutrons, and neutron capture reactions of ^{6}Li, ^{7}Li, ^{3}He, and ^{10}B [10][11]. Lithium isotopes are impurities of the core

graphite material, ^{3}He is an impurity in the helium reactor coolant and ^{10}B is in the control rods, burnable poison, and reflector.

The work of Ohashi and Sherman [10] analyzed the sensitivity of the tritium concentration in the hydrogen produced as a function of several parameters of an HTGR plant. The indirect parallel configuration shown in Figure 1.1 was considered in that study and the reactor power was 600 MWt. The primary and secondary loops were planned to have tritium purification systems to reduce the tritium permeation. A tertiary loop was also set before the hydrogen production plant, which receives 55 MWt from the total power. The tritium concentrations in the HTE process could be reduced in 36% when employing the tertiary loop with SHX and purification systems. In the base case, the tritium concentration in gaseous hydrogen was 2.67×10^{-3} Bq/cm^3, which is slightly less than the gaseous effluent limit (3.7×10^{-3} Bq/cm^3). The tritium concentration in liquid hydrogen of 2.30 Bq/ml was also less than the liquid effluent limit (37 Bq/ml). However, the concentration is greater than the drinking water limit of 0.74 Bq/ml. The tritium concentration in the hydrogen product decreased with the primary fluid temperature at the IHX inlet. This concentration also decreased with the pressure in the tertiary loop, although it was not significant. The effect of the pressure variation of the primary and secondary loops is expected to be lower. A hydrogen injection in the helium coolant was proposed as a measure for decreasing the tritium permeation rate.

Oh and Kim [11] focused on the tritium permeation through PCHE walls used as IHX in an HTGR plant with the same features of that analyzed by Ohashi and Sherman [10]. The effective thickness of the tritium penetration path in the PCHE was estimated because the wall thickness of the semicircular channels in the solid blocks was not easily defined. The effective thickness in the studied PCHE was much smaller than the average thickness between two channels because most of the tritium penetrated through the shortest distance of the channel separation. The influence of the channel diameter, the plate thickness, and the ridge thickness on the effective distance was analyzed.

A PCHE permeation model to predict the tritium permeation rate was developed by Park et al. [72], which showed reduced errors in comparison to existent models. Geometric parameters such as diameter, plate thickness, ridge thickness, offset distance, and thermal parameters such as the average temperature and the temperature difference between channels were studied. The most decisive geometric parameter was the plate thickness, and its increment causes the increase of the travel distance, and then, the reduction of the permeation rate.

Overall, if the required configurations and purification systems are considered, the tritium concentration present in the hydrogen product can be under the limits for gaseous effluent. The IHX is a key point in the permeation toward the rest of the plant. The permeation models for PCHE design have allowed to know the geometric characteristics that reduce the tritium permeation.

1.9.2. *Dynamic performance*

The PCHE performance has been mainly studied in steady-state, but the dynamic analysis is essential to reach safe starts and shutdowns of the reactor and to study possible accident scenarios. The high temperature causes large thermal inertia that does longer the transition times from normal operation to inactivity and

vice versa. The dynamic operation of two straight channel and zigzag channel PCHE was investigated by Chen et al. in [65] and [73], respectively, through a dynamic model that was verified with experimental data. The outlet temperatures in both cold and hot channels when helium inlet temperature changes and helium mass flow rate changed were studied, and the time of the stabilization of the temperature was around fifteen seconds for straight channels and five seconds for zigzag channels.

On the other hand, understanding the transient scenarios under accident conditions is fundamental in the nuclear industry. Liu et al. [74] simulated a horizontal cylinder in helium gas in flow decay conditions. It was found that the cylinder temperature increased quickly for a shorter flow decay time during the flow decay process, which demonstrates the importance of the thermal-hydraulic processes in the reactor core and the IHX. The work of Ravindran et al. [75] analyzed the PCHE performance as IHX in a loss of coolant accident (LOCA) using the simulation tool RELAP5-3D, in which the variation of the primary loop and secondary loop parameters was considering. An exponential transient process of loss of pressure in the primary side over a period of 20 seconds was simulated. The results of the simulation indicated that heat is initially transferred from the primary loop to the secondary loop, but after the loss of pressure occurs, heat is transferred from the secondary loop to the primary loop. Overall, decay heat exchangers have been considered to work with IHX during the heat extraction from the reactor in accident scenarios.

1.10. Chapter summary

This chapter presented the HTGR technology as part of the NGNP, which allows efficient hydrogen production and the Brayton cycle utilization in the power system. Some of the possible plant configurations were depicted and the safety advantages of the indirect parallel cycle were shown. Many heat exchanger types were compared and the PCHE evidenced the highest overall heat transfer coefficient and the lowest volume. The straight and the zigzag channel PCHE were demonstrated as the better channel configurations with helium fluids at relatively low Reynold numbers.

To assess the thermal-hydraulic performance of the PCHE, some approaches have been used, but in general, the Nusselt number and the Fanning friction factor calculation have been a common target of many authors. The available correlations to obtain these non-dimensional numbers in the open literature were presented, most of which were reached under very specific geometric conditions and Prandtl numbers. With this in view, the current research is focused on proposing new heat transfer correlations in wider ranges of the geometric parameters, to assist more accurate calculations in the heat exchanger design.

2. APPROACHES FOR THE STRUCTURAL ASSESSMENT OF THE PCHE

The structural analysis of the heat exchangers in common temperature ranges is mostly focused on the mechanical stress calculation. However, the structural assessment is more complex when the temperature reaches the values present in the HTGR because of the degradation of the material properties with the time and the temperature, and the consequent need to reduce the stress field in the structure up to very low levels. In this chapter, the procedures to achieve the structural assessment of the PCHE under IHX condition in an HTGR are presented.

2.1. Particularities of the structural analysis at very high temperatures

The safety and lifetime associated with the heat exchangers operation depend on its structural functioning. The operating conditions of the heat exchangers in the nuclear power plants based on advanced reactors can be critical to the structural stability, caused by the pressure and temperature ranges and the fluid characteristics. One of the most challenging technology is the HTGR, where the hot fluid temperature can reach 1173 K and the pressures of the fluids are between 7 MPa and 8 MPa in the IHX, as seen in Chapter 1. In general, the degradation of structural material properties is one of the most key problems of the high temperature industries.

An important issue in the heat exchangers' structural performance is the temperature gradient, which creates expansion and contraction of the structures on heating and cooling, respectively. The simplest case of the thermal expansion can be analyzed as a one-dimensional problem of a rod, which is heated from the room temperature T_0 to a higher temperature T_1. The length of the rod is increased in a proportional value to the temperature difference, $\Delta T (= T_1 - T_0)$, according to the Eq. 2.1.

$$\Delta l = \alpha_L \, \Delta T \, l \tag{2.1}$$

where l is the length of the rod, Δl is the change of the length and α_L is the coefficient of linear expansion. There is no stress in the material when the free expansion or contraction is allowed. If the thermal expansion is restricted, a thermal stress field appears, which can be calculated using Eq. 2.2. This kind of mechanical restraint is external because it constrains the external movement in all directions.

$$\sigma_{th} = E \, \alpha_L \, \Delta T \tag{2.2}$$

where σ_{th} is the thermal stress and E is Young's modulus. But the heating or cooling of the structures from the room temperature until the working temperature in the industry is managed in such a way that the change of volume is allowed almost without external restraints. However, always that a temperature gradient takes place, the differential expansion of the material fibers causes that there are internal restraints, and then, the thermal stress fields occur [76]. The natural growth of one fiber at a temperature value is influenced by the different growth requirements of adjacent fibers at a different temperature. The result is distortion, in which the fibers at higher temperatures are compressed and those at lower temperatures are tensed.

The thermal stress fields generated by the internal restraints are inherent to the heat exchangers operation due to the temperature difference between fluids. The calculation of these stress fields in the PCHE is notably more complex than the simple use of Eq. 2.2, because it depends on the temperature field in the structure, the heat exchanger geometry, and the local variation of the coefficient of linear expansion and Young's modulus with the temperature [76], as it will be seen later. The thermal stress reduction is most important at high temperatures because the structural properties of the materials are notably affected. Therefore, reducing the thermal gradient is essential to avoid failure due to excessive deformations.

The mechanical stress is also present in the IHX structure and it can be caused by fluid pressures, vibrations, and other external forces. As a pressure vessel, the internal pressures in the heat exchanger constitute the most dangerous loading in normal operation. There is a wide knowledge about the mechanical stress management in these vessels collected in the ASME BPVC, Section VIII, Division 1 [77]. The requirements applied to the high temperature reactors are treated in the ASME BPVC, Section III, Division 5 [78], while Division 1, Subsection NH [79] is specifically dedicated to the high temperature components in nuclear power plants, such as the IHX.

Other structural characteristics particularly present in the IHX functioning include fatigue strength, creep deformation, and plasticity. The fatigue strength is related to the stress or strain intensification by each strain cycle, which can be elastic before the yielding point or inelastic when the initial strain state is not recovered after loading retirement. Creep is the special case of inelasticity that relates to the stress-induced time-dependent deformation under load. Plasticity is the special case of inelasticity where the material undergoes time-independent nonrecoverable deformation [79]. These features generate structural risks during the dynamic operation of the IHX and are very accentuated at high temperatures.

The procedures to establish the allowable stress values for each loading conditions are considered in the ASME BPVC. Details about the application of these codes in the PCHE structural analysis will be presented below.

2.2. Structural assessment procedures in the ASME BPVC

In this section, the loading classification and the requirement that the IHX should satisfy to reach a safe operation according to the ASME codes are presented. The current research is focused on the analysis of the PCHE functioning as IHX in an HTGR plant, therefore, the ASME BPVC, Section III, must be used to assess the structural performance of the device. But, the ASME BPVC, Section VIII, is also considered for greater applicability of the current study because similar high temperature levels than those of the HTGR can be reached by heat exchangers in other non-nuclear applications such as concentrating solar power [19][80].

The ASME BPVC, Section III, Subsection NH, classifies components of a nuclear power plant from Class 1 to Class CS, according to their levels of importance [79]. Class 1 includes valves, piping, pumps, pressure vessels, and steam generators as parts of the reactor coolant system. Also, different loading conditions are defined as a function of the operation mode where they could appear. Level A Service Loading corresponds to the most severe temperature, pressure, and mechanical loads in the system, which are defined as normal

operation, including startup and shutdown. Levels B, C, and D Service Loadings are deviations from normal operating conditions, increasing severity and reducing probability. The conditions and requirements of the PCHE used as IHX considered in this work are within the Class 1 of components and the Level A Service Loading of the Subsection NH for components at elevated temperatures.

The following definitions and equations are applied when the stress level is within the linear elastic region of the materials. The stresses that are present in pressure vessels are separated into various classes in the ASME BPVC [77][79] following the types of loads that produced them, the hazard that they represent to the vessel, their intensity, and the distance of the incidence region. Each class of stress must be maintained at an acceptable level and the combined total stress must be kept at another acceptable level [76].

The primary stress is created by mechanical load and exclude that stress caused by structural discontinuities. It is classified as primary membrane stress (P_m) and primary bending stress (P_b). The fluids pressure in the PCHE channels mainly causes P_m. The own weight and the supports of the device cause bending, but these loads are beyond the scope of the current research. The secondary stresses are self-limiting loads caused by junctures, structural discontinuities, and temperature gradients, which are relieved once a slight deformation occurs. They are also classified as membrane stress (Q_m) and bending stress (Q_b), but the temperature gradient mainly causes membrane stress [76].

The excessive membrane stress resulting from mechanical loads in structural discontinuities is considered as secondary stress by ASME BPVC, Section VIII [77], dedicated to the non-nuclear industry because higher risk levels are accepted. However, Section III, Subsection NH, classifies that as local primary membrane stress (P_L), which has lower allowable stress values than the secondary stress [76]. The basic difference between a P_L and secondary stress is that the first one is produced by a load that is unrelenting where the stress is just redistributed, while considering secondary stress, yielding relaxes the load and it is self-limiting [76].

The tips of the semicircular channels of the PCHE could be sources of this local stress. To consider the mechanical stress concentration as local primary membrane stress or secondary stress, the stress field should satisfy Eq. 2.3 and 2.4 according to Subsection NH [79].

$$d_1 \leq \sqrt{R \times t} \tag{2.3}$$

$$d_2 \geq 2.5\sqrt{R \times t} \tag{2.4}$$

where d_1 is the distance over which the maximum stress intensity exceeds the value of $1.1S_o$, d_2 is the meridional direction distance between regions of maximum stress intensity greater than $1.1S_o$, S_o is the maximum allowable stress intensity under Design Loadings [79], R is the minimum midsurface radius of curvature, and t is the minimum material thickness in the region considered. In the structural analysis of the PCHE that will be presented later, R and t in Eq. 2.3 and 2.4 will be substituted by r and t_f from Figure 1.9, respectively.

The thermal stresses that could concentrate on the tips of the semicircular channels of the PCHE and in other local discontinuities are considered as peak stresses (F). The basic characteristic of peak stress is that

it does not cause any noticeable distortion and is objectionable only as a possible source of a fatigue crack or a brittle fracture, and, at elevated temperatures, as a possible source of localized rupture or creep-fatigue failure [79]. The failures that can occur during the PCHE operation are mainly produced by the excessive plastic deformation, the rupture stress because of creep deformation, and the plastic instability caused by the cyclic strain.

The stress intensity values should meet the conditions of Eq. 2.5 and 2.6 in Design Loadings analysis according to the ASME BPVC, Sections III [79].

$$P_m \leq S_o \tag{2.5}$$

$$P_L + P_b \leq 1.5S_o \tag{2.6}$$

For Class 1 component Level A Service Loading limits specified by the ASME BPVC, Sections III [79], the calculated stress intensity values shall satisfy the Eq 2.7 – 2.10.

$$P_m \leq S_{mt} \tag{2.7}$$

$$P_L + P_b \leq KS_m \tag{2.8}$$

$$P_L + \frac{P_b}{K_t} \leq S_t \tag{2.9}$$

$$K_t = \frac{K+1}{2} \tag{2.10}$$

where S_{mt} is the allowable limit of the general primary membrane stress intensity for a time of service and the maximum wall averaged temperature, which is the lower of two allowable stress intensity values, the S_m (time-independent) and the S_t (time-dependent). The K factor is a value to consider the geometry of the cross-section of the device, which could take values from 1.0 [81] to 1.5 [82]. The value of S_t in Section III is the lowest among the following three stress values: 100% of the average stress to obtain a total strain of 1%, 80% of the minimum stress to cause initiation of tertiary creep or 67% of the minimum stress to cause rupture [79]. In non-nuclear applications, the stress limits imposed by the BPVC Section VIII, Division 1, can be applied, which are more permissible than those in Section III.

According to Section VIII, Division 2 [76], calculated stress intensity values shall also satisfy Eq. 2.11 – 2.12, which consider the thermal stress by mean of the secondary stress and the peak stress.

$$P_m + P_b + Q_m + Q_b \leq 3S_{mt} \tag{2.11}$$

$$P_m + P_b + Q_m + Q_b + F \leq 2S_a \tag{2.12}$$

where S_a is the allowable stress for a given number of cycles from design fatigue curves. The value of S_a in Section III is the lowest among the following two stress values: 1.25×S_t using the highest wall averaged

temperature during the cycle in a time of 10^4 h or the average of the two yield stress (S_y) values associated with the maximum and minimum wall averaged temperatures during the cycle.

Otherwise, the most used stress theories to calculate the stress values in the structural analysis are the maximum stress theory and the maximum shear stress theory. Both ASME BPVC, Section VIII, Division 1 [77], and Section I, base the stress analysis on the maximum stress theory, which only considers the value of the maximum principal stress. It is non-conservative in some instances and requires a higher safety factor for its use. While, the maximum shear stress theory is used by both ASME BPVC, Section VIII, Division 2, and Section III, which concerns that yielding starts in planes of maximum shear stress and considers the values of the maximum and minimum principal stresses [76]. In a thin-wall vessel, the maximum stress theory could be accurate because the radial stress is insignificant compared with the hoop stress. But, the PCHE must be studied as a thick-wall vessel in which biaxial stress state has been verified; therefore, the maximum shear stress theory is most adequate to apply. That is, the elastic stress intensity (S) is assumed as the difference between the maximum and minimum principal stresses (σ_1, σ_2, and σ_3 in the three principal planes) at a point for triaxial conditions, as shown in Eq. 2.13.

$$S = Max\{|\sigma_1 - \sigma_2|, |\sigma_2 - \sigma_3|, |\sigma_3 - \sigma_1|\} \qquad (2.13)$$

ASME BPVC, Section VIII, Division 2 is designed by analysis whereas Division 1 is designed by rules. Just as the design of a nuclear reactor would not be carried out using the rules of Division 1, the design of an air receiver would not be conducted by the techniques of Division 2 [76].

The allowable stress value and other structural properties such as Young's modulus and Poisson's ratio, essential to the structural calculation, depending on the material selection. Considering the complex operation condition of the PCHE used as IHX in an HTGR system, special alloys have been investigated to be employed. Those with higher possibilities of application will be compared then.

2.3. Special metals used as structural material

The degradation of the structural material properties with the time is a great difficulty at very high temperatures; therefore, time-dependent allowable stress is usually more appropriate than conventional allowable stress to evaluate the materials' strength [83]. Structural properties of some special alloys at high temperatures have been tested in recent years, such as Alloy 617 (UNS N06617) [84][85][86], Alloy 800H (UNS N08810) [87], Alloy 230 (UNS N06230) [88][89], Alloy 276 (UNS N10276) [90] and Alloy X (UNS N06002) [35]. The chemical composition of these metals is shown in Table 2.1. The nickel-based alloys exhibit better structural characteristics, as it will be seen later.

The most important structural properties at high temperature are related to the stress-strain relationships at different times of exposure, and the corrosion resistance. The decreasing of allowable stress, the reduced lifetime, and the oxidation increase have been evidenced for all materials. Figure 2.1 shows the maximum allowable stress intensity for the Design Condition calculation and the allowable stress intensity for a time of service of 100,000 hours of the metals with greater possibilities of application in the high temperature reactor plants [79][91][92]. Alloys 617 and 230 display the highest allowable design stress intensities. Alloy

X [35] and Alloy 230 [93] are being studied as a structural material in the HTGR plants. They have presented similar strength at very high temperatures than Alloy 617, and even they have shown smaller corrosion rate than Alloy 617 [35]. However, neither has been judged to have sufficient technical maturity and creep properties to proceed with ASME BPVC, Section III, Division 5 qualification. For example, Alloy 230 is more prone to carburization [94]. In general, Alloy 617 has offered better strength behaviors than other alloys at temperatures up to 1273 K according to the high temperature tensile testing of Wright et al. [95].

Table 2.1: Chemical composition in weight percent of some alloys tested at high temperatures.

Material	Ni	C	Fe	Si	Mn	Co	Cr	Ti	P	S	Mo	Al	B	Cu	V	W
N06617 [96]	Base	0.08	1.49	0.06	0.11	11.58	22.16	0.35	0.003	0.001	9.80	1.12	0.002	0.08	-	-
N10276 [90]	58.33	0.006	5.94	0.008	0.42	0.10	15.84	-	0.002	0.001	15.93	-	-	-	0.01	3.40
N08810 [95]	30.45	0.06	Base	0.37	1.31	0.11	19.30	0.45	-	-	0.21	0.43	-	0.21	-	-
N06230 [97]	Base	0.11	0.94	0.38	0.5	0.19	22.39	0.01	0.008	0.02	1.36	0.37	0.03	-	-	14.3
N06002 [94]	Base	0.10	18.0	< 1	< 1	1.50	22.0	-	-	-	9.0	-	0.008	-	-	0.60
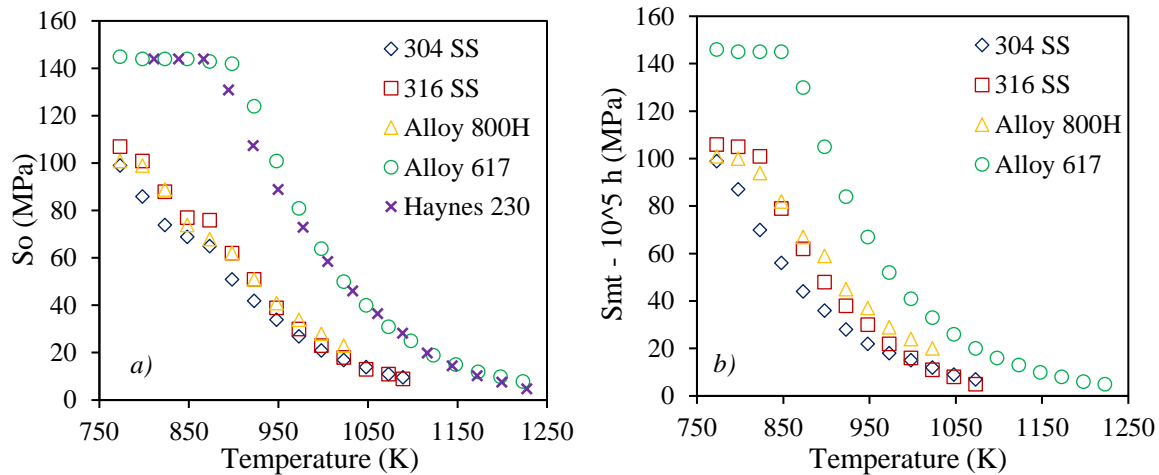
Figure 2.1: Structural data for several special metals: a) Maximum allowable stress intensity for Design Condition calculation and b) allowable stress intensity for a time of service of 10^5 hours [79][91][92]*.*

The long durations tests require several years of measurements to qualify a material for the ASME BPVC because yield, allowable and rupture stresses are necessary for a time of services up to 30 years and limited time extrapolations are possible. Ferritic steels 2.25Cr-1Mo and 9Cr-1Mo-V, and stainless steels 304 and 316 are qualified in the ASME BPVC, Section III, Division 5, but not as Class 1 component at high temperature. Alloy 800H was the only one fully qualified in the ASME BPVC, Section III, Division 5, as Class 1 component at high temperature, but at temperatures up to 1037 K and a maximum time of service of 300,000 hours [79][95]. Alloy 617 has been included in the Code with temperatures up to 1200 K and

time of service of 100,000 hours in May 2020 [98]. Therefore, in this research, the Alloy 617 was selected as structural material.

The material strength performance of the Alloy 617 has been tested under conditions of an IHX in an HTGR plant using helium atmospheres in the tensile tests. Kim et al. [96][86][99] found similar structural properties degradation in both air and helium atmospheres, although it happened faster in helium, which was attributed to the variation of the microstructural characteristics such as the carbide depleted zone, oxidation structures, surface cracking, voids below the surface, and voids in the matrix. They determined that the thickness of the oxide layer has a parabolic increase with the rupture time. This layer was reduced at 1123 K up to 50% in comparison with those at 1173 K and 1223 K. The relationships among the creep strain, the stress intensity, and the rupture were also proposed by Kim et al. [85], which can allow the estimation of the time of work up to rupture of a piece of Alloy 617 knowing the stress intensity. The temperature and strain rate impact on the properties was assessed by Kaoumi et al. [100]. All these studies and others as [95] contributed to the creation of a Draft ASME Code [91] and the subsequent qualification of the Alloy 617 in the ASME BPVC, Section III, Division 5.

The thermophysical properties of Alloy 617 as density and thermal conductivity can be found in this Draft Code [91], as temperature functions. The structural properties as S_y, ultimate tensile stress (S_u), coefficient of linear expansion, Young's modulus, and Poisson's ratio (v) in the temperature range of interest are presented in Table 2.2.

Table 2.2: Structural properties of Alloy 617 at high temperatures [91]*.*

Temp. (K)	S_y (MPa)	S_u (MPa)	α_L (μm/m/K)	E (GPa)	v [92]
998	161	459	15.2	-	0.3
1023	161	428	15.3	156	0.3
1048	161	394	15.5	-	0.3
1073	156	359	15.6	152	0.3
1098	151	322	15.7	-	0.3
1123	144	284	15.9	146	0.3
1148	136	246	16	-	0.3
1173	127	208	16.1	141	0.3
1198	117	172	16.3	-	0.3
1223	106	139	16.4	136	0.31

Within the most important issues presented in the Draft Code is the definition of the allowable stress intensity values (S_{mt}) of the Alloy 617. Figure 2.2 presents the variation of the S_t and S_m with the temperature taken from the Draft ASME BPVC [91]. The no influence of the time on the allowable stress is verified at a relatively low temperature.
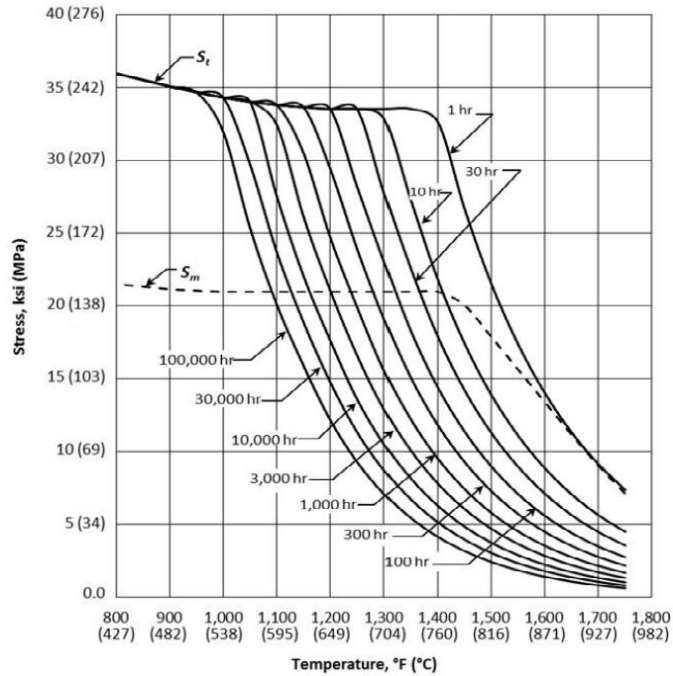
Figure 2.2: Allowable stress intensities for Alloy 617 [91]**.**

Table 2.3 shows some values of S_{mt} taken from the Draft ASME BPVC for Alloy 617 [91]. The decrease of the allowable stress intensity can be observed with the temperature and with the time of service.

Table 2.3: Allowable stress intensity (S_{mt}) values for Alloy 617 [91]**.**

T (K)	1 h	10 h	100 h	1,000 h	10,000 h	100,000 h
998	145	145	133	89	60	40
1023	145	145	108	72	47	31
1048	144	133	87	57	38	25
1073	132	109	71	46	30	19
1098	118	89	57	37	24	15
1123	104	72	46	29	19	12
1148	90	59	37	23	15	9.3
1173	76	48	30	19	12	7.3

Once the material properties are known, different procedures have been used to calculate the stress intensity in the PCHE structure under different operating conditions, which shall satisfy the equation presented before according to the ASME BPVC, Section III.

2.4. Analytical calculation for the structural analysis of the PCHE

The analytical calculation of the thermal and mechanical stresses in ducts is only available when the cross-section shows a very elemental shape such as a hollow cylinder [101][102]. Although the shape of the channels of the PCHE is usually semicircular, as shown in Figure 1.9, it has been calculated using the thick-wall cylinder theory by some authors [12][103][40]. There are two principal stresses in a hollow cylinder considering a plane stress state according to this theory, the hoop and the radial stresses. The maximum mechanical stress (σ_m) is reached in the inner wall channel and it can be obtained by the hoop stress (σ_h) and the radial stress (σ_r), according to Eq. 2.14 and 2.15, respectively [101].

$$\sigma_{h,max}^m = \frac{P_i\left[\left(\frac{D}{2}\right)^2 + t_p{}^2\right] - 2P_o t_p{}^2}{t_p{}^2 - \left(\frac{D}{2}\right)^2} \tag{2.14}$$

$$\sigma_{r,max}^m = -P_i \tag{2.15}$$

where the inner radius equal to half of the channel diameter (*D/2*), and the outer radius equal to the plate thickness (t_p), were adjusted as dimensions of the hollow cylinder from Figure 1.9, and P_i and P_o are the pressures at the inner and outer radii, respectively. These equations are also known as Lame's equations. The stress intensity can be calculated through Eq. 2.13, or equivalent stress according to the von Mises criterion can be obtained from Eq. 2.16, using Eq. 2.14 and 2.15.

$$\sigma_v = \sqrt{\sigma_h{}^2 - \sigma_r\sigma_h + \sigma_r{}^2} \tag{2.16}$$

This procedure is suggested by Hesselgreaves [103] to evaluate the mechanical stress of the PCHE and other simplified equations are obtained considering the pressure difference between channels. Those equations were employed in the PCHE design fabricated by Mylavarapu et al. [12] to be used in a helium test facility at high temperatures. Required and available ratios among characteristic dimensions of the channels were proposed considering the allowable stress, as shown in Eq. 2.17 and 2.18.

$$\left(\frac{t_f}{D}\right)_{required} \cong 0,1 \tag{2.17}$$

$$\left(\frac{t_p}{D}\right)_{required} \cong 0,55 \tag{2.18}$$

Mylavarapu et al. [12] obtained that the pressure of design should be lower than half of the allowable design stress. This non-conservative approach of the thick-wall cylinder approximation is useful to estimate the mechanical stress caused by the internal pressure, but it does not consider the effect of the channel geometry details.

Another method to calculate the mechanical stress is based on the ASME BPVC, Section VIII, Division 1 [77], where the configuration of the semicircular channel is analyzed as stayed plates on a flat plate. Several criteria are considered to compare the membrane and the bending stresses with the allowable stress

multiplied by a join factor of 0.7. The Code proposes a safety factor used in situations where there is no knowledge about the actual stress field. Overall, the detailed evaluation and more realistic estimation of the PCHE structural integrity have not been achieved under these bases because they do not consider the thermal stress field and the stress concentration.

The hollow cylinder approximation could be also used to estimate the thermal stress (σ_{th}) in the PCHE channels, and the hoop and radial stresses due to the thermal gradient can be obtained [102]. The theory for the thermal stress calculation in a hollow cylinder requires a thorough analysis and the knowledge of the temperature gradient function ($\Delta T(r_x)$) in the radial direction. The maximum equivalent thermal stress takes place in the inner wall, where there is no radial stress, and the hoop stress with free traction is calculated as Eq. 2.19 [102].

$$\sigma_{h,max}^{th} = \frac{\alpha_L E}{\left(\frac{D}{2}\right)^2} \left[\frac{2\left(\frac{D}{2}\right)^2}{t_p^2 - \left(\frac{D}{2}\right)^2} \int_{\frac{D}{2}}^{t_p} \Delta T(r_x) r_x dr_x - \Delta T(r_x) \right] \tag{2.19}$$

where r_x is the cylinder radius between the inner ($D/2$) and outer (t_p) radii. A linear variation of the temperature gradient function can be considered in some applications as the heat exchangers. This equation can give an approximated mean value of the thermal stress in the semicircular channels of the PCHE because the thermal stress is self-limited [78]. That is, the thermal stress concentration in some wall regions of the non-circular channels causes the stress decrease in other regions. However, the simulation process is necessary to have more precise information about the stress concentration points and the influence of the geometric parameters.

Furthermore, to have precise information about the stress field in the PCHE structure under conditions of the IHX in an HTGR plant is essential to achieve its safe operation. Finite Element Analysis offers the possibility of carrying out accurate calculations considering geometric and loading details.

2.5. Structural analysis of the PCHE using Finite Element Analysis

Numerical simulations using Finite Element Analysis (FEA) have offered information about the stress field in the PCHE under several loading conditions. Lee and Lee [81] analyzed the structural integrity of the PCHE under IHX conditions for a Sodium-cooled Fast Reactor (SFR). They considered liquid sodium at a pressure of 0.1 MPa and a temperature of 799 K as primary fluid and supercritical CO_2 at 19.7 MPa and 781 K as secondary fluid. The highest stress value was at the tips of the semicircular channels, and the mechanical stress due to fluids pressure was higher than the thermal stress. The influence of the pressure difference on the stress field in a PCHE with supercritical CO_2 as fluids in both sides was investigated by Wang et. al [104]. The operating conditions included a temperature of 600 K and pressures from 0.1 MPa to 22.5 MPa in the hot channel and fixed values of 400 K and 22.5 MPa in the cold channel. The mechanical stress increased with the hot fluid pressure and it was more significant than the thermal stress. The higher values of the total stress, which consider both pressure and thermal loadings, were at the tips of the cold channel. A rectangular micro-sized PCHE was studied by Yaqiong and Guihua [27] with helium and hydrogen fluids at pressures of 6 MPa and 20 MPa and temperatures of 700 K and 667 K, respectively. An

51

abrupt increase of stresses was obtained at the tip region, and the mechanical and thermal stresses are found to be equally important sources of stress. Operating conditions corresponding to an IHX in an HTGR plant were considered in the PCHE structural analysis of Mahajan et al. [105]. Helium fluids in both sides with pressures of 7 MPa and 2 MPa and hot temperature of 1223 K were defined. Geometric designs with different rounded tip radii (r) and semielliptical shape of the channels were investigated. The increase of the rounded tip radius caused the exponential decrease of the creep strain. All these works were conducted through two-dimensional (2D) models of the PCHE.

The use of three-dimensional (3D) models are mainly necessary if the flow channels have complexities in the flow direction. When the fluid flow changes its direction, the fluid-structure interaction (FSI) could be essential to reach more precise information on the stress concentration regions. Zhang et al. [106] studied the stress field in an S-shape PCHE as IHX in an SFR plant using a simplified 3D model due to the need for simulating the complicated flow channel geometry. The fluids were helium and supercritical CO_2 with temperatures around 550°C. They were focused on the effect of the pressure difference variation in a range from 13 MPa to 70 MPa on mechanical stress according to ASME BPVC rules. The tips were identified as the highest stress concentration zones. The zigzag channel PCHE presents continuous changes of direction. A reduced 3D model of a bend of the zigzag channel PCHE was studied by Bennett and Chen [82] using a one-way FSI analysis. Different temperature gradients between fluids were considered, and the cold side showed the highest total stress value. The geometric domain of this 3D model had two hot channels and one cold channel, which could be imprecise according to the multichannel domain analysis developed by Lee and Lee [81]. Overall, there are limited works dedicate to the PCHE structural assessment and the influence of the geometric design on the stress fields have not been accomplished.

2.6. Chapter summary

The problem associated with the thermal stress in the heat exchangers was presented in this chapter, which is caused by the internal restraints of fibers in a temperature field and produces failures by excessive deformation and fatigue crack. The structural properties degradation was identified as a challenge of the high temperature industry. The requirements that shall be accomplished for each kind of stress in the IHX were discussed according to the ASME BPVC, Section III, Division 5 and Division 1, Subsection NH. The operation condition to be considered in the structural analysis of the PCHE in this research was defined as Class 1 of components and the Level A Service Loading of the Subsection NH for components in elevated temperature.

Alloy 616 (UNS N06617) was found as the material with the better structural performance at high temperature, which was included in the ASME BPVC, Section III, Division 5, for temperatures up to 1200 K and a lifetime of 100,000 hours. The analytical calculation procedures of the stress values in the PCHE and their approximations were analyzed and the need of the FEA for detailed studies was proved. Works about the analysis of the design effect on the structural assessment of the PCHE was not found in the open literature. The fluid-structure interaction in the zigzag channel PCHE has not been accurately considered.

3. DESCRIPTION OF THE COMPUTATIONAL MODELS

The previous chapters have demonstrated the existence of research gaps in the thermal-hydraulic and structural analyses of the straight and zigzag channel PCHE, which could be filled using simulation tools. In this chapter, the computational models of the PCHE developed using CFD and FEA techniques are described, which allow conducting the thermal-hydraulic and structural studies, respectively.

3.1. Mathematical models

Two different mathematical models were used in the thermal-hydraulic and structural calculations using CFD and FEA, respectively. Both are presented below.

3.1.1. Computational Fluid Dynamics

The CFD commercial software Ansys CFX [107] was used to simulate the straight and zigzag channel PCHE. It allows resolving the CFD governing equations in three-dimensional geometric domains, as shown in Eq. 3.1-3.3 at steady state [107]. They represent the conservation of mass, momentum, and energy, respectively.

$$\nabla \cdot (\rho \, \vec{u}) = 0 \tag{3.1}$$

$$\nabla \cdot (\rho \, \vec{u} \, \vec{u}) = -\nabla P + \nabla \cdot (\tau) \tag{3.2}$$

$$\nabla \cdot \left(\rho \, \vec{u} \left(H + \frac{1}{2} u^2 \right) \right) = \nabla \cdot (k \nabla T) \ + \nabla \cdot (\tau \cdot \vec{u}) \tag{3.3}$$

where u is the velocity vector, H is the enthalpy and T is the temperature. The stress tensor (τ) is calculated according to Eq. 3.4.

$$\tau = \mu \left[(\nabla \vec{u} + \nabla \vec{u}^{\mathrm{T}}) + \frac{2}{3} I \, \nabla \cdot \vec{u} \right] \tag{3.4}$$

where I is the unit tensor and the index T denotes the transpose.

When fluid flows are in the transition regimen to the turbulence, the Shear Stress Transport k-ω (SST k-ω) turbulence model was used in the calculation, because it takes the advantages of k-ε and k-ω models [107] with a blending function. The k-ω model is used in the near-wall fluid elements, while the k-ε is applied in the fluid elements near boundary layer edges and free-shear layers [108]. In turbulent boundary layers, the maximum value of the eddy viscosity is limited by forcing the turbulent shear stress to be bounded by turbulent kinetic energy times [108].

In this work, the heat transfer parameters are analyzed from CFD results as averaged values in a full channel. The averaged Reynolds number is obtained through Eq. 1.7 using density, velocity, and viscosity values averaged in the fluid volume of the channel. As seen before, the heat transferred can be computed with Newton's cooling law, according to Eq. 1.3. The heat transfer rate and the surface temperature are averaged

in the heat transfer area, and the bulk temperature is obtained through the rate of the thermal energy advection integrated over the cross-sectional area (A_{cs}), as Eq. 3.5.

$$T_b \int_{A_{cs}} u\rho c_p dA_{cs} = \int_{A_{cs}} u\rho c_p T dA_{cs}$$

(3.5)

Eq. 3.6 can be reached integrating over the real channel length (L_R) both sides of Eq. 3.5.

$$\int_{L_R} T_b \int_{A_{cs}} u\rho c_p dA_{cs}\, dL_R = \int_V u\rho c_p T dV$$

(3.6)

To obtain the average value of the Nusselt number in each channel, the mean value of the bulk temperature in all the cross-sectional areas of a channel can be calculated by Eq. 3.7.

$$\overline{T_b} = \frac{\int_V u\rho c_p T dV}{\int_V u\rho c_p dV}$$

(3.7)

Then, the average Nusselt number in a channel is calculated through Eq. 3.8.

$$Nu = \frac{q D_h}{k A (T_s - \overline{T_b})}$$

(3.8)

where the thermal conductivity of the fluid is also averaged in the fluid volume.

The apparent Fanning friction factor is calculated using Eq. 1.11 considering averaged values of the density and the velocity in the fluid domain. To obtain the pressure drop due to friction losses, the pressure drop due to acceleration of the fluid at the inlet and outlet of the channel must be subtracted, and thus be able to reach the actual Fanning friction factor. The pressure drop due to acceleration (ΔP_{ac}) can be calculated as Eq. 3.9.

$$\Delta P_{ac} = (\rho u^2)_o - (\rho u^2)_i$$

(3.9)

then,

$$\Delta P_{fric} = \Delta P - \Delta P_{ac}$$

(3.10)

where ΔP_{fric} is the pressure drop due to friction losses.

3.1.2. *Finite Element Analysis*

The FEA of the PCHE was developed using Ansys Mechanical. The governing equations of the solid mechanic are fulfilled in the FEA. They guarantee the force balance between the surface forces and the body forces by Eq. 3.11 [109]. They allow the normal strain and the shear strain calculations by Eq. 3.12

and 3.13 [109], respectively, and the application of the generalized Hooke's law by Eq. 3.15 and 3.16 [102]. All these equations are expressed in the cartesian system.

$$\frac{\partial \sigma_x}{\partial x} + \frac{\partial \tau_{xy}}{\partial y} + \frac{\partial \tau_{xz}}{\partial z} + b_x = 0; \quad \frac{\partial \sigma_y}{\partial y} + \frac{\partial \tau_{yx}}{\partial x} + \frac{\partial \tau_{yz}}{\partial z} + b_y = 0; \quad \frac{\partial \sigma_z}{\partial z} + \frac{\partial \tau_{zx}}{\partial x} + \frac{\partial \tau_{zy}}{\partial y} + b_z = 0 \quad (3.11)$$

$$\varepsilon_x = \frac{\partial s_x}{\partial x}; \quad \varepsilon_y = \frac{\partial s_y}{\partial y}; \quad \varepsilon_z = \frac{\partial s_z}{\partial z} \quad (3.12)$$

$$\varepsilon_{xy} = \frac{1}{2}\left(\frac{\partial s_x}{\partial y} + \frac{\partial s_y}{\partial x}\right); \quad \varepsilon_{yz} = \frac{1}{2}\left(\frac{\partial s_z}{\partial y} + \frac{\partial s_y}{\partial z}\right); \quad \varepsilon_{zx} = \frac{1}{2}\left(\frac{\partial s_z}{\partial x} + \frac{\partial s_x}{\partial z}\right) \quad (3.13)$$

$$\varepsilon_x = \frac{\sigma_x}{E} - v\frac{\sigma_y}{E} - v\frac{\sigma_z}{E} + \alpha_L \Delta T; \quad \varepsilon_y = \frac{\sigma_y}{E} - v\frac{\sigma_x}{E} - v\frac{\sigma_z}{E} + \alpha_L \Delta T; \quad \varepsilon_z = \frac{\sigma_z}{E} - v\frac{\sigma_x}{E} - v\frac{\sigma_y}{E} + \alpha_L \Delta T \quad (3.15)$$

$$\varepsilon_{xy} = \frac{\tau_{xy}}{G}; \quad \varepsilon_{yz} = \frac{\tau_{yz}}{G}; \quad \varepsilon_{zx} = \frac{\tau_{zx}}{G} \quad (3.16)$$

In these equations, σ_i is the normal stress in Pascals, τ_{ij} is the shear stress in Pascals, b_i is the body force in N/m^3, ε_i is the normal strain, s_i is the displacement, ε_{ij} is the shear strain, v is the Poisson's ratio, and G is the shear modulus. The subscripts i and j represent the three cartesian coordinates in the equations.

3.2. Geometric domains

Different geometric domains were considered to reach the goals of this research. To analyze the relationship between the heat transfer and the cross-sectional dimensions, a 3D domain of a straight channel PCHE was created with one channel per fluid, as shown in Figure 3.1. The parameters analyzed were the channel diameter (D), the rounded tip radius (r), the ridge thickness (t_f), and the plate thickness (t_p), which were displayed in Figure 1.9. The PCHE channel length considered in the CFD calculations was 245 mm. However, the analysis of the cross-sectional dimensions using the FEA model was conducted with a pseudo-2D model of the solid domain because the stress gradient in the flow direction can be negligible in straight channels, and the need to consider multiple channels to reach accurate simulation in the structural analysis [81]. A pseudo-2D geometry with a channel thickness of 0.1 mm was used. The reference geometric design was defined with a channel diameter of 1.5 mm, a plate thickness of 1.5 mm, and a ridge thickness of 0.675 mm. The tips of the semicircular channels present a minimum roundness due to the fabrication process, which was defined as 0.0075 mm, as shown in Figure 3.1. The boundary conditions allow to obtain an equivalence between the reduced geometric domains and the real PCHE core, as it will be seen later.

The plate thickness, the ridge thickness, and the tip radius are expressed below as proportional relationship with the diameter, according to ratios t_p/D, t_f/D, and r/D, respectively. The geometric parameters were studied in ranges of 1.5 mm $\leq D \leq$ 2.0 mm, $0.8 \leq t_p/D \leq 1.2$, $0.15 \leq t_f/D \leq 0.75$ and $0.005 \leq r/D \leq 0.08$. Table 3.1 presents the five studied values per each one of these dimensions.
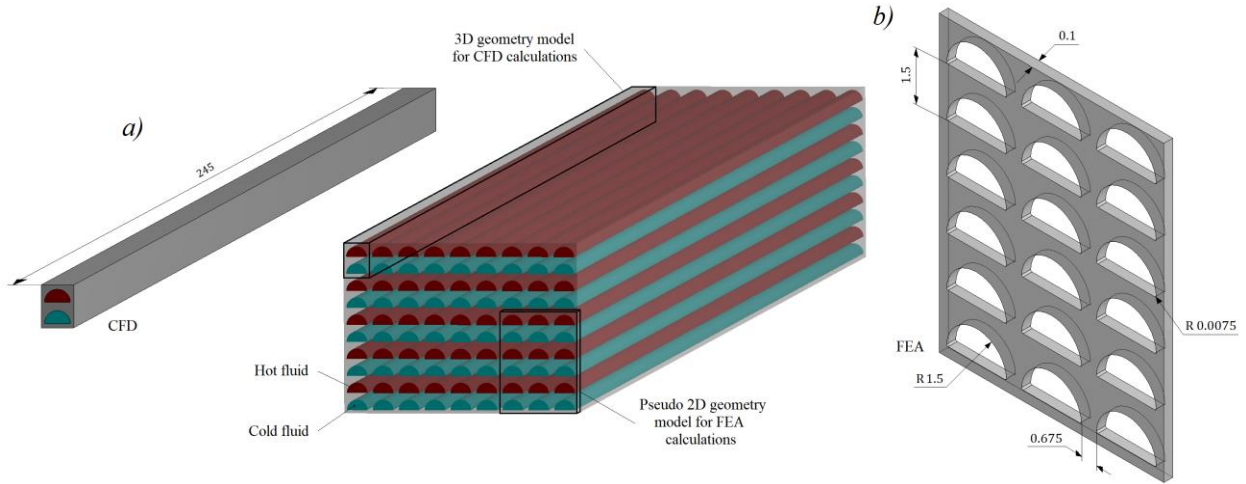
Figure 3.1: a) 3D geometric model and b) pseudo-2D geometric model extracted of a PCHE core and dimensions of the reference design of the cross-sectional dimensions (values in millimeters).

Table 3.1: Studied values of the cross-sectional dimensions.

Parameter	Reference design	Studied values				
D (mm)	1.50	1.50	1.625	1.75	1.875	2.00
t_p/D	1.00	0.80	0.90	1.00	1.10	1.20
t_f/D	0.45	0.15	0.30	0.45	0.60	0.75
r/D	0.005	0.005	0.02	0.04	0.06	0.08

The influence of the zigzag channel dimensions on the thermal-hydraulic and structural performances was also analyzed. Three of these dimensions are the zigzag pith length (l_Z), the zigzag angle (α), and the bend radius (Br), as shown in Figure 1.9. An additional geometric parameter is studied in this work: the zigzag phase-shift (λ), which indicates if the zigzag ripples of the cold and hot channels are in-phase or out-of-phase. Figure 3.2 displays two PCHE cores with different zigzag phase-shift. When zigzag is in-phase, the reduction of the geometric domain can be similar to the straight channel model presented before because the two fluid bodies and the solid body have the same path. However, the zigzag out-of-phase requires a more complex simplification due to the solid must cover the entire volume reached by the fluids in different paths to ensure heat conduction. A model with these characteristics was used by Khan et al. [61], but the accuracy of this model simplification to predict the temperature was not examined. An equivalent geometric model must be considered in the zigzag in-phase for comparison purposes, as shown in Figure 3.2.
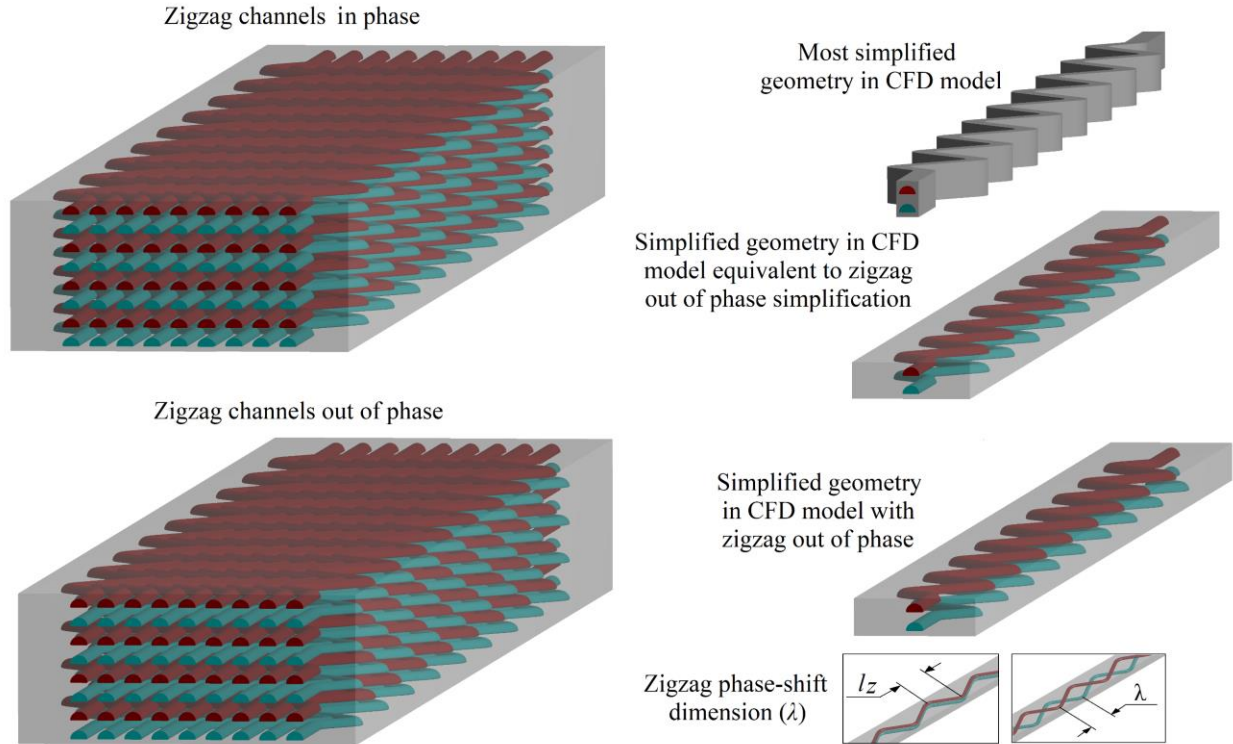
Figure 3.2: 3D geometric model simplifications of a zigzag channel PCHE with different zigzag phase-shift and illustration of the zigzag phase-shift dimension.

The same reference design presented in Table 3.1 was also considered to analyze the influence of the zigzag dimensions on the thermal-hydraulic performance of the PCHE. Then, the reference design was $\alpha = 0°$ or straight channels. All cross-sectional dimensions including diameter were fixed, while zigzag dimensions were tested. These dimensions were changed in ranges of 9.225 mm $\leq l_z \leq$ 18.45 mm, 5° $\leq \alpha \leq$ 45°, 0 $\leq Br$ $\leq$ 6.0 mm, and zigzags in-phase and out-of-phase. The zigzag pitch length and the bend radius were studied as proportional relationships with the hydraulic diameter, which was calculated as 0.9514 mm with Eq. 1.8. The straight section at the inlets and the outlets of the zigzag channels took values from 11.8 mm to 14.9 mm because several zigzag pitch amounts fit inside of the PCHE length for different designs. Table 3.2 shows the studied values of the zigzag dimensions.

The structural analysis of the zigzag channel PCHE needs a 3D geometric model. However, there is the requirement of multichannel models in this kind of study and the limitation of the high computational cost of the FEA calculations. Then, the geometric model considered was reduced to a zigzag bend region where fluids' direction changes. This geometric model with boundary conditions will be presented in the next section.

Table 3.2: Study values of the zigzag channel dimensions.

Parameter	Reference design	Studied values			
l_Z/D	-	9.70	12.93	16.16	19.39
α (degrees)	0	5	15	30	45
Br/D	-	0	2.10	4.20	6.31
λ/l_Z	-	0	1	-	-

3.3. Operating conditions

The operating conditions of the PCHE used as IHX were taken from the work of Wang et al. [60], in which the operating conditions of all devices of an HTGR plant were optimized. Thus, the temperatures in the cold and hot inlets were defined as 762 K and 1173 K, respectively, and the fluid pressures were 7.99 MPa and 7.73 MPa in the cold and hot channels, respectively. Similar operating conditions to be required in the IHX were also proposed by Aquaro and Pieve [110]. Counter-flow arrangements were established with *mass flow inlet* and *pressure outlet* boundary conditions on the inlet and outlet surfaces of the channels, respectively, according to Figure 3.3. The geometric model of the zigzag channel presents three channels per fluid because of the temperature field exactness, as it will be seen later.
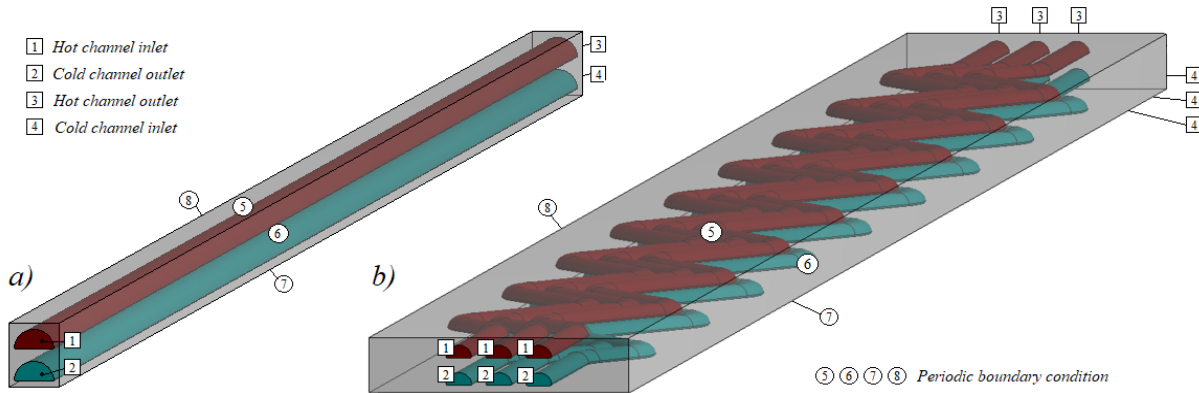
Figure 3.3: Boundary conditions of the a) straight and b) zigzag channel PCHE in the CFD models.

Many mass flows rates per channel were considered within values from 2.367×10^{-5} kg/s to 1.302×10^{-4} kg/s, which involve Reynolds numbers in a range from 550 to 3200. The critical Reynolds number in a straight circular duct is around 2300. However, there is some uncertainty about this value in channels with a semicircular cross-sectional shape. Figley et al. [26] suggested a critical Reynolds number in a straight semicircular channel of 3100 through simulations, while the experimental test analysis of Yoon et al. [111] for a similar PCHE was carried out with a value of 2100. Chen et al. [39] experimentally detected the transition regime from $Re = 2200$ in a zigzag channel PCHE with $\alpha = 15°$. A similar design of a zigzag channel PCHE was analyzed by Kim and Sun [71] considering the laminar regime up to $Re = 3000$. PCHE

with several zigzag angles up to 45° were numerically studied by Kim and No [58] and Yoon et al. [70], and laminar regimes were considered up to Reynolds numbers of 2500 and 2000, respectively. In the current work, the laminar regime was established up to $Re = 2200$, which is a reasonable value according to the literature.

On the other hand, the analysis of the influence of the cross-sectional and zigzag dimensions on the structural performance was developed taking the temperature fields from CFD results. Because the degradation of the material strength properties increases at higher temperatures, the most hazardous region is in the hot channel inlet and the cold channel outlet considering a counter-flow configuration. This region was chosen to analyze the cross-sectional dimensions through the pseudo-2D model, as shown in Figure 3.1.

Therefore, constant wall temperatures were defined in the surfaces of the channels to obtain the temperature field for the pseudo-2D model structural calculations. Symmetry boundary conditions on the two lateral surfaces and periodicity on the top and bottom surfaces were established for heat transfer calculation, as shown in Figure 3.4. The hot wall temperature was fixed in 1173 K, while the cold wall temperature was changed from 923 K to 1163 K to study the effect of the temperature difference between channels in a cross-sectional area (ΔT) on the thermal stress. Thus, temperature differences of 10 K, 25 K, 50 K, 100 K, 150 K, 200 K, and 250 K were analyzed. Lower and higher temperature gradients can be present in the counter-flow and parallel-flow configurations, respectively. The body temperature field was imported in the Ansys Mechanical as loading, and unrestrained supports were defined in the external boundary surfaces to calculate the thermal and mechanical stresses.

The 3D model considered to analyze the zigzag dimensions presented periodic boundary conditions and unrestrained supports on the outside surfaces for the CFD and the FEA calculations, respectively, as illustrates in Figure 3.4. In this case, the influence of the one-way FSI was considered as imported body temperature in the structural model. It also has a temperature gradient in the flow direction because convective heat transfer between fluids takes place. Wall channel pressures and unrestrained supports were also defined to calculate the mechanical stress field caused by the pressure of the fluids. The hot and cold channels pressures were specified as 7.73 MPa and 7.99 MPa, respectively, according to the optimized facility of Wang et al. [60].

Material properties were differently defined in the CFD and the FEA models. The helium properties used in the CFD calculations were described as temperature functions using polynomials that interpolate the data of helium at 7 MPa extracted from the National Institute of Standards and Technology webpage [112]. Besides, the polynomials of the solid domain were defined with the thermo-physical properties corresponding to Alloy 617 in [92]. These polynomials used in the CFD calculations are presented in Table 3.3. While, the structural properties of the Alloy 617 for the FEA model were taken from the Draft ASME BPVC [91], as it was presented in Table 2.2.
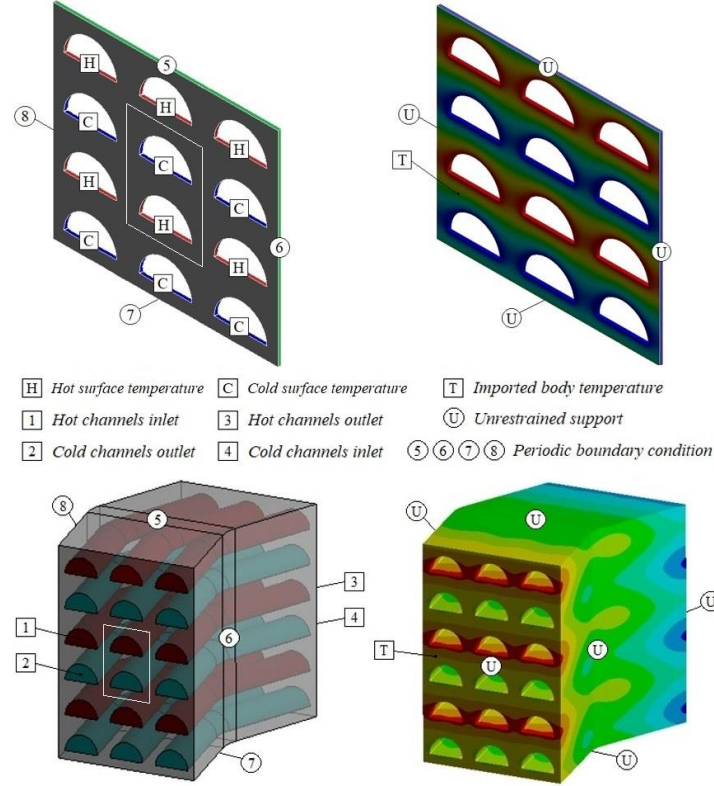
Figure 3.4: Boundary conditions defined in the CFD/FEA models to structural analysis (central channels are highlighted).

Table 3.3: Thermo-physical properties of helium at a pressure of 7 MPa [112] **and Alloy 617** [92]**.**

Property	Polynomial
Helium	
ρ (kg m^{-3})	$\rho = 9.697 - 0.009302\,T + 2.953 * 10^{-6}\,T^2$
c_p (J kg^{-1}K^{-1})	$c_p = 5127 + 0.2225\,T - 3.015 * 10^{-4}\,T^2 + 1.833 * 10^{-7}\,T^3 - 2.953 * 10^{-11}\,T^4$
μ (Pa $\cdot$ s)	$\mu = 7.764 * 10^{-6} + 4.42 * 10^{-8}\,T - 5.714 * 10^{-12}\,T^2$
k (W m^{-1}K^{-1})	$k = 0.07705 + 3.219 * 10^{-4}\,T - 3.493 * 10^{-8}\,T^2$
Alloy 617	
ρ (kg m^{-3})	$\rho = 8360$
c_p (J kg^{-1}K^{-1})	$c_p = 415.1 + 0.2454\,T$
k_w (W m^{-1}K^{-1})	$k_w = 13.12 + 0.01553\,T$

The computational models developed in this research took into account some assumptions to reduce the complexity remaining accuracy. In the CFD model, the fluid flows were considered steady and uniformly distributed by channels. The pressure drop across the heat exchanger has been small enough to assume that the fluids are incompressible in steady states, although the reference value can change appreciably when

going to different operating pressures. Also, the contact thermal resistance was considered insignificant and the heat losses to the surroundings were negligible. Although temperatures up to 1223 K can be present in the current application, the results of Kim et al. [38] showed that heat losses by radiation have a mean value of 1.53%, and Kim et al. [68] calculated the heat losses by radiation and convection with a mean value of 0.102% of the total heat transferred. Nevertheless, Yoon et al. [111] demonstrated that heat losses should be considered in the analysis of the experimental tests. In the FEA model, the structural material was considered homogeneous with isotropic properties, and external forces, such as vibrations, wind or supports effects, were not introduced.

3.4. Grid independence tests

Two mesh independence tests were carried out for both CFD and FEA calculations. Meshes with different numbers of elements, mainly in the cross-sections, were considered. The mesh study in the CFD model was developed in the three channels per fluid model shown in Figure 3.3. Seven meshes in a design with $D = 2.0$ mm, $l_Z = 12.3$ mm, $\alpha = 15°$ and $Br = 4.0$ mm, was considered. The Nusselt number and the Fanning friction factor for each grid were calculated with $Re = 957$. The grid independence test in the FEA model was developed with a pseudo-2D geometric domain of 4×3 channels (4 rows and 3 columns). All tested meshes have several element layers in the hot and cold wall channels. Table 3.4 shows the number of elements and nodes of the meshes created in both CFD and FEA models. Although the FEA meshes have fewer elements and nodes than the CFD meshes, structural calculations require high computer resources, with around 1 GB of memory per 16,000 nodes. Figure 3.5 shows the tetrahedral and hexahedral elements in the CFD and FEA meshes. Rounded tips have the highest elements density.

Table 3.4: Number of elements and nodes in the grid independence study of the CFD and FEA models.

	Mesh 1	Mesh 2	Mesh 3	Mesh 4	Mesh 5	Mesh 6	Mesh 7
CFD model							
Elements	3,856,671	9,075,961	24,942,010	38,087,146	48,669,005	57,163,318	99,865,457
Nodes	2,493,099	5,226,720	10,263,655	15,745,658	19,839,006	23,574,809	37,731,981
FEA model							
Elements	72,095	86,485	126,895	167,050	242,915	451,670	-
Nodes	344,725	411,565	600,290	786,652	1,139,745	2,108,195	-

The results of the CFD model with different meshes are presented in Figure 3.6. Since mesh 6 and mesh 7 provided almost the same values, and the maximum relative error between the Nusselt numbers calculated with these two grids was 0.74%, mesh 6 with around 57 million elements was selected because of accurate and time-saving simulations. The front view of the meshed volumes can be seen in Figure 3.5 a), in which hexahedral elements were created in the fluid domains and prismatic and tetrahedral elements were shaped in the solid domain to achieve a good mesh metric considering the zigzag ways inside the structure and the rectangular parallelepiped shape outside.
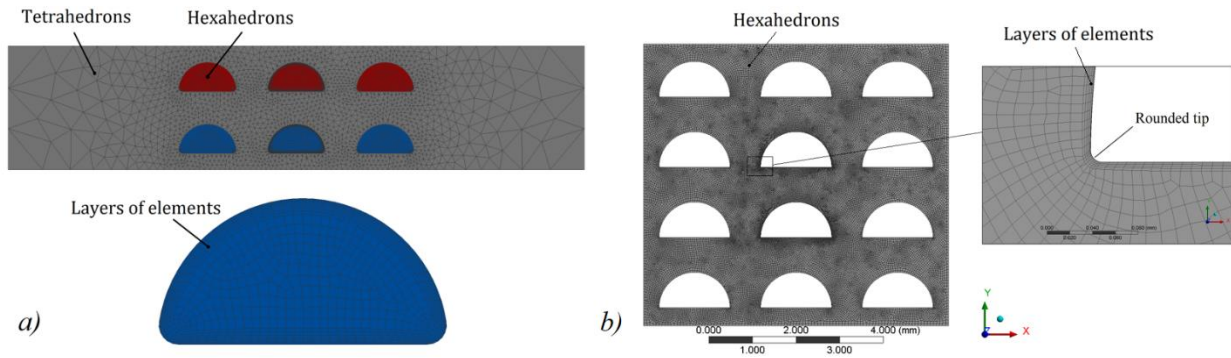
Figure 3.5: Elements distribution of the mesh 6 and 4 in the a) CFD model and b) FEA model, respectively.
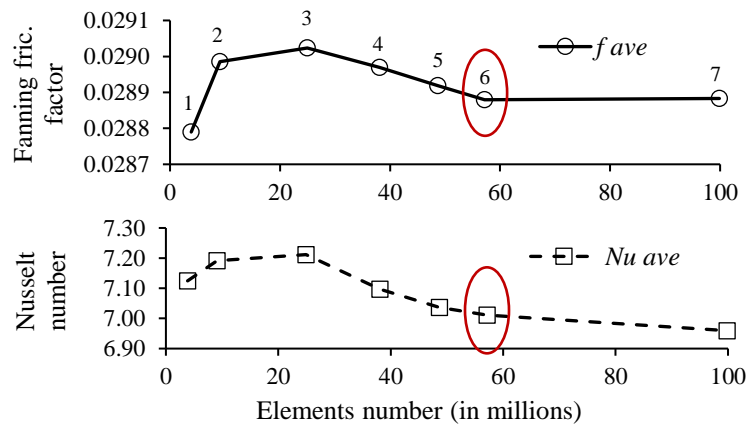
Figure 3.6: Fanning friction factor and Nusselt number averaged among all channels for several tested meshes.

Otherwise, the FEA model grids were assessed comparing the stress fields of each simulation with different mesh. The analysis of the stress fields was done in the walls of the hot and cold central channels, which are highlighted in Figure 3.4. Hereinafter, the reported values of the FEA results correspond to these central channels. Paths were defined in both channels according to Figure 3.7, in which the arrow indicates the direction of the stress or strain value along the channel path.

The total stress (σ_t) considering both thermal and mechanical loading was calculated for each mesh. In this grid independence test, the temperature difference between the hot and cold channels was 100 K, and the pressures on the hot (P_h) and cold (P_c) channels walls were 7.73 MPa and 7.99 MPa, respectively. Figure 3.8 displays the von Mises stress calculated as Eq. 2.16 across the cold channel path.

The variation of the von Mises stress in the path is very similar for all meshes. Only the peak stress at the tips changes due to the mesh refinement in this zone with very little roundness radius ($r = 0.01$ mm). The tips were evidenced as the critical points of stress concentration. In general, four critical points can be chosen as maximum stress points and they are indicated in Figure 3.7. Some analyses will be presented in

Chapter 5 at these four points. The maximum stress is almost constant considering both thermal and mechanical loading since mesh 4; hence, it was selected to be accurate with a reduced number of elements.
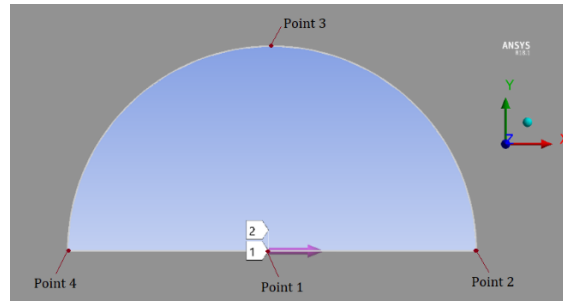
Figure 3.7: Path to analyze the stress and strain in the channel wall.
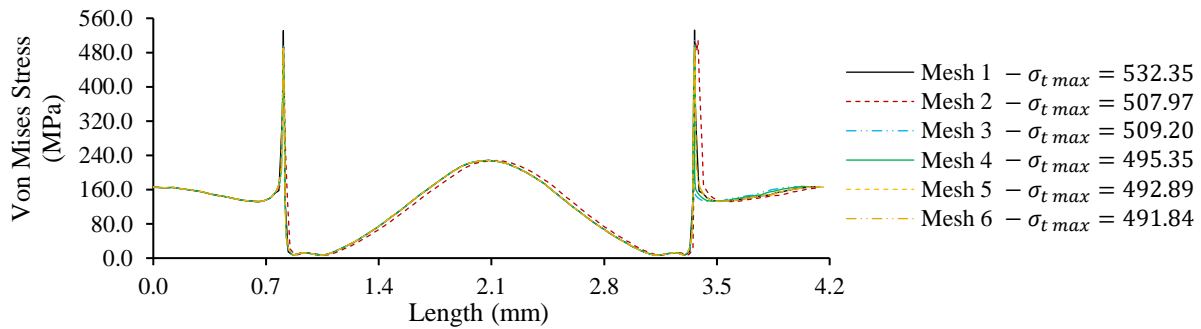
Figure 3.8: Von Mises total stress distribution in the path of the cold channel.

3.5. Simplification of the geometric domains

Two geometric domains were analyzed to achieve accurate and simplified models. First, CFD models of the zigzag channel PCHE with several channels amount were tested to verify the accuracy of the temperature field when zigzag are out-of-phase. Else, the influence of the amount of the channels on the stress field calculated using the pseudo-2D FEA model was evaluated.

3.5.1. *CFD model of the zigzag channel PCHE*

Because of the complexity of the manufacturing process, the PCHE plates have a width of up to 600 mm, and each plate normally has more than 200 channels etched [25]. However, some experimental tests have been accomplished using reduced devices with plates of around 12 channels [12][39]. The numerical analyses also have been done with domains reduced using boundary conditions. To simulate a straight channel PCHE or a zigzag channel PCHE with channels in-phase ($\lambda/l_z = 0$), periodic boundary conditions can be applied on external surfaces in a model with only one channel per fluid, as shown in Figure 3.3 a). However, more than one channel per fluid can be necessary to simulate zigzag channels out-of-phase.

Although some research have been developed considering the simplest model with one channel per fluid in zigzag channels out-of-phase [61][113], it has adjacent channels represented by periodic boundary conditions further away than real devices, which can affect the exactness of the heat transfer solution. The presence of closer adjacent channels can contribute to a more accurate simulation. Four geometric domains were created with one channel per fluid (2×1), three channels per fluid (2×3), five channels per fluid (2×5), and seven channels per fluid (2×7), as it is illustrated in Figure 3.9. The dimensions considered were D = 1.5 mm, l_Z = 12.3 mm, Br = 4.0 mm and α = 30°. Periodic boundary conditions were applied on the outside surface, as shown in Figure 3.3 b). The results analyzed in this section and throughout this research are taken from the central channels in darker colors in Figure 3.9.
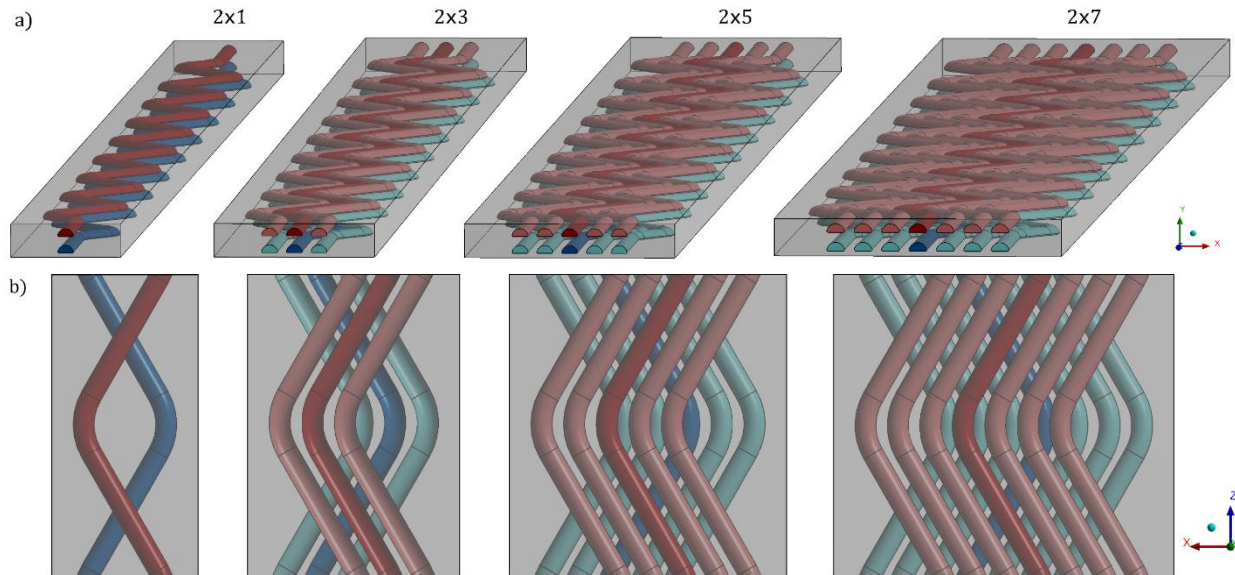
Figure 3.9: Geometric models with one channel per fluid (2×1), three channels per fluid (2×3), five channels per fluid (2×5), and seven channels per fluid (2×7), a) isometric view, and b) top view of one zigzag pitch.

Because one of the goals of this research is to study the heat transfer parameters in the fluid domains, the temperature field in the cross-sections of the inlets, the outlets, and the zigzag bends of both cold and hot central channels were obtained in each geometric model for Re = 957. Figure 3.10 shows them corresponding to the 2×3 model. The average temperatures of these contours were plotted in Figure 3.11 as a function of the channel length. Their values across the length of the central channels were very similar in the domains with adjacent channels. However, the 2×1 model underestimates the heat transfer with the highest temperature differences between the cold and hot channels, which is caused by the distance among adjacent channels. The maximum temperature difference between the geometric models with 2×3 channels and 2×7 channels was 0.73%, while the simplest model with 2×1 channels had up to 3.34% difference with 2×7 model. The solution of the model with 2×3 channels was considerably faster than that with 2×7 channels. Hence, the design with 2×3 channels was more advantageous to reach accurate solutions in a reduced time, which was essential to achieve a great number of calculations required in this work.
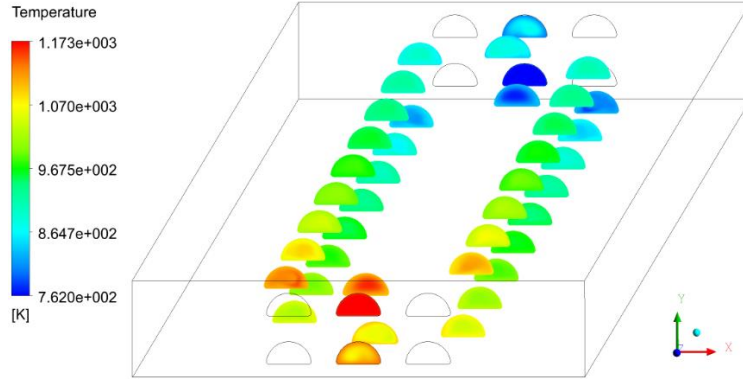
Figure 3.10: Temperature contours in the zigzag bend of the central channels of the 2×3 model.
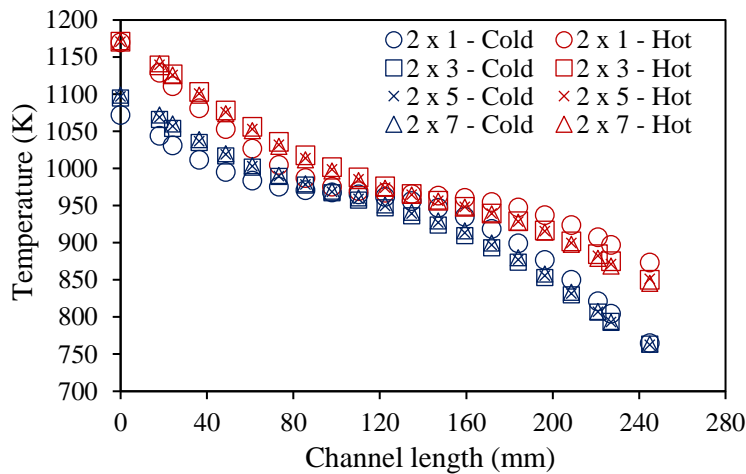
Figure 3.11: Averaged temperature variation across the zigzag bend of the central channels in designs with 2×1, 2×3, 2×5, and 2×7 channels.

3.5.2. FEA model with pseudo-2D geometry.

The influence of the channels number on the structural model accuracy has been proved before [81][11], different from the common domain simplification using symmetry and periodicity in CFD simulations. Thus, six geometric domains with different channels number were considered with similar boundary conditions presented before. The thermal, mechanical, and total stresses were calculated considering the same loading conditions of the grid independence test ($\Delta T = 100$ K, $P_h = 7.73$ MPa and $P_c = 7.99$ MPa). Domains with 2×1, 4×3, 6×3, 8×5, 10×5, and 12×7 (rows × columns) were tested, as they are displayed in Figure 3.12.

Figure 3.13 presents the thermal stress variation across the path length of both hot and cold central channels. Hereinafter, the discussed FEA results correspond to both central channels. The inadequacy of using the 2×1 array and the influence of the neighbor channels were evidenced. Great differences appeared when the

65

number of channels was increased, but similar stress variation across path can be verified for 4×3 and 6×3 arrays. It can also be seen for 8×5, 10×5, and 12×7 arrays. These last three arrays exhibited almost the same stress intensity in the hot and cold channels. For the thermal stress calculation purposes, 8×5 was the configuration with a better relationship of accuracy and simplicity.
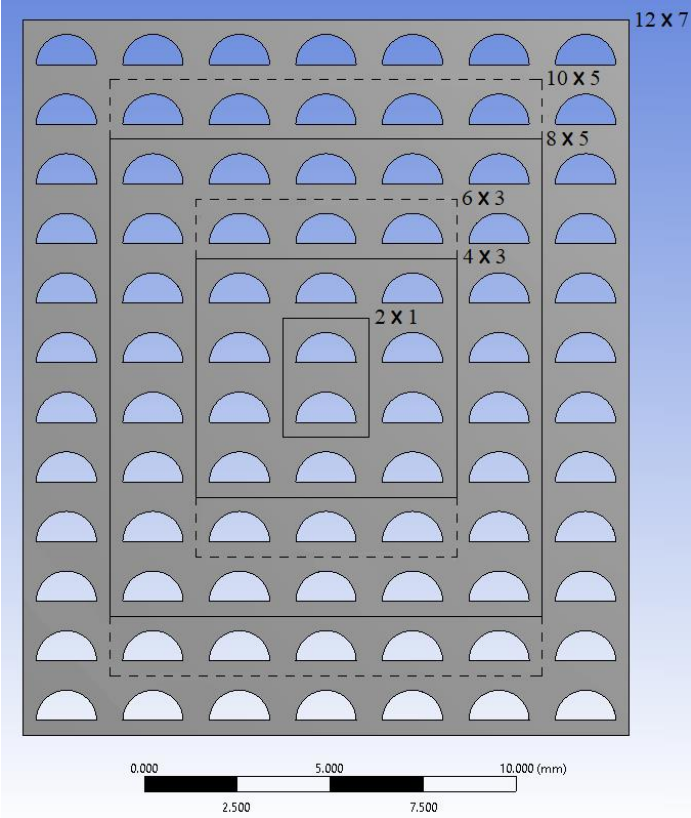
Figure 3.12: Channels arrays considered in the domain simplification of the FEA model.
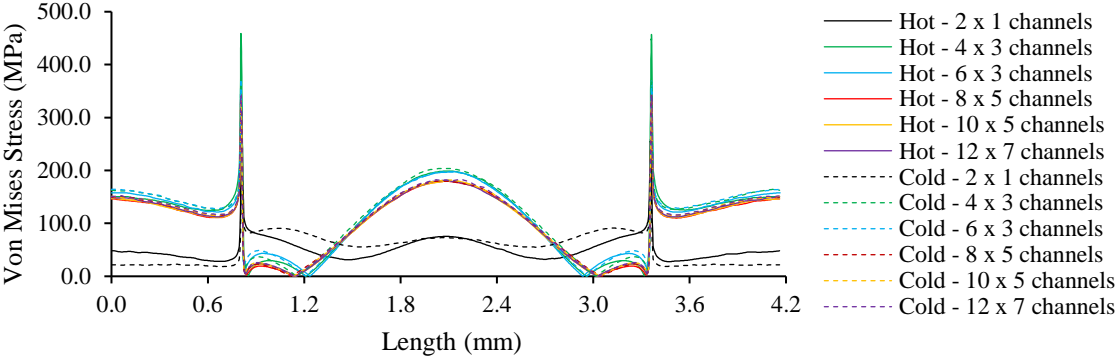
Figure 3.13: Thermal stress in the path of the hot and cold central channels for different channels arrays.

In the same way, the mechanical stress variation with the channels number is presented in Figure 3.14. In this case, the stress value was higher in the 2×1 array because there were only two channels, which are equivalent to the central channels of the other configurations, but without the presence of the neighbor channels that constrain the strain by the pressure effect. An array with 4×3 channels is suitable for calculating the mechanical stress in the central channels. However, an array of 8×5 channels was considered in this research to guaranty the accuracy of both thermal and mechanical stresses. Figure 3.15 exhibits the total stress caused by both thermal and mechanical loading. The configurations with 8×5 or more channels had similar total stress values across paths. Because of the tensile effect of both thermal stress and mechanical stress in the cold channel, the total stress was higher in the cold channel.
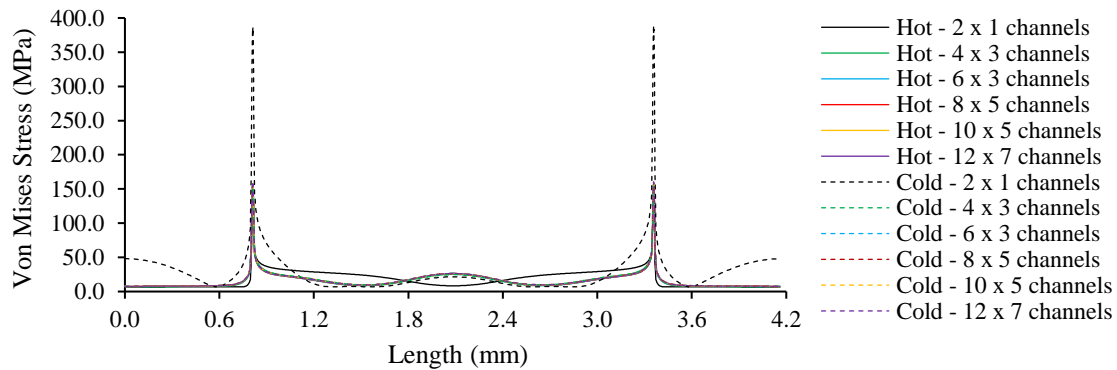
Figure 3.14: Mechanical stress in the path of the hot and cold central channels for different channels arrays.
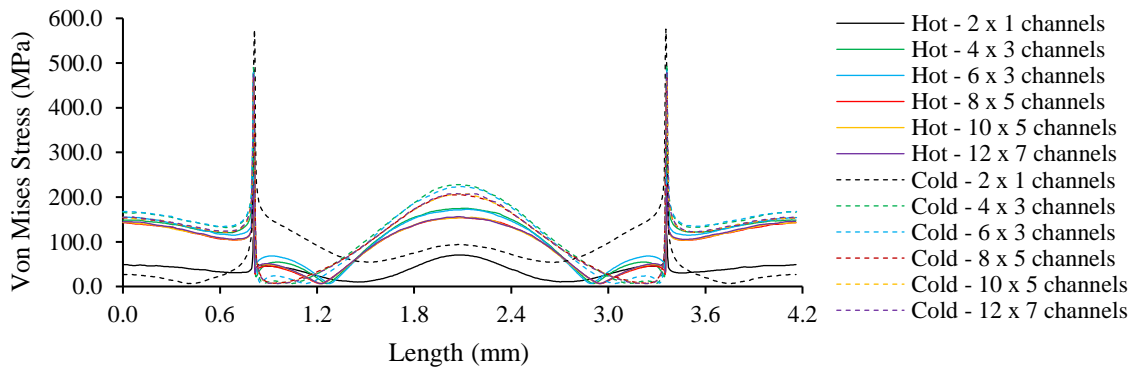
Figure 3.15: Total stress in the path of the hot and cold central channels for different channels arrays.

3.6. Taguchi method

Considering the studied values of the geometric parameters in Tables 3.1 and 3.2, if a full factorial design is used, it would be necessary to calculate 625 (=5×5×5×5) cases in the analysis of the cross-sectional dimensions and 128 (=4×4×4×2) cases in the analysis of the zigzag dimensions. However, the Taguchi method offers an alternative that considerably reduces the computing time, which uses a mathematical tool

named orthogonal arrays to analyze the effect of main and interacting control factors through a minimized number of simulation trials [114]. In these arrangements, setting levels for each one of the studied parameters allows later identifying on which level the optimal design is obtained for each parameter. Tables 3.5 and 3.6 show the values of the geometric parameters divided by levels, where the levels increment represents the increase of each parameter value. Then, Table 3.7 presents an orthogonal arrangement of the cross-sectional parameters with twenty-five cases (L_{25}) considering five levels shown in Table 3.5. In the same way, Table 3.8 gives an orthogonal arrangement of the zigzag dimensions with sixteen cases (L_{16}) considering four levels shown in Table 3.6. The geometric designs of the sixteen zigzag geometries are displayed in Appendix B. These arrays had balanced parameters distributions according to the procedure of the Taguchi method [114].

Table 3.5: Studied values of the cross-sectional dimensions divided by levels.

Levels	D	t_p/D	t_f/D	r/D
1	1.5 mm	0.8	0.15	0.005
2	1.625 mm	0.9	0.3	0.02
3	1.75 mm	1.0	0.45	0.04
4	1.875 mm	1.1	0.6	0.06
5	2.0 mm	1.2	0.75	0.08

Table 3.6: Studied values of the zigzag dimensions divided by levels.

Levels	l_Z/D_h	α	Br/D_h	λ/l_Z
1	9.70	5°	0.00	0
2	12.93	15°	2.10	1.0
3	16.16	30°	4.20	-
4	19.39	45°	6.31	-

Therefore, CFD and FEA simulations were carried out for 25 cases and 16 cases to analyze the cross-sectional dimensions and the zigzag dimensions, respectively. Several mass flow rates per case were considered in the thermal-hydraulic calculations, and several loading conditions per case were tested in the structural calculations. The results of the designs presented in Tables 3.7 and 3.8 were grouped to study the influence of each parameter according to the Taguchi method procedure [114]. That is, the values of the designs that have one equal dimension in the orthogonal array are summed to analyze the influence of each parameter separately, according to Eq. 3.17-3.20. The stress intensity (S) was analyzed in the central channels. Also, the Reynolds number, the Nusselt number, and the Fanning friction factor were analyzed as averaged values between the cold and hot channels, due to the very similar fluid characteristics and thermo-hydraulic performances in both channels.

$$Re_{ave} = \frac{\sum_{i=1}^{n}\left(Re_{c,i} + Re_{h,i}\right)}{2n} \qquad (3.17)$$

$$Nu_{ave} = \frac{\sum_{i=1}^{n}(Nu_{c,i} + Nu_{h,i})}{2n} \tag{3.18}$$

$$f_{ave} = \frac{\sum_{i=1}^{n}(f_{c,i} + f_{h,i})}{2n} \tag{3.19}$$

$$S = \frac{\sum_{i=1}^{n}(S_i)}{n} \tag{3.20}$$

where i represents the designs where one geometric parameter is the same in the orthogonal arrays, and n is the number of i designs, which are 5 ($\sqrt{25}$) and 4 ($\sqrt{16}$) for the cross-sectional and zigzag dimensions, respectively.

Table 3.7: Orthogonal array L₂₅ of the cross-sectional dimensions distributed by levels.

Cases	D	t_p/D	t_f/D	r/D
1	1	1	1	1
2	1	2	2	2
3	1	3	3	3
4	1	4	4	4
5	1	5	5	5
6	2	1	2	3
7	2	2	3	4
8	2	3	4	5
9	2	4	5	1
10	2	5	1	2
11	3	1	3	5
12	3	2	4	1
13	3	3	5	2
14	3	4	1	3
15	3	5	2	4
16	4	1	4	2
17	4	2	5	3
18	4	3	1	4
19	4	4	2	5
20	4	5	3	1
21	5	1	5	4
22	5	2	1	5
23	5	3	2	1
24	5	4	3	2
25	5	5	4	3

Table 3.8: Orthogonal array L₁₆ of the zigzag dimensions distributed by levels.

Cases	l_Z/D_h	α	Br/D_h	λ/l_Z
0	Straight channels			
1	1	1	1	1
2	1	2	2	2
3	1	3	3	2
4	1	4	4	1
5	2	1	2	2
6	2	2	3	1
7	2	3	4	1
8	2	4	1	2
9	3	1	3	1
10	3	2	4	2
11	3	3	1	2
12	3	4	2	1
13	4	1	4	2
14	4	2	1	1
15	4	3	2	1
16	4	4	3	2

3.7. Chapter summary

In this chapter, the governing equations used in the CFD and FEA simulations of the PCHE were described. The 3D geometric domains with one channel per fluid and the pseudo-2D multichannel per fluid were chosen to analyze the effect of the variation of the cross-sectional dimensions. To study the effect of the zigzag dimensions, it was demonstrated the need to consider more complex domains with 3D multichannel per fluid. Operating conditions with values of the pressure and the temperature like those of the IHX of an optimized HTGR plant by other authors were used. The applied boundary conditions in the computational models were explained. The grid independence and the analysis of the geometric model reduction allowed to obtain computational models with optimized relationships between the computation time and the accuracy of the results. The utilization of the Taguchi method and orthogonal arrays of the parameters to reduce the trial number were described. The next two chapters will present the results obtained from the models described here.

4. ANALYSIS OF THE THERMAL-HYDRAULIC PERFORMANCE

The thermal-hydraulic performance of the PCHE depends on the operating conditions and several design parameters. The criterion to choose an optimum design can change as a function of each application and the requirement of the device in the system. In this chapter, the cross-sectional and zigzag dimensions of the PCHE are thermally and hydraulically analyzed, and optimized designs are found according to different objective functions. Heat transfer correlations are proposed to assist further optimizations.

4.1. Validation of the thermal-hydraulic computational model

The validation of the thermal-hydraulic model of the PCHE was carried out by comparing the simulation results of a zigzag channel design with experimental data published by Chen et al. [39][115], Yoon et al. [70] using a similar test facility, and that by Kim et al. [38]. An analogous design of the PCHE to those presented in [39], [70] and [115] was considered in this section, with values of $D = 2.0$ mm, $t_p = 1.6$ mm, $t_f = 0.5$ mm, $l_Z = 12.3$ mm, $\alpha = 15°$, $Br = 4.0$ mm and $\lambda = 0$. The PCHE design of Kim et al. [38] had the same zigzag pitch length and zigzag angle, although a sharp-shape at the bends were considered ($Br = 0$). Figures 4.1 and 4.2 show the plotted values of the Nusselt numbers and the Fanning friction factors. The data were presented in [38] as average values of the cold and hot channels in a laminar range of Reynolds number from 350 to 800, and from 350 to 1150, respectively. The Nusselt number data taken from Chen et al. [115] are in the laminar region, while those taken from Yoon et al. [70] include both laminar and transition-to-turbulent regimes. Although both data sets seem to refer to the same experimental measurements, a difference of around 17% among them was observed. The Fanning friction factors correspond to apparent values and they were reported by Chen et al. [39] and Yoon et al. [70].

From Figure 4.1, a good agreement can be seen between the CFD model and the experimental results of Nusselt number, especially considering the error bars of the result graphs of Chen et al. [115] and Yoon et al. [70]. The model results overestimate the data of Chen et al. [115] and underestimate the data of Yoon et al. [70], but the model is quite accurate comparing to either one. All but very low Reynolds number range have low relative errors. Although the maximum difference is around 40% when $Re \leq 440$, the difference is below 10% for $Re \geq 550$. The operating condition in the current work was defined in the range $550 \leq Re \leq 3200$. The Fanning friction factor of the CFD model predicts very accurately the experimental results of Kim et al. [38], where the sharp-shape of zigzag bends was considered. It underestimates the experimental data of Chen et al. [39] and Yoon et al. [70] with round-shape ($Br = 4$ mm), and the difference is more notable in the transition-to-turbulent of the hot flow. The maximum relative difference with Kim's data is very small, but for higher values it increases, being up to 18% with $Re \approx 1500$ and with $Re \approx 2850$. That can be caused by the distortion of the channel cross-sectional area of the experimentally tested PCHE during the diffusion-bonding process and in operation because of thermal stress-induced deformations. Distortion was found as a significant source of overestimation of the experiment values over simulation values of friction factor by Yoon et al. [111]. Because the channel geometry has a great effect on the pressure drop, but not so much on the heat transfer, the Nusselt number comparison is less affected by distortion. Another reason for uncertainty can be the non-uniform distribution of the total mass flow rate by channels in the experimental tests. Flow maldistribution intensification was detected by Ma et al. [116] with the Reynolds number increase. Kim et at. [68] found that uniform flow assumption in the simulation is less accurate when

71

the experimental tests of reference are accomplished with channels in a horizontal array. In general, an acceptable accuracy of the current computational model can be observed.
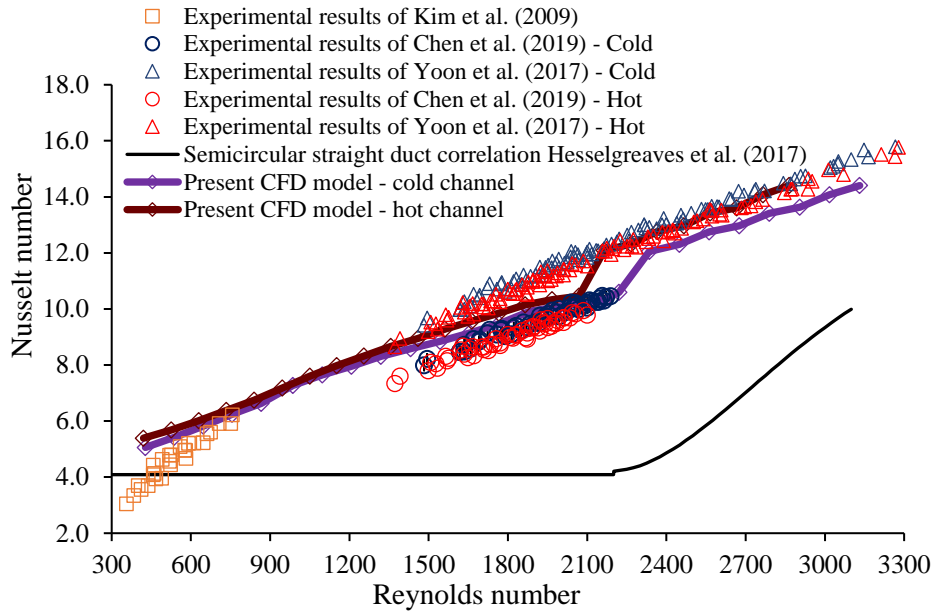
Figure 4.1: Nusselt number values obtained through the CFD model and experimental data of Chen et al. [115], Yoon et al. [70], and Kim et al. [38].
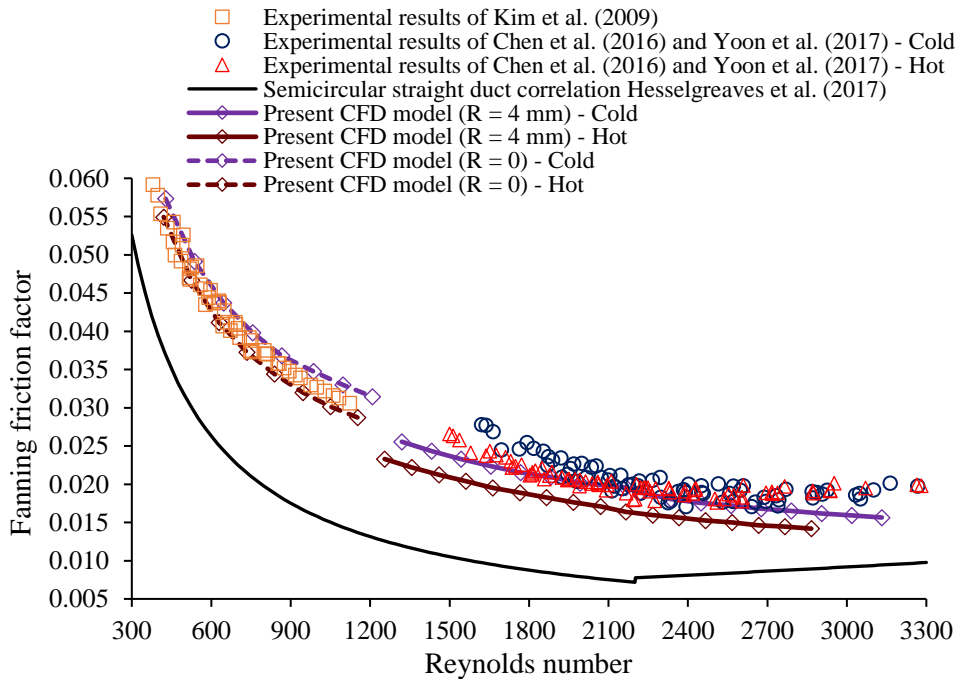
Figure 4.2: Fanning friction factor values obtained through the CFD model and experimental data of Chen et al. [39], Yoon et al. [70], and Kim et al. [38].

4.2. Cross-sectional dimensions analysis

The Nusselt number of fully developed laminar flows in straight channels can be considered constant as was presented in Figure 4.1, being 4.089 in semicircular profile ducts [63]. While the Fanning friction factor can be calculated as $f \times Re = 15.78$. However, these values are particularly good in channels with relatively high axial length [15]. The hydrodynamic entry length (x_{hl}) is the distance that the fluid flow must travel when entering to a duct to have the hydraulic parameters fully developed. It can be calculated using Eq. 4.1 [15] for laminar flows in circular tubes. While the thermal entry length related to the thermal boundary layer can be obtained according to Eq. 4.2 [15].

$$x_{hl} = 0.05 Re D_h \tag{4.1}$$

$$x_{tl} = 0.05 Re D_h Pr \tag{4.2}$$

where x_{hl} is the hydrodynamic entry length and x_{tl} is the thermal entry length. The PCHE designs usually have hydraulic diameters between 0.001 m and 0.005 m. The length of the straight flow path is lower than 1.5 m because of the manufacturing limitations [25], but the heat transfer calculations give values around 0.5 m under conditions considered in this research [11]. Therefore, the hydrodynamic and thermal entry lengths of a straight channel PCHE can represent a great portion of the channel length with high Reynolds numbers in the laminar region. This effect is more notable in semicircular ducts according to the results of Mylavarapu et al. [67], which found that the non-dimensional hydrodynamic entrance length, defined as $x_{hl}/Re D_h$, for laminar flow is 0.07-0.08. Furthermore, the fully developed flow conditions are not reached in the PCHE under presented conditions due to the variation of the thermophysical properties with high temperature gradients [64]. Therefore, the influence study of the geometric parameters of the straight channel PCHE on the Nusselt number and the friction factor is useful for design purposes.

The Nusselt number and the friction losses in the cross-sectional dimensions' study were achieved for the twenty-five designs proposed in Table 3.7 according to the Taguchi method. These non-dimensional numbers were plotted as a function of the Reynolds number in Appendix C. Nevertheless, these values were grouped by geometric parameters to analyze the results in a more illustrative way according to Eq. 3.17-3.19.

The effect of the channel diameter on the Nusselt number and the Fanning friction is evidenced in Figure 4.3. The Nusselt number presents little variation when the diameter is changed, although an increase of around 5% is observed for very low Reynolds numbers if the diameter is reduced from 2.0 mm to 1.5 mm. That can be caused by the effect of the hydraulic diameter on the length of the hydraulic and thermal entrances. The diameter increase is compensated with the pressure drop increase in the friction factor calculation, hence, it is almost independent of the diameter.

The friction factor is independent of the plate thickness increase, while the Nusselt number decreases, as shown in Figure 4.4. This geometric parameter determines the distance between the cold and hot channels, and thus, it affects the thermal process, but not the hydraulic. As expected, the heat transfer process is enhanced while the distance between the cold and hot channels is reduced. Nevertheless, this reduction also has structural effects that will be seen later. Otherwise, the ridge thickness defines the distance between

channels of the same fluid, and therefore, it does not have notable effects on the Nusselt number and the Fanning friction factor.
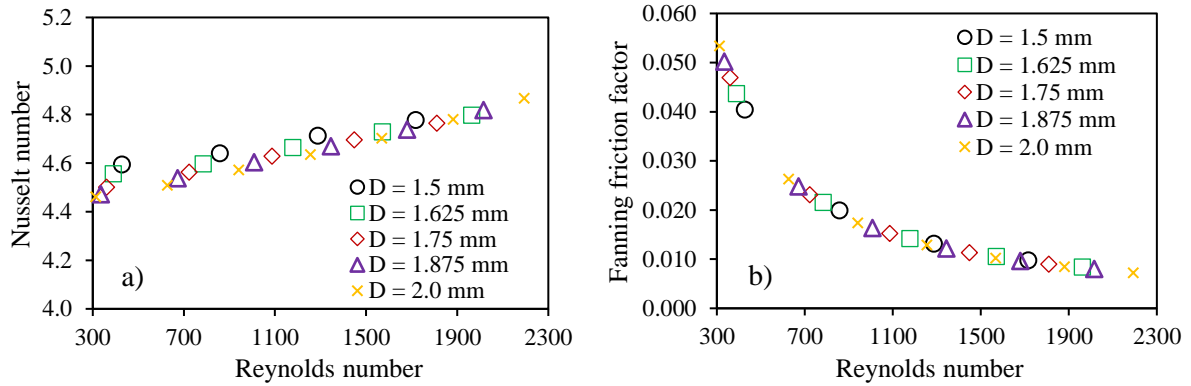
Figure 4.3: Influence of the diameter on a) the Nusselt number, and b) the Fanning friction factor in a straight channel PCHE.
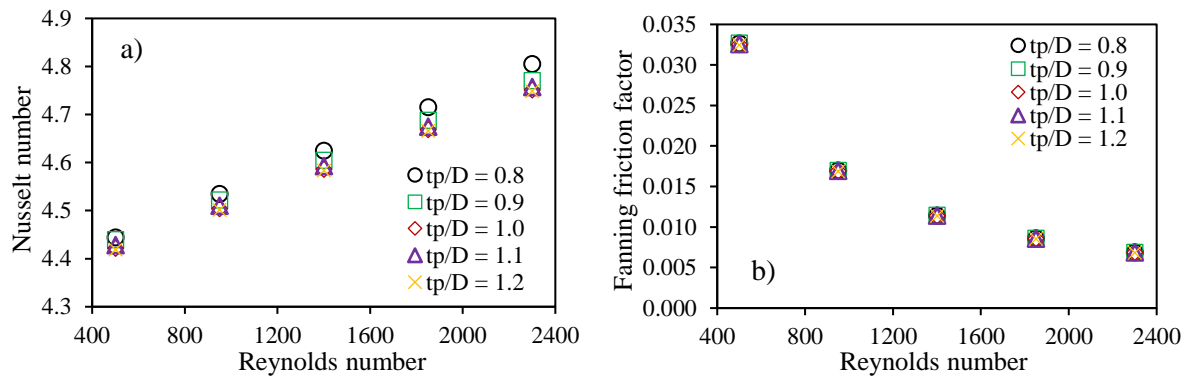
Figure 4.4: Influence of the plate thickness on a) the Nusselt number, and b) the Fanning friction factor in a straight channel PCHE.

Figure 4.5 presents the influence of the rounded tip radius on the Nusselt number and the Fanning friction factor. The roundness increment causes the Nusselt number and friction factor increment. The effect of this geometric parameter on the Nusselt number is up to 8% when the *r/D* ratio is increased from 0.005 to 0.08. That can be because with more sharp-shapes at the tips (lower *r/D* ratio), the local heat transfer coefficient is near zero in these zones [15], and hence, the mean value of the Nusselt number decrease. Although the percentual increment of the friction factor is similar to the Nusselt number, the heat transfer generally has a higher weight than the friction losses in the thermal-hydraulic optimizations. Then, the *r/D* ratio increase is recommended.
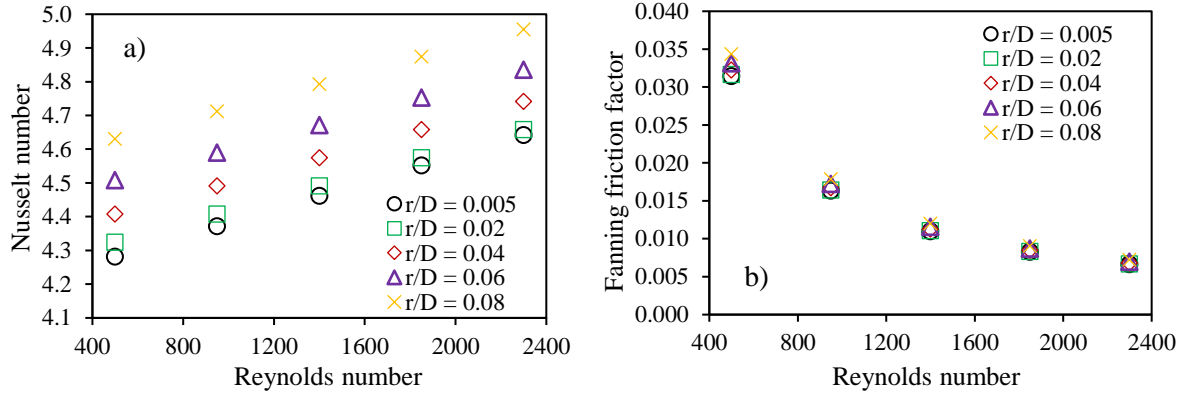
Figure 4.5: Influence of the rounded tip radius on a) the Nusselt number, and b) the Fanning friction factor in a straight channel PCHE.

As expected, the cross-sectional dimensions have a little influence on the heat transfer parameters in a straight channel PCHE, but their analyses allow to obtain enhanced designs. Next, the analysis of the zigzag dimensions of a zigzag channel PCHE is accomplished, in which the change of the flow direction affects both hydraulic and thermal processes.

4.3. Zigzag dimensions analysis

The Nusselt number and Fanning friction factor values in the zigzag dimensions' analysis were obtained for the sixteen designs presented in Table 3.8. These results and those of the reference design with straight channels are displayed in Appendix C, in the full range of Reynolds number values proposed before. As in the cross-sectional dimensions' analysis, grouped values by geometric parameters were considered.

4.3.1. Parametric analysis and optimization

The influence of each geometric parameter on the Nusselt number and the Fanning friction factor is evidenced by Figures 4.6 and 4.7, respectively. The better values of the geometric parameters are highlighted with boxes in the legends. The increase of zigzag angle from 30° until 45° offers a very little increment of the Nusselt number, while the friction factor is notably increased. Similar results were obtained by Kim and No [58] for zigzag angles higher than 30°, and it was mainly noted for $Re > 1000$. The zigzag angle increase was favorable when the Reynolds number decreases, according to an assessment of the total cost of the heat exchanger [58]. Hence, it is the most decisive parameter to increase the Nu, but its influence can be effective up to $\alpha = 30°$ because at higher angles the friction losses are leading in Figures 4.6 b) and 4.7 b). When the bends have a sharp-shape ($Br = 0$), the Nu has a little increment. Round-shape ($Br > 0$) is essential to reduce the friction losses in Figure 4.7 c). However, this reduction is not evidenced when the quotient Br/D_h is increased from 4.20 to 6.31. The zigzag pitch length has a good thermal-hydraulic balance between heat transfer and friction losses for $l_Z/D_h = 9.70$ due to the friction losses are moderated.
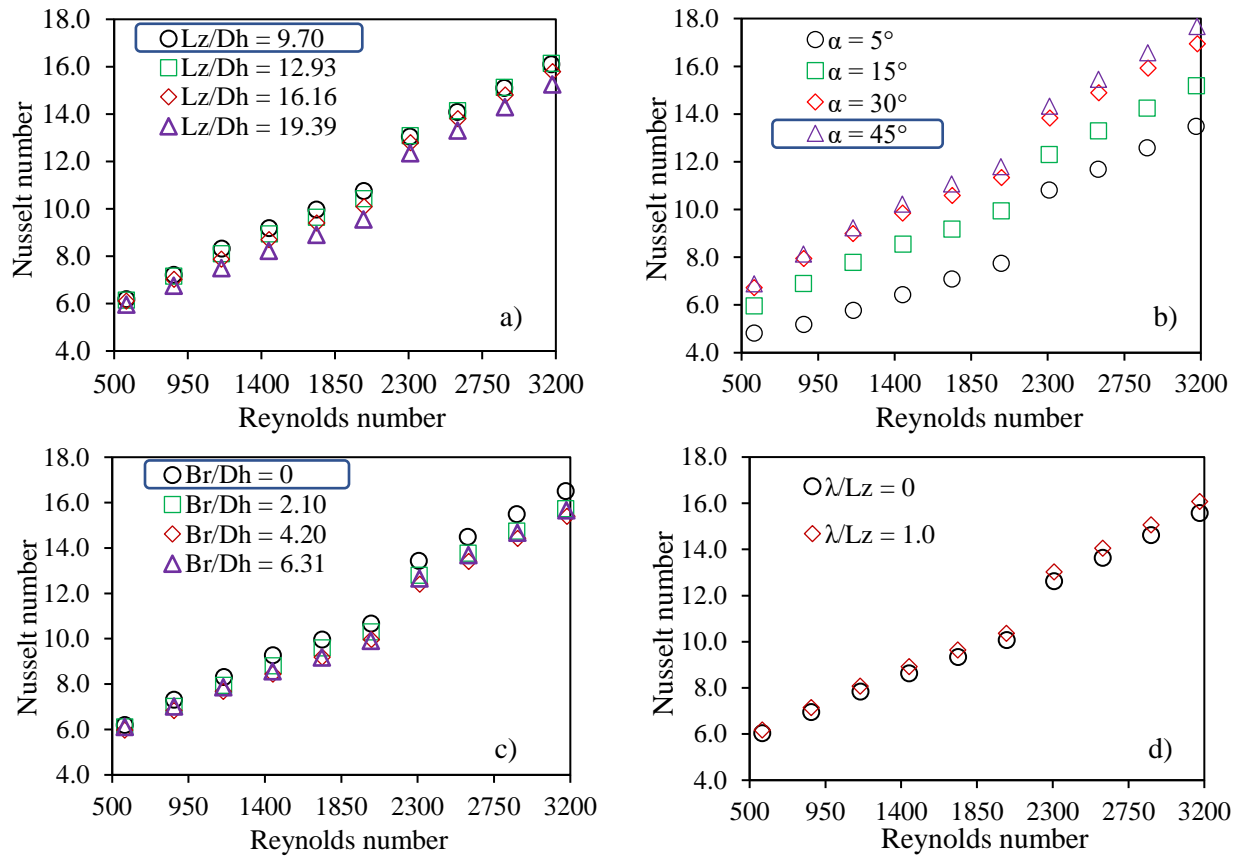
Figure 4.6: Influence of four geometric parameters: a) zigzag pitch, b) zigzag angle, c) bend radius and d) zigzag phase-shift on Nusselt number.

The Nusselt number presents a little increase with the zigzag channels out-of-phase ($\lambda = 1$), which can be caused by the error of the method application, as it will be seen later. The zigzag phase-shift shows a higher influence on the friction factor, which is opposite to the expected result because this parameter should influence the thermal process, but not the hydraulic. That can be because of the errors of the Taguchi method, in which cases 8 and 11 of Table 3.8 with sharp-shape at the bend ($Br = 0$) and zigzag angles of 30° and 45° are out-of-phase, while cases 1 and 14 with sharp-shape at the bend ($Br = 0$) and zigzag angles of 5° and 15° are in-phase. The effect of the bend radius increase on the friction loss is quite essential at higher angles, as is shown in Appendix C. Then, the average values of the friction factor changing the phase-shift are affected. Figure 4.8 analyzes the influence of this dimension on the friction factor considering designs where it is only changed and the other dimensions are $D = 1.5$ mm, $l_Z = 12.3$ mm, $Br = 4.0$ mm, and $\alpha = 30°$.

Similar behavior of the influence of the zigzag phase-shift on the Nusselt number is observed in Figures 4.6 d) and 4.8 in the laminar region and the little advantage of the zigzag out-of-phase is noted. The Fanning frictions factor showed to be independent of this dimension, as expected. The accuracy of the Taguchi

76

method procedure to analyze the heat transfer is evidenced, but its application to predicting friction losses requires more analysis.
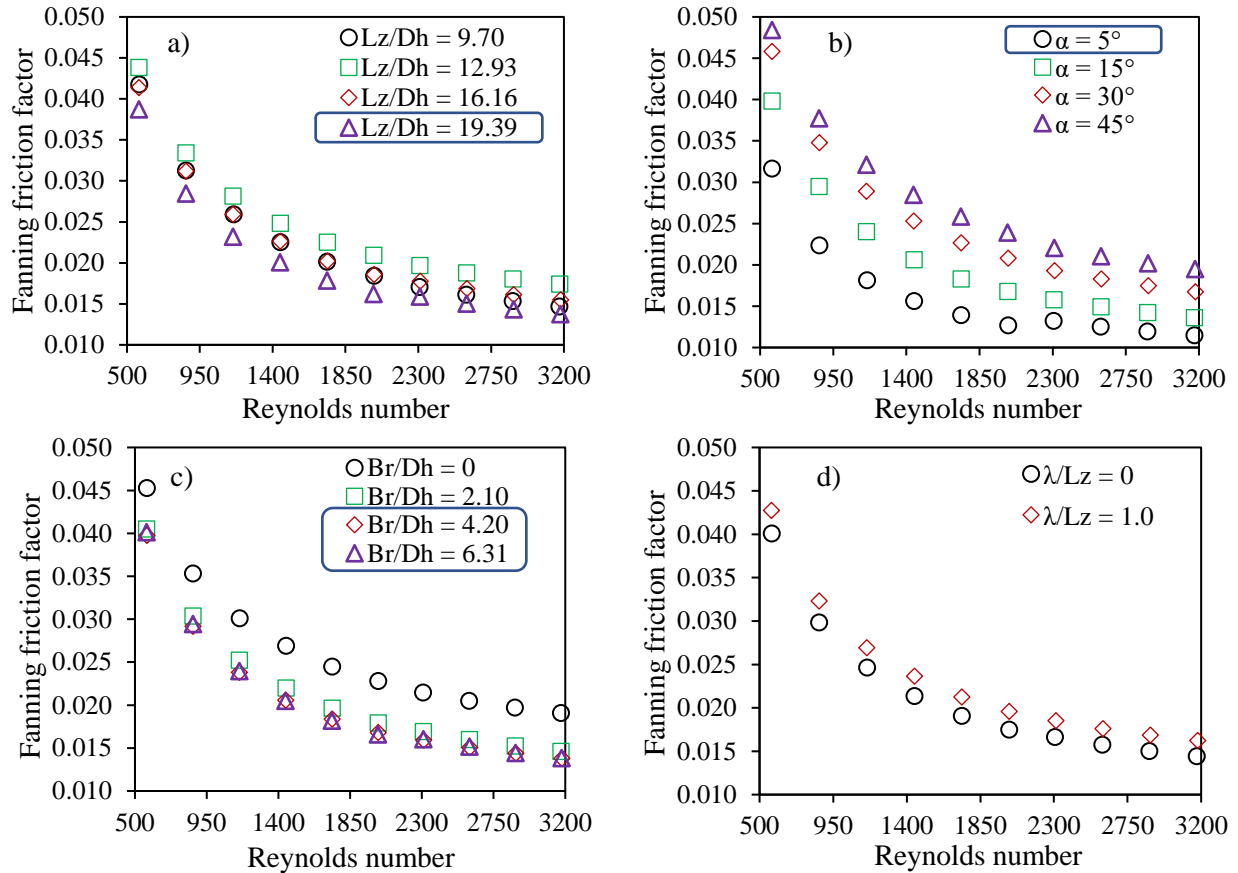
Figure 4.7: Influence of four geometric parameters: a) zigzag pitch, b) zigzag angle, c) bend radius and d) zigzag phase-shift on Fanning friction factor.

Designs with higher Nusselt numbers increase the heat transfer coefficient and the temperature fields of those evidence higher heat transfer. Figure 4.9 shows the temperature contours of the cold channels of cases 1, 2, 3, and 4, which have zigzag angles of 5°, 15°, 30°, and 45°, respectively, and bend radii of 0, 2 mm, 4 mm and 6 mm, respectively. The Nusselt number increases with the zigzag angle and with the bend radius reduction, but the zigzag angle has the highest influence in Figure 4.6. Then, the temperature at the cold central channel outlet ($T_{c,o}$) is increased in Figure 4.9 when the zigzag angle is increased, although the bend radius is also incremented. The increase of the fluid length path and the effect of the abrupt change of direction are the reason for the temperature gradients' behavior.

The effect of the interaction between the zigzag angle and the bend radius on the friction losses can be analyzed through pressure drop contours. These contours in Figure 4.10 show that when $\alpha = 45°$ (cases 4, 8, and 12 in Table 3.8), the bend radius is necessary to decrease the energy losses by eddies appearances. Although cases 4 and 8 have the same zigzag angle and case 4 has a greater bend number (minor l_Z), a

reduction of around 35% of the pressure drop is observed for case 4, because case 8 has a sharp-shape ($Br = 0$), while the bend radius takes its maximum value of $Br = 6$ mm in case 4. In cases 13, 5, and 1, the pressure drop is very similar, although the bend radius is different with values of $Br = 6$ mm, $Br = 2$ mm, and $Br = 0$, respectively. That is because the effect of the bend radius on the pressure drop is more significant at higher zigzag angles. The pressure drop increases with the zigzag angle, but this energy loss can be reduced if the roundness is increased.
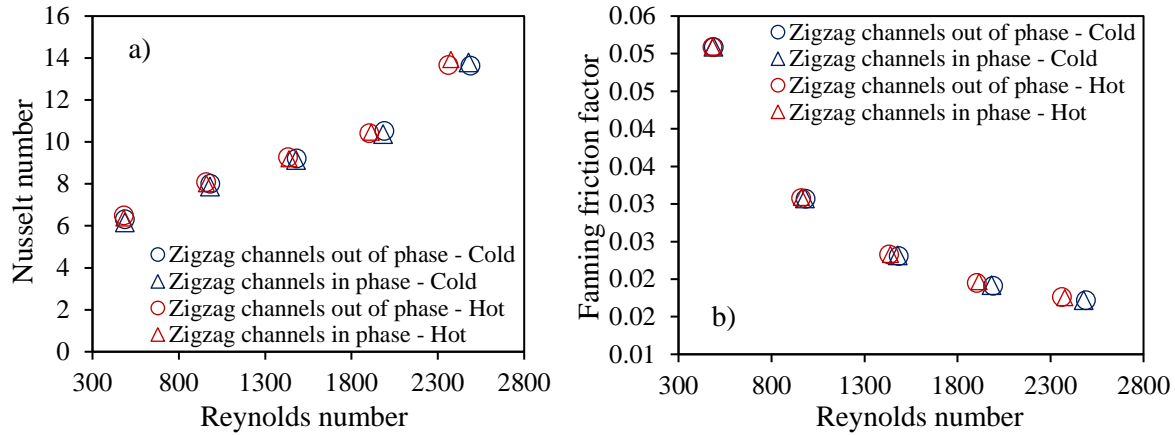
Figure 4.8: Variation of the a) Nusselt number and b) Fanning friction factor in models with different zigzag phase-shift.
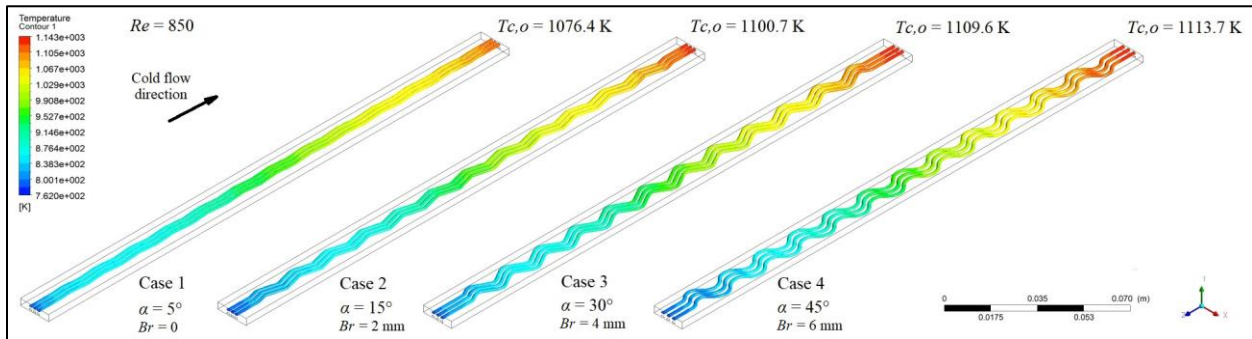
Figure 4.9: Temperature contours of the cold channels increasing the zigzag angle and the bend radius when Re = 850.

The increase of the pressure drop when $\alpha = 45°$ is caused by the increment of the real length (L_R) of the channels and by the appearance of the reverse and stagnation flow zones in the zigzag elbows, which can be observed in Figure 4.11. The velocity streamlines at the elbow of the central bend of the channels show that in these zones appear regions of stagnation flow that increase the energy losses of the fluid flow. Case 8 with $Br = 0$ shows many streamlines with reverse direction, which are notably reduced with a roundness of 2 mm (case 12) and almost disappear with $Br = 6$ mm (case 4).
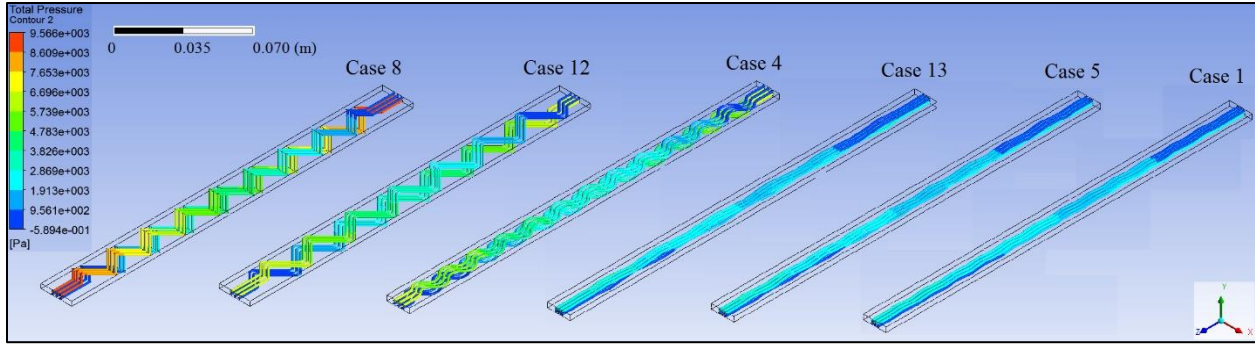
Figure 4.10: Pressure drop for cases with α = 45° (cases 8, 12 and 4) and α = 5º (cases 13, 5 and 1) when Re = 850.
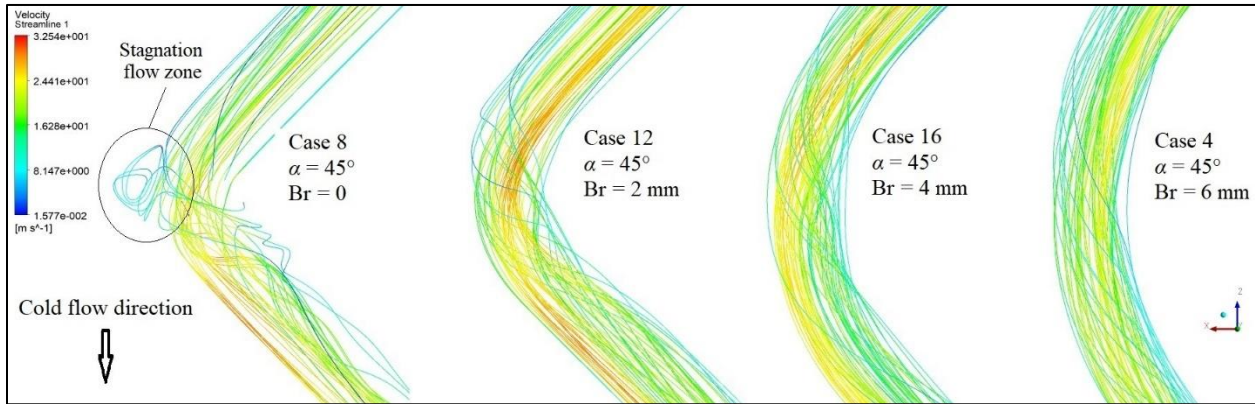
Figure 4.11: Velocity streamlines in elbow zones of cold channels for cases with α = 45° and different bend radii when Re = 850.

An optimized design is not necessarily that with the highest Nusselt number or the lowest friction factor. The determination of the best heat exchanger design should consider both, and it changes as a function of the application requirements. The use of a blending parameter or equation has been proposed by many authors, and different weights have been assigned to the heat transfer and the friction losses in the compact heat exchangers study. Some of them include the minimization of entropy generation [63] or the exergy losses [53]. Zheng et al. [117] also showed a relationship based on the quotient between the number of heat transfer units ($NTU = UA/(\dot{m}c_p)$) and the pressure drop, which allows to obtain an enhanced heat exchanger design in terms of the fluid properties, the allowable pressure drop and the fluid temperatures. A named *JF* factor also stablishes a relationship between the heat transfer coefficient and the friction losses [118]. The heat transfer coefficient can be expressed through the Nusselt number or the Colburn factor (*j*), which is a function of the dimensionless Reynolds, Nusselt and Prandtl numbers (*Pr*), as shown in Eq. 4.3.

$$j = \frac{Nu}{RePr^{1/3}} \tag{4.3}$$

79

Then, the *JF* factor is defined by Eq. 4.4.

$$JF = \frac{j/j_0}{(f/f_0)^{1/3}}$$

(4.4)

where the subscript *0* refers to the reference design (with straight channels).

Figure 4.12 displays the *JF* factor variation with the Reynolds number for each zigzag dimension. The *JF* factor increases with the Reynolds number in the laminar regime achieving values higher than 1.0, which indicates that the increase of the heat transfer is higher than friction losses concerning the reference design. However, in the transition-to-turbulent regime, both effects have similar importance due to *JF* factor takes almost constant values very close to 1.0. Therefore, better thermal-hydraulic performance is archived in the laminar regime. According to the highest *JF* factor criterion, a design with l_Z/D_h = 9.70, α = 30° and Br/D_h = 2.10, and independent of the zigzag phase-shift, can be proposed as an optimized combination of parameters. Also, it is demonstrated that the zigzag angle increase is effective only up to 30° for *JF* factor.
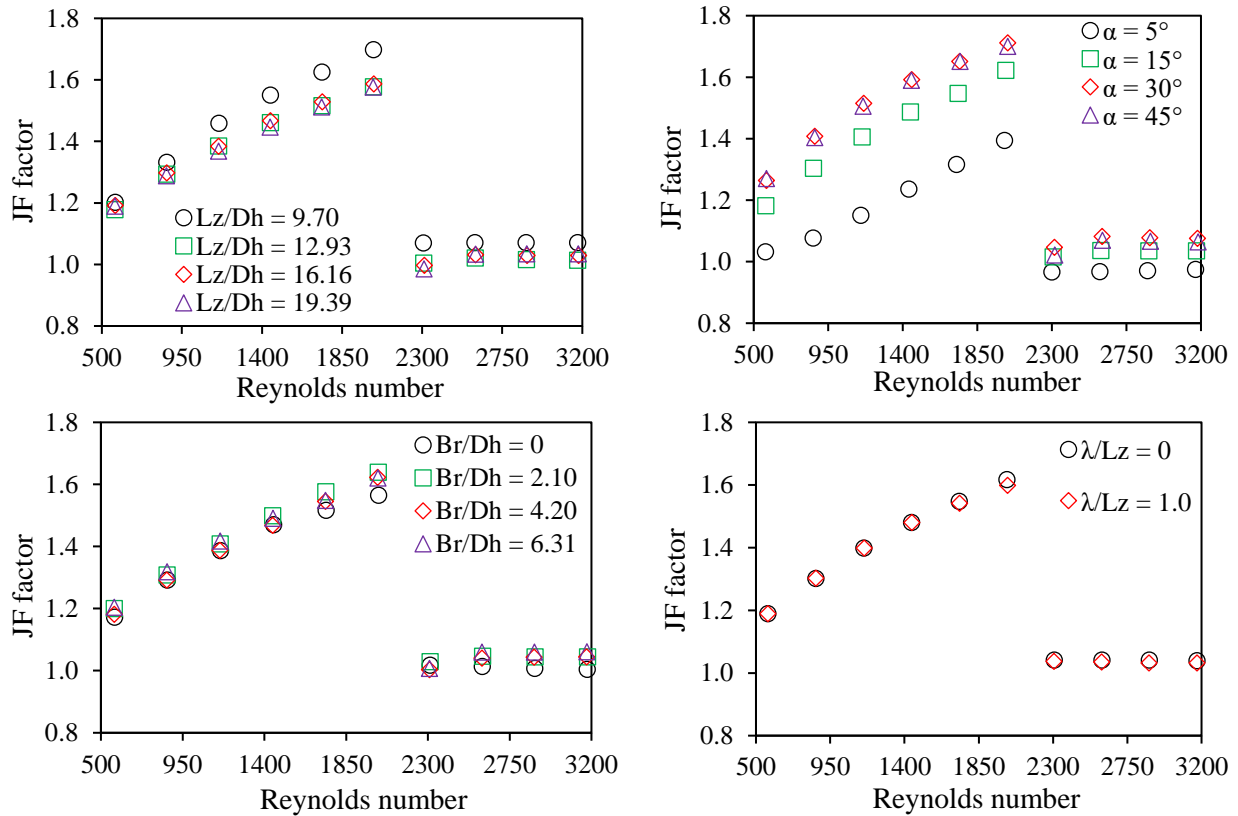
Figure 4.12: Influence of four geometric parameters: a) zigzag pitch, b) zigzag angle, c) bend radius and d) zigzag phase-shift, on JF factor.

Figure 4.13 presents the results of three optimized designs according to the maximum Nusselt number, the maximum *JF* factor, and the minimum friction factor criteria. The design of maximum *Nu* has the dimensions: $l_Z/D_h = 9.70$, $\alpha = 45°$ and $Br/D_h = 0$, the design of maximum *JF* factor has $l_Z/D_h = 9.70$, $\alpha = 30°$ and $Br/D_h = 2.10$, and the design of minimum *f* has $l_Z/D_h = 19.39$, $\alpha = 5°$ and $Br/D_h = 4.20$. The difference between the results of the designs that offer the maximum Nusselt number and the minimum friction factor could be considered as the highest results difference among all possible zigzag designs. That is, the top and bottom limits of the Nusselt number and the friction factor of the zigzag channel PCHE can be defined by these two extreme designs. Then, the design of the maximum *JF* factor achieves an increase of the Nusselt number value around 72% and a decrease of the Fanning friction factor around 61% at the same time considering all the Reynolds numbers range.
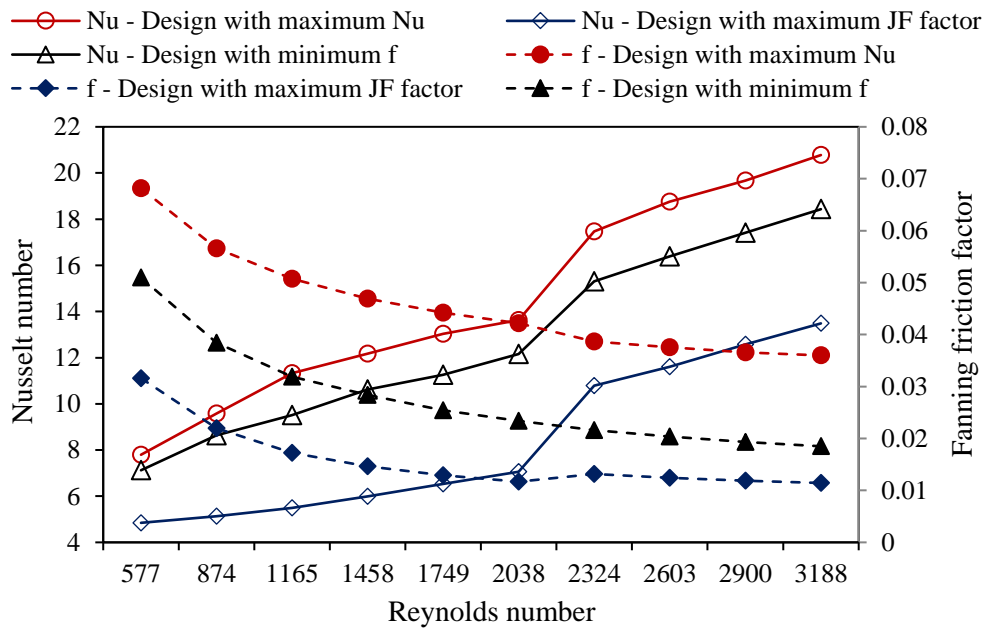
Figure 4.13: Nusselt number and Fanning friction factor in three optimized designs.

An important optimization methodology for the PCHE analysis under IHX conditions is based on the total cost analysis, which relates the Nusselt number and the friction factor with the capital cost and the operating cost, respectively. This method requires the attainment of the heat transfer correlations as functions of the Reynolds number and the geometric parameters. Then, the Nusselt number and Fanning friction factor correlations are developed later, and after that, an additional optimized design according to the total cost criterion is proposed.

4.3.2. Contribution ratio

Although in Figures 4.6 and 4.7 the influence of each parameter on the thermal-hydraulic performance of the zigzag channel PCHE can be analyzed, the signal to noise ratio (*SNR*) has been used in quality

engineering analysis and experimental design coupled to the Taguchi method. The extreme simulation results of some cases such as the pressure drop of case 8 in Figure 4.10, can give misleading conclusions. The *SNR* reduces the influence of this kind of extreme results on the analysis of the average value. The results from the numerical simulation are transformed to signal to noise ratio to evaluate the best-level combination. Noise factors are those that can influence the performance of a system but are not under control. The idealized physical model and boundary conditions in the numerical simulations eliminate the deviation resulting from the noise factors; therefore, these are not considered. The Nusselt number and the Fanning friction factor in the thermal-hydraulic analysis were used as the signal factors. The geometric parameters were considered as the control factors.

In the thermal-hydraulic study, two categories can be used to obtain the *SNR*. If the lower value of the objective function is the better characteristic, as the Fanning friction factor, Eq. 4.5 is employed, else the larger value is the better performance, as the Nusselt number, Eq. 4.6 is used.

$$SNR = 10 \log\left(\frac{1}{y^2}\right) \tag{4.5}$$

$$SNR = 10 \log(y^2) \tag{4.6}$$

where y is the value of the objective function, which represents the frictions factor in Eq. 4.5 and the Nusselt number in Eq. 4.6, in the current research.

The *SNR* results for the Nusselt number and the Fanning friction factor are presented in Table 4.1, considering a flow regime with a Reynolds number of 574. Then, the highest values of *SNR* mean the best quality of the parameter, that is, the highest Nusselt number or the lowest friction factor. The combination of the best quality can be obtained through the analysis of the noise performance statistics (*NPS*), which is the arithmetic average of the *SNR* for the same geometric parameter, according to Eq. 4.7.

$$NPS_i = \frac{\sum_{i=1}^{n} SNR_i}{n} \tag{4.7}$$

Tables 4.2 and 4.3 show the *NPS* for each level obtained for the *SNR* of the Nusselt number and the Fanning friction factor, respectively, when $Re = 574$. The influence of each parameter can be analyzed with the contribution ratio, which represents the percent of the maximum difference between the lowest and the highest *NPS* by parameter divided by the sum of the maximum differences of all parameters. In both Tables 4.2 and 4.3, the highest contribution of the zigzag angle is verified. However, this parameter has a greater influence on the Nusselt number than on the Fanning friction factor. Very similar *NPS* values of the Nusselt number were found when the zigzag angle was increased from 30° to 45°. It indicates that the zigzag angle increment over 30° does not cause a great modification in the heat transfer of the PCHE, as it was commented before. Also, the bend radius is very significant to reduce the friction losses, but the increase of Br/D_h is effective only up to 4.20.

Table 4.1: Signal Noise ratio of Nu and f for each case when Re = 574.

Cases	Nu	SNR of Nu	f	SNR of f
0	4.529	13.12	0.0287	30.85
1	4.729	13.49	0.0316	30.01
2	6.014	15.58	0.0415	27.65
3	6.773	16.62	0.0468	26.60
4	7.224	17.18	0.0473	26.50
5	4.861	13.73	0.0311	30.16
6	6.009	15.58	0.0402	27.93
7	6.481	16.23	0.0428	27.37
8	7.274	17.24	0.0608	24.33
9	4.861	13.74	0.0317	29.97
10	5.915	15.44	0.0389	28.21
11	6.873	16.74	0.0499	26.04
12	6.781	16.63	0.0451	26.93
13	4.847	13.71	0.0316	30.01
14	5.927	15.46	0.0389	28.20
15	6.787	16.63	0.0439	27.16
16	6.279	15.96	0.0405	27.85

Table 4.2: Noise performance statistic of Nusselt number by level of the geometric parameters for Re = 574.

Level	l_Z/D_h	α	Br/D_h	λ/l_Z
1	**15.717**	13.665	**15.733**	15.532
2	15.691	15.514	15.641	15.710
3	15.636	16.556	15.471	-
4	15.440	**16.749**	15.639	-
Difference	0.278	3.084	0.261	0.179
Contribution ratio (%)	7.30	81.13	6.88	4.70

Table 4.3: Noise performance statistic of Fanning friction factor by level of the geometric parameters for Re = 574.

Level	l_Z/D_h	α	Br/D_h	λ/l_Z
1	27.691	**29.995**	27.144	28.025
2	27.405	27.997	27.933	27.568
3	27.786	26.793	**28.088**	-
4	**28.305**	26.402	28.023	-
Maximum difference	0.899	3.592	0.944	0.457
Contribution ratio (%)	15.26	60.96	16.02	7.76

The optimum levels in Tables 4.2 and 4.3 are highlighted in bold, which are mashed with Table 3.6 to obtain the optimum parameters combination. Thus, the geometric design to achieve the greatest *NPS* of the Nusselt number are $l_Z/D_h = 9.70$, $\alpha = 45°$, and $Br/D_h = 0$ for $Re = 574$. While, the greatest *NPS* of the Fanning friction factor (equivalent to the lowest friction losses) is attained when $l_Z/D_h = 19.39$, $\alpha = 5°$, and $Br/D_h = 4.20$. These designs are the same proposed before considering the results displayed in Figures 4.6 and 4.7. The apparent effect of the zigzag phase-shift on the thermal-hydraulic performance is noted, but as it was discussed before, this parameter only has a little influence on the Nusselt number. An analogous analysis was accomplished for the other flow regimes (other nine *Re* values) considered in this work, which is presented in [Appendix D](). Figure 4.14 displays the optimum levels for all Reynolds numbers according to the *NPS* criterium and almost identical results are evidenced. Although with three *Re* values, the Br/D_h relation had the level 4 ($Br/D_h = 6.31$) as optimum to reach the highest *NPS* of *f*, the results were very similar. As it was expected, the optimal designs according to the *Nu* and *f* objective functions have almost opposite geometric features.
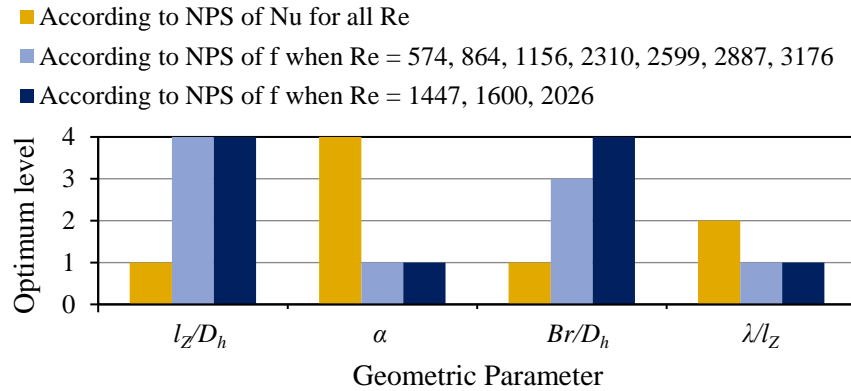
Figure 4.14: Optimum level of each geometric parameter for all Reynolds number.

The contribution ratios of the parameters on the *NPS* of Nusselt number and Fanning friction factor for all Reynolds numbers were plotted in Figures 4.15 and 4.16, respectively. The highest influence of the zigzag angle on *NPS* of *Nu* and *f* is common in both figures. The angle contribution decreases as the *Re* increases in the *NPS* of *Nu*. The heat transfer is enhanced with a more disordered fluid movement and eddies appearances, which is attained with the zigzag angle increase, but this influence is less significant when the flow regime is closer to the turbulence. However, the angle contribution on the *NPS* of *f* increases as the *Re* increases. Besides, the bend radius has great importance in friction losses because the sharp-shape of corners increases the shear stress due to the abrupt change of the fluid direction.
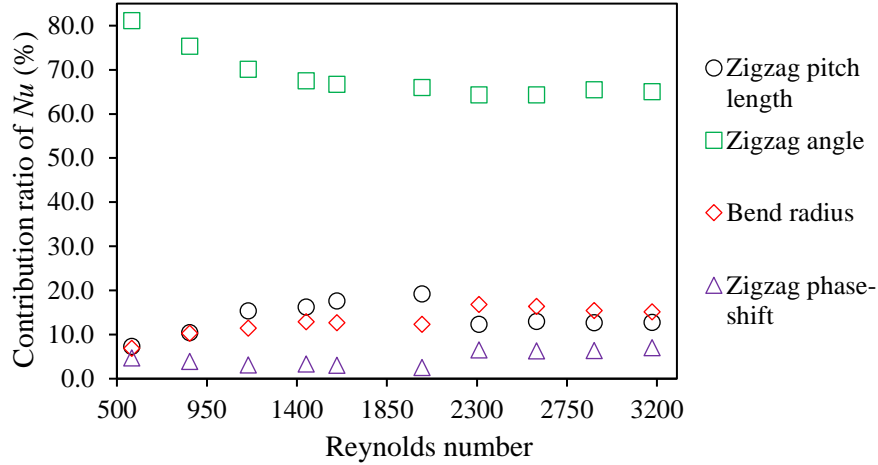
Figure 4.15: Contribution ratio of each parameter on NPS for Nusselt number.
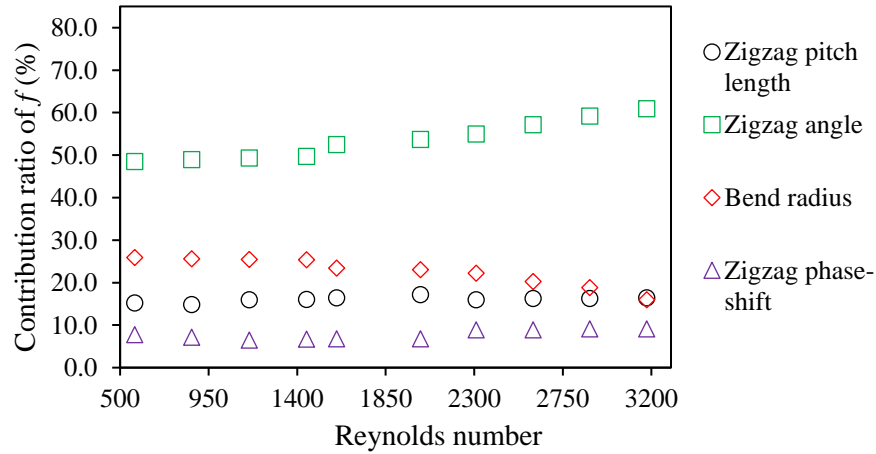
Figure 4.16: Contribution ratio of each parameter on NPS for Fanning friction factor.

4.3.3. Verification test

The purpose of the results verification is to determine the accuracy of the general process of analysis. In this way, the performance of the optimum parameters' combination can be predicted and compared with the real values obtained through simulation. The predicted values of the *NPS* (η) were calculated using its values in the optimum levels of each geometric parameter according to Eq. 4.8.

$$\eta = \eta_m + \sum_{i=1}^{p}(\widehat{\eta}_i - \eta_m) \tag{4.8}$$

where η_m is the mean of the *NPS* of the sixteen cases, $\widehat{\eta}_i$ is the *NPS* value at the optimum level and p is the number of parameters, which is four in this work. Table 4.4 presents the Nusselt number and Fanning friction factor values of the optimized designs for all considered flow regimes according to the prediction

and the simulation. The relative error of the Taguchi method prediction (δ_{TM}) in percent is calculated with Eq. 4.9.

$$\delta_{TM} = \frac{y_{simulated} - y_{predicted}}{y_{simulated}} \times 100 \; (\%) \tag{4.9}$$

Table 4.4: Nusselt number and Fanning friction factor prediction in optimized designs according to PS and NPS values.

Re_{ave}	Optimized Nusselt number			Optimized Fanning friction factor		
	Simulation	*NPS*	δ_{TM} (%)	Simulation	*NPS*	δ_{TM} (%)
574	7.796	7.117	8.7	0.0316	0.0281	11.1
864	9.585	8.698	9.3	0.0220	0.0191	13.0
1156	11.335	10.167	10.3	0.0172	0.0151	12.6
1447	12.180	11.415	6.3	0.0146	0.0126	13.7
1600	13.031	12.333	5.4	0.0129	0.0111	14.2
2026	13.636	13.096	4.0	0.0117	0.0099	15.0
2310	17.473	15.381	12.0	0.0131	0.0109	17.3
2599	18.760	16.592	11.6	0.0124	0.0102	17.5
2887	19.678	17.736	9.9	0.0119	0.0097	18.1
3176	20.777	18.899	9.0	0.0114	0.0093	18.3

In general, the exactness of the optimized Nusselt number according to the Taguchi method is quite good applying the prediction procedure with the *NPS* values, which shows relative errors under 12%. However, the prediction of the optimized Fanning friction factor shows higher relative errors, which are between 11.1% and 18.3%. This can be because of the exponential variation of the friction losses is more difficult to estimate. The Taguchi method applicability to predict the two optimized design performances according to the highest *NPS* of *Nu* and *f* criteria is acceptable.

The maximum relative difference of the average friction factor for the two zigzag phase-shifts in Figure 4.7 d) is lower than 12% and the contribution ratio of this dimension in Figure 4.17 is lower than 9.16%. They are under the prediction error of the Taguchi method for the friction factor in Table 4.4, which takes values up to 18.3%. The zigzag phase-shift should not be studied through the Taguchi method due to its little influence. Figure 4.8 demonstrates the non-influence of this dimension on the friction losses.

4.3.4. Correlations development

The correlations development is carried out considering the Nusselt number and the Fanning friction factor results by cases presented in Appendix C. The Taguchi method approach is employed to find correlations' coefficients as functions of the geometric parameters. Although the critical Reynolds number could fluctuate with the zigzag geometry, fixing a value is practical to develop correlations. But the user of the

proposed correlations can apply them considering reductions of critical Reynolds number when the zigzag angle is increased.

The Nusselt number presents a quite linear variation to the Reynolds number for sixteen cases in the laminar and transition-to-turbulent regimes, as shown in Appendix C. Therefore, a Nusselt number correlations structure as $Nu = C_1 \times Re + C_2$ in both regimes can be considered. Then, first-order polynomials were found for all sixteen cases and the C_1 and C_2 coefficients were attained for each case as functions of the geometric parameters. Following the Taguchi method procedure of averaging the results of the cases with common parameters, these coefficients can be expressed as Eq. 4.10 and 4.11.

$$C_1 = F_1(\alpha, D_h, l_z, R, \lambda) \cong \overline{C_1} \times f_1(\alpha) \times f_2(l_z/D_h) \times f_3(Br/D_h) \times f_4(\lambda/l_z) \qquad (4.10)$$

$$C_2 = F_2(\alpha, D_h, l_z, R, \lambda) \cong \overline{C_2} \times f_5(\alpha) \times f_6(l_z/D_h) \times f_7(Br/D_h) \times f_8(\lambda/l_z) \qquad (4.11)$$

where $\overline{C_1}$ and $\overline{C_2}$ are the mean values of the C_1 and C_2 coefficients, respectively. The f_1 to f_8 are scaled functions with a mean value of one. They represent the influence of each geometric parameter on the values of the coefficients C_1 and C_2. They take mean values of $\overline{C_1} = 2.8476 \times 10^{-3}$ and $\overline{C_2} = 4.5634$ in laminar regime and $\overline{C_1} = 3.4534 \times 10^{-3}$ and $\overline{C_2} = 4.8634$ in the transition-to-turbulent regime. Figure 4.17 presents the variation of the f_1 to f_8 functions in both regimes, where the levels represent the values of each geometric parameter according to Table 3.6. The scope of the f_1 to f_8 functions determine the influence of the geometric parameters on each coefficient. It must be noted that to obtain the correlations the zigzag angle is analyzed in radians.
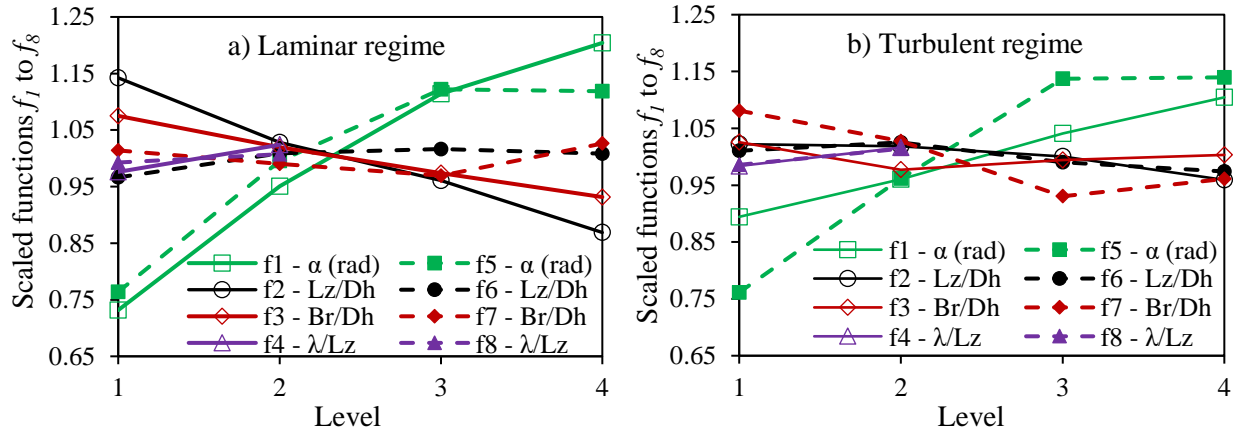
Figure 4.17: Behavior of the scaled functions of C_1 and C_2 to each geometric parameter in a) laminar and b) turbulent Nusselt number correlations.

The coefficients of the Nusselt number correlations in both regimes are mainly influenced by the zigzag angle functions because their ranges of variation are higher than those of the other functions, as expected. The dependency analysis of the scaled functions with each parameter was carried out considering the exactness of the obtained correlation in comparison with the simulation results. In general, it was observed

that the accuracy is almost independent of a geometric parameter when the variation of the scaled function is between 0.95 and 1.05. In this way, the zigzag phase-shift (λ) does not have relevance on both correlations. In the laminar regime, C_2 only depends on the zigzag angle and C_1 is a function of the zigzag angle, the zigzag pitch length, and the bend radius, as it is shown in Eq. 4.12.

$$Nu = 5.54 + 2.2655 \times 10^{-6}\, \alpha^{0.2263}\, (50.954 - L_Z/D_h)(47.234 - Br/D_h)\, Re\, -\frac{0.3119}{\alpha + 0.06419} \quad (4.12)$$
$$550 \leq Re \leq 2200,\, Pr = 0.66,\, 9.70 \leq L_Z/D_h \leq 19.39,\, \frac{\pi}{36} \leq \alpha \leq \frac{\pi}{4},\, 0 \leq Br/D_h \leq 6.31$$

In the transition-to-turbulent regime, the C_1 and C_2 coefficients were mainly a function of the angle, but it was also necessary to consider the influence of the zigzag pitch and the bend radius to reach a good accuracy of Eq. 4.13.

$$Nu = 6.63 \times 10^{-6}\, (\alpha + 2.9223)\, (170.627 - Lz/D_h)\, Re + 1.3046 \times 10^{-1}\, \alpha^{0.1893}\, (49.097 - Br/D_h) \quad (4.13)$$
$$2200 < Re \leq 3200,\, Pr = 0.66,\, 9.70 \leq L_Z/D_h \leq 19.39,\, \frac{\pi}{36} \leq \alpha \leq \frac{\pi}{4},\, 0 \leq Br/D_h \leq 6.31$$

The experimental results obtained from the open literature were used to compare the proposed correlation in this work and other correlations, which can be seen in Table 1.2. A good exactness of the proposed correlations in a wide range of Reynolds numbers when $\alpha = 15°$ is demonstrated in Figure 4.18.

Kim's correlation in 2012 [58] and Yoon's correlation [70] studied the variation of the geometric features of the zigzag channels through CFD-based simulations. But, the proposed correlation in this research enlarges the application range of the Reynolds number and reaches accurate results in this wide range. Kim's correlations in 2009 [38] and 2011 [68], and Chen's correlation [39] show good accuracy with experimental data. Both experiments and correlations considered a zigzag angle of 15°. A comparison between all the correlations commented before and the simulation results of the current work was carried out to estimate the applicability of each correlation when the zigzag angle is 5°, 30°, and 45°. The relative differences among them and the simulation results for each one of the sixteen cases were averaged considering the ten analyzed values of the Reynolds numbers. They were grouped by the same zigzag angle. Figure 4.19 shows the average difference of the correlations and the CFD results with different zigzag angles.

As expected, the proposed correlation has a much smaller average difference from simulation for all zigzag angles. Kim's correlations in 2009 and 2011 and Chen's correlation present a little averaged difference for $\alpha = 15°$ due to these were obtained from data of a PCHE with $\alpha = 15°$. However, this difference increases when the zigzag angle takes other values. Kim's correlations in 2012 present an accurate performance for smaller zigzag angles than 15°. Figure 4.19 presents average values, but there are geometric designs where the other authors' correlations have a quite higher difference with the simulation results of this work. Yoon's correlation shows the greatest difference, which could be caused by differences in the computational model definition and the method applied to obtain it.
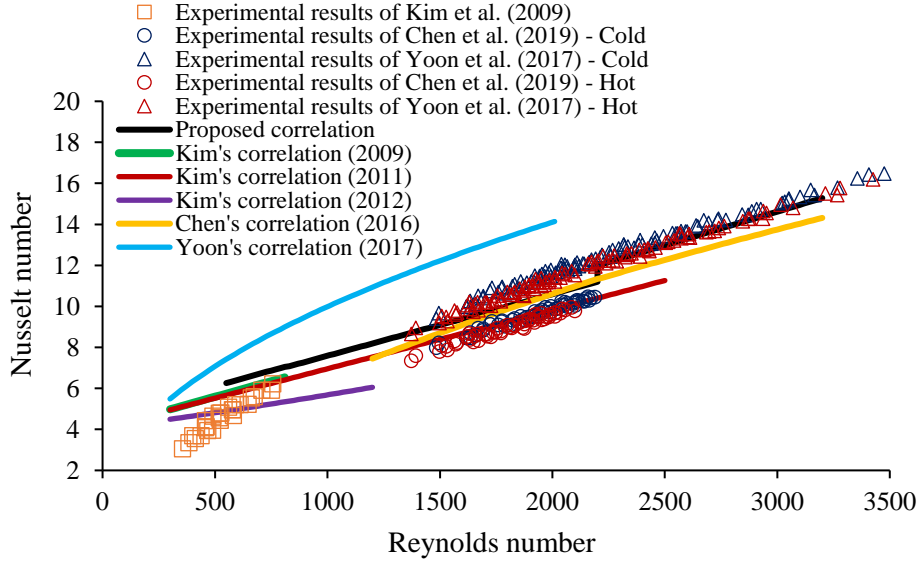
Figure 4.18: Nusselt number obtained from available correlations and experimental data.
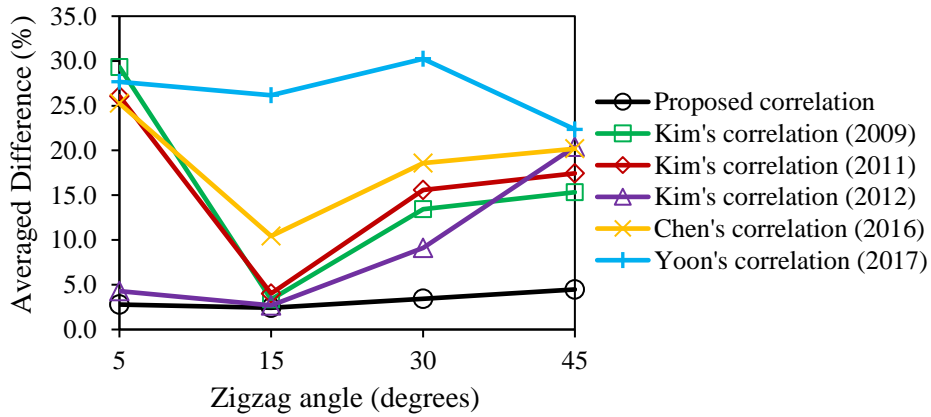
Figure 4.19: Averaged differences among Nusselt number correlations and simulation for several zigzag angles.

The friction losses variation with the Reynolds number in the laminar regime can be described as Kim et al. [38] and Yoon et al. [70] proposed, according to the form $f \times Re = C_1 \times Re + C_2$. A simpler model with linear relationship between f and Re can be used in the transition-to-turbulent regime by means of an equation as $f = C_1 \times Re + C_2$. The assumption of Eq. 4.10 and 4.11 was considered, and the scaled functions f_1 to f_8 were plotted in Figure 4.20. The coefficients take mean values of $\overline{C_1} = 9.517 \times 10^{-3}$ and $\overline{C_2} = 18.594$ in the laminar regime and $\overline{C_1} = -2.588 \times 10^{-6}$ and $\overline{C_2} = 2.349 \times 10^{-2}$ in the turbulent regime.
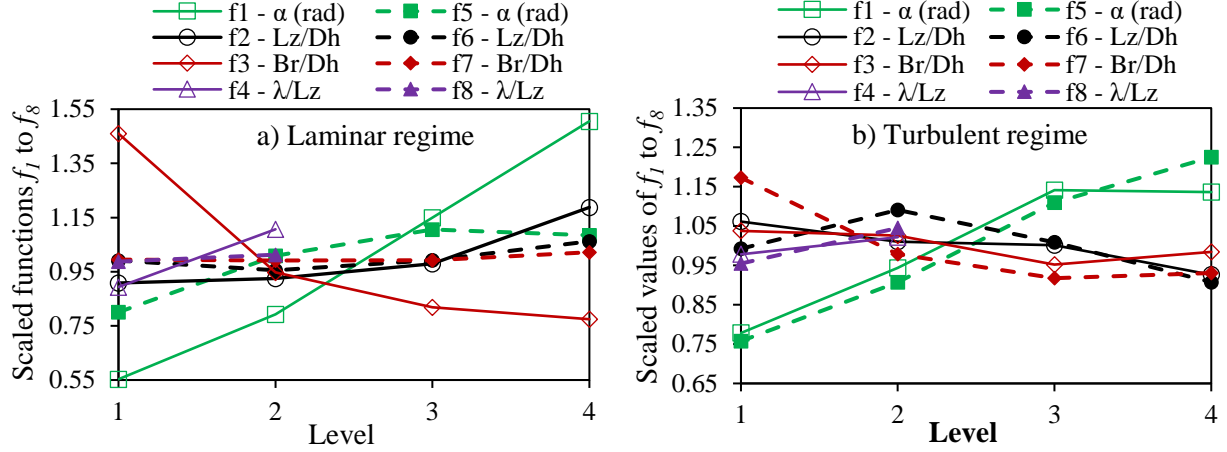
Figure 4.20: Behavior of the scaled values of C_1 and C_2 to each geometric parameter in a) laminar and b) turbulent Fanning friction correlations.

The coefficients C_1 and C_2 mainly depend on the scaled function of the zigzag angle and the bend radius. In concordance with the contribution ratios in Figures 4.15 and 4.16, the coefficients in the Fanning friction factor correlations are more dependent on the zigzag pitch and the bend radius than those in the Nusselt number correlations. The friction factor correlations were reached with a similar procedure as the Nusselt number correlations. They refer to the apparent values of the Fanning friction factor. These are presented in Eq. 4.14 and 4.15 for the laminar and transition-to-turbulent regimes, respectively. Figure 4.21 shows the available experimental data and several correlations in the open literature, and the results of the proposed correlation to calculate the Fanning friction factor with $\alpha = 15°$.

$$f \times Re = 0.01731 \times \frac{(\alpha + 0.3185)}{1.0321^{\left(0.6343\frac{L_Z}{D_h} - 8.414\right)^2}} \times \left(0.5908 + \left(\frac{Br}{D_h} + 1.2849\right)^{-1}\right) \times Re$$
$$+ 0.72425 \times (29.525 - \alpha^{-0.9007})$$

$$550 \leq Re \leq 2200, Pr = 0.66, 9.70 \leq L_Z/D_h \leq 19.39, \frac{\pi}{36} \leq \alpha \leq \frac{\pi}{4}, 0 \leq Br/D_h \leq 6.31$$

(4.14)

$$f = 2.4169 \times 10^{-8} \times (\alpha^2 - 1.36\,\alpha - 0.5939) \times \left(92.513 - \frac{L_Z}{D_h}\right) \times Re$$
$$+ 1.5267 \times 10^{-5} \times (\alpha^2 - 2.314\,\alpha - 1.406) \times \left(\left(\frac{L_Z}{D_h}\right)^2 - 26.902\frac{L_Z}{D_h} - 42.563\right)$$
$$\times \left(3.043 + \frac{1}{\frac{Br}{D_h} + 0.9821}\right)$$

(4.15)

$$2200 < Re \leq 3200, Pr = 0.66, 9.70 \leq L_Z/D_h \leq 19.39, \frac{\pi}{36} \leq \alpha \leq \frac{\pi}{4}, 0 \leq Br/D_h \leq 6.31$$

From Figure 4.21, there are several Fanning friction factor correlations with good accuracy. The proposed correlation displays a great exactness when the zigzag bends have a sharp-shape ($Br = 0$) by comparing with the experimental results of Kim et al. in 2009 [38]. However, it offers lower f values than experiments with a maximum error of 20% for $Re \leq 2800$ when the zigzag bends have a round-shape. This indicates that

the friction losses reduction with the increase of the bend radius is overestimated by the proposed correlation. Even so, it allows calculating the Fanning friction factor within an acceptable error as a function of the geometric parameters.
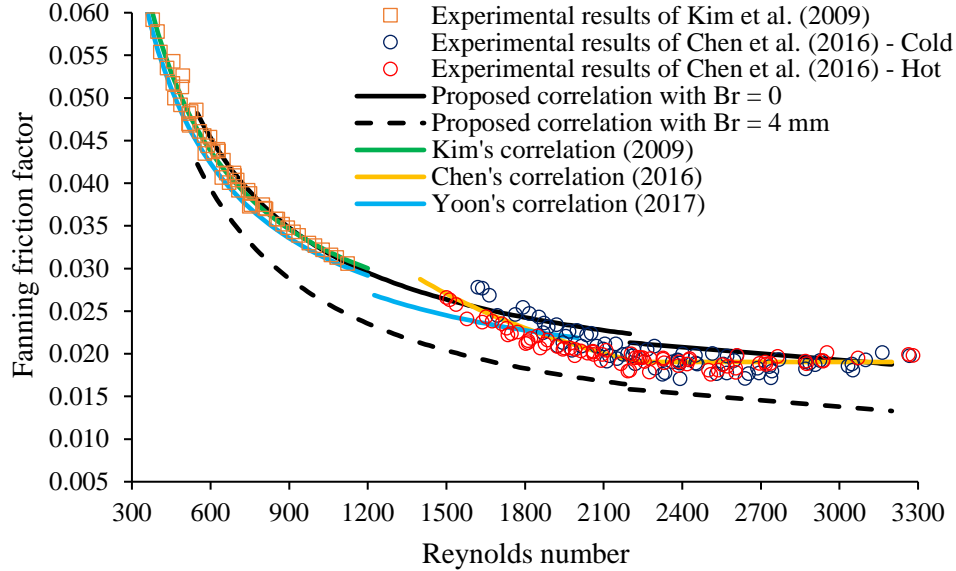
Figure 4.21: Apparent Fanning friction factor obtained from available correlations and experimental data.

4.3.5. Total cost optimization

The utility of the proposed correlations can be focused on design optimization. They can be used to obtain the heat transfer parameters and an optimized design with the lowest total cost per year. This optimization methodology developed by Kim et al. [57] is based on the thermal design calculation procedure presented in Appendix A, in which the overall heat transfer coefficient, the heat transfer area, the channel length, the core volume, the pressure drop, and other parameters can be calculated. These were calculated considering values close to those proposed by Oh and Kim [11], which were used in the thermal design calculation of Section 1.4. Thus, a thermal duty of 600 MWt, fluid pressures of 7 MPa, inlet temperatures in the cold and hot channels of 762 K and 1173 K, respectively, and outlet temperatures in the cold and hot channels of 1155 K and 867 K, respectively, were defined in a counter-flow PCHE configuration.

Then, the structural material weight was achieved using Eq. 4.16.

$$M_s = \rho_s \times V \tag{4.16}$$

where M_s is the structural material weight, ρ_s is the density of the structural material, and V is the volume of the PCHE core. The capital cost was estimated after knowing the material cost per kilogram, as shown in Eq. 4.17. In this work, the Alloy 617 was considered as structural material, which has an approximate cost of 120 \$/kg [57].

$$C_C = C_M \times M_s \tag{4.17}$$

where C_C is the capital cost (\$) and C_M is the material cost (\$/kg). However, the capital cost is obtained in \$ unit, while the operating cost is related to the expenses in a period. Therefore, the capital cost per year should be calculated considering the lifetime of the device. In this regard, the structural performance at a high temperature significantly limits the time of service of the PCHE, but several works have considered lifetimes higher than 20 years, according to the perspectives of the HTGR plants. In the current research, the capital cost per year (\$/y) was computed dividing the capital cost in 20 years.

Otherwise, the operating cost is associated with energy losses by pressure drop. The compressor work in both cold and hot sides was calculated using Eq. 4.18.

$$W_E = \frac{\Delta P \times \dot{m}}{\rho_f} \tag{4.18}$$

where W_E is the compressor work in Watts. The electricity cost was considered as 0.05 \$/kWh, which is a generation cost close to the average in many countries. The operating cost was obtained as Eq. 4.19.

$$C_O = C_E \times W_E \times 365\frac{days}{year} \times 24\frac{hours}{day} \tag{4.19}$$

where C_O is the operating cost (\$/y) and C_E is the electricity cost (\$/kWh). Finally, the total cost per year was computed as the sum of the operating cost per year and the capital cost per year.

The total cost per year of all possible designs within the ranges of 1.5 mm $\leq D \leq$ 2.0 mm, 9.225 mm $\leq l_Z \leq$ 18.45 mm, $5° \leq \alpha \leq 45°$, $0 \leq Br \leq 6.0$ mm, and $550 \leq Re \leq 2200$, was calculated. The optimum design was found with $D = 1.5$ mm, $l_Z = 9.225$ mm, $\alpha = 45°$, $Br = 6.0$ mm, and Reynolds numbers in the cold and hot sides of 572 and 702, respectively. This Reynolds numbers ratio allows a similar number of channels on both sides considering current operating conditions. The minimum total cost per year was \$451,783. This design had an overall heat transfer coefficient of 1360.8 W/(m²K), a heat transfer surface area of 8938 m², a core volume of 7.84 m³, and pressure drops of 1491 Pa and 2112 Pa in the cold and hot sides, respectively.

The optimized dimensions were fixed, while the Reynolds number was analyzed in the laminar range and one dimension was changed. Figure 4.22 displays the results of the designs with different zigzag angles, bend radius, and zigzag pitch length. A significant reduction of the total cost with the zigzag angle was found. The optimum Reynolds number decreased with the zigzag angle, which is due to the increase of the operating cost at higher angles. The influence of the bend radius on the total cost was evidenced, which is expected considering $\alpha = 45°$. The design with $Br = 0$ presented a great increase in the total cost at high Reynolds number. The total cost increased with the zigzag pitch length, although higher l_Z can be preferable when the Reynolds number is increased.
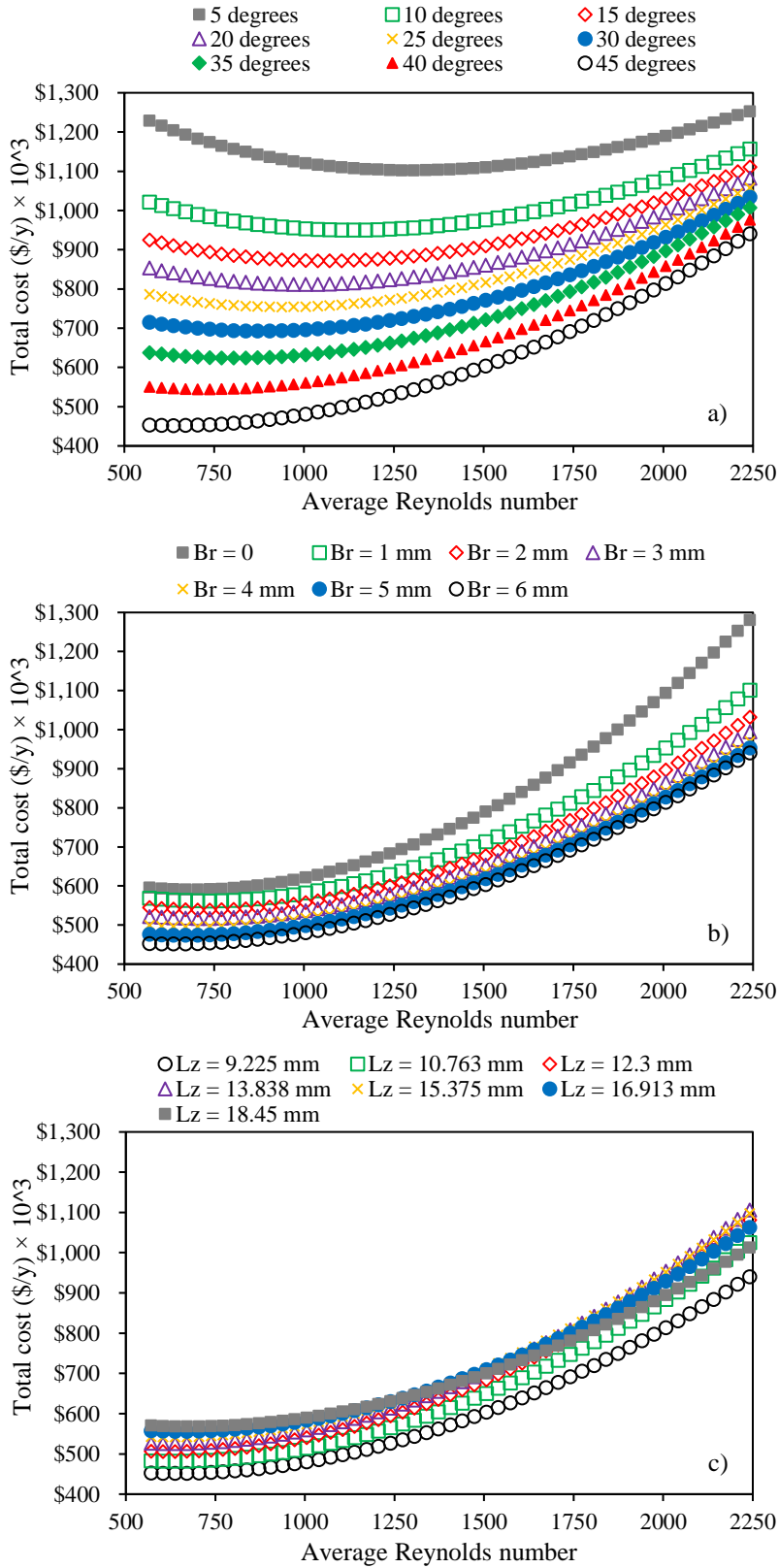
Figure 4.22: Total cost per year variation with the average Reynolds number with several a) zigzag angles, b) bend radii, and c) zigzag pitch lengths.

This optimization method has been widely applied in the PCHE analysis. Nevertheless, others can be more useful as a function of the application requirements. The design also depends on the pressure drop limits and structural performance.

4.4. Chapter summary

The thermal-hydraulic analysis of the PCHE under IHX condition in an HTGR plant was presented in this chapter. The computational model was validated by comparison of the Nusselt number and the Fanning friction factor obtained in the current CFD model and the experimental data available in the open literature. The cross-sectional dimensions were studied in a straight channel PCHE. The increase of the tip radius enhances the thermal-hydraulic performance, although in straight ducts it is not very significant.

The geometric design of the zigzag channel PCHE was explored considering the variation of the zigzag angle, the bend radius, the zigzag pitch length, and the zigzag phase-shift. The contribution ratio of the zigzag angle on the thermal-hydraulic performance was the highest by far. The increase of this dimension can be only beneficial up to 30° according to the JF factor maximization criterion. However, another optimization methodology based on the total cost reduction found that a design with $\alpha = 45°$, $D = 1.5$ mm, $l_Z = 9.225$ mm, $Br = 6.0$ mm, $Re_c = 572$ and $Re_h = 702$ is the better. The most valuable contribution of this analysis was the development of the Nusselt number and Fanning friction factor correlations as functions of the zigzag dimensions and the Reynolds number. The Nusselt number correlation demonstrated better accuracy than those in the open literature with a Prandtl number of 0.66.

5. STRUCTURAL ANALYSIS OF THE PCHE

The structural performance of the PCHE under IHX conditions is an issue that requires more precise analyses, as was commented before. The influence of the cross-sectional dimensions on stress fields in the straight channel PCHE is studied in this chapter, and several design recommendations are given. The importance of the time of service at high temperature is examined. Then, the stress fields in the zigzag channel PCHE is obtained for different zigzag dimensions.

5.1. Verification tests

A comparison between the stress values in the PCHE obtained through simulation and analytical calculation is presented in this section. The equations for the analytical calculation of the structural performance of the PCHE were presented in Section 2.4, where the approximation of the semicircular channels as hollow cylinders was applied. Thus, Eq. 2.14 and 2.15 were used to calculate the maximum hoop and radial stresses caused by the mechanical loading, which take place in the channel wall. The highest thermal stress is also in the channel wall, and its value was given by Eq. 2.19.

Considering the reference design dimensions presented in Table 3.1, and pressures in the channels of 7.99 MPa and 7.73 MPa from boundary conditions, the principal stresses were: $\sigma_{r,max}^m = -7.99\ MPa$ and $\sigma_{h,max}^m = -7.29\ MPa$. The equivalent stress according to the von Mises criterion is related to the principal stresses by Eq. 2.16. Therefore, the maximum mechanical stress in the inner wall was $\sigma_{m,max} = 7.67\ MPa$. The minimum value of the mechanical stress in the channel path from the simulation results was 7.62 MPa considering the reference design, as shown in Figure 5.1. The channel path was presented in Figure 3.7. That is because the internal pressure is an unrelenting load distributed in the entire channel wall, which produces non-self-limited stress. It demonstrates that the semicircular shape of the real geometric design of the PCHE channels induces stress concentration, especially near to the tips.
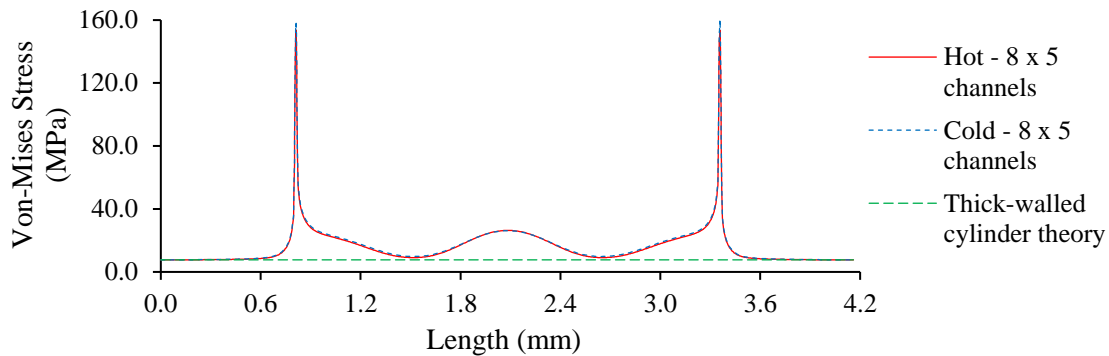
Figure 5.1: Mechanical stress values in the channel path from simulation and analytical value.

A linear variation of the temperature gradient function, $\Delta T(r_x)$, was considered to calculate the thermal stress using Eq. 2.19. If the temperature difference between inner and outer walls is 100 K and the reference

design dimensions are used, the thermal stress applying the von Mises criterion is 94.3 MPa. The mean value of the thermal stress from simulation results was 93.3 MPa, as shown in Figure 5.2. The mean value is more appropriate to compare with the analytical calculation because the thermal stress depends on the fiber tensile and contraction, and it is self-limited stress [78]. A great coincidence was evidenced between the analytical calculation and the mean value of the pseudo-2D model results in the channel path. The necessity of the simulation process was evidenced to reach more precise information about the stress concentration points and the influence of the geometric parameters.
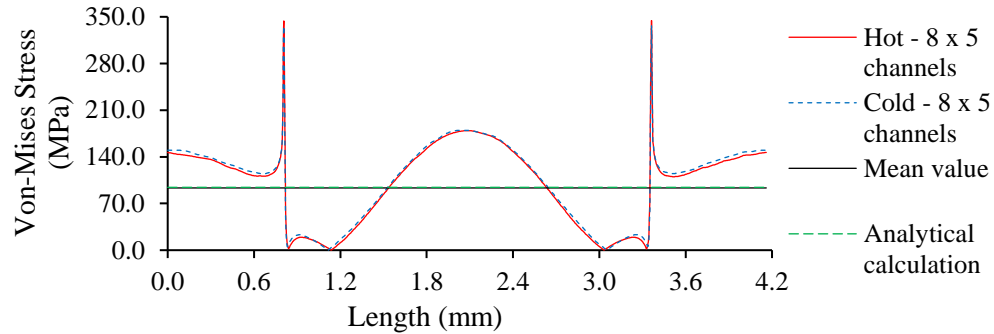
Figure 5.2: Thermal stress values in the channel path from simulation and analytical value.

5.2. Cross-sectional dimensions analysis

The effects of the temperature gradient and the cross-sectional dimensions on the thermal and mechanical stresses are first discussed using the pseudo-2D model, considering a linear elastic model of the stress-strain curve. Then, a more realistic plasticity model with isochronous stress-strain curves is used to analyze the plastic strain.

5.2.1.   *Effect of temperature gradient on the thermal stress*

The thermal stress fields of all twenty-five designs proposed in Table 3.7 were calculated with different temperature gradients. Appendix E presents the thermal stress variation across the hot channel paths for these designs. The thermal stress was obtained in the four critical points stress of Figure 3.7. These values show a proportional variation of the thermal stress with the change of the temperature gradient, as shown in Figure 5.3, where the proportionality constant (C) depends on the design features and the position on the channel wall.

Unrestricted boundary condition supposes the free expansion of the heat exchanger core from room temperature until the minimum operating temperature. However, the thermal stress by a thermal gradient is caused by the differential expansion of fibers, as was commented before. Reducing the thermal gradient in the heat exchanger structure is essential to avoid failure due to excessive deformations.
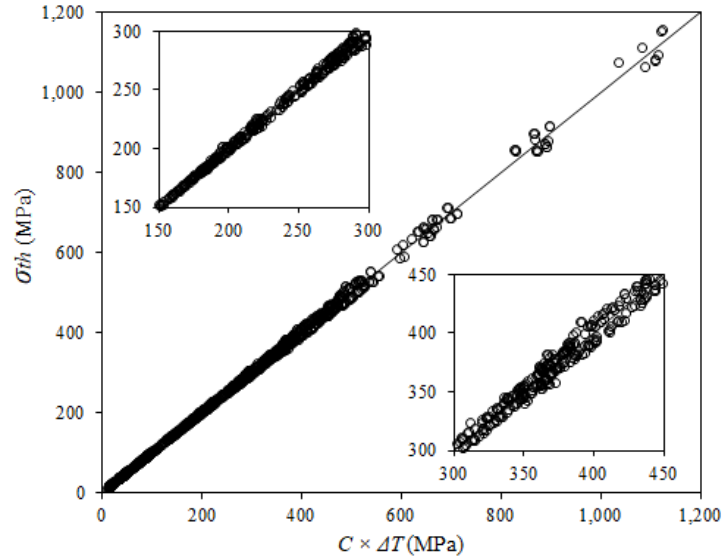
Figure 5.3: Proportional relationship between the thermal stress and the temperature gradient using a linear elastic model.

5.2.2. Effect of channel diameter

The effect of the channel diameter was studied through two approaches. The first one only considers the change of this dimension in the reference design. Designs with proportional dimensions were created with diameters from 1.5 mm to 2.0 mm, as shown in Table 3.1, and $t_p/D = 1.0$, $t_f/D = 0.45$ and $r/D = 0.005$, corresponding to the reference design. The thermal stress across the cold channel path of these designs is presented in Figure 5.4, considering $\Delta T = 25$ K. Path lengths were normalized for a better assessment. Almost the same results were obtained for these proportional designs. The channel diameter was also studied using the results of the twenty-five designs of Table 3.7, which are averaged by the same diameter according to Eq. 3.20.
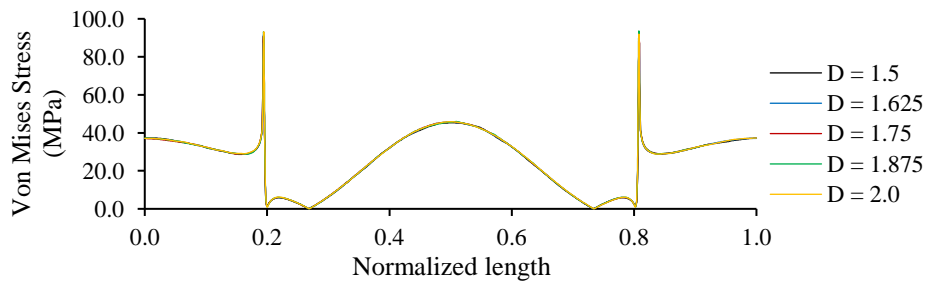
Figure 5.4: Thermal stress variation across the cold path of designs with different channel diameters and $\Delta T = 25$ K.

The influence of the diameter change was analyzed at the critical points while all geometric parameters are modified. The thermal stress for $\Delta T = 25$ K and the mechanical stress were obtained and averaged, as it is depicted in Figure 5.5. A very similar structural performance is observed with different diameters, but when $D = 1.5$ mm, the reduction of the thermal stress and the increase of the mechanical stress were reached at the tips. However, this is caused by the influence of the variation of other dimensions and the Taguchi method application. The mechanical stress at the flat part center (point 1) was not presented because there the minimum stress values take place.

Figure 5.5: Average of a) thermal stress with $\Delta T = 25$ K and b) mechanical stress by channel diameter at the critical points of the hot and cold channels.

5.2.3. Effect of plate thickness

The thermal stress in designs with several plate thickness ratios t_p/D was investigated with fixed values of $D = 1.5$ mm, $t_f/D = 0.45$ and $r/D = 0.005$. The stress behavior in the normalized path length of the cold central channel is presented in Figure 5.6. Similar thermal stress in the semicircle zone (normalized length between 0.2 and 0.8) can be verified. A reduction of this value with the increase of t_p/D ratio at point 1 is displayed, but opposite effects took place at points 2 and 4 (tips), where the stress concentration increases with the t_p/D ratio. That was analyzed through the averaged values of the thermal stress with $\Delta T = 25$ K and mechanical stress at the critical points of the twenty-five designs, as it is depicted in Figure 5.7.
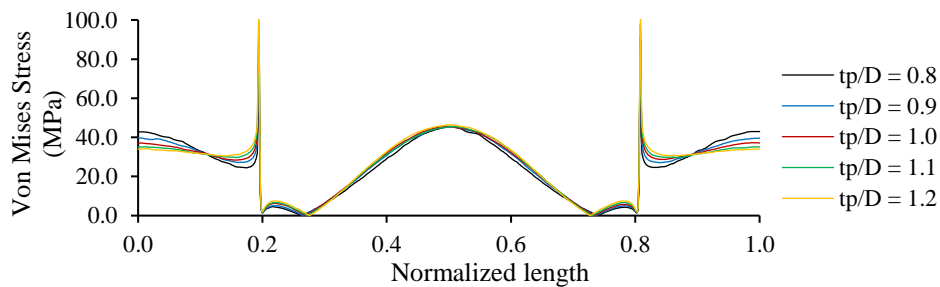
Figure 5.6: Thermal stress variation across the cold path of designs with different tp/D ratios and $\Delta T = 25$ K.

The thermal stress decreases at point 1 of the hot and cold channels, but the increase of those at points 2 and 4 are more notable considering the performance of the twenty-five designs. Instead, the mechanical stress at all critical points is reduced with the plate thickness. The stress by pressure has a great concentration in the tips zone. Because the thermal stress shows a higher dependence on the plate thickness change, this parameter decrease could be a better option to reduce the total stress at the tips. However, the mechanical stress is the primary stress with higher significance. Hence, it should be evaluated in each application with specific values of temperature gradient and internal pressures.

Figure 5.7: Average of a) thermal stress with ΔT = 25 K and b) mechanical stress by tp/D ratio at the critical points of the hot and cold channels.

5.2.4. *Effect of ridge thickness*

The influence of the ridge thickness ratio t_f/D on the thermal stress was evaluated while other dimensions as $D = 1.5$ mm, $t_p/D = 1.0$ and $r/D = 0.005$ remained constant. The stress field in the cold channel path is shown in Figure 5.8. In this case, a decrease of the thermal stress up to 11.2% can be reached reducing the t_f/D ratio from 0.75 to 0.15 at the arc center (point 3), but the highest reduction around 30% can be achieved at the tips (points 2 and 4).

Figure 5.8: Thermal stress variation across the cold path of designs with different tf/D ratios and ΔT = 25 K.

Analyzing the results of the average thermal and mechanical stresses for designs grouped by t_f/D ratio in Figure 5.9, the thermal stress increase is verified at the four points per channel, while the mechanical stress is reduced at the tips. Therefore, the ridge thickness has a great influence on the mechanical stress concentration at the tips.
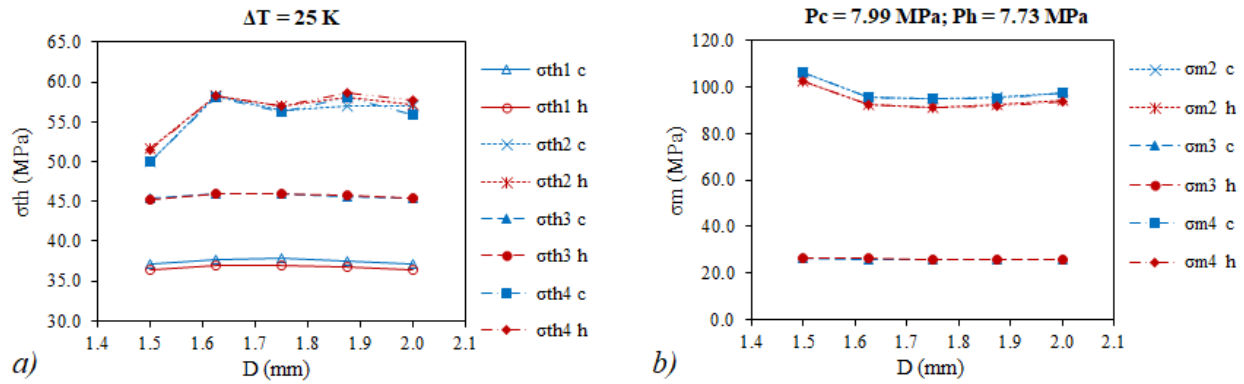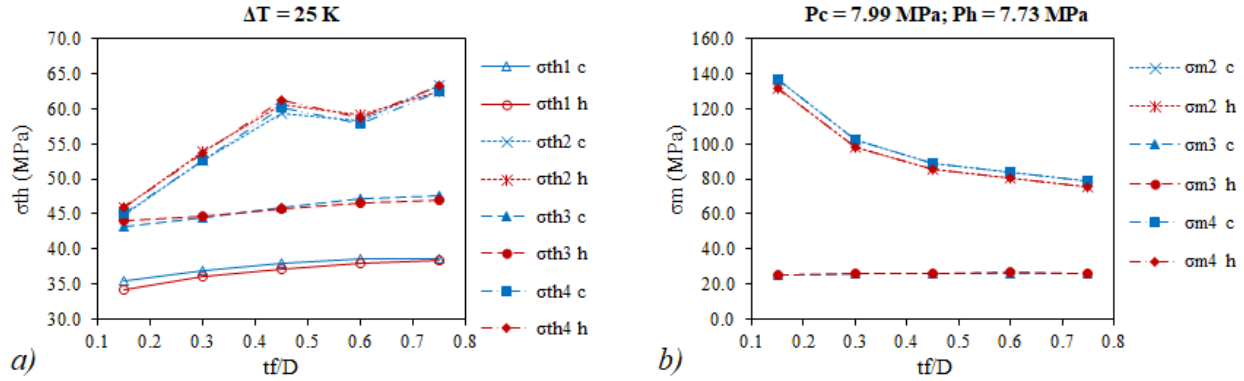

Figure 5.9: Average of a) thermal stress with $\Delta T = 25$ K and b) mechanical stress by tf/D ratio at the critical points of the hot and cold channels.

The temperature fields allow explaining why the thermal stress values increase with the ridge thickness. Figure 5.10 demonstrates that the temperature gradient is mainly observed in the vertical direction between the hot and cold channels. When fibers are at the same temperature, they do not compress or tense the other ones. While this condition is more noted in the horizontal direction, the uniaxial thermal stress condition is predominant. The horizontal temperature gradient increases with the ridge thickness; then, the biaxial thermal stress state is intensified. This geometric parameter affects the value of the equivalent thermal stress in all the channel walls, but especially in the channel tip region, where the increase of the peak stress is evidenced. Furthermore, the creep rupture life of Alloy 617 under the biaxial stress state is reduced compared to the results obtained by uniaxial tensile creep tests [32]. Consequently, the intensification of the biaxial stress state must be avoided. The mechanical stress increase with the ridge thickness indicates that the assessment of this dimension is necessary for each combination of temperature gradient and internal pressures.

5.2.5. Effect of rounded tip radius

The effect of the rounded tip radius on the structural performance of the PCHE was analyzed in-depth because the highest stress values were at the tips. The average values of the stresses were calculated by the same r/D ratio at the four points. As expected, the tip radius did not influence the stress at points far from the tip region, as shown in Figure 5.11. Asymptotic decrease of both thermal and mechanical stresses is observed at the tips. Most of the stress reduction took place increasing the r/D ratio from 0.005 to 0.02 because the almost sharp-shape of the tips is removed. The thermal stress reduction is 35.8% and the mechanical stress drop is 44.2% when the r/D ratio is increased from 0.005 to 0.02, but those are 23.8%

and 46.4%, respectively, when the r/D ratio is increased from 0.02 to 0.08. Among all the cross-sectional dimensions, the tip radius shows a higher influence to reduce the concentration of both thermal and mechanical stresses.
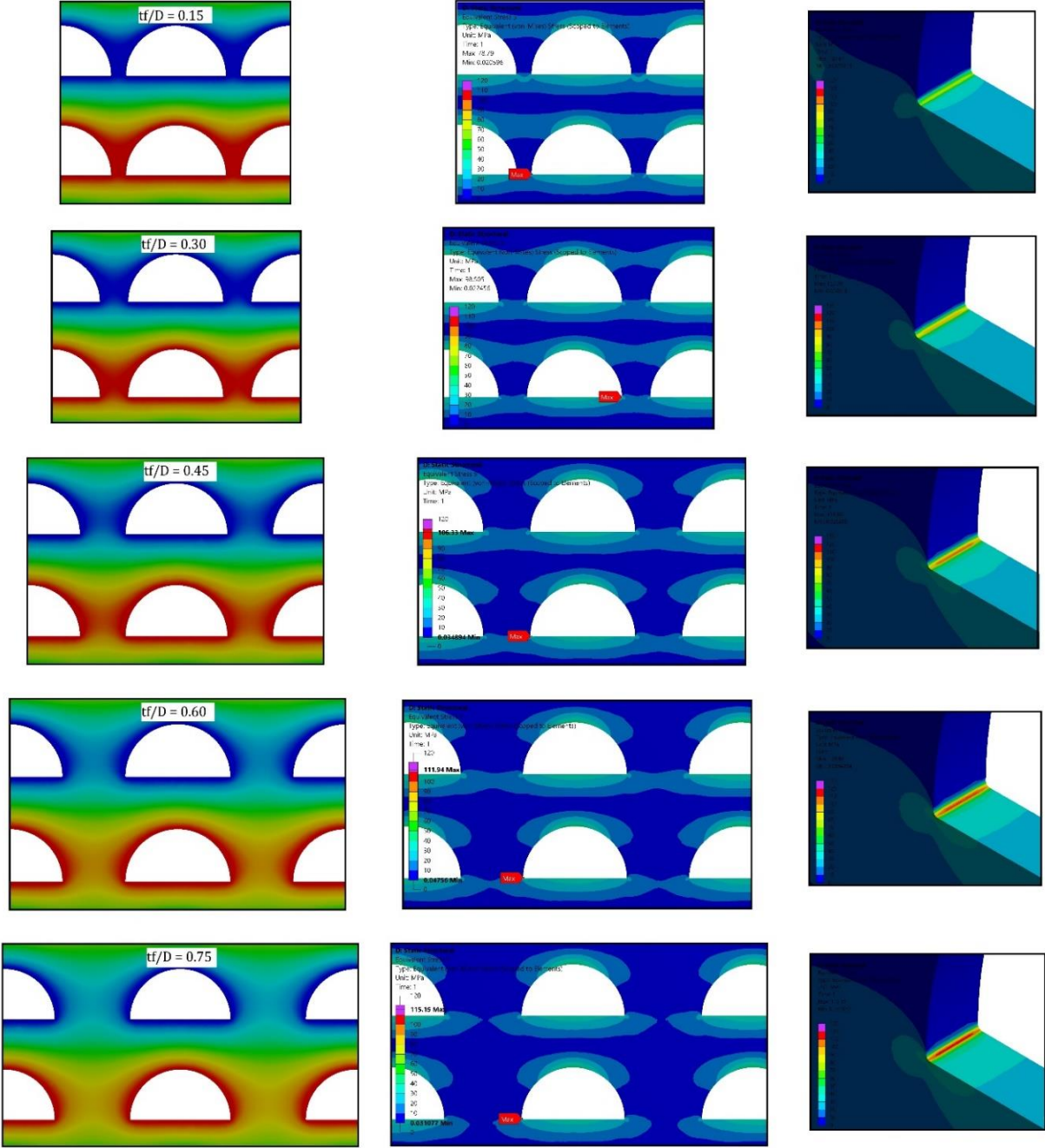
Figure 5.10: Influence of the ridge thickness on the temperature gradient, the thermal stress field, and the peak thermal stress at the tips.
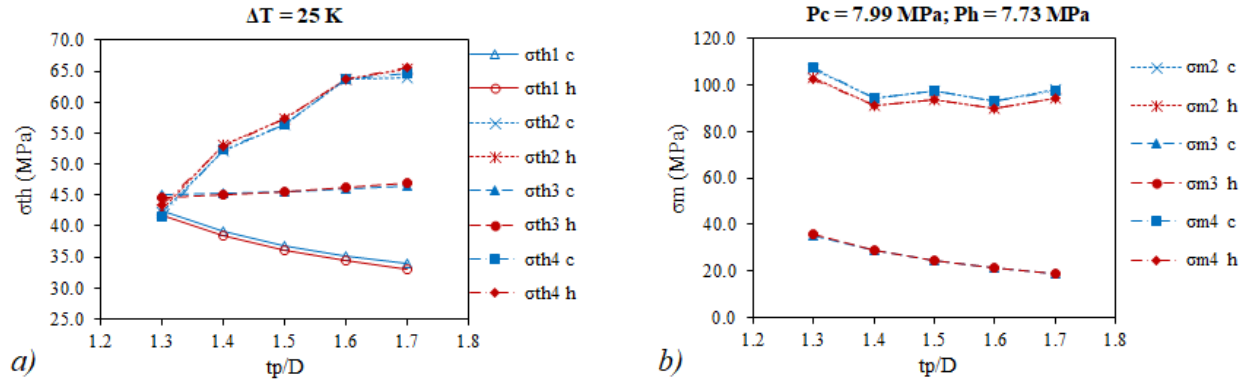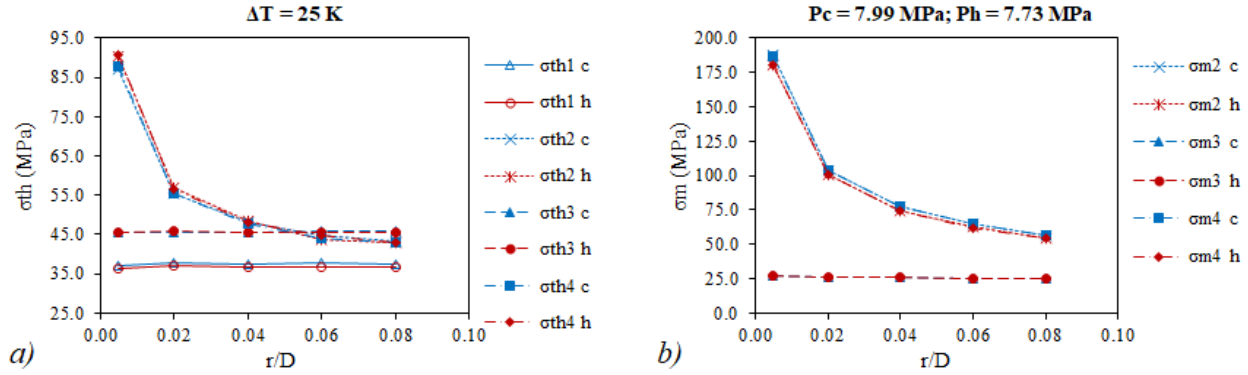
Figure 5.11: Average of a) thermal stress with $\Delta T = 25$ K and b) mechanical stress by r/D ratio at the critical points of the hot and cold channels.

Thermal, mechanical and total stresses of designs with different r/D ratio and constant $D = 1.5$ mm, $t_p/D = 1.0$ and $t_f/D = 0.45$ were tested. Figure 5.12 presents the thermal stress caused by $\Delta T = 25$ K across the cold channel path for these designs. Data of the rupture and allowable stresses are plotted for different times of service of the Alloy 617 at 1173 K. The thermal stress decrease with r/D ratio was evidenced at the tips. The peak stress zone became to be wider and it was displaced toward the flat surface of the channel. Peak stress values of designs with r/D ratio of 0.005, 0.02, and 0.04 exceed the allowable stress after 10 h, and, even, the rupture stress was exceeded when tips have a sharp-shape ($r/D = 0.005$). The allowable stress with 1,000 h of work was under the thermal stress obtained in almost all paths, and the rupture value was exceeded at the tips and the arc center regions. Considering 100,000 h of service, the thermal stress was higher than the rupture value in almost all the channel walls. Nevertheless, the peak thermal stress is redistributed after deformation and its effect mainly causes failure under fatigue condition.
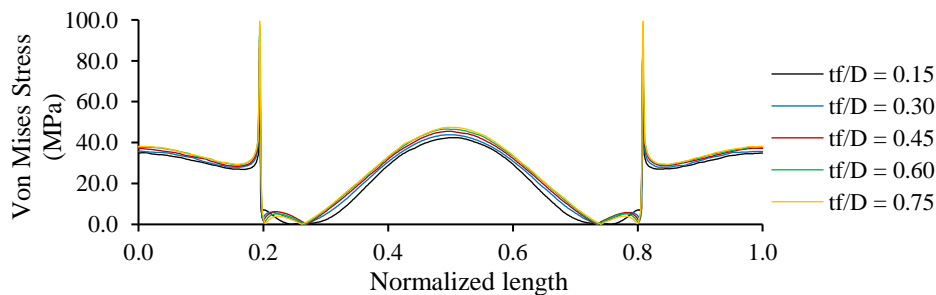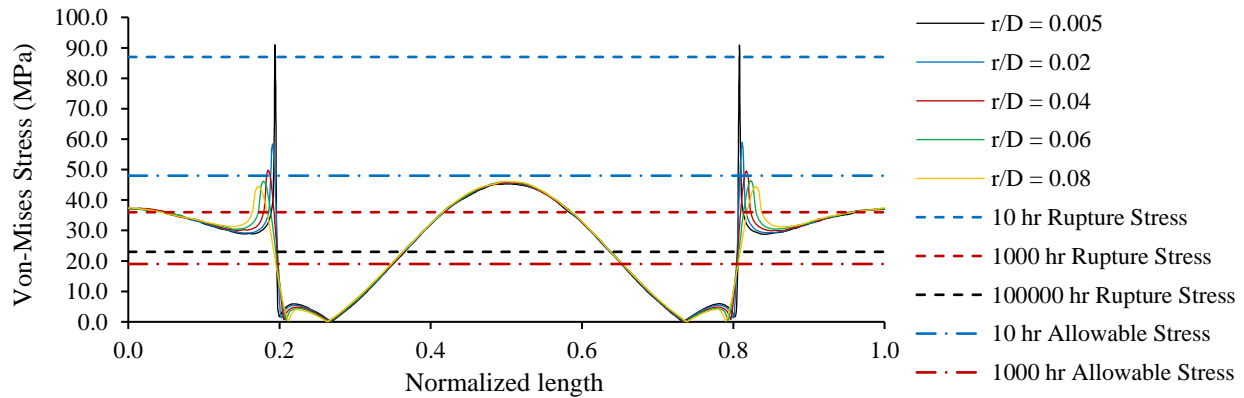

Figure 5.12: Thermal stress variation across the cold path of designs with different r/D ratios and $\Delta T = 25$ K.

Figure 5.13 shows the great value of the local mechanical stress at the tips and its significant decrease with roundness. The allowable stress after 1 h was exceeded with $r/D = 0.005$ and $r/D = 0.02$, and still, the

102

rupture stress for this time was considerably exceeded with a sharp-shape. After 10,000, the allowable stress was lower than the stress by the pressure effect in most of the channel walls, but the rupture stress was only exceeded at the tip regions. The mechanical stress at the tip is local primary membrane stress, which should be evaluated by Eq. 2.6, 2.8, and 2.9. However, the allowable stresses and rupture stresses allow to have an approximation of the risk level in the PCHE structure.
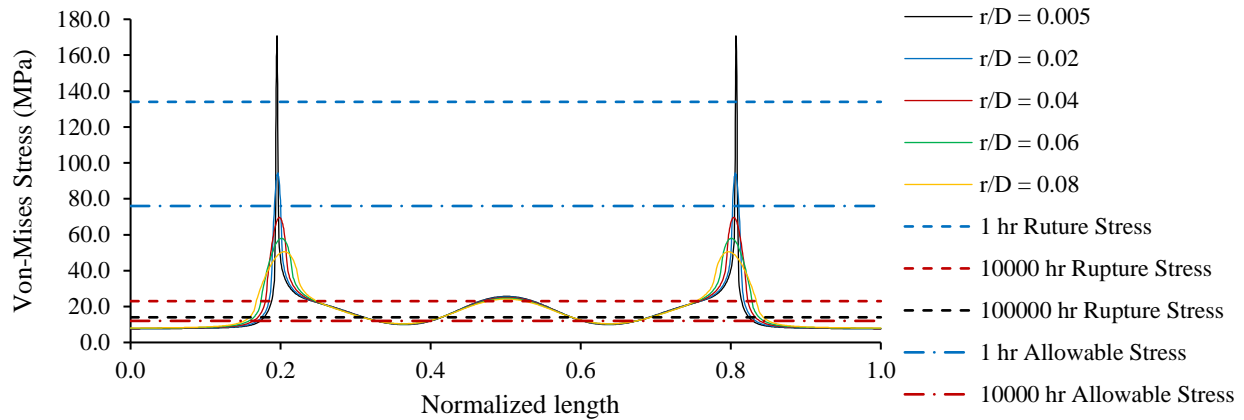
Figure 5.13: Mechanical stress variation across the cold path of designs with different r/D ratios and Ph = 7.73 MPa and Pc = 7.99 MPa.
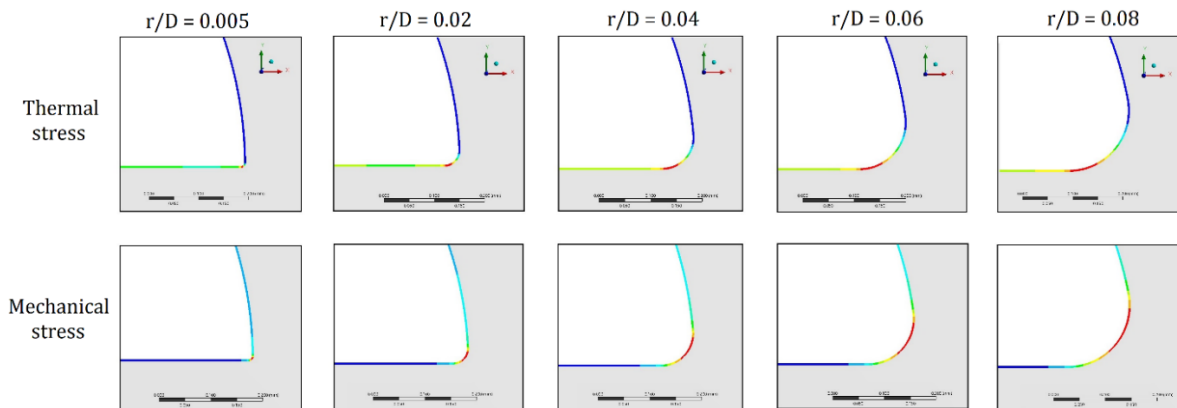
Figure 5.14: Displacement of the maximum thermal and mechanical stresses points at the tip region with the tip radius increase.

A stress displacement at the tips toward the arc center of the channel can be observed in Figure 5.13. That is, the opposite direction of the thermal stress displacement in Figure 5.12, which offers a valuable characteristic when the thermal and mechanical stresses are simultaneously present. The displacements of the maximum stresses at the tips with different roundness are shown in Figure 5.14. The red color of the maximum stresses demonstrates the opposite movement and the widening of them. Because the total stress

in the cold channel is approximately the addition of both values, as will be seen later, a greater reduction of stress concentration is expected at the tip regions. The total stress of the cold channel was computed for the same five designs, and results are shown in Figure 5.15. The allowable stress was exceeded after 1 h by all designs, except for that with r/D = 0.08. It shows the risk of the PCHE operation under very high temperature and internal pressure conditions as an IHX in an HTGR plant. Peak stresses are important in fatigue analysis because they are sources of fatigue cracks. In this way, some experimental tests to analyze the PCHE operation under HTGR conditions have used fluids with hot temperatures lower than 1063 K and internal pressures under 3 MPa [12][111].
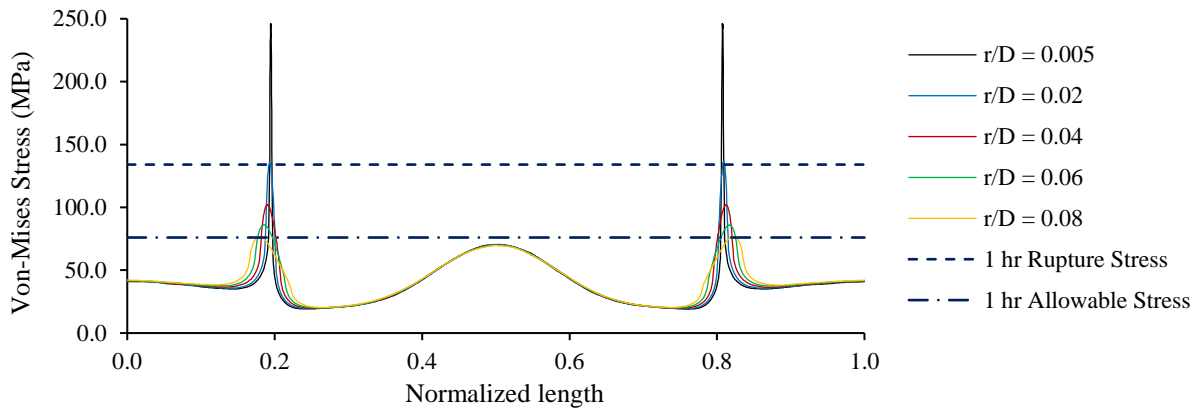
Figure 5.15: Total stress variation across the cold path of designs with different r/D ratios and loading: ΔT = 25 K, Ph = 7.73 MPa and Pc = 7.99 MPa.

The stress concentration factor is equal to the maximum stress divided by the average stress in the channel wall. Figure 5.16 displays the exponential decrease of the stress concentration factor of the thermal, mechanical and total stresses at the tip region when r/D is increased. The higher concentration of mechanical stress was found with a maximum value near to eight with sharp tips. The roundness of tips is always essential to decrease the peak stresses, but mainly to reduce the mechanical and total stresses.
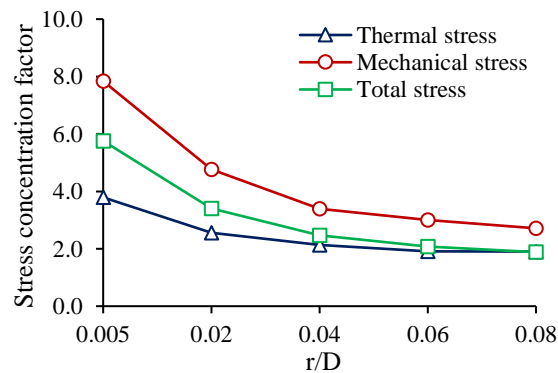
Figure 5.16: Stress concentration factor at the tip region with different r/D ratios.

A more safe and durable operation could be reached reducing the temperature gradient, rounding the channel tips, and optimizing the other dimensions according to the operating conditions. Alternative cross-sections of the PCHE channels without sharp tips could also decrease the stress concentration. Because of circular cross-sections reduce drastically the heat transfer area density, two-sided etched PCHE with semicircular paths bonded in front of semielliptical paths [119] could be a possibility to consider in further structural studies.

5.2.6.   *Effect of channels configuration*

The thermal effectiveness of several channel configurations shown in Figure 5.17 was analyzed by Chen et al. [115]. They found that types A and E offer the lowest effectiveness values, while types C and D have the highest values. However, remarkable performance improvement was not evidenced. The temperature fields change with the channel configuration is presented in Figure 5.17. These design variations also cause different thermal and mechanical stresses distribution. Although only two channels per fluid have been represented in Figure 5.17, the thermal and mechanical stresses were calculated considering geometric domains equivalent to the verified geometric model obtained in Subsection 3.5.2 with 8×5 channels.
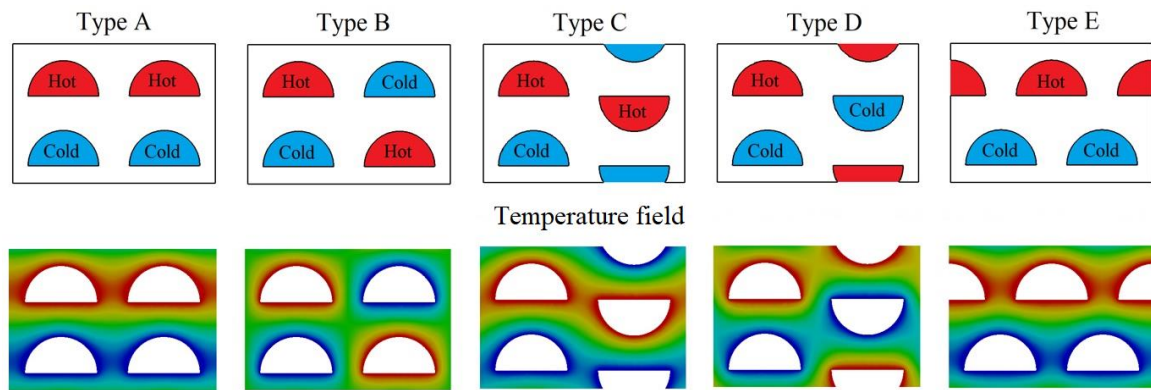
Figure 5.17: Possible channel configurations of the PCHE and temperature fields in the central channels.

The critical points in the channel path were selected to analyze the structural performance changes with the channel configuration. The thermal stress was calculated considering hot and cold channel temperatures of 1173 K and 1073 K, respectively, while the mechanical stress was obtained with hot and cold channel pressures of 7.73 MPa and 7.99 MPa, respectively. Table 5.1 presents the stresses at the critical points, the mean stress along the path, and the stress concentration factor at the tips.

The lowest mean value of the thermal stress was in type A (reference design). Although the stress at point 1 was higher than other configurations, the maximum stress at point 2 (tip) was quite lower than types B, D, and E. The lowest stress concentration factor was in type C, which presented the smallest thermal stress change at the critical points. There was a more balanced distribution of the thermal stress in the channel path of type C, and it can be preferable before others. The mechanical stress was very similar for all

configurations except type E. Channel configurations A and C are recommended according to the structural results, but type C is more suitable because it also offers better thermal-hydraulic performance [115]. However, the PCHE fabrication of type C can be a challenge with plates etched on top and bottom faces.

Table 5.1: Thermal and mechanical stresses at critical points, means values and concentration factor at point 2 with different channels configuration.

Configura-tion	Thermal stress at critical points [MPa]					Mechanical stress at critical points [MPa]				
	Point 1	Point 2	Point 3	Mean value	Concentra-tion factor	Point 1	Point 2	Point 3	Mean value	Concentra-tion factor
Type A	149.77	337.06	179.8	95.83	3.52	7.62	153.67	26.38	20.62	7.45
Type B	101.42	469.23	147.71	115.79	4.05	7.54	159.2	25.99	21.28	7.48
Type C	159.03	298.18	185.26	102.33	2.91	8.06	142.19	27.32	18.07	7.87
Type D	107.46	554.95	188.39	105.89	5.24	7.94	142.89	27.33	18.13	7.88
Type E	89.462	598.94	169.0	109.02	5.49	12.65	180.49	9.337	24.45	7.38

5.2.7. *Allowable design parameter ranges*

In this section, the ranges of the design parameters and the temperature gradient are proposed to satisfy the allowable stress after different times of work according to the previous results. The analysis was conducted considering the stresses at the tips and the arc center. The stress at the tips can be peak stress or local primary membrane stress if it is thermal or mechanical, respectively. The stress at the arc center can be secondary stress when it is caused by the temperature gradient, or primary when it is caused by the internal pressure. In this way, the secondary stress can be considered almost independent of the cross-sectional dimensions according to the results presented before. However, the peak stress, the local primary membrane stress, and the primary membrane stress changed with the plate thickness, the ridge thickness, and the tip radius, as shown in Figure 5.18. Although, these values must be assessed with the corresponding allowable stress value using Eq. 2.7 – 2.12, a more conservative approach was applied in this section. The possibility of cracks source under cyclic operation causes that tips are an essential base to reach a safe design, mainly in the nuclear industry. Then, both thermal and mechanical stresses were compared with the same significance with allowable stress or rupture stress.

The tensile and compression effects of the thermal and mechanical stresses in the cold and hot sides were considered to propose the allowable design parameter ranges. The thermal stress in the cold and hot channels causes tensile and compression strains, respectively, due to the higher expansion of the hottest fibers. While the mechanical stress produces tensile strains in both channels by internal pressure. Therefore, the total stress can be approximated as the addition of both stresses in the cold channel with a conservative margin of difference, as shown in Figure 5.19 a). In the hot channel, the total stress was quite overestimated by the addition of the thermal and mechanical stresses, but more realistic and conservative total stress values can be estimated taking the maximum value among the thermal and mechanical stresses, as it is depicted in Figure 5.19 b). The conditions considered in Figure 5.19 were: $\Delta T = 25$ K, $P_c = 7.73$ MPa and $P_h = 7.99$ MPa.
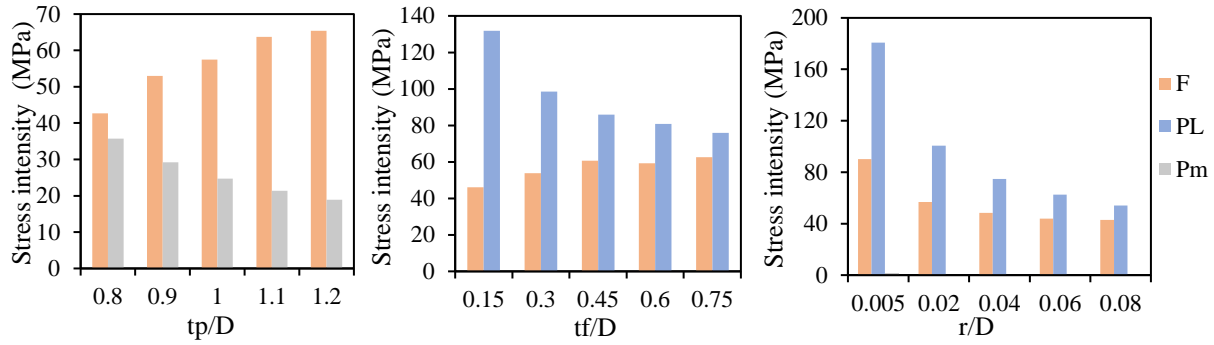
Figure 5.18: Variation of the P_m, P_L, and F with the cross-sectional dimensions.
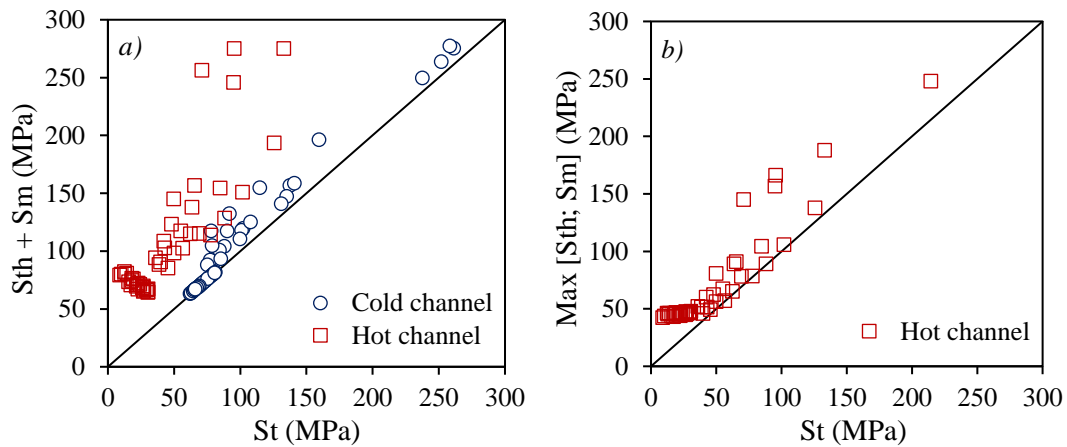
Figure 5.19: Total stress estimation in the cold and hot channels through a) the thermal and mechanical stresses addition, and b) maximum value between the thermal and mechanical stresses.

First, the allowable design was analyzed in the hot channel with only the thermal stress. The round tip radius and the temperature gradient were those with the highest influence on the thermal stress at the tips. Interpolated equations of the thermal stress as a function of the temperature gradient or the tip radius can reach for point 2 of the hot side from Figures 5.3 and 5.11. If the moderated influences of the plate and ridge thicknesses are not considered, the relationship between the temperature gradient and the tip radius to reach a peak thermal stress lower or equal to the allowable stress can be found. The allowable stresses of the Alloy 617 at 1173 K presented in the Draft ASME BPVC [91] were used to obtain the design parameter ranges. Figure 5.20 presents the allowable ranges of *ΔT* and *r/D* in the hot channel for various times of service.
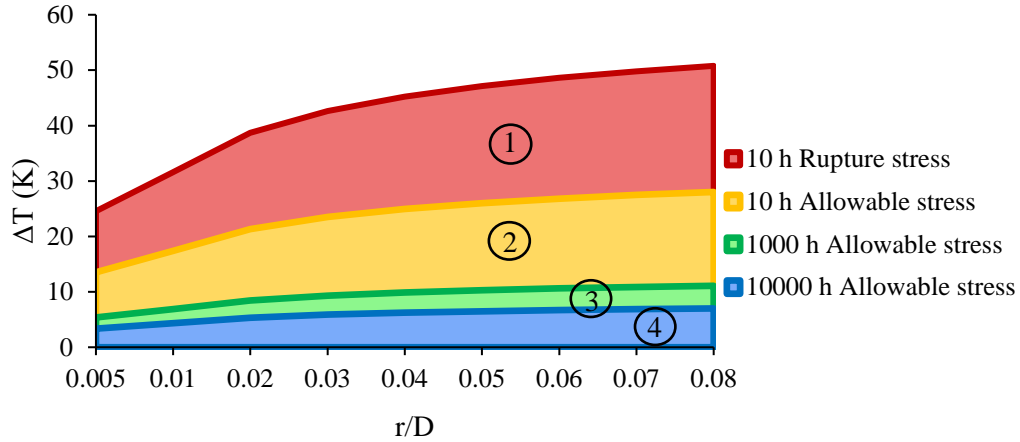
Figure 5.20: Allowable design relationship between temperature gradient and tip radius in the hot channel with different times of service considering thermal loading.

Higher temperature gradients are possible increasing the tip radius. For design purposes of the PCHE, values inside the region 1 in red allow operation under the 10 h rupture stress on the hot side. In that time, the allowable stress is reached with a lower temperature gradient, which is under 10 K increasing the time of service until 1,000 h and 10,000 h. In practice, the temperature gradient between fluids is around the analyzed values, but this gradient is very low in the channel walls of a straight channel PCHE. The mechanical stress must be added to the thermal stress in the cold channel to consider the pressure effect, which mainly depends on the tip radius. In the cold channel, the increase of temperature gradient caused the increase of the thermal stress, but also the allowable stress of Alloy 617 in the cold channel wall had an increment due to a lower temperature, as shown in Figure 2.2. The allowable relationship between ΔT and r/D in the cold channel is presented in Figure 5.21. If sharp tips ($r/D = 0.005$) are defined, the total stress is higher than the allowable stress after 1 h.
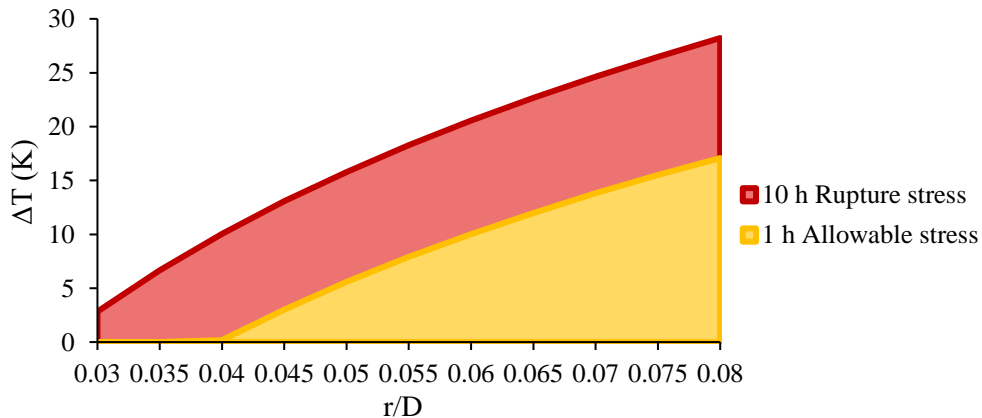
Figure 5.21: Allowable design relationship between temperature gradient and tip radius in the cold channel with different times of service considering the pressure and thermal loadings.

Due to the addition of both thermal and mechanical stresses, the allowable temperature gradient is lower on the cold side of the PCHE than that on the hot side. Therefore, the cold channel determines the design parameters when the internal pressure conducts a relatively high mechanical stress. Here, the pressures were fixed as 7.99 MPa and 7.73 MPa in the cold and hot channels, respectively, corresponding to operating conditions of an HTGR plant [60], but several experimental tests consider pressures under 3 MPa. In those cases, using Figure 5.20 to obtain the allowable design parameter ranges can be more appropriate.

Another hazardous region is located at the arc center, where the stress level is lower than the peak stress at the tips, but it is distributed in a wider wall surface, and therefore, they are not considered peak or local stresses. Instead, the thermal stress and the mechanical stress at the arc region are considered as secondary stress and primary stress, respectively. The geometric parameters have a little influence on the thermal stress at the arc center, but the plate thickness is important to reduce the mechanical stress, as was seen before. The total stress in the cold channel was considered to analyze the arc region because of the addition of both stresses. The relationship between the temperature gradient and the plate thickness ratio was obtained, and the curves of allowable values were calculated for the rupture and allowable stresses after 10 h, as it is illustrated in Figure 5.22. The increase of ΔT is possible when t_p/D increase because the mechanical stress is reduced while the thermal stress is increased. The designs with ΔT and t_p/D inside the region 1 in red reach the rupture stress after 10 h, but for this time, the designs must be inside the region 2 to satisfy allowable stress. The cold channel was studied at the arc center because it is the most dangerous side when relatively high pressure is present.
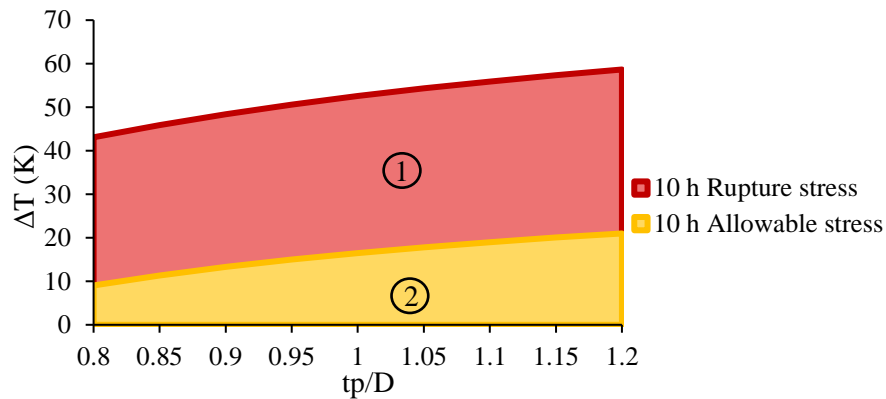
Figure 5.22: Allowable design relationship between temperature gradient and plate thickness in the cold channel before 10 h of time of service considering the pressure and thermal loadings.

5.2.8. *Plastic strain analysis*

The plastic strain of materials is essential to analyze the cyclic loading operation of the structures. This residual deformation can appear at the critical points under determined temperature and time of service, and it can cause crack and failure. An important structural behavior of materials to analyze the plastic strain at high temperature is the isochronous strain-stress curve. It is a constant-time stress-strain curve for a given temperature. Here, some points of the isochronous strain-stress curves of Alloy 617 within the Draft ASME

BPVC [91] were chosen to define a multilinear isotropic hardening plasticity model for different temperatures and times of service. These points are plotted in Figure 5.23. It allows simulating the plastic deformation beyond the yield stress considering the material conditions in the hot tensile test (initial time) and after times of service of 10 h, 1,000 h, and 10,000 h.
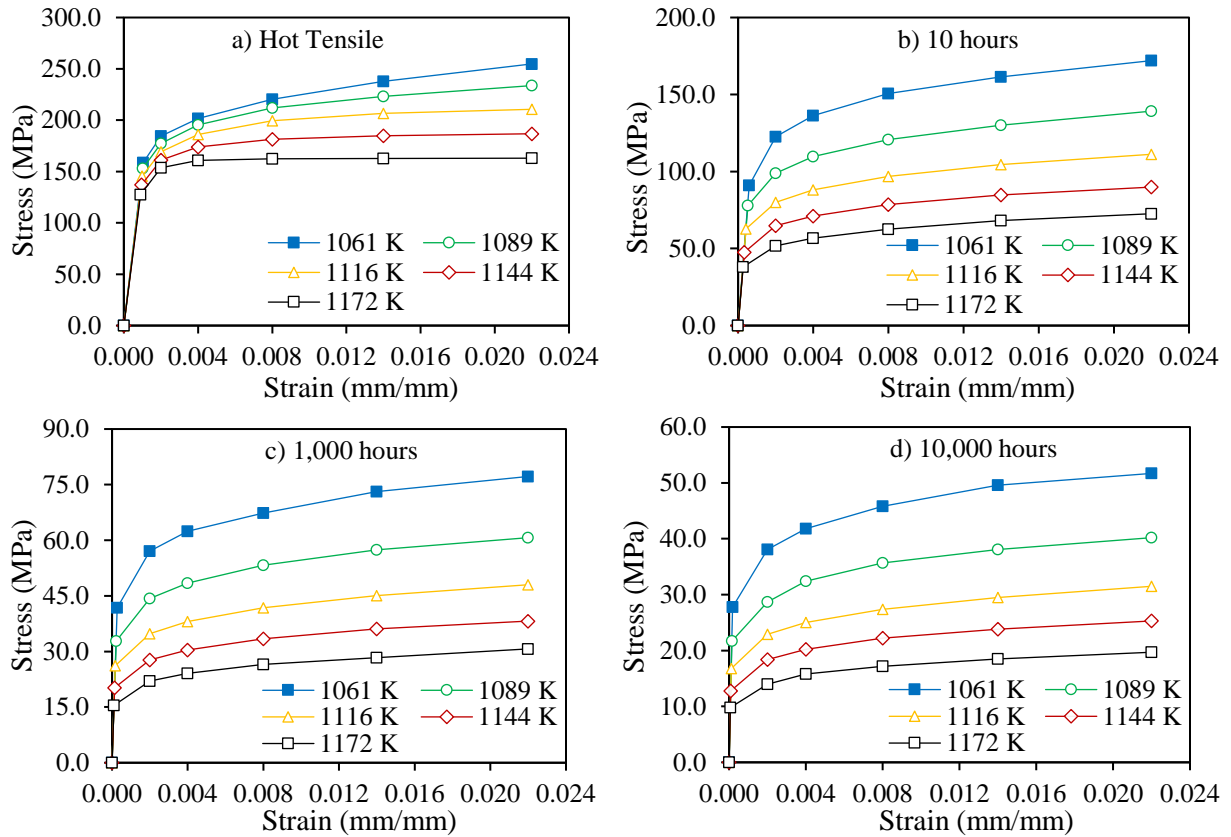
Figure 5.23: Points of the isochronous strain- stress curves of Alloy 617 used to simulate the plastic strain considering a) the hot tensile test and the time of exposure of b) 10 h, c) 1,000 h, and d) 10,000 h.

The design methodology employed for the evaluation of strain limits in the Draft ASME BPVC [91] is based on the small strain theory elastic-perfectly plastic material model, where the yield stress is obtained as the pseudo yield stress selected to bound accumulated inelastic strain. The pseudo yield stress refers to the temperature-dependent isochronous stress-strain curves presented in Figure 5.23. In this section, the geometric parameters of the reference design were used.

The plasticity influence on the thermal stress fields with $\varDelta T = 25$ K and using material models with 10 h, 1,000 h, and 10,000 h isochronous curves is presented in Figure 5.24. A great reduction of the maximum thermal stress was obtained by applying the plasticity models, in which the hot channels are those with lower stress values. That is because plasticity takes place in a lower stress value. While the time of work was increased, the thermal stress decreased due to the reduction of the yield stress. However, the plastic

strain was more significant with the time, as shown in Figure 5.25. The higher plastic strain was at the hot channel tips, but this deformation was also notable at the center of the flat and arc surfaces.
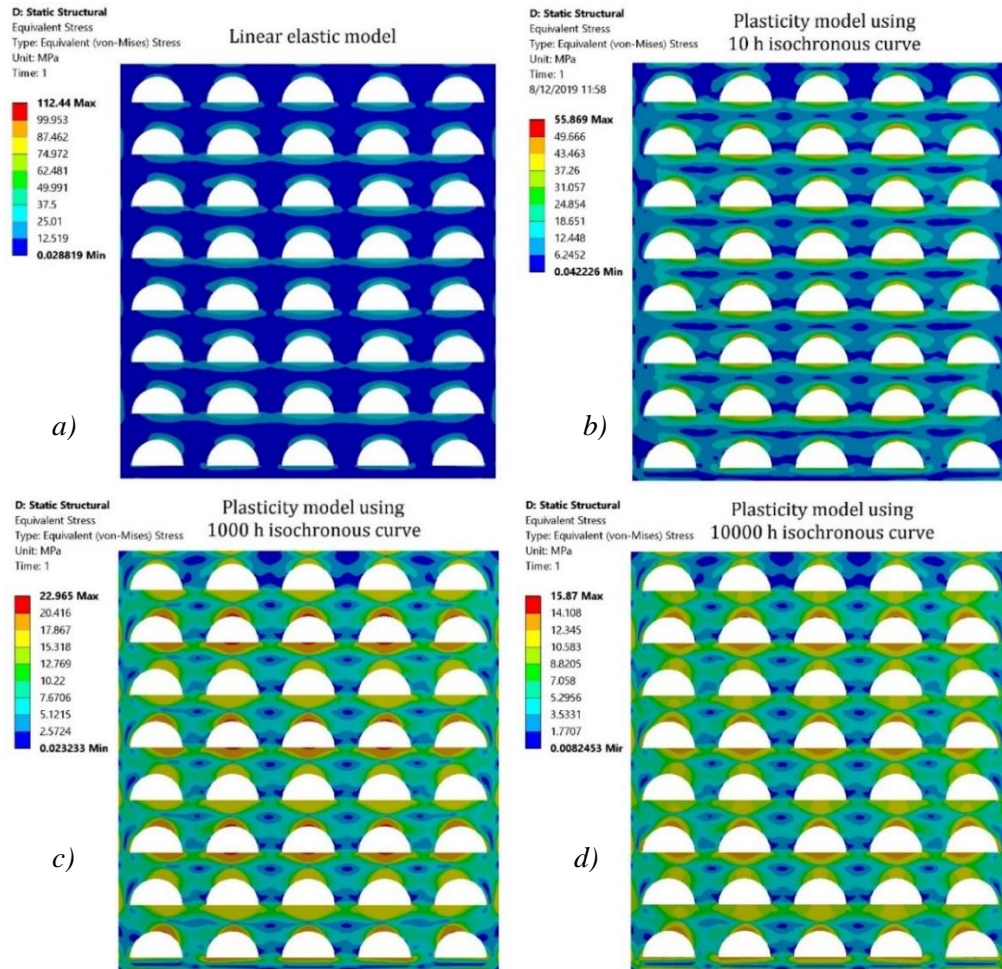
Figure 5.24: Thermal stress field considering a) the linear elastic model and plasticity models with b) 10 h, c) 1,000 h, and d) 10,000 h isochronous strain-stress curves.

The rounded tips were tested under conditions of $\Delta T = 25$ K and time of service of 10,000 h. Figure 5.26 presents the plastic strain at the tip region due to the thermal stress in three similar designs with $r/D = 0.005$, $r/D = 0.02$ and $r/D = 0.04$. The plastic strain at the tips significantly decreased when the r/D ratio was increased from 0.005 to 0.04. The importance of the roundness at the tips was verified. Although the plastic deformation beyond the yield stress is lower than 0.2%, the structure failure could take place due to the presence of the cyclic loadings, where the plastic deformations are accumulated. Furthermore, the primary stress normally presents the highest risk in the structure; therefore, the presence of the pressure of the fluids gets even worse the risk associated with the plastic deformations.
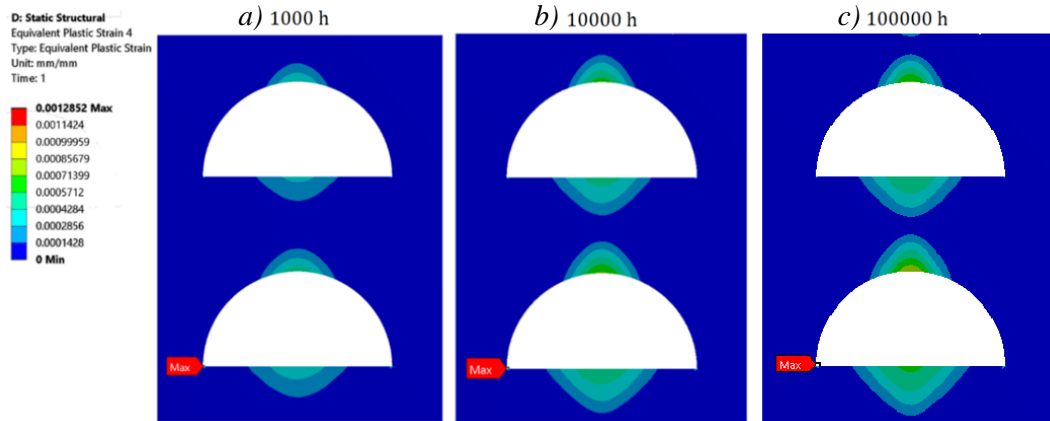
Figure 5.25: Plastic strain due to thermal stress in the central channels after a) 1,000 h, b) 10,000 h, and c) 100,000 h of time of service.
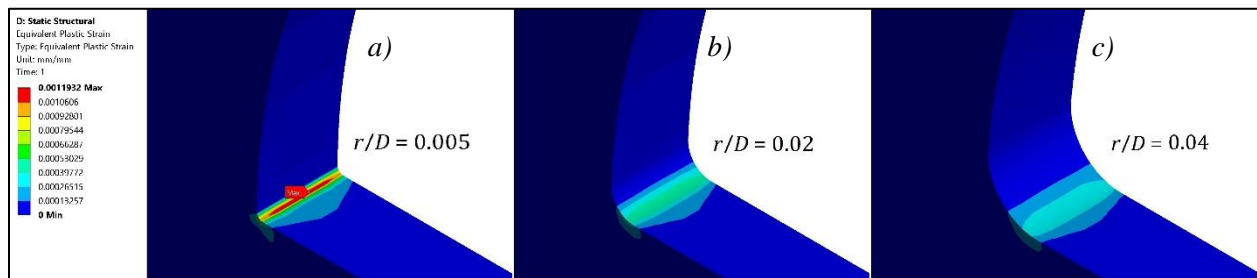
Figure 5.26: Plastic strain at the tip region after 10,000 h of designs with a) r/D = 0.005, b) r/D = 0.02, and c) r/D = 0.04.

If the temperature gradient is increased, the plastic strain grows even with a reduced time of service, as it is depicted in Figures 5.27 and 5.28 for the cold and hot channel paths, respectively. Temperature gradients of 25 K, 50 K, and 100 K were tested considering isochronous curves for 10,000 h, 1,000 h, and 10 h, respectively, and the hot tensile stress-strain graph. In the cold channel path, the strain increment can be noted when ΔT changes from 25 K to 50 K and 100 K, and the time of service is reduced from 10,000 h to 1,000 h and 10 h. The increase of temperature gradient from 50 K to 100 K caused almost the same plastic strain in the channel wall, but in a time of service 100 times lower. Even considering the hot tensile stress-strain curves, a plastic strain was noted for $\Delta T = 100$ K. In the hot channel path, the higher temperature in the wall caused that the increment of the temperature gradient from 50 K to 100 K had a higher effect on the plastic strain, which was increased in a time of service of 10 h.
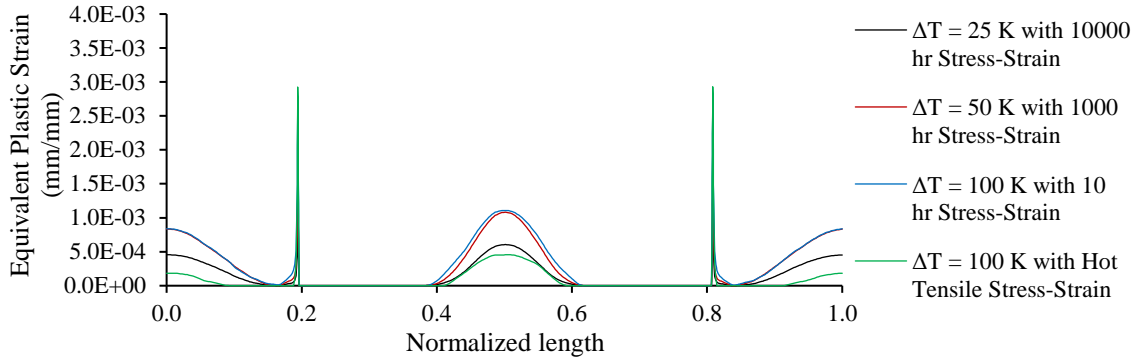
Figure 5.27: Equivalent plastic strain in the cold channel path for several temperature gradient and isochronous curves.
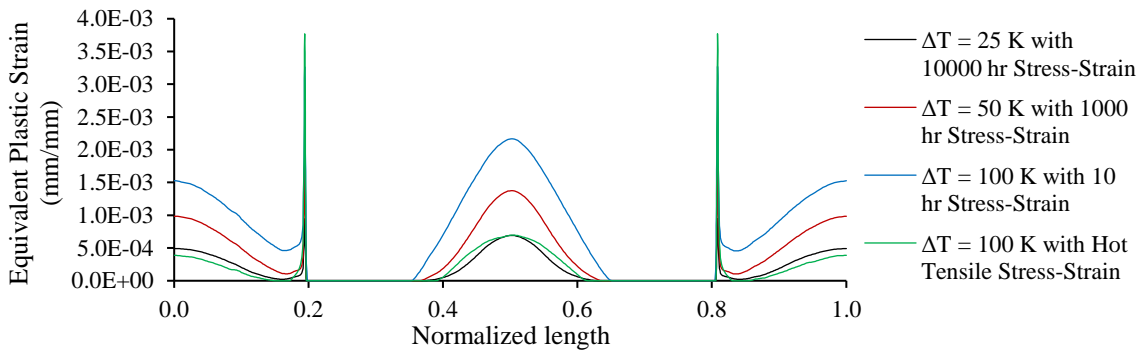
Figure 5.28: Equivalent plastic strain in the hot channel path for several temperature gradient and isochronous curves.

5.3. Zigzag dimensions analysis

The stress fields in a single bend of a zigzag channel PCHE was analyzed through the 3D model presented before. The non-uniform temperature fields in the cross-sectional planes of the 3D model due to the fluid-structure interaction is an essential difference with the pseudo-2D model. To analyze these temperature fields, three sections' views were considered in the bend region with $\alpha = 15°$ and $Br = 0.5$ mm, as shown in Figure 5.29. A fully sharp-shape ($Br = 0$) of the bend was not considered in the FEA simulation to avoid unrealistically overestimation of the stress at the zigzag corner by the linear elastic model. The section view A corresponds to the center of the bend, where the counter fluid flows have not changed their directions. The section views B and C are passing the bend in the hot flow direction, but near and far from the bend, respectively.
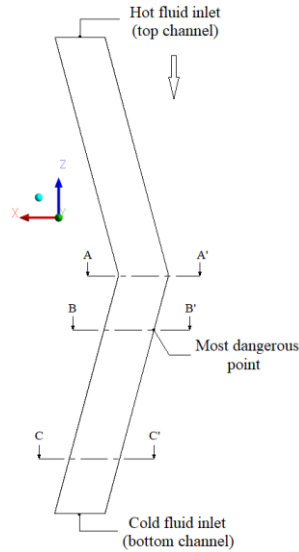
Figure 5.29: Section view at the central plane A, section view at the most dangerous plane B after bend and section view in a plane C away from the bend.

5.3.1. *Velocity and temperature fields in the zigzag bend*

Figure 5.30 presents the velocity and temperature contours in the three section views. The two first columns correspond to the velocity and temperature contours in the fluid domains. The symmetry in the *ZY* plane of the temperature field of the solid domain at the bend (view A) is evidenced. However, the change of flow direction of the hot fluid after the bend causes the appearance of the stagnant fluid regions in the section view B, and the fluid motion is concentrated toward the wall tangent to the zigzag bend. In these regions, the highest velocity values are achieved, and therefore, the highest temperatures are concentrated. The most dangerous region in fatigue conditions was there with the maximum peak thermal stress, as will be presented later. The section view C, far from the bend, presents a similar trend to the section view B, although it is less noticeable. Although a reduced geometric model of the PCHE with a zigzag bend was considered, all zigzag bend portions have almost the same proportional temperature field according to the results of Ma et al. [62], and the most dangerous bend of the PCHE is expected to be the studied portion at the highest temperature.

The temperature contours of the solid domain of the zigzag channel PCHE showed an important thermal gradient in the channel wall direction of the section view B, which remarks the biaxial stress state of the thermal stress. It is a fundamental result of the FSI to calculate the peak thermal stress in a zigzag channel, that 2D models do not consider. Also, the maximum temperature gradients were 1.58 K, 2.76 K, and 2.59 K at the sections A, B, and C, respectively, which contributed to the higher thermal stress concentration in the section B. Figure 5.31 presents the thermal stress fields in the wall of the walls of the cold and hot channels with the stress concentration region after the bend in the fluid direction, considering a temperature difference between fluids (ΔT_f) of 27.6 K. ΔT_f is defined as the difference between the mean values of the hot fluid temperature and the cold fluid temperature. The section view B is that *XY* plane with the maximum

114

thermal stress. The obtained temperature gradients in the solid domain were around one order lower than the temperature gradient between fluids.

a) Section view A

b) Section view B
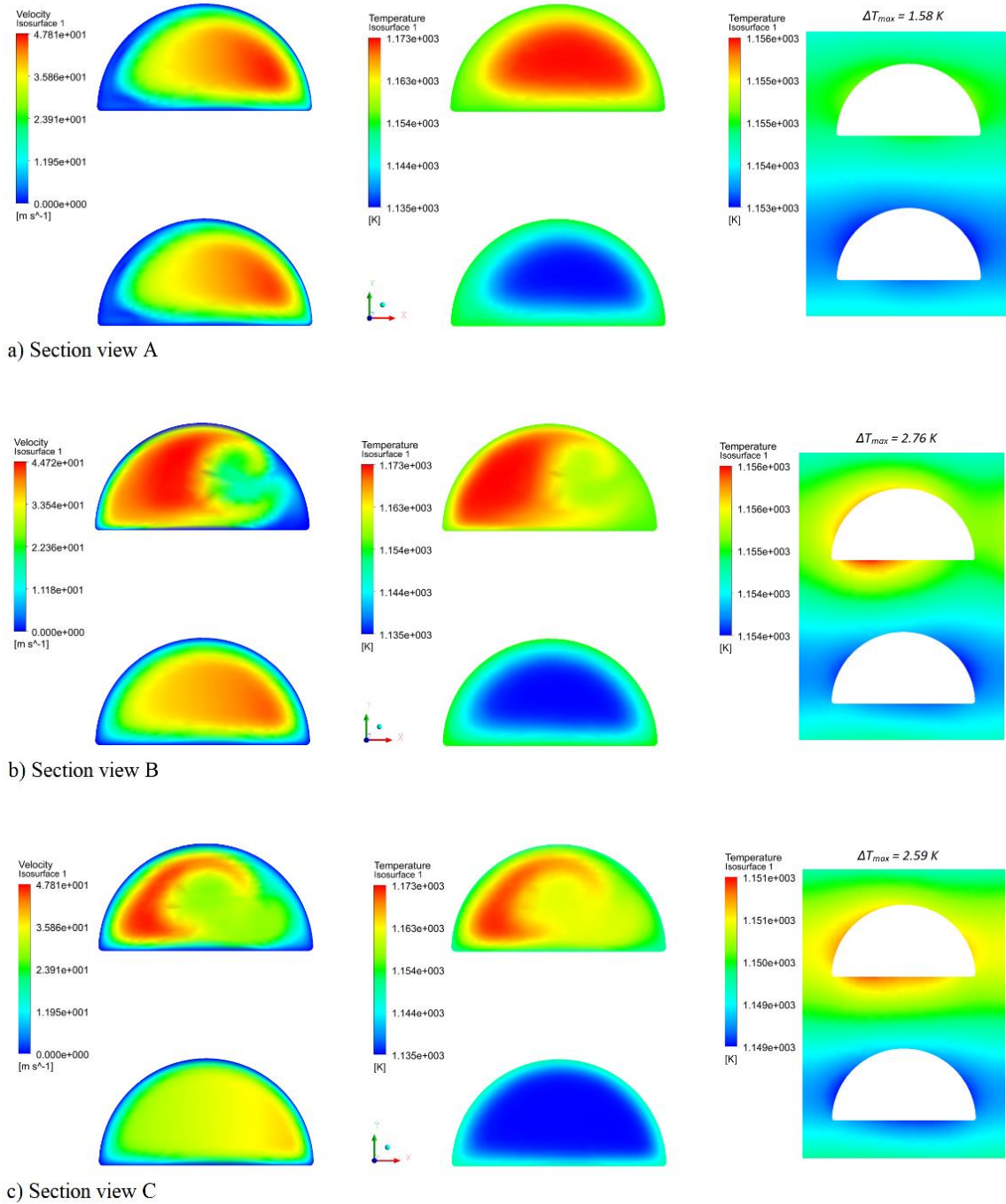
c) Section view C

Figure 5.30: Velocity and temperature contours of the fluids and solid domains at the section views a) A, b) B, and c) C of the central channels.
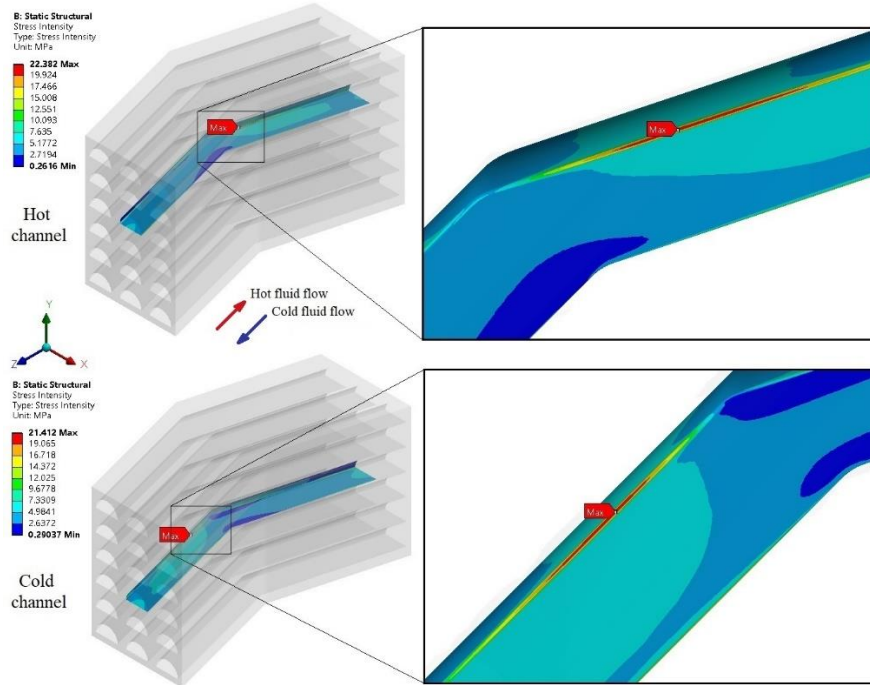
Figure 5.31: Detailed view of the thermal stress intensity field on the wall in the hot and cold central channels
ΔT_f = 27.6 K

If the wall temperatures using the 2D model are defined according to the fluid values, the thermal gradient between the walls overestimates the real gradient using a 3D model. Another assumption in the pseudo-2D model is that the wall temperature is the same in all the surface, while the wall temperature using a 3D model changes in the cross-section perimeter, creating a wall temperature gradient, as shown in Figure 5.32. The effect of the thermal gradient in the channel wall can be neglected for thermal stress calculation if the PCHE design presents straight channels, but it is essential to study the zigzag channels PCHE. Therefore, the pseudo-2D model is mainly accurate to simulate the stress fields in the straight channel PCHE. The main difference between the stress field obtained from the pseudo-2D model and the 3D model in the straight channel PCHE is the middle region of the channels, but the thermal stress at the critical points are very similar, as shown in Figure 5.33. Nevertheless, the wall temperature could be defined in the pseudo-2D model as a function of the wall position to reach a greater accuracy of the thermal stress field [120], but this can be difficult in a design study where several parameters are changing. A great temperature gradient is observed in the section view B of the zigzag channel PCHE, which creates stress values considerably higher than that in the straight channel PCHE. The maximum thermal stress with straight channels is 7.65 MPa, while this value is 27.1 MPa with zigzag channels. Furthermore, the stress field is very different among them. It should be noted that the mean value of the temperature in the channel walls of the 3D model with zigzag channels is lower than those of the pseudo-2D or 3D models with straight channels.

116
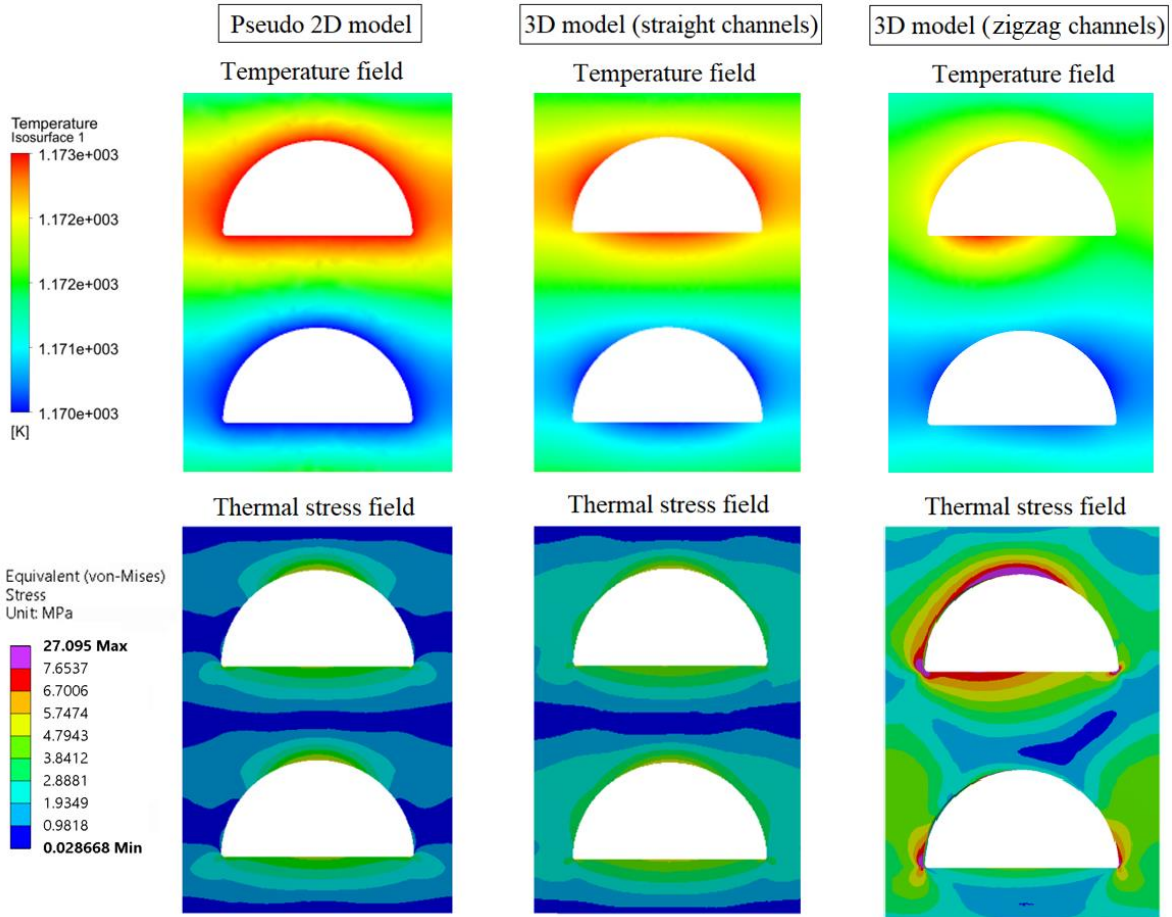
Figure 5.32: Influence of the temperature field in the solid wall on the thermal stress field with a maximum temperature gradient of 2.76 K.
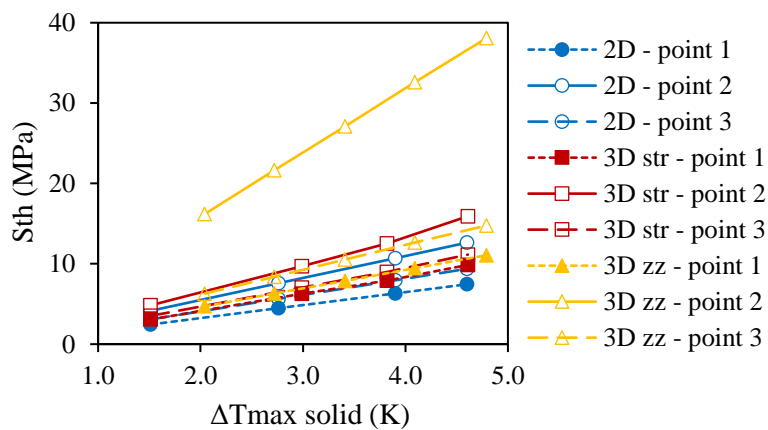
Figure 5.33: Influence of the maximum temperature gradient in the solid wall on the thermal stress value in the critical points of the hot side.

5.3.2. *Effect of zigzag dimensions*

The presence of the non-uniform temperature field in the solid domain of the zigzag channel PCHE suggests that several factors can have an influence on the thermal stress field, such as the flow regime and the geometric design. The effect of the Reynolds number was investigated in design with $\alpha = 15°$ and $Br = 0.5$ mm. For this purpose, the temperature difference between fluids was fixed. The peak thermal stress was obtained while the Reynolds number was increased, as shown in Figure 5.34. As expected, the thermal stress increases with the temperature difference between the fluids. A great influence of the Reynolds number was evidenced with a power-law behavior. The increase of the Reynolds number creates more parabolic profiles of the velocity and thermal boundary layers, and therefore, the temperature gradient between the hot and cold channels walls decreases. However, the stagnation and the eddies' appearance increase the temperature gradient concentration after the bend. Thus, the heat exchanger working with a low Reynolds number is recommendable to reduce the peak thermal stress.
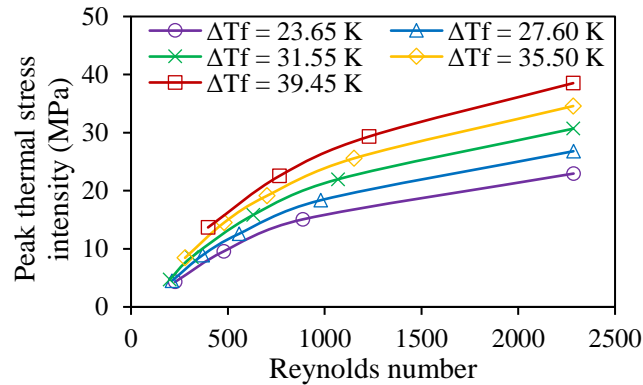
Figure 5.34: Peak thermal stress intensity after the hot channel bend at different Reynolds numbers.

The influence analysis of the zigzag angle and the bend radius variation on the thermal stress fields was carried out considering constant temperature difference between fluids of 27.6 K and a Reynolds number of 1400. Figures 5.35, 5.36, and 5.37 present the bottom view of the temperature and thermal stress fields of the hot central channel with zigzag angles of 15°, 30°, and 45°, respectively. The temperature concentration after the bend caused the highest temperature gradient and peak stress at the tips. Figure 5.35 shows the reduction of the temperature and stress concentrations when the bend radius is increased from 0.5 mm to 6 mm with $\alpha = 15°$, as a result of the smoother change of the flow direction. When the zigzag angle was increased to 30°, a notable temperature concentration increment after the bend and the reduction of that with the bend radius was obtained. Similar temperature field in a zigzag bend with $\alpha = 30°$ and $Br = 0.05$ mm was presented by Ma et al. in a full zigzag channel model, which verifies the validity to use a reduced model with a single zigzag bend in the current study. The reduction of the peak thermal stress with the bend radius was more significant at higher zigzag angles. This effect is mainly observed in Figure 5.37 with $\alpha = 45°$, where the fluid flow has a perpendicular change of direction. There was no presence of stress concentration at the center of the bend, even with the almost sharp-shape of the bend. It demonstrates that there is no thermal stress concentration in the flow direction because the temperature gradient in this direction is negligible in comparison with the gradient in the cross-sectional directions.
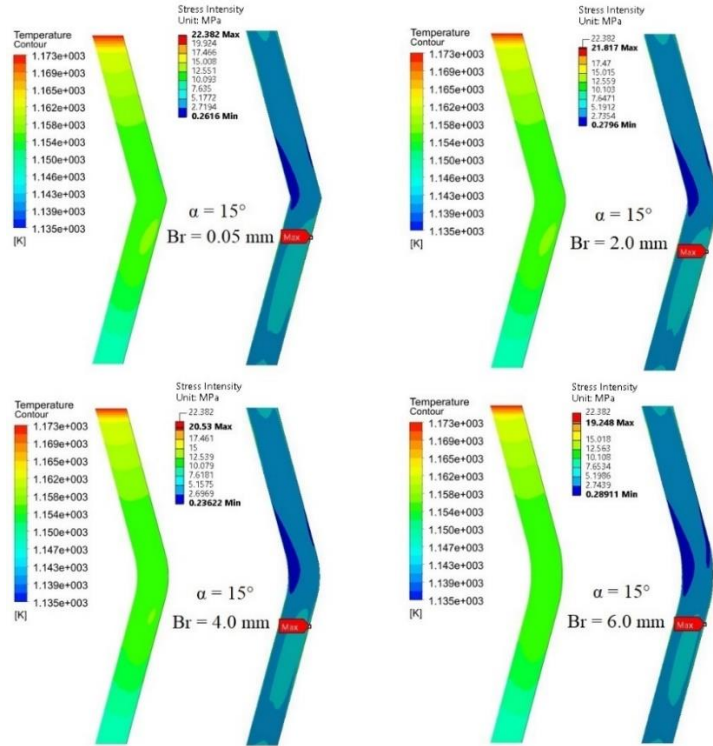
Figure 5.35: Temperature contours and thermal stress intensity fields in the hot central channel for different bend radius with α = 15°.
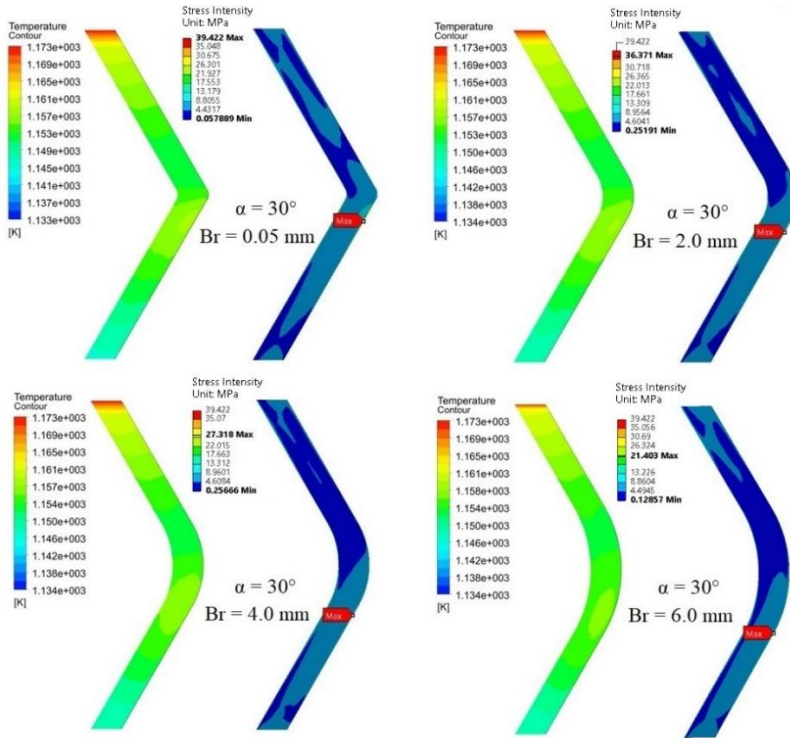
Figure 5.36: Temperature contours and thermal stress intensity fields in the hot central channel for different bend radius with α = 30°.
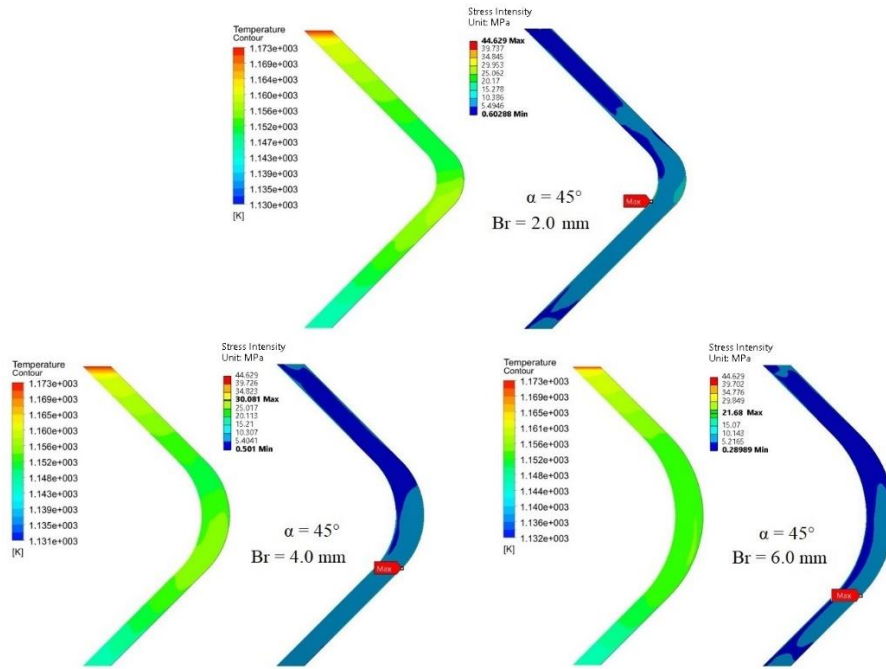
Figure 5.37: Temperature contours and thermal stress intensity fields in the hot central channel for different bend radius with α = 45°.

The peak value of the thermal stress after the bend as a function of the bend radius was plotted in Figure 5.38 for the three zigzag angles. The thermal stress decreased from 22.38 MPa to 19.25 MPa when the bend radius was increased from 0.5 mm to 6 mm with $\alpha = 15°$, which represents 14%. However, the peak stress had a decrease of 45.7% from 39.42 MPa to 21.4 MPa with $\alpha = 30°$, although most of this was reached up to $Br = 4$ mm. When the zigzag angle was 45°, the increase of the bend radius from 2 mm to 6 mm caused a reduction of 51.4% of the peak thermal stress. The peak stress after the bend with design dimensions of $\alpha = 45°$ and $Br = 6$ mm was near to the values obtained with $\alpha = 15°$.
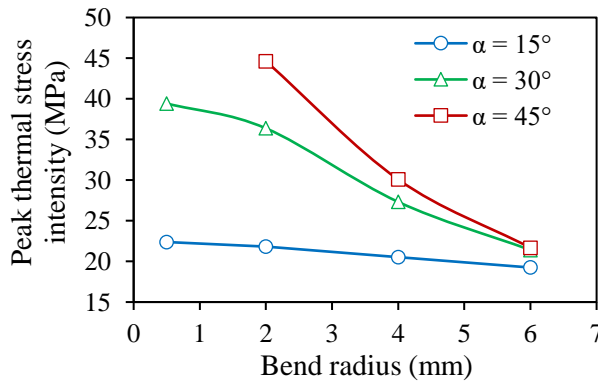
Figure 5.38: Maximum value of the thermal stress intensity after bends in the flow direction for different zigzag angles when $\Delta T_f = 26.7$ K.

120

The primary stresses were calculated considering the internal pressures of the fluids. The pressure drop in the PCHE channel is relatively negligible in comparison with the gauge pressure of the fluid. Then, the mechanical stress field has not much change in the cross-sections of the PCHE and it is very similar for all design with different zigzag dimensions considered in this work. Two conditions of the internal pressures were considered: the first one with values of $P_c = 7.99$ MPa and $P_h = 7.73$ MPa corresponding to optimized conditions of the IHX considered in this work [60]; and the second one with values of $P_c = 2.5$ MPa and $P_h = 2.0$ MPa, which is near to the common pressure values in some helium test facilities [65][38][67]. Figure 5.39 shows the mechanical stress field in the central hot channel of the zigzag bend with $\alpha = 15°$ and $Br = 0.5$ mm, and the internal pressures of the optimized IHX. The stress contour is very similar in the flow direction. The local primary membrane stress can be obtained from the concentration zone at the tips. Both pressure conditions gave similar contours, although with different stress values.
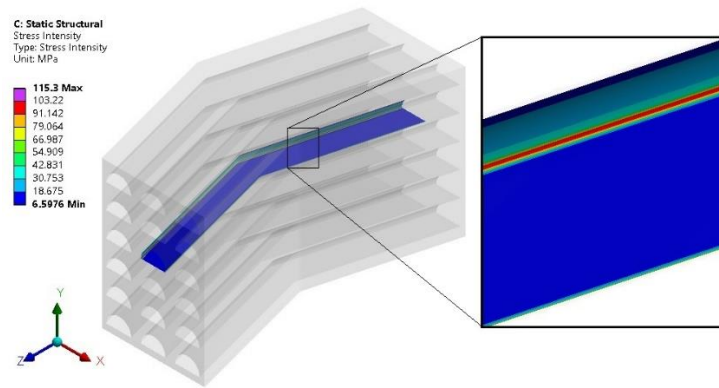
Figure 5.39: Detailed view of the mechanical stress intensity field on the wall in the central hot channels with Pc = 7.99 MPa and Ph = 7.73 MPa.

5.3.3. Assessment of the allowable designs

The values of the secondary stress and the peak stress were taken from the results of the thermal stress field, and the primary membrane stress and the local primary membrane stress were obtained from the results of the mechanical stress field. Table 5.2 shows the results of the Eq. 2.7 – 2.12 to be compared with the corresponding allowable stress values, which were taken from the Draft ASME BPVC for N06617 [91]. The time of service considered was 10,000 h with a maximum wall temperature of 1173 K. The comparisons were done with $S_{mt} = 12$ MPa, $1.5S_m = 114$ MPa, $S_t = 12$ MPa, $3S_{mt} = 36$ MPa and $2S_a = 30$ MPa. S_a was calculated as $S_a = 1.25S_t$ using the highest wall averaged temperature during the first cycle in a time of 10,000 h [91][79]. The values that exceed the allowable stresses are highlighted with red borders in Table 5.2. All zigzag design overcomes the allowable stress considering P_m and $P_L + P_b/K_t$ under the highest pressures conditions, although the $P_L + P_b$ values are lower than $1.5S_m$ using Eq. 2.8. These designs are inside the allowable ranges if 1 h of time of service is considered. The primary membrane stress is in the allowable ranges with the lowest pressures and the value of $P_m + P_b + Q_m + Q_b$ is lower than 36 MPa. However, the peak of the secondary stress causes that several designs could fail under fatigue conditions.

The concentration of the local primary stress under laboratory conditions was considered as secondary stress because higher values of this stress are allowable [76].

Table 5.2: Results comparison of the allowable stresses for several designs with the Level A Service Loading limits.

Design		$P_c = 7.99$ MPa and $P_h = 7.73$ MPa				$P_c = 2.5$ MPa and $P_h = 2.0$ MPa		
α	Br (mm)	P_m	$P_L + P_b/K_t$	$P_m + P_b + Q_m + Q_b$	$P_m + P_b + Q_m + Q_b + F$	P_m	$P_m + P_b + Q_m + Q_b$	$P_m + P_b + Q_m + Q_b + F$
15°	0.5	20.19	67.89	36.29	42.57	5.93	16.69	28.31
15°	2.0	20.19	67.89	36.17	42.01	5.93	16.57	27.75
15°	4.0	20.19	67.89	35.90	40.72	5.93	16.30	26.46
15°	6.0	20.19	67.89	35.57	39.44	5.93	15.97	25.18
30°	0.5	20.19	67.89	40.57	59.61	5.93	20.97	45.35
30°	2.0	20.19	67.89	39.82	56.56	5.93	20.22	42.30
30°	4.0	20.19	67.89	38.26	47.51	5.93	18.66	33.25
30°	6.0	20.19	67.89	37.51	41.59	5.93	17.91	27.33
45°	0.5	20.19	67.89	-	-	5.93	-	-
45°	2.0	20.19	67.89	41.64	64.82	5.93	22.04	50.56
45°	4.0	20.19	67.89	38.56	50.27	5.93	18.96	36.01
45°	6.0	20.19	67.89	38.15	41.87	5.93	18.55	27.61

The results show that the zigzag angle is the most essential dimension in the thermal-hydraulic and structural performances of the zigzag channel PCHE. However, the heat transfer is mainly enhanced up to $\alpha = 30°$ and the maximum thermal stress is drastically increased changing the zigzag angle from 15° to 30° when the bend radius is lower than 2 mm. The bend radius allows the reduction of the pressure drop and the peak thermal stress for zigzag angles higher than 15°. The straight channels PCHE could be a better option to be used as IHX in an HTGR plant, although the thermal-hydraulic performance is lower than that in the zigzag channels PCHE. Nevertheless, the operating conditions change under accident scenarios, and more dangerous levels of Service Loading than Level A could appear, with higher and variable temperature and pressure gradients. These kinds of loading must be analyzed in further works.

5.4. Chapter summary

The thermal and mechanical stress fields analysis of a PCHE in conditions of an IHX with fluids at very high temperatures has allowed determining several essential matters for the safe operation of the device. The thermal stress fields were proportional to the temperature gradient between the cold and hot channels. When the temperature gradient between channel walls was 25 K, the values of the thermal and mechanical stresses were similar. The temperature gradient between channel walls was quite lower than that between fluids. The flow configuration as counter-flow is recommended to reduce the temperature gradient in the cross-section planes.

All cross-sectional dimensions except for the rounded tip radius produced opposite effects on the thermal and mechanical stresses at the tips. The ridge thickness increased the temperature gradient between adjacent

channels with the same temperature, which caused the appearance of biaxial loadings and the equivalent thermal stress increases at the tips. The rounded tip radius increment reduced the stress concentration at this critical point. The total stress at the tips was also reduced with the roundness due to the separation of the critical points for the thermal and mechanical stresses. Therefore, a better distribution of the stress field with a flatter shape in the critical zone was found. The thermal stress was sensitive to the channel configurations change, and the reference design (type A) and type C are recommended. A more safe operation of the PCHE can be reached with a little temperature gradient and r/D higher than 0.04. The plastic strain was strongly dependent on the temperature and the time of service. Considering the roundness at the tips decreases the strain peak value in these regions.

The requirement of the FSI analysis was evidenced for the thermal stress calculation in a zigzag bend domain of the PCHE. The velocity and temperature contours of the fluids showed concentration regions after the bend in the flow direction. Although the temperature gradient in the channel walls was relatively low, the thermal stress concentration after the bend created high stress level in comparison with that in straight channel PCHE. Flow regimes with low Reynolds numbers are suggested in the zigzag channel PCHE to decrease the temperature concentration effect after the bend in the flow direction. The bend radius showed a great impact when the zigzag angle is increased due to the smooth change of the flow direction. All design had stresses higher than allowable stresses under IHX condition, but most of them can be safe under low pressures conditions.

6. CONCLUSIONS AND FUTURE WORK

The functioning of the IHX in an HTGR plant is essential for the safety and efficient operation of the system. In the current research, the favorable behavior of the PCHE in terms of heat transfer and compactness was demonstrated for this application, and the thermal-hydraulic and structural performances of the PCHE under IHX conditions were analyzed through simulation tools.

The most important thermal-hydraulic results gave the following key contributions to the PCHE performance study:

I. Novel heat transfer correlations of the zigzag channel PCHE with helium fluids were developed through CFD simulations, which allow the precise calculation of the Nusselt number and the Fanning friction factor within wide ranges of the zigzag dimensions and the Reynolds number. The Nusselt number correlation was able to reach a very good accuracy within different geometric configurations, while the Fanning friction factor correlation was particularly precise when the design had a sharp-shape of the zigzag bends.

II. An optimization study of the zigzag channel PCHE was accomplished considering the simultaneous interaction of four geometric parameters: zigzag pitch length, zigzag angle, bend radius, and zigzag phase-shift. The zigzag angle was found as that with the greatest influence on the heat transfer coefficient and the friction losses, which reaches 81.13% and 60.96%, respectively, considering the four geometric parameters. For angles higher than 30°, the friction losses are greatly increased with a little enhance of the heat transfer. The bend radius showed a great impact on the pressure drop when the zigzag angle is increased due to the removal of reverse flow zones.

III. Two optimum designs based on the *NPS* results were proposed to reach the maximum Nusselt number and the minimum Fanning friction factor. Designs with zigzag angles up to 30° and round-shape of the zigzag bend were recommended considering the *JF* factor calculation. The optimization methodology based on the total cost minimization found that a design with $\alpha = 45°$, $D = 1.5$ mm, $l_Z = 9.225$ mm, $Br = 6.0$ mm, $Re_c = 572$ and $Re_h = 702$ offers the lowest total cost.

Otherwise, the structural analysis of the PCHE under high temperature conditions allowed to find the following conclusions:

IV. The rounded tip radius was found as a key parameter to avoid the extreme values of both thermal and mechanical stresses at the tips. The ridge and plate thicknesses increment produced mechanical stress reduction, but they increased the thermal stress at the tips. In those cases, the mechanical stress reduction could be preferable as primary stress. Allowable ranges of the cross-sectional dimensions with the thermal gradient were proposed for different times of service.

V. The mechanical stress presented low variation with the zigzag dimensions in the reduced 3D model of a zigzag bend, while the thermal stress was strongly influenced by those parameters and by the flow regime. The zigzag angle increase carried out the stagnation of the fluid after the bend, and there was the peak stress because of temperature concentration. The temperature concentration and

the peak stress value increased with the Reynolds number. The roundness of the zigzag bend was crucial to reduce that problem when the zigzag angle is increased.

VI.   The study of the cross-sectional dimensions' influence on the thermal and mechanical stresses in the PCHE structure using a pseudo-2D FEA model with constant wall temperature was particularly accurate for straight channel configuration. The importance of using a 3D model with the fluid-structure interaction consideration to obtain the thermal stress field in a zigzag channel PCHE was evidenced.

VII.   The ASME BPVC, Section III, was used to assess the compliance of its requirements in the reduced 3D model of a zigzag bend. The corresponding allowable stresses were not fulfilled considering the operating conditions of an IHX of an HTGR plant and 10,000 h as the time of service. However, several designs satisfied the allowable stresses under facility test conditions.

Furthermore, the following recommendations can be offered for the operating conditions of the PCHE as IHX in an HTGR plant:

VIII.   Counter-flow configurations should be used because of the temperature gradient in the solid domain is reduced throughout the device, and thus, the thermal stress decreases.

IX.   The laminar regimes of the fluid flows through PCHE with low Reynolds numbers are preferable because they allow a good heat transfer with a moderate pressure drop, while the thermal stress could be reduced in the zigzag channels.

There are some possible future works about the PCHE use in the NGNP that are recommended by the author based on the current research results, such as:

i.   The proposed heat transfer correlations can be only used in ducts with fluid flows with Prandtl numbers around 0.67, the value of helium at the studied conditions. However, the power plants based on VHTR can include fluids as supercritical CO_2, sodium, or molten salts. Therefore, including the Prandtl number in the proposed correlations could be very useful in the design calculations of the PCHE in the high temperature nuclear industry.

ii.   The analysis of the fluid-structure interaction in this research considered one-way simulation, where CFD results were used to calculate the stress fields. But the solid structure deformation can affect the exactness of the heat transfer correlations, thus, two-ways simulations could be important to obtain more accurate correlations.

iii.   The FEA simulation results of the zigzag channel PCHE coupled to an advanced method as artificial neural networks could be applied to predict the value and the location of the peak thermal stress in the zigzag channels PCHE knowing the channel inlets parameter, the geometric design, and the material properties.

iv.   Some alternative designs of the PCHE are proposed in the open literature, which usually offer heat transfer improvements with friction loss penalties. However, design modifications also affect stress fields. The structural analysis of these designs using reduced 2D or 3D models developed by FEA techniques could allow to assess their safe operation.

APPENDICES

Appendix A

Appendix A presents the thermal design calculation procedure used in Section 1.4 and Subsection 4.3.5, and the heat transfer correlations of the heat exchanger types considered in Section 1.4. In this work, the thermal duty, the temperatures in the inlets and the outlets of both cold and hot side, and the pressure of the fluids, are known parameters. The fluid properties such as viscosity, thermal conductivity, and density are obtained using equations of Table 3.3 for the mean temperature of the fluids in each side. The mean temperature is the average between the inlet and outlet values. The cross-sectional dimensions of the ducts are considered constant.

The log mean temperature difference was computed considering a counter-flow arrangement as shown Eq. 1.5. The Reynolds number is defined and changed in different ranges depending on the heat exchanger type. Then, the mass flow per duct is calculated by Eq. A.1.

$$\dot{m} = \frac{Re\ \mu\ A_c}{D_h} \qquad (A.1)$$

The number of channels or tubes (N) is reached as shown Eq. A.2.

$$N = \frac{q_t}{\dot{m}c_p(T_o - T_i)} \qquad (A.2)$$

where q_t is the thermal duty of the heat exchanger.

The Nusselt number is computed by correlations for each heat exchanger type. Those used in Section 1.4 are presented in Table A1, while the proposed ones in this research were employed in Subsection 4.3.5.

Thus, the local heat transfer coefficients are calculated by Eq. A.3 and the overall heat transfer coefficient is computed by Eq. 1.6.

$$h = \frac{k\ Nu}{D_h} \qquad (A.2)$$

The overall heat transfer coefficient is achieved by Eq. 1.6. Then, the heat transfer area and the flow length are obtained as shown Eq. A.3 and A.4.
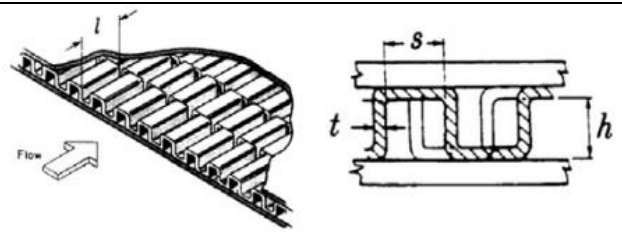
$$A_s = \frac{q_t}{U\ \Delta T_{ml}} \qquad (A.3)$$

$$L_f = \frac{A_s}{P_{cs}N} \qquad (A.4)$$

where L_f is the flow length. The core volume calculation is possible knowing this value and the cross-sectional dimensions.

Table A 1: Heat transfer correlations used in the thermal design calculations of several heat exchanger types.

Type	Correlations		Ref.
Double pipe heat exchanger	$Nu = 4.36$ $Re \leq 2300$ $Nu = \dfrac{\left(\frac{f}{2}\right)(Re - 1000)Pr}{1 + 12.7\left(\frac{f}{2}\right)^{0.5}\left(Pr^{\frac{2}{3}} - 1\right)}$ $3000 \leq Re \leq 5 \times 10^6$	$f \times Re = 16$ $Re \leq 2300$ $f = (1.58 \ln Re - 3.28)^{-2}$ $3000 \leq Re \leq 5 \times 10^6$	[15]
Shell and tube heat exchanger	Shell side: $Nu = 0.36 \times Re^{0.55}Pr^{0.5}\left(\dfrac{\mu}{\mu_{tube}}\right)^{0.14}$ $2000 \leq Re \leq 10^6$ Tube side: $Nu = 4.36$ $Re \leq 2300$ $Nu = \dfrac{\left(\frac{f}{2}\right)(Re - 1000)Pr}{1 + 12.7\left(\frac{f}{2}\right)^{0.5}\left(Pr^{\frac{2}{3}} - 1\right)}$ $3000 \leq Re \leq 5 \times 10^6$	Shell side: Friction factor graphically obtained from [17] Tube side: $f \times Re = 16$ $Re \leq 2300$ $f = (1.58 \ln Re - 3.28)^{-2}$ $3000 \leq Re \leq 5 \times 10^6$	[15] [17]
OSFHE	 $Nu = 0.6522\, Re^{-0.5403}\left(\dfrac{s}{h}\right)^{-0.1541}\left(\dfrac{t}{l}\right)^{0.1499}\left(\dfrac{t}{s}\right)^{-0.0678}$ $\times \left[1 + 5.269 \times 10^{-5}Re^{1.34}\left(\dfrac{s}{h}\right)^{0.504}\left(\dfrac{t}{l}\right)^{0.456}\left(\dfrac{t}{s}\right)^{-1.055}\right]^{0.1} RePr^{1/3}$ $f = 9.6243\, Re^{-0.7422}\left(\dfrac{s}{h}\right)^{-0.1856}\left(\dfrac{t}{l}\right)^{0.3053}\left(\dfrac{t}{s}\right)^{-0.2659}$ $\times \left[1 + 7.669 \times\times 10^{-8}Re^{4.429}\left(\dfrac{s}{h}\right)^{0.92}\left(\dfrac{t}{l}\right)^{3.767}\left(\dfrac{t}{s}\right)^{0.236}\right]^{0.1}$ $120 < Re\ 3000, \quad 0.5 < Pr < 15, \quad 0.646 < D_h < 3.414$		[121] [40]

Straight channel PCHE	$Nu = 4.089$ $Re \leq 1200$ $Nu = 0.01352 \times Re^{0.80058}$ $1200 \leq Re \leq 1850$ $Nu = 3.6361 \times 10^{-4} \times Re^{1.2804}$ $1850 < Re \leq 2900$	$f \times Re = 15.78$ $Re \leq 2300$ $f = \dfrac{1}{4}\left(\dfrac{1}{1.8 \log Re - 1.5}\right)^2$ $2300 \leq Re \leq 5 \times 10^6$	[63] [65] [26]
Zigzag channel PCHE	$Nu = 4.065 + 0.00305 \times Re$ $350 < Re < 800, \quad Pr = 0.66$ $Nu = 0.05516 \times Re^{0.69195}$ $1400 \leq Re \leq 2200$ $Nu = 0.09221 \times Re^{0.62507}$ $2200 < Re \leq 3558$	$f \times Re = 16.51 + 0.01627 \times Re$ $350 < Re < 1200$ $f = \dfrac{17.639}{Re^{0.8861}}$ $1400 \leq Re \leq 2200$ $f = 0.019044$ $2200 < Re \leq 3558$	[38] [39]

Appendix B

In this appendix, the top views of the geometries of the sixteen cases considered in the thermal-hydraulic and structural performance analysis of the study of the zigzag dimensions are presented. Figure B 1 displays the sixteen designs with different zigzag angles, zigzag pitch length, bend radius, and zigzag phase-shift. Specifications of these designs were determined according to the orthogonal array distribution in Table 3.8.
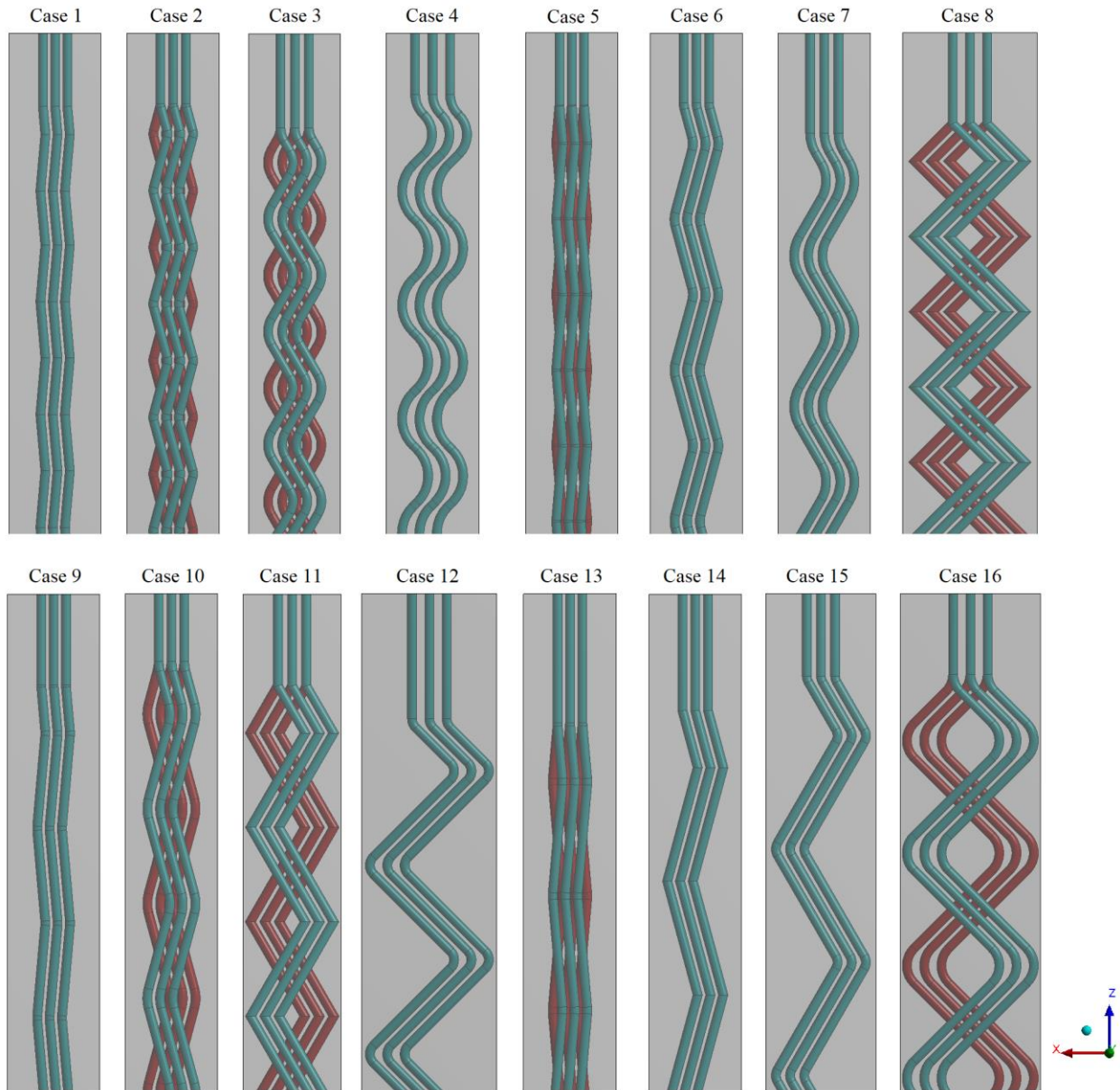
Figure B 1: Top view of the sixteen designs developed according to the orthogonal array presented in Table 3.8.

Appendix C

The variation of the Nusselt number and the Fanning friction factor by case, respectively, is presented in Figures C1 and C2 for a wide range of the Reynolds number.
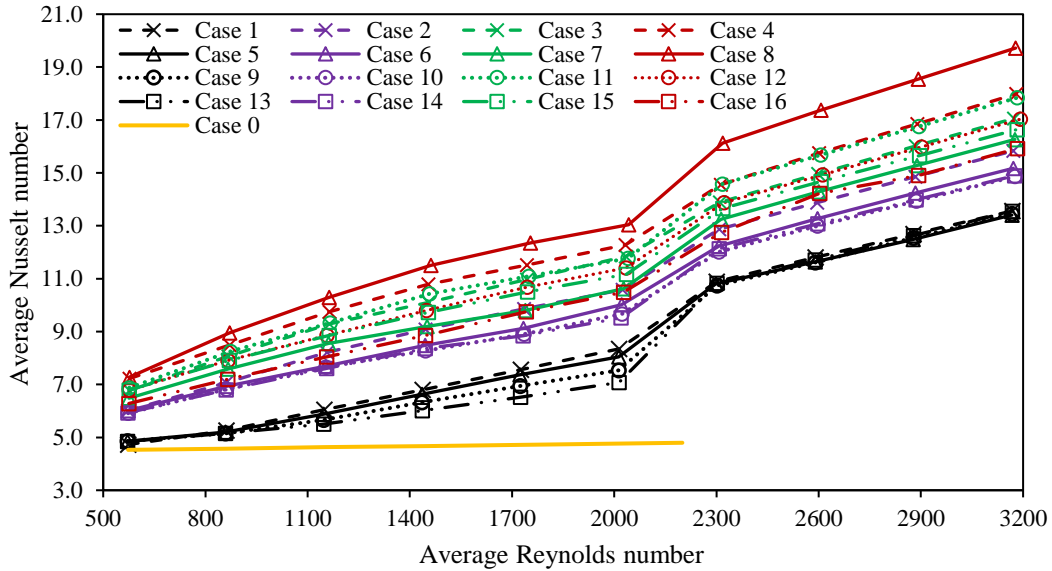
Figure C 1: Averaged Nusselt number vs averaged Reynolds number between cold and hot channels for 16 cases. Case 0 corresponds to the straight channel PCHE.
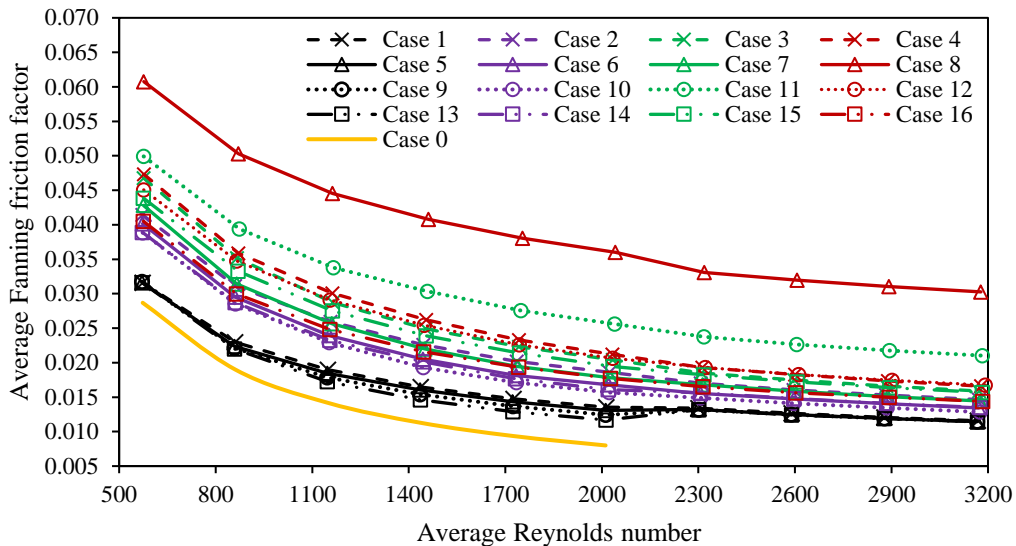
Figure C 2: Averaged Fanning friction factor vs averaged Reynolds number between cold and hot channels for 16 cases. Case 0 corresponds to the straight channel PCHE.

131

Appendix D

This appendix shows tables of Noise Performance Statistic (NPS) for each Reynolds number considered in the thermal-hydraulic study of the zigzag channel PCHE. The optimum levels by parameter are highlighted in bold.

Table D 1: Noise performance statistic of Nusselt number by level of four geometric parameters for Re = 864.

Level	l_Z/D_h	α	Br/D_h	λ/l_Z
1	**17.032**	14.304	**17.111**	16.716
2	16.939	16.78	16.804	**16.918**
3	16.802	18.006	16.582	-
4	16.496	**18.179**	16.771	-
Maximum difference	0.535	3.875	0.529	0.202
Contribution ratio (%)	10.41	75.37	10.29	3.93

Table D 2: Noise performance statistic of friction factor by level of the geometric parameters for Re = 864.

Level	l_Z/D_h	α	Br/D_h	λ/l_Z
1	30.224	**33.011**	29.418	**30.629**
2	29.909	30.616	30.473	30.101
3	30.317	29.200	**30.812**	-
4	**31.009**	28.632	30.757	-
Maximum difference	1.100	4.380	1.394	0.528
Contribution ratio (%)	14.86	59.17	18.83	7.14

Table D 3: Noise performance statistic of Nusselt number by level of four geometric parameters for Re = 1156.

Level	l_Z/D_h	α	Br/D_h	λ/l_Z
1	**18.263**	15.223	**18.223**	17.762
2	17.999	17.831	17.888	**17.940**
3	17.768	19.080	17.564	-
4	17.374	**19.271**	17.728	-
Maximum difference	0.889	4.048	0.659	0.179
Contribution ratio (%)	15.40	70.09	11.42	3.09

Table D 4: Noise performance statistic of Fanning friction factor by level of the geometric parameters for Re = 1156.

Level	l_Z/D_h	α	Br/D_h	λ/l_Z
1	31.859	**34.837**	30.891	**32.306**
2	31.484	32.401	32.083	31.763
3	31.981	30.825	**32.582**	-
4	**32.815**	30.075	**32.582**	-
Maximum difference	1.331	4.762	1.691	0.543
Contribution ratio (%)	15.98	57.19	20.31	6.52

Table D 5: Noise performance statistic of Nusselt number by level of four geometric parameters for Re = 1447.

Level	l_Z/D_h	α	Br/D_h	λ/l_Z
1	**19.140**	16.170	**19.167**	18.610
2	18.869	18.630	18.795	**18.804**
3	18.640	19.868	18.403	-
4	18.178	**20.159**	18.463	-
Maximum difference	0.962	3.989	0.764	0.195
Contribution ratio (%)	16.27	67.50	12.93	3.29

Table D 6: Noise performance statistic of Fanning friction factor by level of the geometric parameters for Re = 1447.

Level	l_Z/D_h	α	Br/D_h	λ/l_Z
1	33.077	**36.126**	31.938	**33.561**
2	32.651	33.728	33.287	32.950
3	33.196	32.007	33.851	-
4	**34.098**	31.161	**33.945**	-
Maximum difference	1.447	4.965	2.007	0.610
Contribution ratio (%)	16.02	54.99	22.23	6.76

Table D 7: Noise performance statistic of Nusselt number by level of four geometric parameters for Re = 1600.

Level	l_Z/D_h	α	Br/D_h	λ/l_Z
1	**19.869**	17.004	**19.808**	19.309
2	19.547	19.248	19.552	**19.486**
3	19.320	20.486	19.153	-
4	18.854	**20.852**	19.077	-
Maximum difference	1.015	3.847	0.730	0.177
Contribution ratio (%)	17.59	66.69	12.66	3.07

Table D 8: Noise performance statistic of Fanning friction factor by level of the geometric parameters for Re = 1600.

Level	l_Z/D_h	α	Br/D_h	λ/l_Z
1	34.050	**37.137**	32.818	**34.554**
2	33.574	34.780	34.266	33.913
3	34.184	32.962	34.851	-
4	**35.127**	32.057	**35.000**	-
Maximum difference	1.554	5.080	2.181	0.641
Contribution ratio (%)	16.43	53.72	23.07	6.78

Table D 9: Noise performance statistic of Nusselt number by level of four geometric parameters for Re = 2026.

Level	l_Z/D_h	α	Br/D_h	λ/l_Z
1	**20.543**	17.769	**20.429**	19.985
2	20.237	19.947	20.176	**20.123**
3	19.951	21.089	19.858	-
4	19.484	**21.409**	19.751	-
Maximum difference	1.059	3.640	0.678	0.138
Contribution ratio (%)	19.21	66.00	12.30	2.50

Table D 10: Noise performance statistic of Fanning friction factor by level of the geometric parameters for Re = 2026.

Level	l_Z/D_h	α	Br/D_h	λ/l_Z
1	34.818	**37.958**	33.489	**35.328**
2	34.256	35.524	35.059	34.654
3	34.938	33.710	35.613	-
4	**35.952**	32.773	**35.803**	-
Maximum difference	1.696	5.185	2.314	0.674
Contribution ratio (%)	17.19	52.54	23.45	6.83

Table D 11: Noise performance statistic of Nusselt number by level of four geometric parameters for Re = 2310.

Level	l_Z/D_h	α	Br/D_h	λ/l_Z
1	**22.261**	20.680	**22.461**	21.975
2	22.251	21.802	22.102	**22.220**
3	22.081	22.819	21.831	-
4	21.798	**23.091**	21.997	-
Maximum difference	0.462	2.411	0.630	0.245
Contribution ratio (%)	12.33	64.33	16.80	6.55

Table D 12: Noise performance statistic of Fanning friction factor by level of the geometric parameters for Re = 2310.

Level	l_Z/D_h	α	Br/D_h	λ/l_Z
1	35.450	**37.572**	33.917	**35.729**
2	34.714	36.050	35.513	34.990
3	35.236	34.358	**36.020**	-
4	**36.038**	33.458	35.987	-
Maximum difference	1.324	4.114	2.103	0.738
Contribution ratio (%)	15.99	49.69	25.40	8.92

Table D 13: Noise performance statistic of Nusselt number by level of four geometric parameters for Re = 2599.

Level	l_Z/D_h	α	Br/D_h	λ/l_Z
1	**22.933**	21.358	**23.119**	22.644
2	22.919	22.476	22.743	**22.878**
3	22.742	23.458	22.510	-
4	22.450	**23.751**	22.672	-
Maximum difference	0.483	2.393	0.610	0.234
Contribution ratio (%)	12.98	64.35	16.39	6.28

Table D 14: Noise performance statistic of Fanning friction factor by level of the geometric parameters for Re = 2599.

Level	l_Z/D_h	α	Br/D_h	λ/l_Z
1	35.936	**38.050**	34.341	**36.199**
2	35.149	36.529	35.997	35.449
3	35.687	34.831	**36.493**	-
4	**36.524**	33.887	36.466	-
Maximum difference	1.375	4.163	2.153	0.750
Contribution ratio (%)	16.29	49.32	25.50	8.89

Table D 15: Noise performance statistic of Nusselt number by level of four geometric parameters for Re = 2887.

Level	l_Z/D_h	α	Br/D_h	λ/l_Z
1	**23.531**	21.996	**23.705**	23.251
2	23.509	23.075	23.332	**23.482**
3	23.352	24.037	23.147	-
4	23.074	**24.358**	23.281	-
Maximum difference	0.457	2.362	0.558	0.230
Contribution ratio (%)	12.66	65.48	15.47	6.39

Table D 16: Noise performance statistic of Fanning friction factor by level of the geometric parameters for Re = 2887.

Level	l_Z/D_h	α	Br/D_h	λ/l_Z
1	36.375	**38.461**	34.704	**36.621**
2	35.529	36.952	36.420	35.836
3	36.083	35.243	**36.901**	-
4	**36.927**	34.257	36.890	-
Maximum difference	1.397	4.204	2.197	0.784
Contribution ratio (%)	16.28	48.98	25.60	9.14

Table D 17: Noise performance statistic of Nusselt number by level of four geometric parameters for Re = 3176.

Level	l_Z/D_h	α	Br/D_h	λ/l_Z
1	**24.093**	22.601	**24.258**	23.806
2	24.073	23.628	23.896	**24.055**
3	23.917	24.578	23.718	-
4	23.640	**24.915**	23.850	-
Maximum difference	0.453	2.314	0.539	0.249
Contribution ratio (%)	12.75	65.07	15.17	7.01

Table D 18: Noise performance statistic of Fanning friction factor by level of the geometric parameters for Re = 3176.

Level	l_Z/D_h	α	Br/D_h	λ/l_Z
1	36.750	**38.802**	35.013	**36.981**
2	35.863	37.337	36.781	36.185
3	36.428	35.606	37.267	-
4	**37.291**	34.587	**37.270**	-
Maximum difference	1.428	4.214	2.254	0.797
Contribution ratio (%)	16.43	48.48	25.93	9.16

Appendix E

The channel path considered in this appendix is shown in Figure A1. The thermal and mechanical stresses in the hot channel path of the twenty-five designs of Table 3.7 are presented in Figures E2, E3, E4, E5, and E6. The thermal stress was calculated with temperature gradients of 10 K and 5 K, while the mechanical stress was obtained considering P_c = 7.99 MPa and P_h = 7.73 MPa.
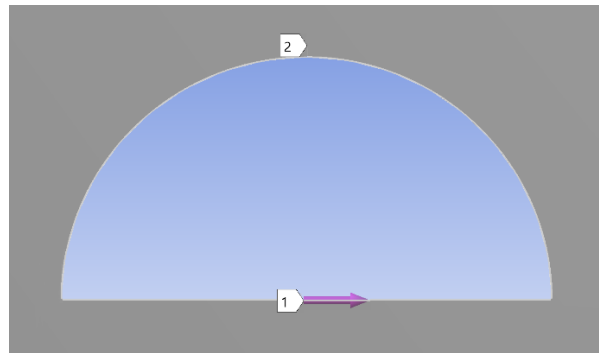
Figure E 3: Path to analyze the stress on the hot channel wall in this appendix.

Figure E 4: Thermal and mechanical stresses in the channel path of cases 1, 2, 3, 4, and 5.

137

Figure E 5: Thermal and mechanical stresses in the channel path of cases 6, 7, 8, 9, and 10.

Figure E 6: Thermal and mechanical stresses in the channel path of cases 11, 12, 13, 14, and 15.

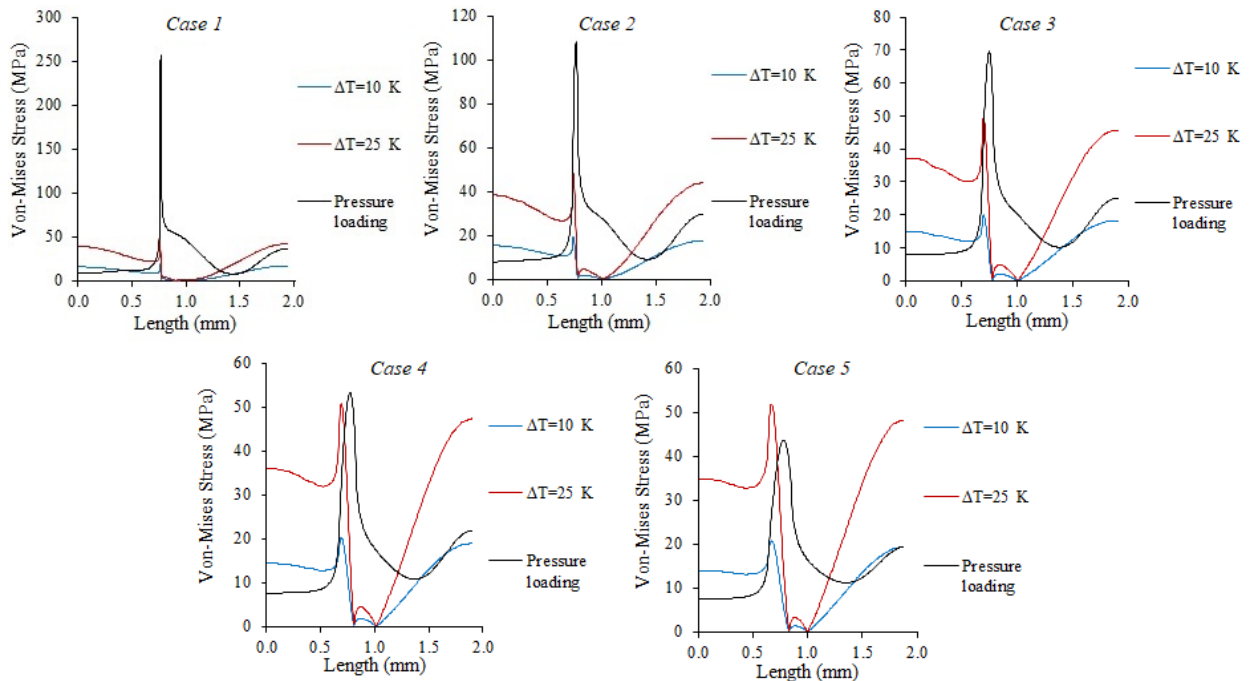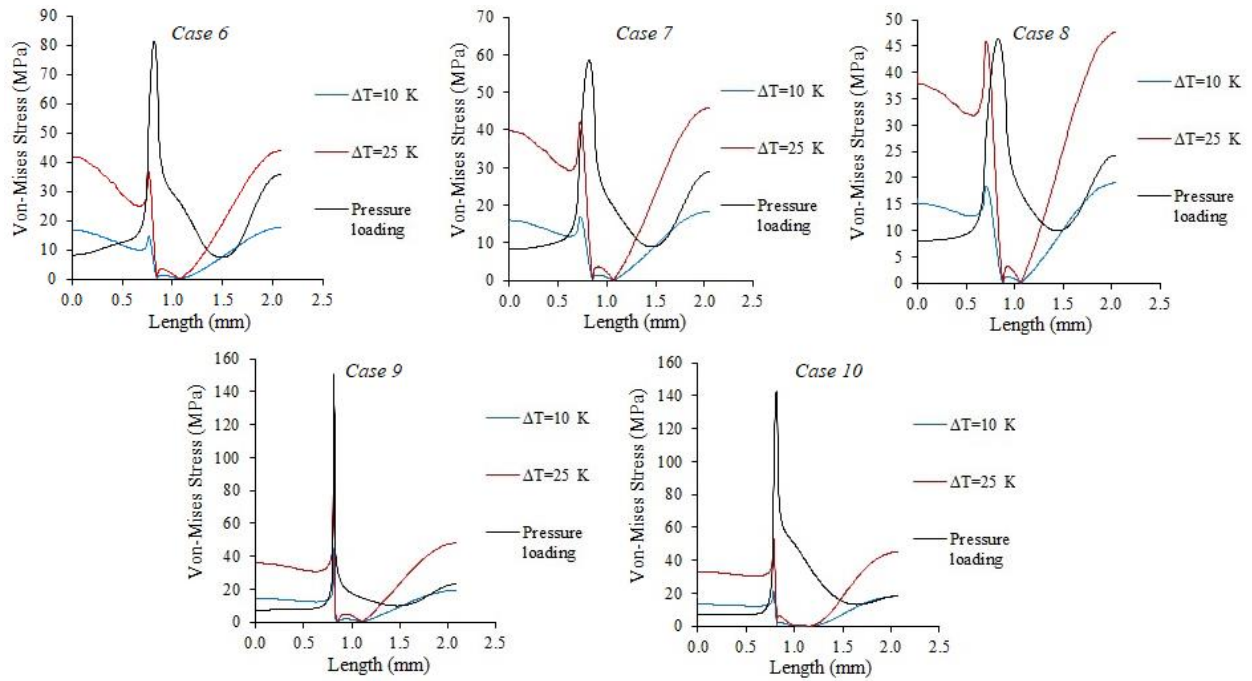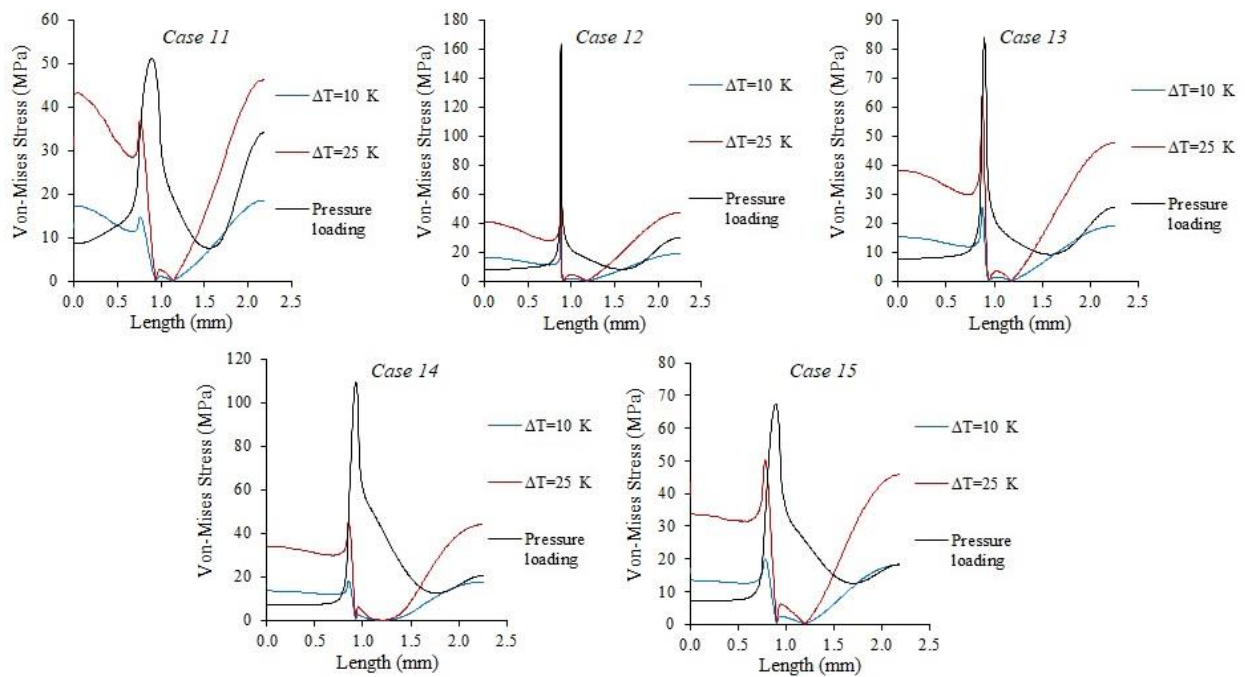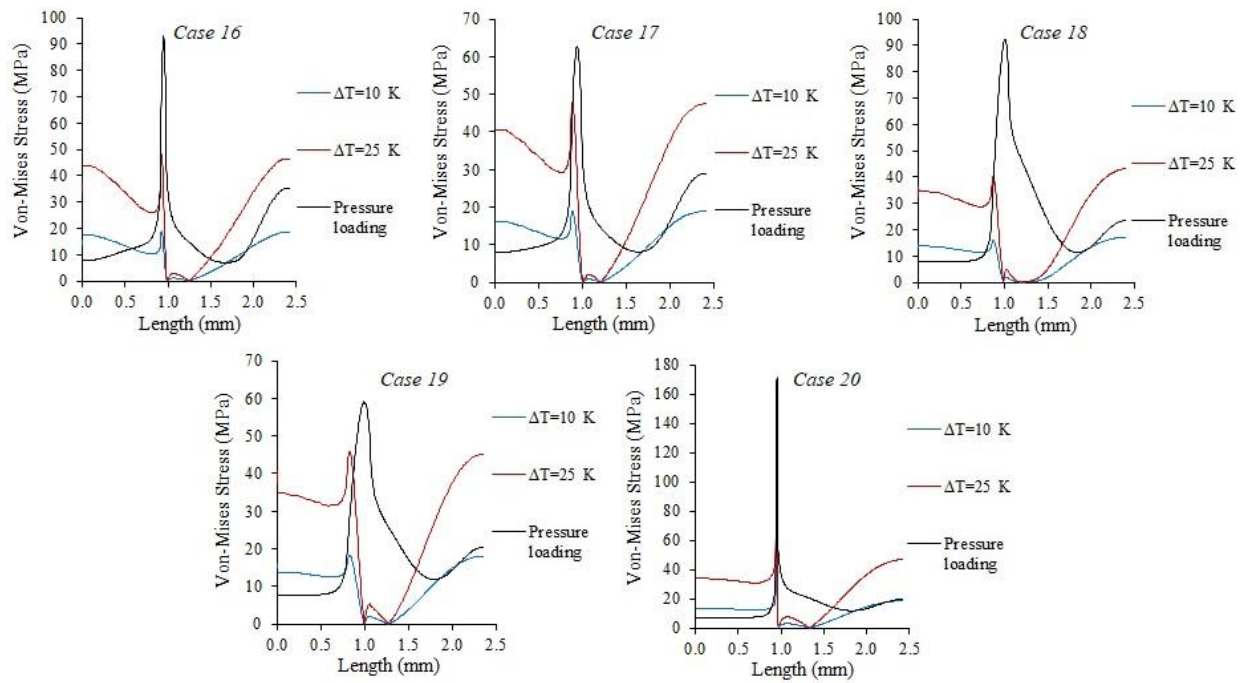*Figure E 7: Thermal and mechanical stresses in the channel path of cases 16, 17, 18, 19, and 20.*

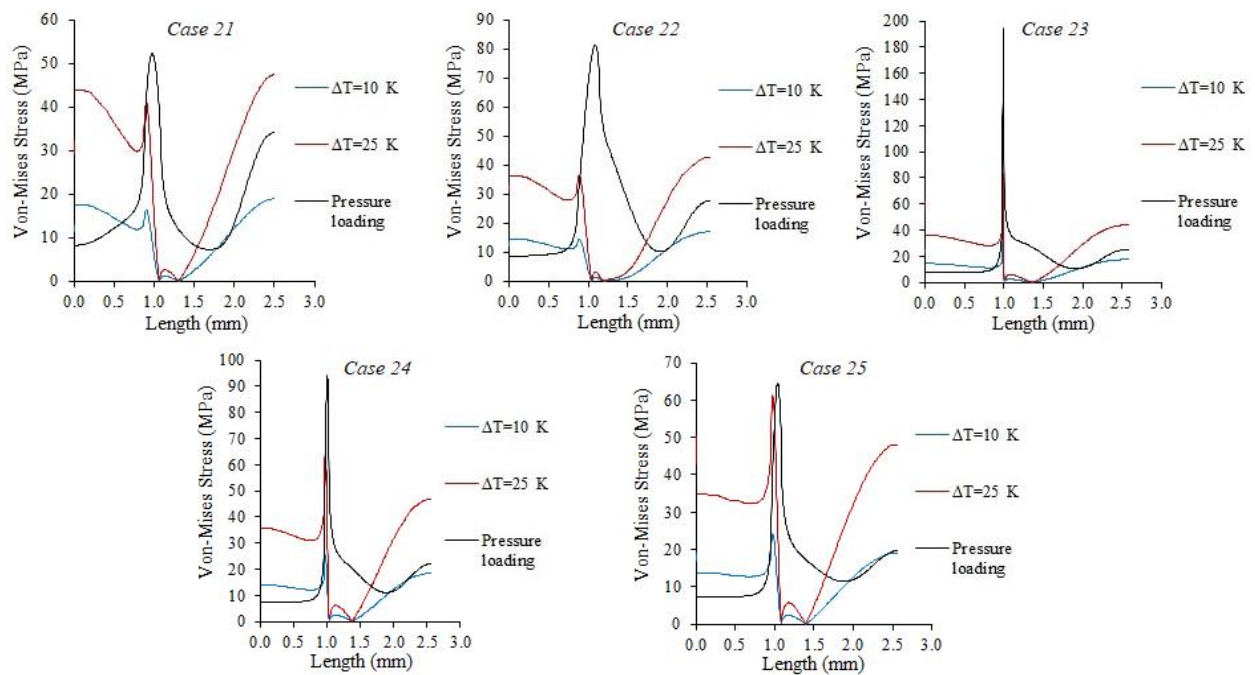*Figure E 8: Thermal and mechanical stresses in the channel path of cases 21, 22, 23, 24, and 25.*

REFERENCES

[1] D. G. Cacuci, *Handbook of Nuclear Engineering*. Springer, 2010.

[2] B. Zohuri, *Compact Heat Exchangers*. Springer, 2017.

[3] M. F. Hordeski, *Hydrogen and Fuel Cells: Advances in Transportation and Power*, vol. 53, no. 9. Taylor & Francis Group, 2008.

[4] X. L. Yan and R. Hino, *Nuclear Hydrogen Production*. Taylon and Francis Group, 2011.

[5] D. González Rodríguez, C. A. Brayner de Oliveira Lira, L. R. García Parra, C. R. García Hernández, and R. de la Torre Valdés, "Computational model of a sulfur-iodine thermochemical water splitting system coupled to a VHTR for nuclear hydrogen production," *Energy*, vol. 147, pp. 1165–1176, 2018.

[6] P. Sabharwall, S. M. Bragg-sitton, and C. Stoots, "Challenges in the development of high temperature reactors," *Energy Convers. Manag.*, vol. 74, pp. 574–581, 2013.

[7] C. F. Mcdonald, "Power conversion system considerations for a high efficiency small modular nuclear gas turbine combined cycle power plant concept," *Appl. Therm. Eng.*, vol. 73, no. 1, pp. 82–103, 2014.

[8] C. B. Davis, R. B. Barner, S. R. Sherman, and D. F. Wilson, "Thermal-Hydraulic Analyses of Heat Transfer Fluid Requirements and Characteristics for Coupling a Hydrogen Product Plant to a High-Temperature Nuclear Reactor," 2005.

[9] S. R. Sherman, R. Vilim, and W. J. Lee, "HyPEP FY-07 Annual Report : A Hydrogen Production Plant Efficiency Calculation Program," 2007.

[10] H. Ohashi and S. R. Sherman, "Tritium Movement and Accumulation in the NGNP System Interface and Hydrogen Plant," 2007.

[11] C. H. Oh and E. S. Kim, "Heat Exchanger Design Options and Tritium Transport Study for the VHTR System," 2008.

[12] S. K. Mylavarapu, X. Sun, R. N. Christensen, R. R. Unocic, R. E. Glosup, and M. W. Patterson, "Fabrication and design aspects of high-temperature compact diffusion bonded heat exchangers," *Nucl. Eng. Des.*, vol. 249, pp. 49–56, 2012.

[13] V. M. Mente, G. K. Pandey, I. Banerjee, S. A. Kumar, G. Padmakumar, and K. K. Rajan, "Experimental studies in water for safety grade decay heat removal of prototype fast breeder reactor," *Ann. Nucl. Energy*, vol. 65, pp. 114–121, 2014.

[14] S. J. Bae, J. Lee, Y. Ahn, and J. I. Lee, "Preliminary studies of compact Brayton cycle performance for Small Modular High Temperature Gas-cooled Reactor system," *Ann. Nucl. Energy*, vol. 75, pp.

11–19, 2015.

[15]   F. P. Incropera, D. P. DeWitt, T. L. Bergman, and A. S. Lavine, *Fundamentals of Heat and Mass Transfer*, 7th Editio. John Wiley & Sons, Inc. All, 2011.

[16]   M. Pavelka, V. Klika, P. Vágner, and F. Maršík, "Generalization of exergy analysis," *Appl. Energy*, vol. 137, pp. 158–172, 2015.

[17]   D. Kern, *Process Heat Transfer*, Internatio. McGraw-Hill, 1965.

[18]   Y. Inagaki, H. Koiso, H. Takumi, and I. Ioka, "Thermal hydraulic study on a high-temperature gas-gas heat exchanger with helically coiled tube bundles," *Nucl. Eng. Des.*, vol. 185, pp. 141–151, 1998.

[19]   Q. Li, G. Flamant, X. Yuan, P. Neveu, and L. Luo, "Compact heat exchangers: A review and future applications for a new generation of high temperature solar receivers," *Renew. Sustain. Energy Rev.*, vol. 15, pp. 4855–4875, 2011.

[20]   L. Wang, B. Sundén, and R. M. Manglik, *Plate Heat Exchangers: Design, Applications and Performance*. Southampton, UK: WIT Press, 2007.

[21]   D. Reay, *Learning from experiences with compact heat exchangers*. Netherlands: Center for the Analysis and Dissemination of Demonstrated Energy Technologies, 1999.

[22]   N. Bartel *et al.*, "Comparative analysis of compact heat exchangers for application as the intermediate heat exchanger for advanced nuclear reactors," *Ann. Nucl. Energy*, vol. 81, pp. 143–149, 2015.

[23]   W. Jiang, J. Gong, S. Tu, and H. Chen, "Modelling of temperature field and residual stress of vacuum brazing for stainless steel plate-fin structure," *J. Mater. Process. Technol.*, vol. 209, pp. 1105–1110, 2009.

[24]   W. Jiang, J. Gong, and S. T. Tu, "A study of the effect of filler metal thickness on tensile strength for a stainless steel plate-fin structure by experiment and finite element method," *Mater. Des.*, vol. 31, no. 5, pp. 2387–2396, 2010.

[25]   Heatric Inc., "Heatric," 2016. .

[26]   J. Figley, X. Sun, S. K. Mylavarapu, and B. Hajek, "Numerical study on thermal hydraulic performance of a Printed Circuit Heat Exchanger," *Prog. Nucl. Energy*, vol. 68, pp. 89–96, 2013.

[27]   Y. Hou and G. Tang, "Thermal-Hydraulic-Structural Analysis and Design Optimization for Micron-Sized Printed Circuit Heat Exchanger," *J. Therm. Sci.*, vol. 28, no. 2, pp. 252–261, 2019.

[28]   S. M. Lee and K. Y. Kim, "Comparative study on performance of a zigzag printed circuit heat exchanger with various channel shapes and configurations," *Heat Mass Transf. und Stoffuebertragung*, vol. 49, no. 7, pp. 1021–1028, 2013.

[29]   Y. Yang, H. Li, M. Yao, W. Gao, Y. Zhang, and L. Zhang, "Investigation on the effects of narrowed channel cross-sections on the heat transfer performance of a wavy-channeled PCHE," *Int. J. Heat Mass Transf.*, vol. 135, pp. 33–43, 2019.

[30]   S. J. Dewson and B. Thonon, "The development of high efficiency heat exchangers for helium gas cooled reactors," in *International Congress on Advances in Nuclear Power Plants ICAP03*, 2003, p. Paper No. 3213.

[31]   H. Cai, S. Liang, C. Guo, T. Wang, and Y. Zhu, "Numerical investigation on heat transfer of supercritical carbon dioxide in the microtube heat exchanger at low reynolds numbers," *Int. J. Heat Mass Transf.*, vol. 151, p. 119448, 2020.

[32]   R. E. Mizia, "Next Generation Nuclear Plant Intermediate Heat Exchanger Acquisition Strategy," 2008.

[33]   W. Kim, Y. Baik, S. Jeon, D. Jeon, and C. Byon, "A mathematical correlation for predicting the thermal performance of cross , parallel , and counterflow PCHEs," *Int. J. Heat Mass Transf.*, vol. 106, pp. 1294–1302, 2017.

[34]   F. Kawashima, T. Igari, Y. Miyoshi, Y. Kamito, and M. Tanihira, "High temperature strength and inelastic behavior of plate – fin structures for HTGR," *Nucl. Eng. Des.*, vol. 237, pp. 591–599, 2007.

[35]   W. Kim, S. Yin, W. Ryu, J. Chang, and S. Kim, "Tension and creep design stresses of the 'Hastelloy-X' alloy for high-temperature gas cooled reactors," *Mater. Sci. Eng. A*, vol. 484, pp. 495–497, 2008.

[36]   P. Sabharwall, D. E. Clark, R. E. Mizia, M. V. Glazoff, and M. G. McKellar, "Diffusion-welded microchannel heat exchanger for industrial processes," *J. Therm. Sci. Eng. Appl.*, vol. 5, no. 1, 2013.

[37]   Z. Zhao, X. Zhang, K. Zhao, P. Jiang, and Y. Chen, "Numerical investigation on heat transfer and flow characteristics of supercritical nitrogen in a straight channel of printed circuit heat exchanger," *Appl. Therm. Eng.*, vol. 126, pp. 717–729, 2017.

[38]   I. H. Kim, H. C. No, J. I. Lee, and B. G. Jeon, "Thermal hydraulic performance analysis of the printed circuit heat exchanger using a helium test facility and CFD simulations," *Nucl. Eng. Des.*, vol. 239, pp. 2399–2408, 2009.

[39]   M. Chen, X. Sun, R. N. Christensen, I. Skavdahl, and V. Utgikar, "Pressure drop and heat transfer characteristics of a high-temperature printed circuit heat exchanger," *Appl. Therm. Eng.*, vol. 108, pp. 1409–1417, 2016.

[40]   I. H. Kim, X. Zhang, R. Christensen, and X. Sun, "Design study and cost assessment of straight, zigzag, S-shape, and OSF PCHEs for a FLiNaK - SCO2 Secondary Heat Exchanger in FHRs," *Ann. Nucl. Energy*, vol. 94, pp. 129–137, 2016.

[41]   J. Gyu, T. Ho, H. Sun, J. Eun, and M. Hwan, "Optimization of airfoil-type PCHE for the recuperator of small scale brayton cycle by cost-based objective function," *Nucl. Eng. Des.*, vol. 298, pp. 192–

200, 2016.

[42]   W. Chu, X. Li, T. Ma, Y. Chen, and Q. Wang, "Study on hydraulic and thermal performance of printed circuit heat transfer surface with distributed airfoil fins," *Appl. Therm. Eng.*, vol. 114, pp. 1309–1318, 2017.

[43]   F. Chen, L. Zhang, X. Huai, J. Li, H. Zhang, and Z. Liu, "Comprehensive performance comparison of airfoil fin PCHEs with NACA 00XX series airfoil," *Nucl. Eng. Des.*, vol. 315, pp. 42–50, 2017.

[44]   S. H. Yoon, H. C. No, and G. B. Kang, "Assessment of straight, zigzag, S-shape, and airfoil PCHEs for intermediate heat exchangers of HTGRs and SFRs," *Nucl. Eng. Des.*, vol. 270, pp. 334–343, 2014.

[45]   T. L. Ngo, Y. Kato, K. Nikitin, and T. Ishizuka, "Heat transfer and pressure drop correlations of microchannel heat exchanger with S-shaped and zigzag fins for carbon dioxide cycles," *Exp. Therm. Fluid Sci.*, vol. 32, pp. 560–570, 2007.

[46]   Y. Baik, S. Jeon, B. Kim, D. Jeon, and C. Byon, "Heat transfer performance of wavy-channeled PCHEs and the effects of waviness factors," *Int. J. Heat Mass Transf.*, vol. 114, pp. 809–815, 2017.

[47]   Z. Wen, Y. Lv, Q. Li, and P. Zhou, "Numerical study on heat transfer behavior of wavy channel supercritical CO2 printed circuit heat exchangers with different amplitude and wavelength parameters," *Int. J. Heat Mass Transf.*, vol. 147, p. 118922, 2020.

[48]   S. Y. Lee, B. G. Park, and J. T. Chung, "Numerical studies on thermal hydraulic performance of zigzag-type printed circuit heat exchanger with inserted straight channels," *Appl. Therm. Eng.*, vol. 123, pp. 1434–1443, 2017.

[49]   Z. Zhao, Y. Zhou, X. Ma, X. Chen, S. Li, and S. Yang, "Effect of different zigzag channel shapes of PCHES on heat transfer performance of supercritical LNG," *Energies*, vol. 12, no. 11, 2019.

[50]   A. M. Aneesh, A. Sharma, A. Srivastava, and P. Chaudhury, "Effects of wavy channel configurations on thermal-hydraulic characteristics of Printed Circuit Heat Exchanger (PCHE)," *Int. J. Heat Mass Transf.*, vol. 118, pp. 304–315, 2018.

[51]   Q. Jing, Y. Xie, and D. Zhang, "Thermal hydraulic performance of printed circuit heat exchanger with various channel configurations and arc ribs for SCO2 Brayton cycle," *Int. J. Heat Mass Transf.*, vol. 150, p. 119272, 2020.

[52]   M. Saeed and M. Kim, "Thermal-hydraulic analysis of sinusoidal fin-based printed circuit heat exchangers for supercritical CO2 Brayton cycle," *Energy Convers. Manag.*, vol. 193, no. December 2018, pp. 124–139, 2019.

[53]   S. Lee, K. Kim, and S. Kim, "Multi-objective optimization of a double-faced type printed circuit heat exchanger," *Appl. Therm. Eng.*, vol. 60, no. 1–2, pp. 44–50, 2013.

[54] A. M. Aneesh, A. Sharma, A. Srivastava, K. N. Vyas, and P. Chaudhuri, "Thermal-hydraulic characteristics and performance of 3D straight channel based printed circuit heat exchanger," *Appl. Therm. Eng.*, vol. 98, pp. 474–482, 2016.

[55] J. Sung and J. Y. Lee, "Effect of tangled channels on the heat transfer in a printed circuit heat exchanger," *Int. J. Heat Mass Transf.*, vol. 115, pp. 647–656, 2017.

[56] A. C. Caputo, P. M. Pelagagge, and P. Salini, "Manufacturing cost model for heat exchangers optimization," *Appl. Therm. Eng.*, vol. 94, pp. 513–533, 2016.

[57] E. S. Kim, C. H. Oh, and S. Sherman, "Simplified optimum sizing and cost analysis for compact heat exchanger in VHTR," *Nucl. Eng. Des.*, vol. 238, pp. 2635–2647, 2008.

[58] I. H. Kim and H. C. No, "Physical model development and optimal design of PCHE for intermediate heat exchangers in HTGRs," *Nucl. Eng. Des.*, vol. 243, pp. 243–250, 2012.

[59] G. Koo, S. Lee, and K. Kim, "Shape optimization of inlet part of a printed circuit heat exchanger using surrogate modeling," *Appl. Therm. Eng.*, vol. 72, no. 1, pp. 90–96, 2014.

[60] C. Wang, R. G. Ballinger, and P. W. Staphle, "Design of a power conversion system for an indirect cycle, helium cooled pebble bed reactor," in *Proceedings of the HTR-2002*, 2002.

[61] H. H. Khan, A. M. Aneesh, A. Sharma, and A. Srivastava, "Thermal-hydraulic characteristics and performance of 3D wavy channel based printed circuit heat exchanger," *Appl. Therm. Eng.*, vol. 87, pp. 519–528, 2015.

[62] T. Ma, L. Li, X. Y. Xu, Y. T. Chen, and Q. W. Wang, "Study on local thermal–hydraulic performance and optimization of zigzag-type printed circuit heat exchanger at high temperature," *Energy Convers. Manag.*, vol. 104, pp. 55–66, 2015.

[63] J. E. Hesselgreaves, R. Law, and D. A. Reay, *Compact Heat Exchangers: Selection, Design and Operation*, Second Edi. Elsevier, 2017.

[64] T. Ma, W. Zhang, Y. Zhang, and T. Tang, "Multi-parameter sensitivity analysis and application research in the robust optimization design for complex nonlinear system," *Chinese J. Mech. Eng.*, vol. 28, no. 1, pp. 55–62, 2015.

[65] M. Chen, X. Sun, R. N. Christensen, S. Shi, I. Skavdahl, and V. Utgikar, "Experimental and numerical study of a printed circuit heat exchanger," *Ann. Nucl. Energy*, vol. 97, pp. 221–231, 2016.

[66] D. Kwon, L. Jin, W. Jung, and S. Jeong, "Experimental investigation of heat transfer coe ffi cient of mini-channel PCHE (printed circuit heat exchanger)," *Cryogenics (Guildf).*, vol. 92, no. March, pp. 41–49, 2018.

[67] S. K. Mylavarapu, X. Sun, R. E. Glosup, R. N. Christensen, and M. W. Patterson, "Thermal hydraulic performance testing of printed circuit heat exchangers in a high-temperature helium test

facility," *Appl. Therm. Eng.*, vol. 65, no. 1–2, pp. 605–614, 2014.

[68]   I. H. Kim and H. C. No, "Thermal hydraulic performance analysis of a printed circuit heat exchanger using a helium-water test loop and numerical simulations," *Appl. Therm. Eng.*, vol. 31, pp. 4064–4073, 2011.

[69]   I. H. Kim and H. C. No, "Thermal-hydraulic physical models for a Printed Circuit Heat Exchanger covering He , He-CO2 mixture, and water fluids using experimental data and CFD," *Exp. Therm. Fluid Sci.*, vol. 48, pp. 213–221, 2013.

[70]   S. Yoon, J. O. Brien, M. Chen, P. Sabharwall, and X. Sun, "Development and validation of Nusselt number and friction factor correlations for laminar flow in semi-circular zigzag channel of printed circuit heat exchanger," *Appl. Therm. Eng.*, vol. 123, pp. 1327–1344, 2017.

[71]   I. H. Kim and X. Sun, "CFD study and PCHE design for secondary heat exchangers with FLiNaK-Helium for SmAHTR," *Nucl. Eng. Des.*, vol. 270, pp. 325–333, 2014.

[72]   M. Y. Park, M. S. Song, and E. S. Kim, "Development of tritium permeation model for Printed Circuit Heat Exchanger," *Ann. Nucl. Energy*, vol. 98, pp. 166–177, 2016.

[73]   M. Chen, X. Sun, R. N. Christensen, I. Skavdahl, V. Utgikar, and P. Sabharwall, "Dynamic behavior of a high-temperature printed circuit heat exchanger: Numerical modeling and experimental investigation," *Appl. Therm. Eng.*, vol. 135, no. October 2017, pp. 246–256, 2018.

[74]   Q. Liu, L. Wang, and K. Fukuda, "Transient Convection Heat Transfer for Helium Gas at Various Flow Decay Times," *Appl. Therm. Eng.*, 2016.

[75]   P. Ravindran, P. Sabharwall, and M. A. Anderson, "Modeling a Printed Circuit Heat Exchanger with RELAP5-3D for the Next Generation Nuclear Plant," 2010.

[76]   D. R. Moss, "Stresses in Pressure Vessels," in *Pressure Vessel Design Manual*, 3rd ed., Gulf Professional Publishing, 2004, pp. 1–14.

[77]   *ASME Boiler and Pressure Vessel Code, Section VIII, Division 1: Rules for Construction of Pressure Vessels*. 2011.

[78]   *ASME Boiler and Pressure Vessel Code. Section III. Division 5*. 2019.

[79]   *ASME Boiler and Pressure Vessel Code. Section III. Division 1. Subsection NH*. ASME, 2015.

[80]   H. Shi, M. Li, W. Wang, Y. Qiu, and W. Tao, "Heat transfer and friction of molten salt and supercritical CO2 flowing in an airfoil channel of a printed circuit heat exchanger," *Int. J. Heat Mass Transf.*, vol. 150, p. 119006, 2020.

[81]   Y. Lee and J. I. Lee, "Structural assessment of intermediate printed circuit heat exchanger for sodium-cooled fast reactor with supercritical CO2 cycle," *Ann. Nucl. Energy*, vol. 73, pp. 84–95, 2014.

[82]   K. Bennett and Y. Chen, "One-way coupled three-dimensional fluid-structure interaction analysis of zigzag-channel supercritical CO2 printed circuit heat exchangers," *Nucl. Eng. Des.*, vol. 358, no. November 2019, p. 110434, 2020.

[83]   P. A. Stiopin, *Resistencia de Materiales*, Cuarta edi. Mir Moscú, 1985.

[84]   W. Kim, J. Park, and S. Hong, "Creep and Oxidation Behaviors of Alloy 617 in Air and Helium Environments at 1173 K," *Procedia Eng.*, vol. 55, pp. 819–822, 2013.

[85]   W. Kim, J. Park, I. M. W. Ekaputra, M. Kim, and Y. Kim, "Analysis of creep behavior of Alloy 617 for use of VHTR system," *Procedia Mater. Sci.*, vol. 3, pp. 1285–1290, 2014.

[86]   W. Kim, I. M. W. Ekaputra, J. Park, M. Kim, and Y. Kim, "Investigation of creep rupture properties in air and He environments of alloy 617 at 800 °C," *Nucl. Eng. Des.*, vol. 306, pp. 177–185, 2016.

[87]   M. Kolluri, P. Pierick, and T. Bakker, "Characterization of high temperature tensile and creep-fatigue properties of Alloy 800H for intermediate heat exchanger components of (V) HTRs," *Nucl. Eng. Des.*, vol. 284, pp. 38–49, 2015.

[88]   D. Kim, I. Sah, and C. Jang, "Effects of high temperature aging in an impure helium environment on low temperature embrittlement of Alloy 617 and Haynes 230," *J. Nucl. Mater.*, vol. 405, pp. 9–16, 2010.

[89]   H. Tung and J. F. Stubbins, "Incipient oxidation kinetics and residual stress of the oxide scale grown on Haynes 230 at high temperatures," *Mater. Sci. Eng. A*, vol. 538, pp. 1–6, 2012.

[90]   A. K. Roy, M. H. Hasan, and J. Pal, "Creep deformation of Alloys 617 and 276 at 750 - 950 °C," *Mater. Sci. Eng. A*, vol. 520, pp. 184–188, 2009.

[91]   J. K. Wright, "Draft ASME Boiler and Pressure Vessel Code Section III, Division 5, Section HB, Subsection B," 2015.

[92]   "Inconel Alloy 617," *Special Metals*. [Online]. Available: http://www.specialmetals.com/tech-center/alloys.html.

[93]   J. G. Yoon, H. W. Jeong, Y. S. Yoo, and H. U. Hong, "Influence of initial microstructure on creep deformation behaviors and fracture characteristics of Haynes 230 superalloy at 900 °C," *Mater. Charact.*, vol. 101, pp. 49–57, 2015.

[94]   C. Cabet and B. Duprey, "Long term oxidation resistance of alloys for gas-cooled reactors," *Nucl. Eng. Des.*, vol. 251, pp. 139–145, 2012.

[95]   J. K. Wright *et al.*, "Characterization of elevated temperature properties of heat exchanger and steam generator alloys," *Nucl. Eng. Des.*, vol. 251, pp. 252–260, 2012.

[96]   W. Kim, J. Park, and S. Hong, "Creep and Oxidation Behaviors of Alloy 617 in Air and Heliu um Environ nments at 1173 K," *Procedia Eng.*, vol. 55, pp. 819–822, 2013.

[97] H.-M. Tung, K. Mo, and J. F. Stubbins, "Biaxial thermal creep of Inconel 617 and Haynes 230 at 850 and 950 °C," *J. Nucl. Mater.*, vol. 447, pp. 28–37, 2014.

[98] H. Hogan, "New Material Finally Makes It Into the Almighty Nuclear Code," *INL Communications & Outreach*, 2020. [Online]. Available: https://inl.gov/article/a-new-material-expands-nuclear-operating-temperature/. [Accessed: 05-May-2020].

[99] W. Kim, J. Park, G. Lee, S. Hong, and Y. Kim, "Temperature effect on the creep behavior of alloy 617 in air and helium environments," *Nucl. Eng. Des.*, vol. 271, pp. 291–300, 2014.

[100] D. Kaoumi and K. Hrutkay, "Tensile deformation behavior and microstructure evolution of Ni-based superalloy 617," *J. Nucl. Mater.*, vol. 454, no. 1–3, pp. 265–273, 2014.

[101] R. Subramanian, *Strength of Materials*, 2nd Editio. Oxford University Press, 2010.

[102] M. R. Eslami, R. B. Hetnarski, J. Ignaczak, N. Noda, N. Sumi, and Y. Tanigawa, *Theory of Elasticity and Thermal Stresses*, Volume 197. Springer, 2013.

[103] J.E. Hesselgreaves, *Compact Heat Exchangers. Selection, Design and Operation*, 1st Editio. Pergamon, 2001.

[104] J. Wang, Y. Sun, M. Lu, X. Yan, and J. Wang, "Stress Intensity Simulation of Printed Circuit Heat Exchanger for S-CO2 Brayton Cycle," in *5th International Conference on Transportation Information and Safety (ICTIS)*, 2019, pp. 406–410.

[105] H. P. Mahajan and U. Devi, "Finite element analysis of Printed Circuit Heat Exchanger core for high temperature creep and burst responses," in *Proceedings of the ASME 2018 Pressure Vessels and Piping Conference*, 2018, pp. 1–9.

[106] X. Zhang, S. Shi, R. N. Christensen, and X. Sun, "Review on mechanical design of Printed Circuit Heat Exchangers," in *25th International Conference on Nuclear Engineering ICONE25*, 2017.

[107] "Solver Theory Guide," *ANSYS CFX 18.1*. ANSYS Inc., 2017.

[108] J. E. Bardina, P. G. Huang, and T. J. Coakley, *Turbulence Modeling Validation, Testing, and Development*. 1997.

[109] P. Kelly, *Solid Mechanics Lecture Notes: An Introduction to Solid Mechanics*. Auckland: The University of Auckland, 2013.

[110] D. Aquaro and M. Pieve, "High temperature heat exchangers for power plants: Performance of advanced metallic recuperators," vol. 27, pp. 389–400, 2007.

[111] S. J. Yoon, J. O'Brien, P. Sabharwall, K. Wegman, and X. Sun, "Study on effects of heat loss and channel deformation on thermal-hydraulic performance of semicircular straight channel printed circuit heat exchangers," *J. Therm. Sci. Eng. Appl.*, vol. 10, no. 4, pp. 1–14, 2018.

[112] "Helium," *National Institute of Standards and Technology*. [Online]. Available: http://webbook.nist.gov/chemistry/fluid/.

[113] M. Saeed and M. Kim, "Thermal and hydraulic performance of SCO2 PCHE with different fin configurations," *Appl. Therm. Eng.*, 2017.

[114] K. Krishnaiah and P. Shahabudeen, *Applied Design of Experiments and Taguchi Methods*. New Delhi: PHI Learning Private Limited, 2012.

[115] M. Chen, X. Sun, and R. N. Christensen, "Thermal-hydraulic performance of printed circuit heat exchangers with zigzag flow channels," *Int. J. Heat Mass Transf.*, vol. 130, pp. 356–367, 2019.

[116] T. Ma, P. Zhang, H. Shi, Y. Chen, and Q. Wang, "Prediction of flow maldistribution in printed circuit heat exchanger," *Int. J. Heat Mass Transf.*, vol. 152, p. 119560, 2020.

[117] Z. Zheng, A. M. Johnston, D. F. Fletcher, and B. S. Haynes, "Heat exchanger specification: Coupling design and surface performance evaluation," *Chem. Eng. Res. Des.*, vol. 93, no. May, pp. 392–401, 2015.

[118] T. Du, W. Du, K. Che, and L. Cheng, "Parametric optimization of overlapped helical baffled heat exchangers by Taguchi method," *Appl. Therm. Eng.*, vol. 85, pp. 334–339, 2015.

[119] T. Ma, U. Pasquier, Y. Chen, and Q. Wang, "Numerical study on thermal-hydraulic performance of a two-sided etched zigzag-type high-temperature printed circuit heat exchanger," *Energy Procedia*, vol. 142, pp. 3950–3955, 2017.

[120] S. Liu, Y. Huang, and J. Wang, "Theoretical and numerical investigation on the fin eff ectiveness and the fin effi ciency of printed circuit heat exchanger with straight channels," *Int. J. Therm. Sci.*, vol. 132, no. June, pp. 558–566, 2018.

[121] R. M. Manglik and A. E. Bergles, "Heat transfer and pressure drop correlations for the rectangular offset strip fin compact heat exchanger," *Exp. Therm. Fluid Sci.*, vol. 10, no. 2, pp. 171–180, 1995.